Alma Mater Studiorum
Università degli studi di Bologna

DIPARTIMENTO DI FISICA E ASTRONOMIA
Dottorato di Ricerca in Astronomia
CICLO XXVII

Galaxy evolution in the VIMOS public extragalactic redshift survey (VIPERS)

Dottorando
Iary Davidzon

Relatori
Dott.ssa Micol Bolzonella
Dott.ssa Olga Cucciati
Prof. Lauro Moscardini

Coordinatore
Prof. L. Moscardini

Settore Concorsuale: 02/C1 – Astronomia, Astrofisica, Fisica della Terra e dei Pianeti
Settore Scientifico-Disciplinare: FIS/05 – Astronomia e Astrofisica

Chi cerca sapienza, trova dolore.

Giordano Bruno
De la causa, principio e uno

Contents

Introduction

The past decade has seen significant advances in the study of galaxy evolution prompted by large astronomical surveys. They have been devised to conduct a census of star-forming and quiescent galaxies at different redshifts, to understand how they grow across cosmic time. By sampling wide portions of the sky, these surveys collect large amounts of data, thus facilitating a number of important statistical studies. Thanks to the development of multi-band photometry and high-quality spectroscopy, estimating galaxy stellar mass ($\mathcal{M}$) has become a feasible (and fundamental) step in these analyses, because one of their main goal is to describe mass assembly and star formation history of galaxies. Moreover, stellar mass can trace, better than luminosity, the dark matter haloes in which galaxies reside (except for the bias factor). Thanks to such a relation one may provide useful constraints to cosmological models.

The galaxy stellar mass function (GSMF), defined as the co-moving number density of galaxies within a stellar mass bin, is one such fundamental statistic, allowing us to trace the history of baryonic mass assembly and its conversion into stars for various galaxy types. Measurements of the GSMF can be used to investigate how galaxy properties change as a function of stellar mass, redshift, and environments (e.g. Bundy et al. 2006; Pozzetti et al. 2007; Bolzonella et al. 2010; Ilbert et al. 2010; Vulcani et al. 2012, and many others) and also helps to put constraints to the cosmic star formation rate (SFR, see e.g. Pozzetti et al. 2010; Behroozi et al. 2013; Ilbert et al. 2013).

In the nearby universe, the total mass function, i.e. the GSMF for all galaxies observed in a given volume, has been measured to high accuracy by exploiting the Two Micron All Sky Survey[1] (2MASS), the 2dF Galaxy Redshift Survey[2] (2dFGRS), and the Sloan Digital Sky Survey[3] (SDSS). The first estimates, at the beginning of the XXI century, were obtained by Cole et al. (2001) and York et al. (2000), with 2dFGRS and SDSS data respectively. Subsequent work has been carried out mainly relying on SDSS data (e.g. Baldry et al. 2008; Li & White 2009; Baldry et al. 2012).

At higher redshift, such statistical studies are more challenging because of the faintness of the objects, which decrease the probability to detect some of the sources. Early seminal work took advantage of the Hubble Space Telescope to construct samples of a few hundred galaxies up to $z \simeq 3$, finding evidence of an increase in the average stellar mass density with cosmic time (Rudnick et al. 2003;

---

[1] http://www.ipac.caltech.edu/2mass/
[2] http://www2.aao.gov.au/2dfgrs/
[3] http://www.sdss.org

Dickinson et al. 2003; Fontana et al. 2003). Later, deeper surveys were able to show the lack of evolution at the high-mass end of the GSMF (Fontana et al. 2006, using the GOODS-MUSIC catalogue), which contrasted with an increase in galaxy density at lower masses (VVDS survey, Pozzetti et al. 2007). This is a result that is consolidated up to $z \simeq 4$ by means of near- and mid-infrared data, which facilitate better estimates of the stellar masses (Pérez-González et al. 2008; Kajisawa et al. 2009). Although some disagreements exist, such findings indicate that massive galaxies were assembled earlier than those with lower stellar mass, suggesting that a "downsizing in stellar mass" has taken place (Fontanot et al. 2009).

Besides these studies, first attempts to study the stellar mass function by dividing blue/active from red/quiescent galaxies provided interesting results. Despite the relatively limited statistics, they revealed that within the mass function the number of blue galaxies at intermediate masses (about $10^{10}\,\mathcal{M}_{\odot}$) decreases as a function of cosmic time, while the fraction of red galaxies increases (e.g. Bundy et al. 2006; Borch et al. 2006). This early work was extended using larger galaxy samples (as in COSMOS and zCOSMOS, Drory et al. 2009; Ilbert et al. 2010; Pozzetti et al. 2010) or very deep observations (GOODS-NICMOS survey, Mortlock et al. 2011), which produced robust results for the evolution in number density of both these galaxy populations.

A fundamental picture emerging from these studies is the transformation of star-forming galaxies into "red and dead" objects through some physical mechanism that halts the production of new stars. Observations suggest the migration from the "blue cloud" to the "red sequence" (Faber et al. 2007) to be rapid, with a timescale of $\sim 1\,\mathrm{Gyr}$ (Bell et al. 2004; Blanton 2006). Moreover, the process seems to depend on several galaxy properties, like stellar mass or halo mass (see e.g. Kauffmann et al. 2003a; Behroozi et al. 2010). The suppression of star formation is needed to explain the GSMF shape and composition, as well as the features of the luminosity function (e.g. Benson et al. 2003). Moreover, the total stellar mass density obtained by integrating the mass function is much less than the total mass density of baryons, indicating that the formation of stars is a very inefficient process, i.e. a large fraction of galactic gas is not able to collapse and form stars. Various mechanisms have been proposed in the literature to explain such a quenching of star formation.

- Virial shock heating produced by the inter-galactic gas falling into the galaxy halo (see e.g. Birnboim & Dekel 2003; Kereš et al. 2005). During the infall, gas energy is converted from gravitational to thermal. The result is a halo of hot virialised gas that prevents (by shock heating) new supplies of cold gas to form stars. This mechanism is efficient in haloes with masses $\gtrsim 10^{12}\,\mathcal{M}_{\odot}$, and thus it is able to explain the exponential decline of the GSMF, which starts at stellar mass values of about $10^{11}\mathcal{M}_{\odot}$.[4]

- Action of active galactic nuclei (AGN). They can be low-luminosity AGN with extended radio lobes ("radio-mode" feedback, Croton et al. 2006) or bright ones triggered by merging with another galaxy ("quasar mode" Springel et al.

---

[4] An estimate of the relationship between dark matter halo and galaxy stellar mass is provided e.g. in Moster et al. (2010, 2013).

2005a; Di Matteo et al. 2005). The processes impacting the surrounding can be mechanical (radio jets and wind) or radiative (Ciotti et al. 2009). In both cases, the AGN heats and/or expel gas from the halo, thus preventing further cooling and star formation.

- Supernovae explosions and stellar winds (Dekel & Silk 1986; Efstathiou 2000) are also able, by means of either shock waves or radiative pressure, to reduce the SFR (Thacker et al. 2000; Springel & Hernquist 2003; Oppenheimer & Dave 2006).

- In the assumption that the reservoir gas falls into the galaxy through cosmic filaments (the so-called cold streams described in Dekel et al. 2009b,a), if these streams contain dense clumps they can stabilise the galactic disc and suppress star formation.

- Dark matter feedback, e.g. neutralino annihilations generating relativistic particles that suppress the cooling flow (see Totani 2005).

To distinguish between these processes, it is crucial to obtain precise and accurate measurements to constrain theoretical models (Lu et al. 2012b; Mutch et al. 2013; Wang et al. 2013). Unfortunately, such comparisons are hard. On one side, modelling galaxy evolution, when based on N-body dark matter simulations (e.g. De Lucia & Blaizot 2007; Bower et al. 2006; Guo et al. 2011, 2013), requires a high level of complexity to parametrise all the physical processes (SFR, supernova ejecta, etc.). This is true for all the models based on N-body dark matter simulations, either using so-called semi-analytical (e.g. Bower et al. 2006; De Lucia & Blaizot 2007; Guo et al. 2013) or hydrodynamical (e.g. Finlator et al. 2007; Vogelsberger et al. 2014; Schaye et al. 2014) treatment of baryons. On the observational side, instead, it is hard to attain the precision required to constrain models, especially for the most massive galaxies, which are highly affected by sample variance and small-number statistics. Moreover, uncertainties in redshift measurements and stellar mass estimates make the analysis even more complicated (Marchesini et al. 2009, 2010).

The latest galaxy surveys are helping with improved measurements of the GSMF and could shed light on the discrepancies between data and models (BOSS, Maraston et al. 2013). State-of-the-art analyses provide new evidence suggesting the dependence on cosmic time and stellar mass of the physical processes that extinguish star formation: from $z = 3$ to $z = 1$, the density of quiescent galaxies increases continuously for $\mathcal{M} \gtrsim 10^{10.8}\,\mathcal{M}_\odot$ (Ilbert et al. 2013, using UltraVISTA data), while at $z < 1$ it evolves significantly at lower masses (Moustakas et al. 2013 using PRIMUS data).

The GSMF is also an effective tool to statistically describe galaxies in various environments, as demonstrated by the abundance of investigations in the literature (e.g. Baldry et al. 2006; Bundy et al. 2006; Bolzonella et al. 2010; Vulcani et al. 2012; Giodini et al. 2012; Annunziatella et al. 2014). From an observational point of view, after many decades from the first pioneering work (e.g. Oemler 1974; Davis & Geller 1976; Sandage & Visvanathan 1978), understanding the role of environment in driving galaxy evolution is still a frontier research. It is commonly accepted

that, in addition to internal processes, the influence of the external conditions has also to be considered. However, whether this influence is of major importance, or rather a secondary effect, represents an open issue (cf Cucciati et al. 2010; Iovino et al. 2010; Peng et al. 2010b; Cooper et al. 2012; Peng et al. 2012; Knobel et al. 2014). The first studies were focused on the striking observational fact that early-type galaxies preferentially resides in cluster cores, while late-type ones are more common in the outskirts or in the general field. This property, the so-called morphology-density relation (Dressler 1980; Postman & Geller 1984), is observed not only when contrasting the densest regions with those scarcely populated: the mix between early- and late-type changes gradually from the former to the latter, over the whole range of local densities (Treu et al. 2003; Weinmann et al. 2006). Many other correlations have been observed in the local universe between the conditions in which galaxies reside and their internal properties, such as colour (more galaxies are red in dense environment, see e.g. Balogh et al. 2004; Cucciati et al. 2010) and star formation rate (which is on average higher in regions less populated, Lewis et al. 2002; Gómez et al. 2003).

These correlations indicate that also the environment should be responsible (at least in part) for quenching star formation, and even for the entire disruption of the galaxy. Theoretical studies proposed several physical mechanisms to interpret those phenomena, the most important being enumerated here.

- Galaxy mergers between gas-rich galaxies may trigger episodes of star formations and AGN (Barnes & Hernquist 1991; Mihos & Hernquist 1994, 1996), but after that the SFR is expected to decline quickly, e.g. because stellar wind feedback (Di Matteo et al. 2005).

- A peculiar kind of merger involves galaxies in the dense environment of clusters. They lose their energy and momentum because of dynamical friction (see Chandrasekhar 1943, for more details) and sink towards the cluster core, merging with the central galaxy. Numerous studies (e.g. Ostriker & Tremaine 1975) point to such a "galactic cannibalism" being responsible for the formation of cD galaxies.

- Besides mergers, during galaxy encounters tidal forces may strip material from the outer parts of the galaxy, forming tidal tails and streams (e.g. Farouki & Shapiro 1981; Moore et al. 1996). In a cluster of galaxies, multiple (high-speed) encounters should modify (or destroy) the structure of the galaxy that goes through them (Moore et al. 1998, 1999). This kind of "galaxy harassment" removes gas and prevents it to collapse and form stars. Tidal interactions can also drive disc instabilities that funnel gas towards the galactic centre, then triggering nuclear activity.

- Also the interaction with the intra-cluster medium (ICM) has been shown to play a role in the cessation of galaxy activity (Gunn & Gott 1972). In fact, if the ram pressure experienced by the galaxy is strong enough, it may strip its cold gas component. Other effects due to interactions between galaxy and ICM can be considered as quenching mechanisms, e.g. thermal evaporation (Cowie & Songaila 1977) and Kelvin-Helmholtz instability (Nulsen 1982).

- A more gentle process than ram-pressure stripping should remove only the outer part of the galaxy (i.e., their hot halo, which is weakly bound to the system). Without this gas reservoir, the SFR gradually declines, and the galaxy becomes passive in a few Gyr (Larson et al. 1980). This process may happen when a galaxy becomes a satellite within a more massive halo (van den Bosch et al. 2008).

However, how these mechanisms actually work in the real universe remain poorly understood (see e.g. Boselli & Gavazzi 2006; Blanton & Moustakas 2009, to find reviewed most of the open issues). Even the well-established morphology-density relation has a number of contrasting interpretations. In fact, it may be related to slow (e.g. ram pressure) stripping that can transform spiral galaxies into "anemic" spiral and later (by fading) into elliptical galaxies (van der Wel et al. 2010; Cappellari et al. 2011). On the other hand, a scenario involving galaxy interactions and mergers has been proposed (Thomas et al. 2010).

In this kind of investigations, a major complication is the interplay between the quantities of interest (e.g. light profile, stellar mass, colours, etc.): some of these quantities could seem influenced by the environment only because they are connected to another galaxy property that is in turn environment-dependent. Such indirect correlations can be disentangled by studying the variation of one parameter, keeping fixed the others. With this approach, Blanton et al. (2005) show that structural properties of local galaxies depend only weakly on environment, after dividing the sample in bins of luminosity and colour. Skibba et al. (2009) also come to similar conclusions by using marked statistics, i.e. computing correlations functions in which each galaxy receives a particular weight (a "mark") depending on a given characteristic (see Sheth 2005). These studies, at odds with those mentioned before, suggest that the only quantity truly connected to the environment is either the stellar or halo mass of the galaxy, whereas the other properties show an environmental dependence just because they are related to mass.

Also at higher redshifts, several questions remain open. Looking at $z \sim 1$, Elbaz et al. (2007) and Cooper et al. (2008) observed the average SFR increasing with local galaxy density, i.e. the opposite of what occurs locally. Although confirmed by other work, this finding has been challenged by recent analyses (see Ziparo et al. 2014). Also the detection of the colour-density relation is uncertain at such redshifts: according to Cooper et al. (2007, 2010) it seems to be already in place at $z < 1.2$, while Cucciati et al. (2006, 2010) observed a flattening in the relation at $z \sim 1$ and possibly a reversal at $z > 1.2$.

In such a complex scenario, it is important to chose an adequate framework. What happens during the lifetime of a galaxy is often thought to be determined by either "nurture" (the surrounding conditions) or "nature" (its intrinsic properties, especially stellar mass); while various authors consider both of them having a major impact (e.g. Gómez et al. 2003; Gallazzi et al. 2009; Bolzonella et al. 2010), others look at the galaxy stellar mass ($\mathcal{M}$) as the main evolutionary driver, with the environment giving a secondary or even negligible contribution (e.g. Pasquali et al. 2009; Thomas et al. 2010; Grützbauch et al. 2011). However, this dichotomy is simplistic, as stellar mass and environment are inter-connected through the halo mass: given the distribution of dark matter haloes, the most massive galaxies

preferentially reside in overdense regions (Kauffmann et al. 2004; Abbas & Sheth 2005; Scodeggio et al. 2009b). For this reason, it is misleading to contrast them as two separate aspects of galaxy evolution (see discussion in De Lucia et al. 2012)

Another crucial point is how the environment is defined. One possibility is to identify high-density regions as galaxy groups and clusters, in opposition to a low-density "field", sometimes ambiguously defined. When halo mass estimates are used, the classification is more tightly related to the underlying distribution of dark matter, with galaxies often divided in satellite and central objects (van den Bosch et al. 2008). Other methods, involving galaxy counts, can identify a broad range of densities with a resolution from a few Megaparsecs down to $\sim 100\,\text{kpc}$; for instance, they are based on two-point clustering (e.g. Abbas & Sheth 2005), Voronoi tessellation (e.g. Marinoni et al. 2002), or the galaxy number density inside a window function (regarding this last kind of estimators, see the comparison by Muldrew et al. 2012). With respect to the scales probed, several studies questioned the importance of the large-scale environment, favouring the picture in which galaxies are affected by external factors mostly on sub-halo scales (e.g Kauffmann et al. 2004; Vulcani et al. 2012). However, other investigations measured environmental dependence of galaxy properties over scales larger than the halo virial radius

Within this context, the VIMOS Public Extragalactic Redshift Survey (VIPERS) provides a novel opportunity. As we describe here, this survey provides a combination of wide angle coverage, depth, and sampling that proves to be ideal for measuring the GMSF at $z \sim 1$ with unprecedented precision. The large volume allows effective probing of the massive end of the GSMF at these redshifts: at the high-mass end, where a few interlopers can dramatically change the shape of the GSMF, accurate spectroscopic redshift measurements are crucial for avoiding contaminations. VIPERS also represents an excellent laboratory to study the galaxy environment. Contrasting the GSMF estimated in regions of low/high galaxy density may provide new clues on how environment affects galaxy evolution.

In this work I present the first measurements of the GSMF from the first public release of the VIPERS catalogue, containing $\sim 55\,000$ objects.

- In Chapter 1, I present the survey design, its scientific goals, the redshift measurement and validation. I also describe the galaxy catalogue that will be used here, which in addition to spectroscopic redshifts includes also photometric data from other surveys.

- Chapter 2 provides details about how galaxy quantities (absolute magnitudes, stellar mass, SFR) have been estimated by fitting their spectral energy distribution (SED). I also apply alternative techniques to estimate galaxy stellar masses and SFRs. The comparison of the latter with the SED fitting technique serves to strength the results and gives an idea of the general uncertainties in this kind of estimates.

- The stellar mass function of the whole VIPERS field is presented in Chapter 3, along with a discussion on the sample completeness and the main sources of uncertainties that could become dominant at the level of precision allowed by the VIPERS data. The VIPERS mass function is compared with the

literature to show the improvements with respect to previous work. A comparison with models is also performed. Then, I focus on the evolution of the GSMF from $z = 1.3$ down to $z = 0.5$, i.e. within the range covered by the VIPERS data, for the whole galaxy sample and separately for different galaxy populations. I discuss in detail the potential systematic effects and their impact on the study of galaxy evolution. In particular, I show how different classifications of galaxy types (e.g. colours, SFR, spectral features) lead to complementary results, which have to be carefully interpreted.

- Chapter 4 contains a description of the VIPERS environment, starting from the computation of local density contrast to the definition of low- and high-density regions. After posing this classification, I estimate the GSMF in the two environments, also considering the passive and active galaxy samples separately. Once compared to each other, the mass functions in low/high densities show differences in their shape and normalisation (which is obtained by means of Voronoi decomposition). I interpret these differences, and their evolution across cosmic time, by using the empirical approach of Peng et al. (2010b).

- Chapter 5 concludes this work, summarising the main findings and the future perspectives.

Unless specified otherwise, the cosmological framework of this work assumes $\Omega_m = 0.25$, $\Omega_\Lambda = 0.75$, and $h_{70} = H_0/(70\,\mathrm{km\,s^{-1}\,Mpc^{-1}})$. All the magnitudes are in the AB system (Oke 1974).

Chapter 1

VIPERS: the VIMOS Public Extragalactic Redshift Survey

VIPERS is a redshift survey that aims at observing $\sim 100\,000$ galaxies and active galactic nuclei (AGN) at intermediate redshifts ($\langle z \rangle \sim 0.8$) in the magnitude range $17.5 \leqslant i \leqslant 22.5$. The survey is planned to cover nearly $24\,\mathrm{deg}^2$ within two fields of the Canada-France-Hawaii Telescope Legacy Survey Wide[1] (CFHTLS-Wide), namely W1 and W4.

The first public data release, consisting of $57\,204$ spectroscopic redshift measurements, is presented in Garilli et al. (2014) and is now available on the survey database[2]. The sky region covered at present is $\sim 7.5\,\mathrm{deg}^2$ in each field, with an effective area of $5.34\,\mathrm{deg}^2$ in W1 and $4.97\,\mathrm{deg}^2$ in W4 after accounting for the photometric and spectroscopic masks. Once completed, VIPERS will be the largest spectroscopic survey at such redshifts in terms of volume explored ($\sim 1.5 \times 10^8\,\mathrm{Mpc}^3\,h_{70}^{-3}$), at least until the development of next-generation instruments like the European Extremely Large Telescope (E-ELT) and the James Webb Space Telescope (JWST). All details about the survey design and construction can be found in Guzzo et al. (2014).

From a cosmological perspective, the main goals of VIPERS are measuring the growth rate of structure (de la Torre et al. 2013), providing new constraints to cosmological parameters (Bel et al. 2014; Di Porto et al. 2014), describing the relation between baryons and dark matter through galaxy clustering (Marulli et al. 2013). Other science drivers refer to extragalactic astrophysics, i.e. a research field in which the statistical power of the VIPERS data can be extremely useful to study a wide range of galaxy properties at an epoch when the Universe was about half its current age (e.g. Marchetti et al. 2013; Małek et al. 2013; Davidzon et al. 2013; Fritz et al. 2014).

The spectroscopic survey (described in Sect. 1.1) is complemented by photometric data (Sect. 1.2) obtained from public surveys and dedicated observations. Such ancillary data are crucial to estimate several galaxy properties with high precision, in particular galaxy stellar masses and rest-frame magnitudes. To conclude this Chapter, I also give a brief overview of the AGN sample and its possible use.

---

[1] `http://www.cfht.hawaii.edu/Science/CFHLS/`
[2] `http://vipers.inaf.it`

1.1 Spectroscopic data

The spectroscopic catalogue used in this work is the first VIPERS Public Data Release (PDR-1). The candidates to be spectroscopically observed are CFHTLS sources in the two fields mentioned above, in the magnitude range $17.5 \leqslant i \leqslant 22.5$. They were selected via two criteria (SC1 and SC2), both of them relying on the CFHTLS optical photometry (i.e. u, g, r, i, z images and magnitudes, see Sect. 1.2).

SC1) The first selection criterion was aimed at separating galaxies from stars. It relies on a point-like classification and on comparing the five optical magnitudes with galaxy and stellar spectral energy distributions (see Coupon et al. 2009). The point-like classification is based on measuring the half-light radius, i.e. the radius of the circle containing half of the objects flux in the selection band. Point-like sources resulting from this selection are targeted as AGN candidates when located in the AGN *loci* of two colour diagrams, namely $(g - r)$ vs $(u - g)$ and $(g - i)$ vs $(u - g)$ (see details in Garilli et al. 2014).

SC2) The second selection criterion is based on the $(g - r)$ and $(r - i)$ colours. We kept only object for which

$$(r - i) > 0.5(u - g) \ \lor \ (r - i) > 0.7 \ . \tag{1.1}$$

This condition was applied to exclude low-redshift ($z < 0.5$) objects, and has been tested to ensure it does not introduce any significant bias. The effectiveness of such a selection is verified in the sky region where VIPERS overlaps with the VVDS-Deep survey (Fig. 1.1). According to the VVDS measurements, most of the low-redshift objects lie below the boundary (orange circles in Fig. 1.1a). Only in a few cases galaxies with known redshift > 0.5 are not selected *a priori* as VIPERS target (Fig. 1.1b). It is important to note that the distance of a galaxy from the threshold is a monotonic function of redshift.

Once selected the targets, the spectroscopic observations were carried out using the VIMOS instrument on VLT (Le Fèvre et al. 2003). An alternative approach instead of SC1 and SC2 could have been using photometric redshifts obtained from the five optical magnitudes. Although such a technique provides comparable performance in terms of completeness and contamination, the VIPERS team preferred to apply the colour selection described above, because it can be reproduced precisely at any time, whereas photometric redshifts depend inevitably on specific features (like the adopted templates) that periodically change thanks to new improvements.

1.1.1 Observations

During the VIPERS campaign, the VIMOS spectrograph was set with the LR-Red grism ($R = 230$), giving a wavelength range of 5 500–9 500 Å that guarantees the observability of the main spectral features in the VIPERS redshift range, e.g. the absorption lines CaII H & K $\lambda\lambda 3934, 3969$ and the emission line [OII] $\lambda 3727$ (see Fig. 1.2). Each pointing is observed for a total time of 2 700 s, during five exposures
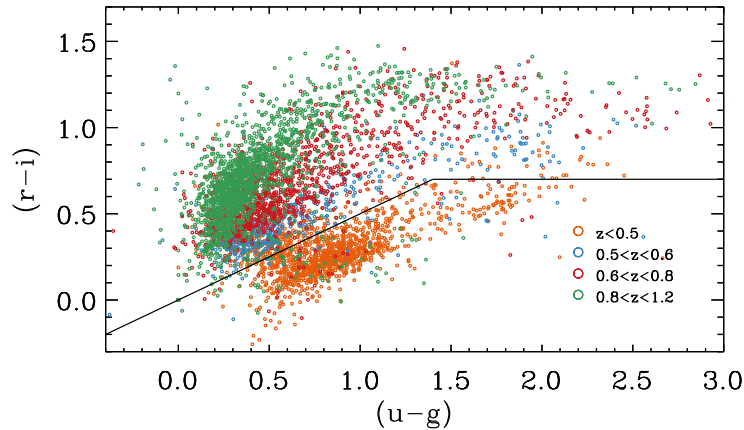
(a)
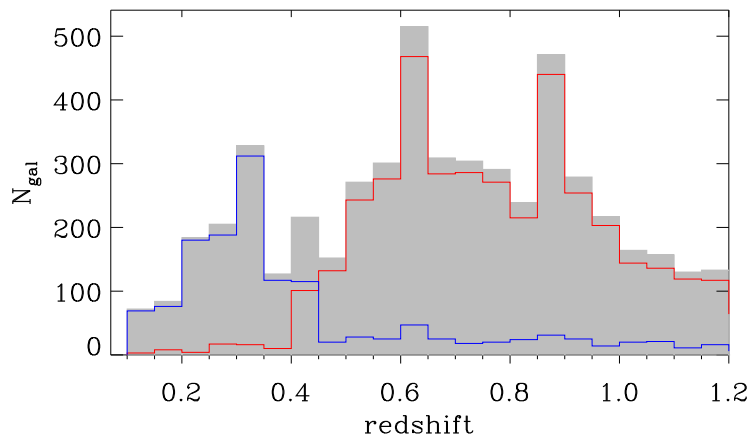
(b)

Figure 1.1   Testing the VIPERS selection criterion SC2 by means of galaxies already observed in the VVDS-Deep survey (Le Févre et al. 2005). In the colour-colour diagram (*panel a*) the black solid line represents Eq. (1.1), used to separate candidate targets from galaxies expected to be at $z < 0.5$ (see z-bins in the legend). The VVDS sample is used also in *panel (b)*: the red-solid histogram is the redshift distribution of objects that were above the green line in the $(r-i)$ vs $(u-g)$ diagram, while the blue-dashed histogram includes those lying in the low-redshift *locus*. The dotted black line shows dN/dz of the total sample.

of nine minutes each. Spectroscopic slits are $1''$ wide. To minimise the impact of atmospheric refraction, slits are aligned along the East-West direction.

To maximise the multiplex capability of VIMOS, the VIPERS team adopted the observational strategy described in Scodeggio et al. (2009a): in the slit positioning optimization process, the size of the sources is arbitrarily assumed equal to $0.5''$. In this way, the number of objects per quadrant increases. The drawback of this approach is that bigger objects may fill most of the slit, whose width is $1''$, making the spectral extraction fail. Despite that, Garilli et al. (2014) verified *a posteriori* that only few among the brightest objects suffer from this problem. Using short slits (the median length is $7''$), the VIPERS survey reached a sampling rate of approximately 40% with a single VIMOS pass, with a median of 87 slits per quadrant (Garilli et al. 2014). This achievement is essential e.g. to estimate the large-scale environment (Cucciati et al., in prep.; Iovino et al., in prep.).

Since the coverage of the VIPERS field is conducted with a single pass of the instrument, the spectroscopic masks that describe the spectroscopically observed area reproduce the footprint of the VIMOS instrument, with $2''$ gaps that separate the four CCD quadrants. As a whole, each VIMOS pointing covers $224\,\mathrm{arcmin}^2$ (see Fig. 1.3). Vignetted parts of the quadrants have been removed to compute the effective area. When preparing the spectroscopic masks, at least $1.8''$ are added on each side of the lists, for sky subtraction (an example of such masks is shown in Fig. 1.3). A few quadrants are missing (cf Fig. 1.4) because of problems in the VIMOS set-up, e.g. during the insertion of the masks with the slits layout.

1.1.2   Data processing

Data reduction and redshift measurements were performed within the software environment Easylife (Garilli et al. 2012), which is based on the VIPGI pipeline (Scodeggio et al. 2005) and EZ (Easy redshift, Garilli et al. 2010). Once automatically measured by the EZ pipeline, the spectroscopic redshifts were then checked and validated independently by two team members, who also assign a quality flag to the measurement (z_{flag}). In case of any discrepancy (in redshift or flag), they were reconciled by direct comparison. In the vast majority of cases, this further step involved spectra with very low S/N, not used in most of the studies.

In general, the quality flag is assigned according to the expected confidence level (CL), based on a well-established scheme developed by previous surveys like VVDS (Le Févre et al. 2005) and zCOSMOS (Lilly et al. 2009). The scheme is exemplified in Fig. 1.2. Spectra with high signal-to-noise ratio (S/N), for which the validators can assess the redshift with $> 95\%$ CL, are classified as $z_{\mathrm{flag}} = 4$. Flag 3 is used when the S/N is lower, but the redshift estimate still has a high probability (comparable to a flag 4) of being correct. Less secure measurements ($\sim 75\%$ CL) result in $z_{\mathrm{flag}} = 2$. In case of tentative measurements ($\lesssim 50\%$ chance to be correct) the quality flag is equal to 1, while it is 0 when z_{spec} is not measurable. Flag 9 was assigned to spectra that do not show any clear feature but one secure emission line (most of the time [OII] emission). For broad-line AGN a similar scheme is adopted, but with z_{flag} values increased by 10. Each spectroscopic flag also has a decimal digit specifying the agreement with the photometric redshift computed from CFHTLS photometry (Coupon et al. 2009). However, for sake of simplicity, in
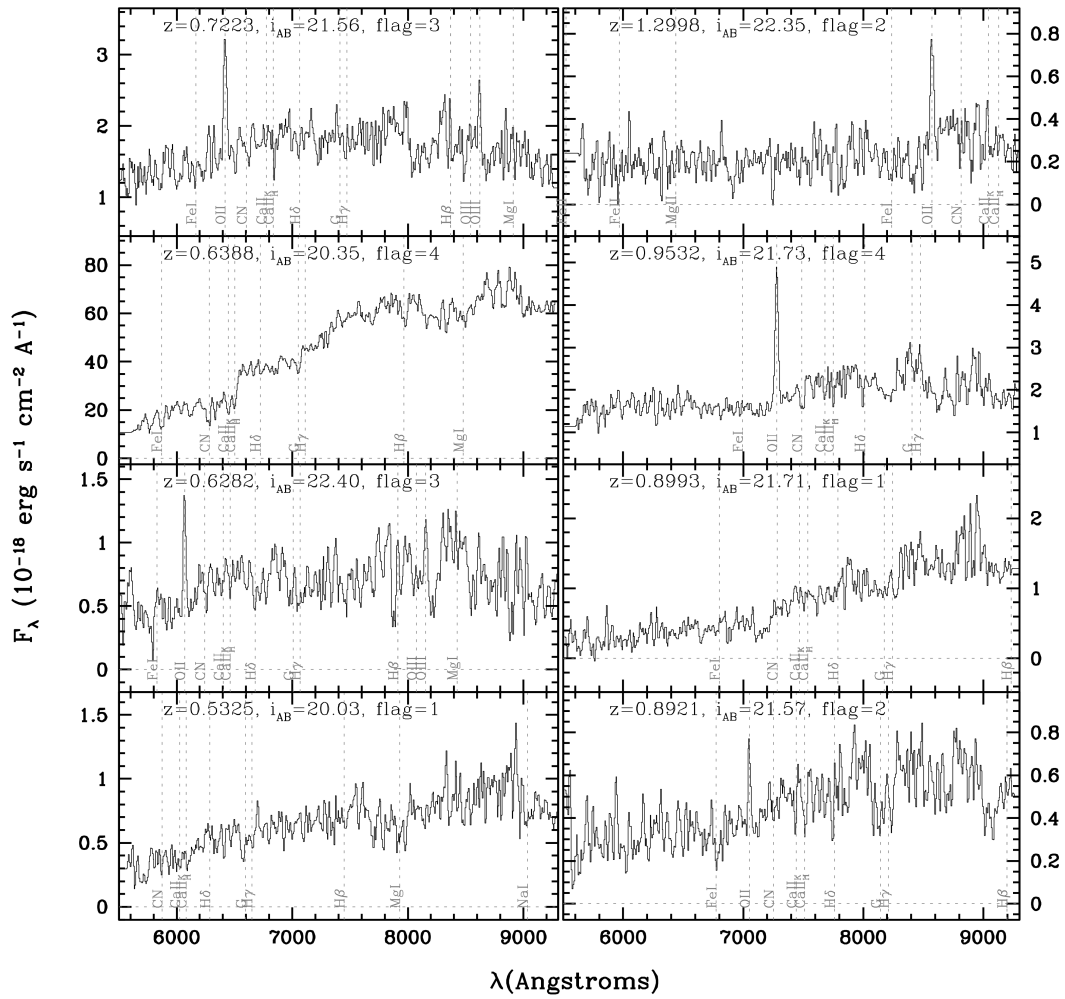
Figure 1.2 Examples of VIPERS spectra of early- and late-type galaxies at various redshifts. Redshift measurements have different accuracy (i.e., $1 \leqslant z_{\text{flag}} \leqslant 4$). The typical spectral features are marked. From Guzzo et al. (2014).
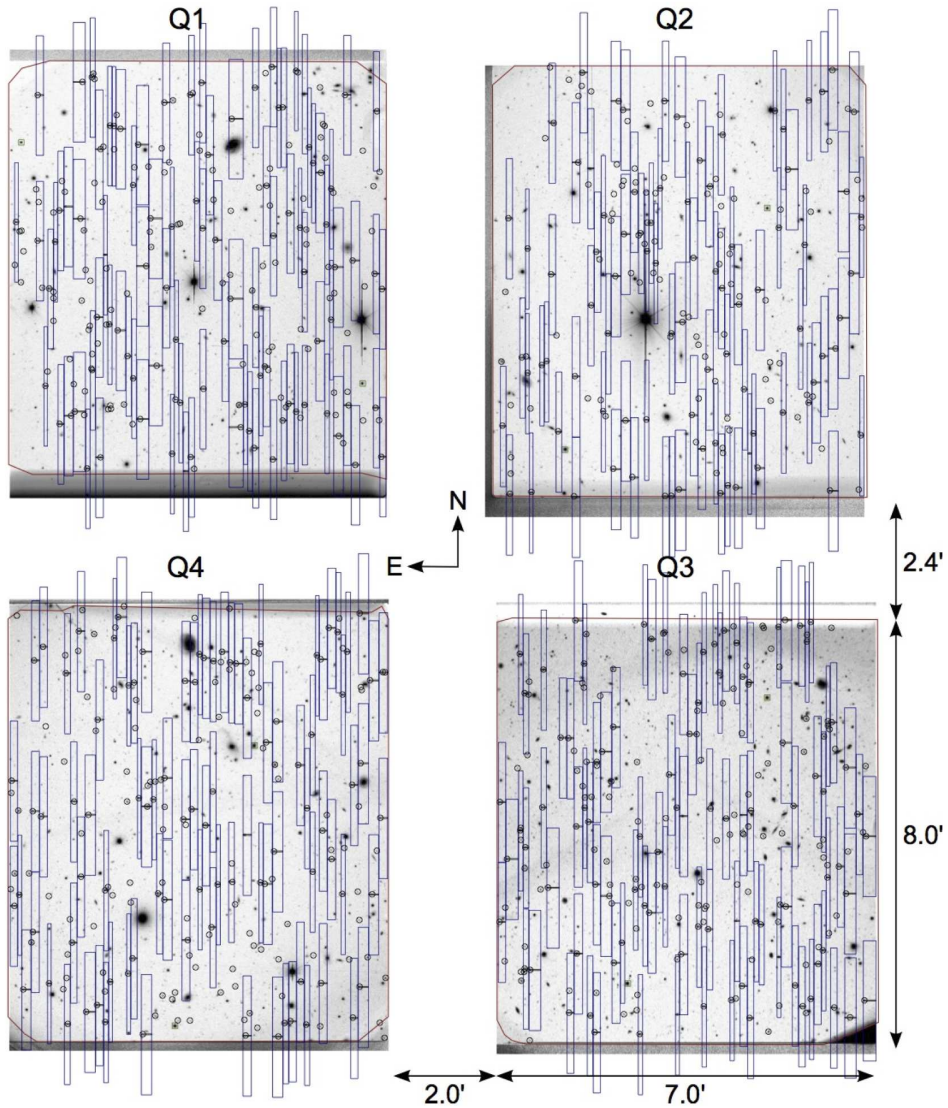
Figure 1.3　The four CCDs of VIMOS, observing an area of the W1 field. In each quadrant, blue rectangles are the slits placed by VMMPS, the software for automatic optimisation of positions and number of slits (Bottini et al. 2005). Note that the borders of the illuminated area do not coincide with the quadrant size. Since in general these borders vary pointing-by-pointing, they are traced and reconstructed (solid red lines) through an automatic detection algorithm. From Guzzo et al. (2014).
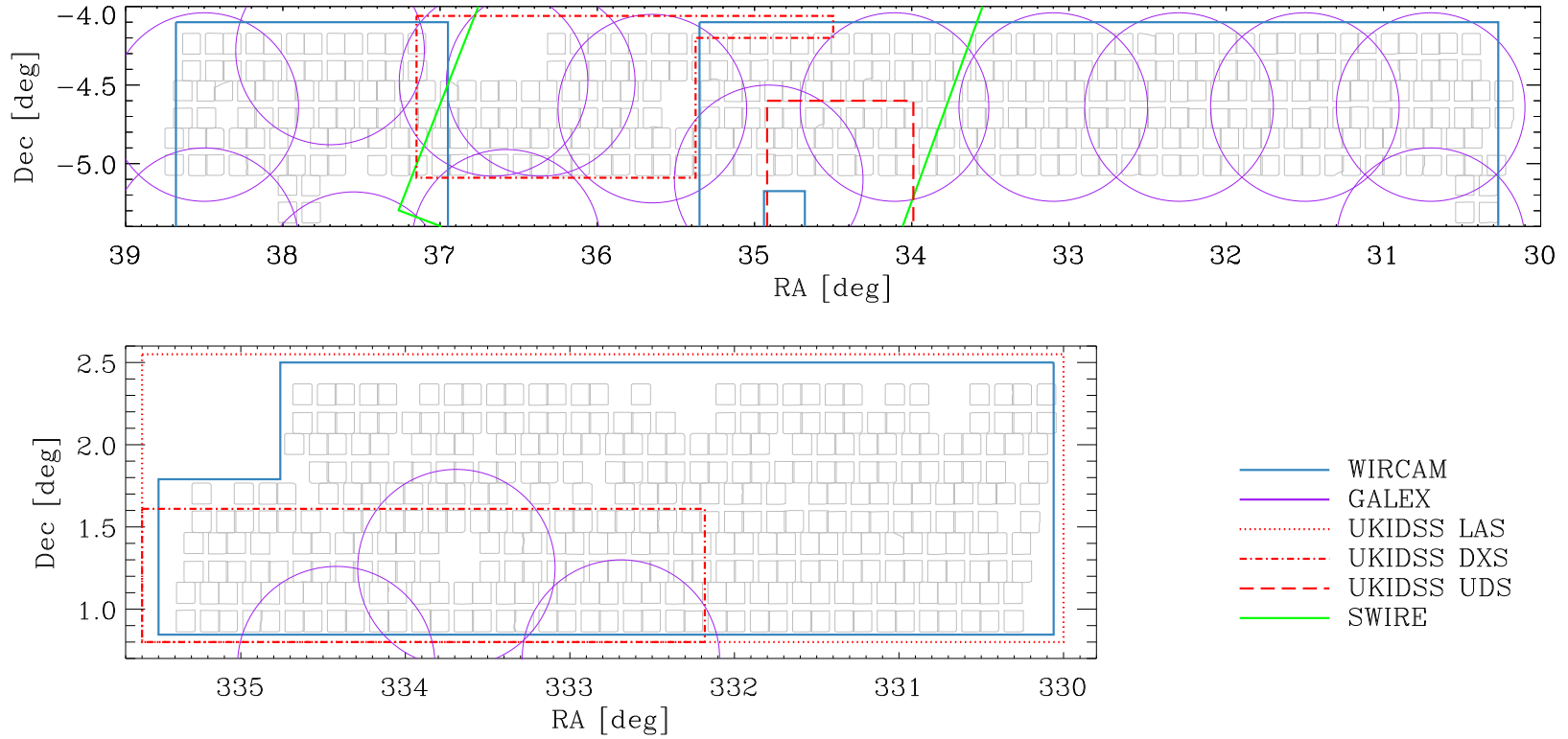
Figure 1.4 The coverage of ancillary data over the two VIPERS fields (W1 and W4 in the upper and lower panels, respectively). The W1 view is limited to the region sampled by VIPERS until now. Each survey is shown with a different colour (see bottom right legend), while grey quadrants are the VIMOS pointings that led to the spectroscopic catalogue used in this work.

the following analysis I will consider only the integer part of each flag (see Fig. 1.5).

After excluding 3 394 objects with no redshift measurement ($z_{\mathrm{flag}} = 0$) and 1 750 stars, the PDR-1 sample contains 53 608 extragalactic sources, nearly equally split between the two fields. The quality of redshift measurements can be verified using objects observed twice. For the sample with spectroscopic flags larger than 2, it is very high, with an estimated CL > 99% (i.e. for almost all those multiple observations, z_{spec} estimated from the two spectra coincide with each other). For flags equal to 2, the confidence remains above 95%, higher than the indicative threshold fixed *a priori*.

Moreover, the sample of objects spectroscopically observed twice can also be used to estimate the uncertainty (σ_z) on the full procedure (reduction and z measurement). Part of the objects with a repeated (and reliable) redshift measurement lie on the border of quadrants (they were therefore observed by two independent pointings that slightly overlap). Other duplicates come from the full re-observation of a few pointings, e.g. after the CCD refurbishment in 2010, when some tiles were observed again to verify the performances with the new set-up (Hammersley et al. 2010). Currently, the duplicate entries in the VIPERS database (with $z_{\mathrm{flag}} \geqslant 2$) are 1 622. I used the distribution of the differences between these double measurements to estimate the redshift error of the sample, as shown in Fig. 1.6. According to this procedure, I obtain $\sigma_z = 0.00045(1 + z)$, corresponding to a velocity dispersion of $130 \, \mathrm{km \, s^{-1}}$.

Since only a fraction of all the photometric objects have been observed by VI-MOS, statistical weights are required to make this subsample representative of all the galaxies with the same limiting magnitude ($i \leqslant 22.5$) in the survey volume. Such weights are calculated by considering

- the fraction of possible targets that have been actually put into a slit (target sampling rate, TSR),

- the fraction of them that yield secure z measurements and that will be used in the statistical analysis (spectroscopic success rate, SSR),

- and the completeness due to the colour pre-selection of the targets by means of SC1 and SC2 (colour sampling rate, CSR).

The statistical weights can depend on the magnitude, redshift, colour, and angular position of the considered object. For each factor of the statistical weight only the main and relevant dependencies are considered, in order to avoid spurious fluctuations when there are small subsamples. In detail, the TSR is a function of the selection magnitude only, the SSR depends on magnitude and redshift, and the CSR is a function of redshift.

The TSR is defined as the fraction of all observed spectroscopic sources (N_{spec}) with respect to the number of CFHTLS photometric galaxies (N_{phot}) in a given range of apparent magnitude: $\mathrm{TSR}(i, i+\delta i) \equiv N_{\mathrm{spec}}(i, i+\delta i)/N_{\mathrm{phot}}(i, i+\delta i)$. From the limiting magnitude down to $i \simeq 19$, the TSR is nearly constant ($\sim 45\%$), but it starts to decline at $i \lesssim 19$ (Garilli et al. 2014). The magnitude dependency of the brightest objects can be due to the short slits strategy (Sect. 1.1.1) that may
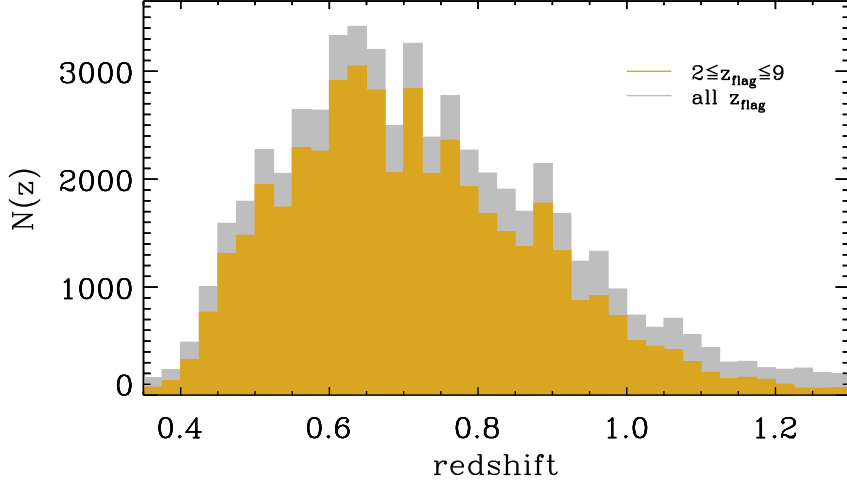
(a)
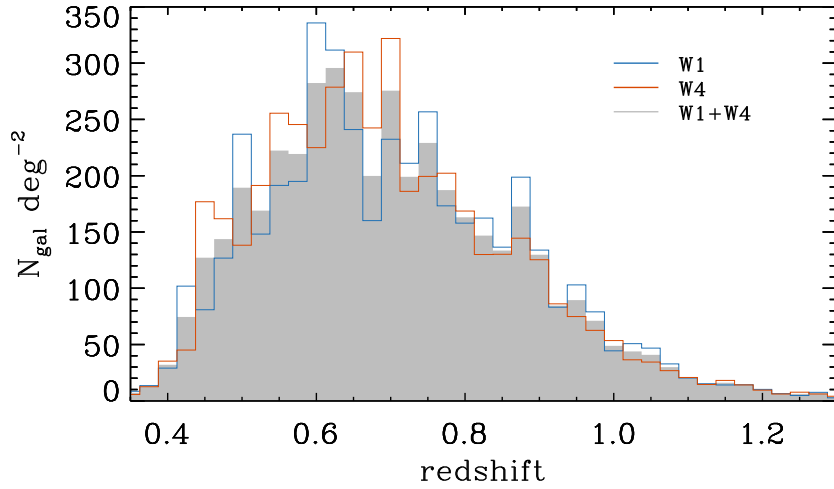
(b)

Figure 1.5 *Panel (a)* shows the redshift distribution of the VIPERS sample, considering all the spectroscopic redshifts ($1 \leqslant z_{flag} \leqslant 9$, grey histogram) or only the reliable ones ($2 \leqslant z_{flag} \leqslant 9$, yellow histogram). *Panel (b)* shows the projected surface density of galaxies with $2 \leqslant z_{flag} \leqslant 9$, considering W1 and W4 independently (blue and red histograms, respectively), and the whole sample (in grey).
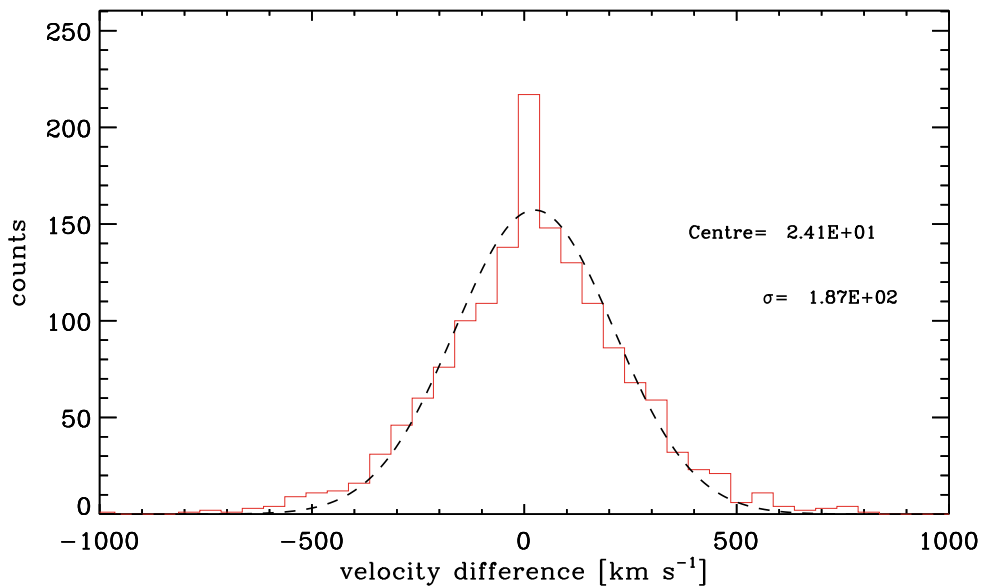
Figure 1.6 Estimate of the uncertainty σ_z (see text) using 1622 re-observed objects with $z_{\mathrm{flag}} \geqslant 2$. When two independent measurements are available, the velocity difference is $\Delta v \equiv c\Delta z/(1 + z)$, where c is the speed of light. The distribution of Δv (red histogram) is well fitted by a Gaussian function with mean $\sim 15\,\mathrm{km\,s^{-1}}$ and dispersion $\sigma \simeq 190\,\mathrm{km\,s^{-1}}$ (dashed line). This translates into an error (for a single object) of $\sigma_z = c\sigma/\sqrt{2} = 0.00045(1 + z)$.

disfavour very large objects. It can be also due to the high angular clustering that characterises the brightest sources, since two slits cannot be placed near each other to observe close pairs.

Regarding the SSR, it is computed by considering the number of reliable redshifts N_{s} among all the measurements N_{spec} within $[i, i + \delta i]$ and $[z, z + \delta z]$. Only galaxies with quality flags between 2 and 9 are included in N_{s} ($\sim 41\,000$ galaxies in the redshift range $0.5 \leqslant z \leqslant 1.2$).

The SSR is sensitive to both the apparent magnitude and redshift. Indeed, it is more difficult to identify spectral features when objects are faint (low S/N) or when they are at a redshift such that principal emission/absorption lines fall in a wavelength range affected e.g. by fringing. Conversely, it can be easier to measure redshifts for strong emission line galaxies, if the emission lines fall within the observed wavelength range.

One can expect also angular variation of TSR and SSR, because of different observing conditions and fluctuations in the surface density of objects from one pointing to another. This dependency is important to describe two-point statistics (e.g. correlation functions) but it is negligible when estimating the galaxy stellar mass function. Such angular-dependent weights, evaluated on a per-quadrant basis, are described in de la Torre et al. (2013).

The CSR accounts for the missed galaxies that do not satisfy SC1 and SC2, although they actually are at $z > 0.5$. This erroneous classification concerns objects at $z \simeq 0.5$, i.e. close to the threshold determined by Eq. (1.1). On the other hand,

galaxies at $0.6 \lesssim z \lesssim 1.2$ are not affected by this kind of incompleteness. In fact, the distance of a galaxy from the threshold in the $(r - i)$ vs $(u - g)$ plane increases as a function of redshift (Fig. 1.1a) at least up to $z \simeq 1.2$. The CSR is estimated by using data from the VVDS survey (Le Févre et al. 2005), which is purely flux limited and shares the same CFHTLS photometry of VIPERS (see details in Guzzo et al. 2014). The measured CSR is well described by the error function $\mathrm{CSR}(z) \equiv 0.5 - 0.5 \, \mathrm{erf}[b(z_\mathrm{t} - z)]$, with $b = 10.8$ and $z_\mathrm{t} = 0.44$. Another way to evaluate the CSR, i.e. by using photometric redshifts, is in good agreement with the previous result, as shown in Garilli et al. (2014, Fig. 10). Eventually, for a galaxy at redshift z with magnitude i, its statistical weight is

$$w(i, z) = \mathrm{TSR}(i)^{-1} \times \mathrm{SSR}(i, z)^{-1} \times \mathrm{CSR}(z)^{-1} \,. \tag{1.2}$$

Once each galaxy in the spectroscopic sample is properly weighed, one can recover the properties of the photometric parent sample starting from the spectroscopic one.

1.2 Photometric data

Photometric data are described below, grouped according to their wavelength range. The coverage of each photometric survey is illustrated in Fig. 1.4. Their main features are summarised in Table 1.1.

1.2.1 Optical data

As mentioned before, the VIPERS spectroscopic sample has been selected from the W1 and W4 fields of the CFHTLS-Wide. Therefore, each galaxy has a photometric baseline consisting of u^*, g', r', i', and z' magnitudes, measured by the Terapix team for the T0005 data release[3]. These magnitudes are `SExtractor`'s MAG_AUTO, derived in double image mode in order to maintain the same aperture in all bands (Bertin & Arnouts 1996). These raw magnitudes have been corrected for Milky Way extinction as follows:

$$\begin{aligned}
u &= u^* - 4.716 \, E(B - V) \\
g &= g' - 3.654 \, E(B - V) \\
r &= r' - 2.691 \, E(B - V) \\
i &= i' - 1.998 \, E(B - V) \\
z &= z' - 1.530 \, E(B - V) \,,
\end{aligned} \tag{1.3}$$

where $E(B - V)$ is the dust extinction derived from the Schlegel et al. (1998) maps at each galaxy's position. Typical errors (including zero-point calibration, tile-to-tile offset, etc.) are on the order of $\Delta \mathrm{mag} = 0.01$–$0.04$ (Fritz et al. 2014). I will refer to this catalogue, limited at $i \leqslant 22.5$, as the photometric VIPERS sample. Applying also SC1 and SC2, the resulting photometric catalogue (a subsample of the previous one) will be called "parent sample". Both samples do not include

---

[3] http://terapix.iap.fr/cplt/oldSite/Descart/CFHTLS-T0005-Release.pdf

sources inside the VIPERS photometric masks, i.e. the angular masks that discard areas around bright stars or with problematic observations. They are a new version of those provided by Terapix: the latter have been revisited by our team in order to recover regions where the photometric quality is deemed sufficient for our analysis (see Fig. 1.7).

The CFHTLS observations were performed in tiles of $\sim 1°$ side, overlapping each other by $\sim 2'$ to allow for cross-calibration. To build the photometric parent sample, the VIPERS team merged adjacent tiles after correcting the tile-to-tile zero point fluctuations. In fact, it was known that in each T0005 tile the zero-points still has a small (but not negligible) offset in some of the photometric bands. Such offsets, which produce colour variations from one tile to another, could introduce systematic effects when selecting the VIPERS spectroscopic target by means of the SC1 and SC2 criteria. For this reason, the VIPERS team made a tile-to-tile homogenisation. The applied correction is based on the well-defined location of stars in colour-colour space, e.g. in the $(r-i)$ vs $(u-g)$ plane. Under the assumption that stars are affected by zero-point shifts in a similar way to galaxies, the observed stellar sequence is used as a calibrator for the colours $(u-g)$, $(g-r)$, and $(r-i)$, which have been corrected before being used in SC1 and SC2. More details are given in Guzzo et al. (2014, see also High et al. 2009 for a description of a similar regression technique). The colour corrections are not applied when performing the SED fitting (Sect. 2.1) because these tile-to-tile variations have a negligible impact in that case.

Photometric redshifts have been estimated using optical magnitudes, according to the procedure described in Coupon et al. (2009); their uncertainty is $\sigma_{\mathrm{zphot}} = 0.035(1+z_{\mathrm{phot}})$ up to $z = 1.0$ and rises to $0.090(1+z_{\mathrm{phot}})$ in the range $1.0 < z < 1.5$ (Coupon et al. 2009, Scodeggio et al., internal VIPERS report).

1.2.2 Infrared data

The VIPERS collaboration has undertaken a follow-up in the K-band in the W1 and W4 fields with the WIRCam instrument at CFHT. The goal was to exploit the full data potential in analysing the galaxy properties as a function of time and environment. The K-band observations were collected between 2010 and 2012 with several discretionary time programmes. The K-band depth has been optimised to match the brightness of the spectroscopic sources: at the magnitude limit ($K_{\mathrm{WIRCam}} \simeq 22.0$ at 5σ), 95% of the spectroscopic sample in W4 is observed in K_{WIRCam}, while in W1 this percentage is approximately 80%. This difference in the percentages is due to the fact that part of the W1 field has not been observed by WIRCam (see Fig. 1.4).

For this reason, in addition to WIRCam data, I matched our CFHTLS optical catalogue with the recent UKIDSS data releases[4] using a matching radius of $0.8''$. The W1 field overlaps with UDS and DXS, whereas the W4 field is fully covered by the shallower LAS and partially covered by DXS. Where K-band photometry

---

[4]DR9 for LAS and DXS, DR8 for UDS. The LAS fields are observed in Y, J, H, K filters, while in DXS and UDS only J, H, K are used. Note that these (Petrosian) magnitudes are in Vega system: I converted them into AB according to the conversion factor provided in the UKIDSS database (`http://www.ukidss.org/`).
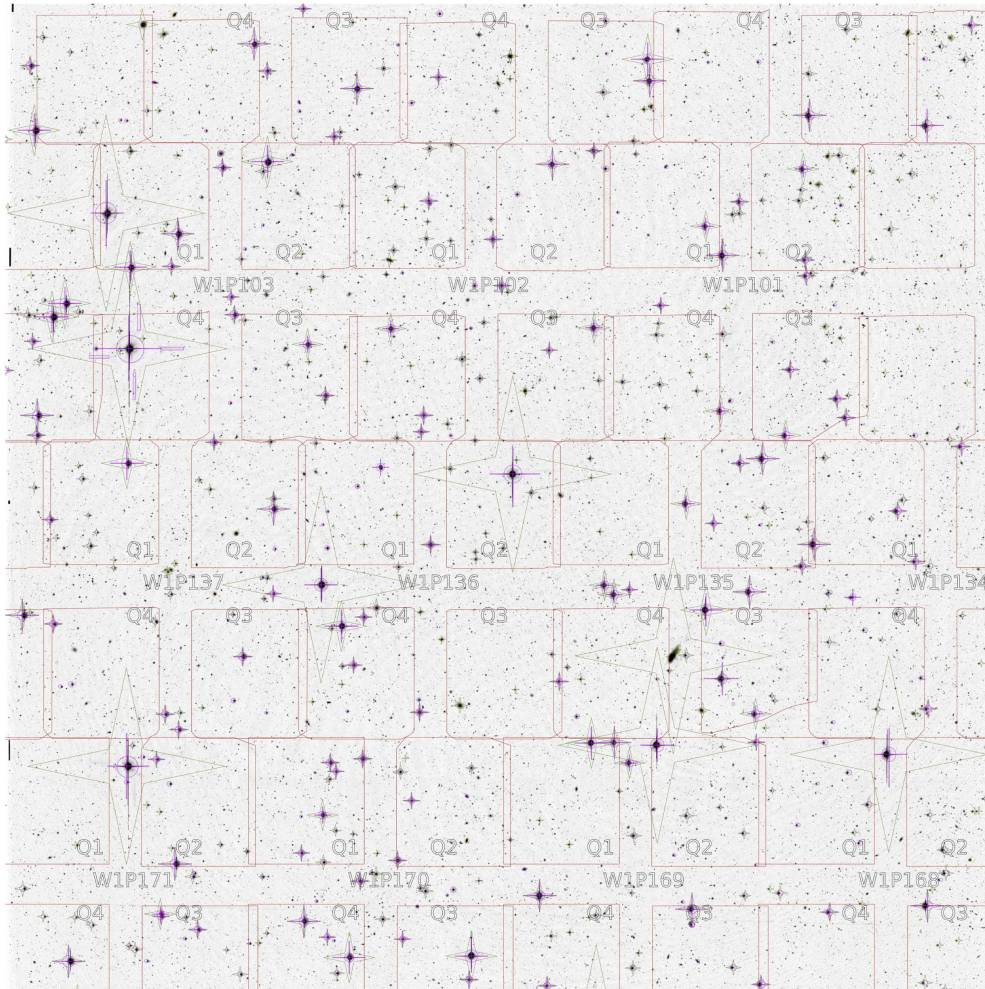
Figure 1.7 Example of photometric masks developed for VIPERS (magenta circles and cross patterns) to exclude regions affected by bright stars. These masks are less conservative than the ones distributed by Terapix, based on the four-point star template (shown in green). They allow a significant gain in terms of usable sky. Along with them, spectroscopic masks that make up the VIPERS pointings are plotted in red. The sky region is the CFHTLS T0005 χ^2-image of the field 020631-050800 produced by Terapix. From Guzzo et al. (2014)
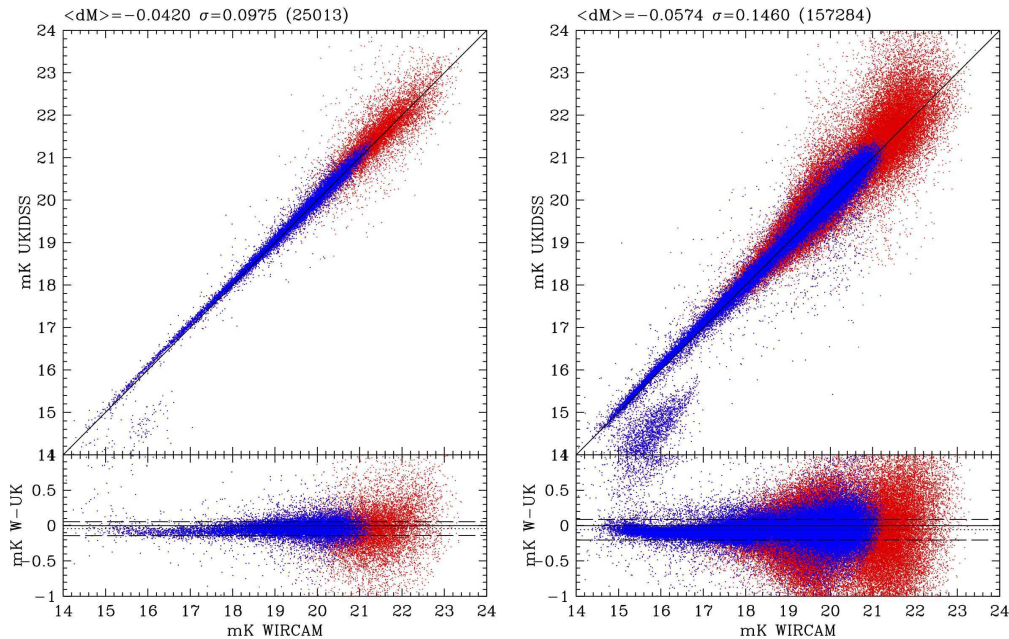
Figure 1.8 Comparison between K_{WIRCam} and K_{UKIDSS} magnitudes of the photometric objects for which both bands are available. The W1 field is on the left panel, W4 on the right one. Only galaxies with $i < 22.5$ are shown in each plot (red dots). The subsample of objects with small photometric errors (Δmag < 0.1, both for WIRCam and UKIDSS data) are highlighted in blue (bright objects substantially out from the 1:1 relation, in the bottom-left corner of each panel, are saturated objects). The mean difference relative to this subsample and its scatter are reported on the top of the plots, as well as the total number of matches (i.e., the number of red points). In W1, where the UKIDSS data are crucial (cf Fig. 1.4), the consistency with WIRCam is good, although the small offset of ~ 0.05 mag. The agreement in W4 is slightly worse, because the UKIDSS photometry mainly comes from the shallow survey UKIDSS-LAS, whereas W1 is covered by UKIDSS-DXS, which is deeper ($K = 21$ mag at 5σ).

is not available, I use instead the J band. When also considering K_{UKIDSS}, the percentage of our spectroscopic sample with K-band magnitude increases to 97% in W1 and 96% in W4.

I compared the K-band photometry for optical sources matched with both UKIDSS and WIRCam surveys, and find a good agreement. In fact, there is a mean difference $\langle \Delta K \rangle = \langle K_{\text{WIRCam}} - K_{\text{UKIDSS}} \rangle \simeq -0.05$, with a small dispersion $\sigma_{\Delta K} \simeq 0.10$ and 0.15, for W1 and W4, respectively (see Fig. 1.8). These differences can be ascribed to the transmission functions of the filters and the definition of the aperture used when measuring magnitudes, and are close to photometric errors. To prevent overweighting the K-band magnitudes in the SED fitting, only the deeper K_{WIRCam} data have been used when both magnitudes were available for the same object.

In addition to NIR, for $\sim 30\%$ of the spectroscopic targets in W1, we cross-correlate VIPERS data with the SWIRE observations[5] (which have been carried

---

[5]   The   Spitzer   Wide-area   Infra-Red   Extragalactic   survey   (SWIRE,

out in the XMM-LSS field). For the SED fitting I take advantage only of magnitudes in the 3.6 μm and 4.5 μm bands, since beyond those wavelengths the survey is shallower, and source detection is very sparse. Moreover, at longer wavelengths – i.e., the MIPS observations at $\lambda > 20\,\mu$m – the re-emission from dust begins to contribute to the flux of galaxies, and this feature is not reproduced by most of the models of stellar population synthesis (see Sect. 2.1).

1.2.3   Ultraviolet data

The UV part of the spectrum can also be important for constraining the galaxy dust content and the star formation rate. In far- and near-UV (FUV and NUV) photometric information has been taken with the GALEX satellite. In both W1 and W4 there are GALEX images from the deep imaging survey (integration time $\sim 3 \times 10^4$ s) in both NUV and FUV channels (Arnouts et al., in prep.). More recently, the coverage in W1 region has been increased with new observations in the NUV channel alone (integration time $T_{\exp} > 1.5 \times 10^4$ s). Because of the GALEX large PSF ($\sim 5''$), the source blending is a major issue in GALEX deep-imaging mode. To measure the UV fluxes of the sources, Arnouts et al. (in prep.) use the dedicated photometric algorithm EMphot (Conseil et al. 2011), which adopts the positions of U-band selected priors and performs a modelled PSF adjustment over small tiles based on the expectation maximisation algorithm (Guillaume et al. 2006). For our spectroscopic sample, 63% (15%) of the sources have an NUV (FUV) flux measurement in W1. In contrast, the W4 field has modest GALEX coverage: 13% (5%) of spectroscopic sources with an NUV (FUV) flux. Because of the inhomogeneous coverage, the GALEX data will be used only for some restricted tests.

1.3   AGN subsample

The PDR-1 catalogue contains 3 371 AGN, selected by Polletta et al. (in prep.) through different techniques. About 1 000 broad-line AGN (BLAGN) are identified by their spectral features (e.g. Figures 1.9 and 1.10). Among them, only 124 have a spectroscopic redshift between $z = 0.5$ and 1. Other emission lines are useful to find obscured AGN, in particular [NeV] λ3426 (cf Mignoli et al. 2013). In this way, 344 galaxies (269 at $0.5 \leqslant z \leqslant 1$) can be regarded as type-2 AGN. In the VIPERS redshift range, one can also apply the spectral diagnostic described in Lamareille (2010), i.e. [OIII]/Hβ vs [OII]/Hβ. This method selects 1 651 possible AGN, almost all at $0.5 \leqslant z \leqslant 1$. Additional candidates ($\sim 1\,600$) in the W1 field have been identified through their X-ray emission, by inspecting the XMM-LSS sources (Chiappetti et al. 2012). Also mid-infrared (MIR) colours from SWIRE can be used in this task, as done e.g. in Stern et al. (2005); in VIPERS, the AGN selection based on MIR fluxes ($F(4.5\,\mu\text{m})/F(3.6\,\mu\text{m}) > 1.3$) is satisfied by 604 entries of the VIPERS catalogue, half of them being at $z < 1.0$.

`http://swire.ipac.caltech.edu`) has been carried out with two distinct instruments in the following channels: $3.6\,\mu$m, $4.5\,\mu$m, $5.8\,\mu$m, $8.0\,\mu$m (IRAC camera) and $24\,\mu$m, $70\,\mu$m, $160\,\mu$m (MIPS camera).

Table 1.1 Photometric passbands in the VIPERS catalogue.

Filter name	Centroid [Å]	range [Å]	AB conv. [mag]	number of sources (out of 53 608)
FUV	1 546.78	262.73	2.07	5 794 (10%)
NUV	2 342.00	767.25	1.66	21 180 (38%)
u	3 844.84	498.04	0.31	53 608
g	4 915.01	1 293.98	-0.08	53 608
r	6 252.39	1 082.23	0.15	53 608
i	7 641.47	1 250.06	0.37	53 608
z	8 852.14	1 042.30	0.51	53 608
J	16 544.53	2 824.64	1.36	277 (< 1%)
K	22 402.56	3 178.50	1.90	4 443 (8%)
Ks	21 630.40	2 976.98	1.83	48 449 (88%)
3.6μm	35 763.44	6 521.24	2.79	8 884 (16%)
4.8μm	45 288.87	8 829.35	3.26	7 135 (13%)

Independent selection criteria can be examined and compared, to study AGN (and host galaxy) properties, and their evolution with z. Several papers on this topic are in preparation (Polletta et al., Małek et al., Marchetti et al.). It should be noted that only BLAGN ($10 \leqslant z_{\text{flag}} \leqslant 19$) are removed from the dataset used in the present work. Further candidates, selected by means of other techniques, are spectroscopic galaxies ($z_{\text{flag}} \leqslant 9$) and therefore are considered in the following analysis. These objects are likely narrow-line AGN (see Fig. 1.9), although some of them are expected to be galaxy contaminants without an active nucleus. I emphasise that these AGN candidates, which are not removed from the sample, do not constitute a problem for the SED fitting derived properties, since in most of the cases their optical and NIR emission are dominated by the host galaxy (Pozzi et al. 2007).

AGN are useful also indirectly, when their light reveals non-emitting matter along the line of sight. During the validation process of the VIPERS redshifts, some team members found a few BLAGN whose spectrum is superimposed on that of an intervening object. They are usually referred to as quasar absorption-line (QAL) systems. An example is shown in Fig. 1.10.

In five cases, absorption lines are sufficiently clear to fit with galaxy templates availble in the EZ software. Thus, I was able to estimate, along with the quasar z_{spec}, also the spectroscopic redshift of the intervening object. The most pronounced line is the MgII resonance doublet ($\lambda\lambda 2796, 2803$, not resolved by VIMOS). This is a feature belonging to a particular kind of absorbers that originate in regions of photoionised gas at temperatures around $T \simeq 10^4\,\text{K}$ (Charlton et al. 2003) and N(HI) $\simeq 10^{16}$ - $10^{22}\,\text{cm}^2$ (Rao et al. 2006). There are opposite interpretations for QAL systems: this kind of absorbers could trace galaxy outflows (e.g. due to star formation driven winds), or conversely they could be part of gas streams falling into the galaxy, perhaps as a consequence of mergers or other accretion
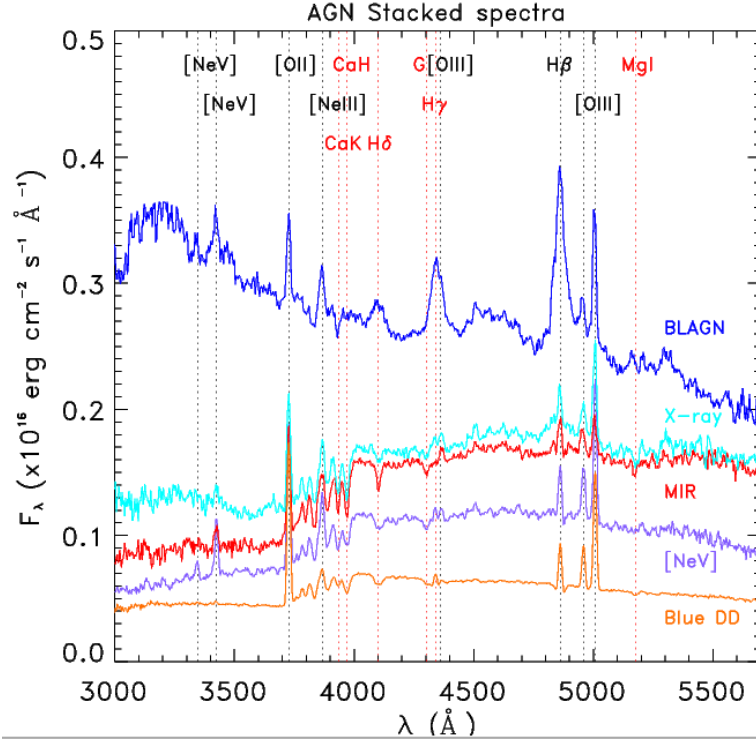
Figure 1.9 AGN stacked spectra for the different selection criteria described in the text. BLAGN (in blue) show blue continuum and broad Balmer lines. X-ray selected AGN (cyan) have either broad or narrow Hβ, but a red continuum. Also MIR and [NeV] selections (red and violet) find preferentially red profiles (D4000 break clearly visible) with spectra similar to normal star-forming galaxies (see the weak [OII] emission). Finally, the stacked spectrum in orange results from objects selected through the blue diagnostic diagram of Lamareille (2010). Interestingly enough, its continuum is bluer than the other samples (excluding BLAGN) and without [NeV] emission; the [OII]/[OIII] ratio is greater than one, like the LINERS populations. Courtesy of M. Polletta.

mechanisms. There could be some analogy to HI clouds observed in 21 cm surveys around individual galaxies (cf Doyle et al. 2005).

Several observations in the local universe highlight the presence of a luminous galaxy close to the QAL system, within a projected radius of 50–100 h^{-1} kpc (see Chen et al. 2010, and references therein). In samples of MgII absorbers serendipitously found along AGN l.o.s, the extent of the MgII halo seems to increase with the stellar mass of the galaxy associated with it, but it correlates only weakly with specific SFR (e.g. Chen et al. 2010). Conversely, galaxy surveys around AGN pre-selected for strong MgII absorption tend to find systems with high sSFRs (e.g. Zibetti et al. 2007).

At present, the connection between QAL systems and their nearby galaxies cannot be investigated in VIPERS, because some of the objects surrounding the studied BLAGN were not spectroscopically observed. In addition, I estimated the equivalent width (EW) of the MgII doublet for each VIPERS QAL system. As mentioned above, the resolution is not high enough to measure separately the two lines, which I fit by a single Gaussian profile. The resulting EWs range from 2.7 to
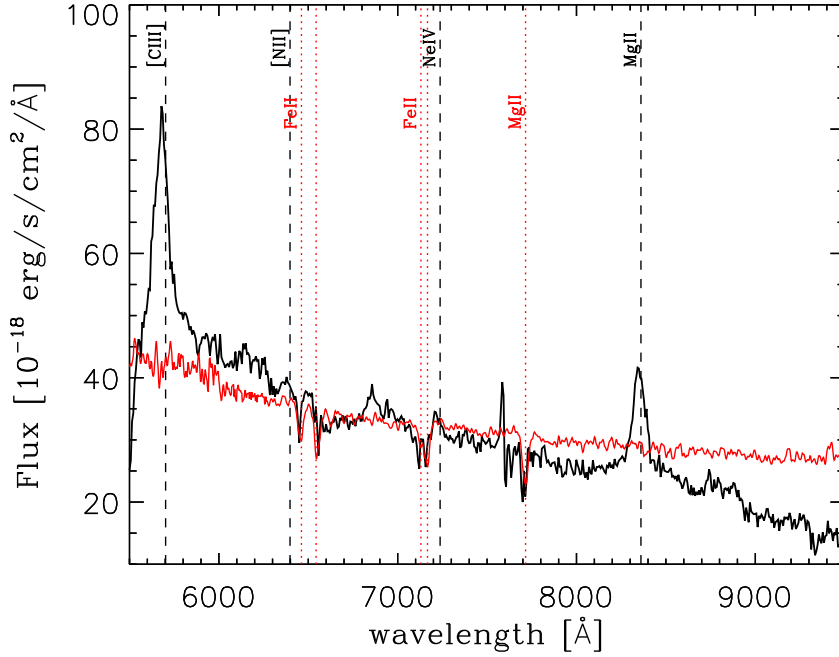
Figure 1.10 VIPERS spectrum of a broad-line AGN at $z = 1.9867$ (magnitude $i = 19.505$, black line). Its main lines are marked with vertical dashed lines. Absorption features of an intervening object are also visible (vertical dotted lines). These features are fit by a galaxy template (red line) redshifted at $z = 1.7564$ (the flux is rescaled to superimpose the template on the AGN spectrum). See discussion on QAL systems in the text.

8.1 Å. These approximate estimates are in general agreement with "strong" QAL systems that can be found in the literature (e.g. in the catalogue of Quider et al. 2011). Despite the observational limitations, it could be worth searching for QAL systems in VIPERS. For instance, since strong MgII absorbers are often associated with damped Lyα systems (e.g. Rao et al. 2006, 2011), it could be interesting to study the UV spectra of these objects (if available) and verify the presence of the Lyα line.

Chapter 2

Data analysis

Once collected spectroscopic and photometric information, several physical quantities can be estimated for the VIPERS galaxy sample. I achieve this goal by fitting a set of spectral energy distributions (SEDs) to the multi-band photometry of each galaxy. This technique is adopted to estimate absolute magnitudes, stellar mass ($\mathcal{M}$), and star formation rate (SFR). A number of tests are also presented to show the reliability (but also the limitations) of such a method. When possible, SED fitting results are compared with estimates obtained through other techniques.

2.1 SED fitting technique

The SED fitting technique has been developed in the last two decades (see seminal papers of Koo 1985; Pello et al. 1996; Lanzetta et al. 1996), and is now widespread used in observational astrophysics. The keystone of the method is to find the SED in better agreement with the observed magnitudes of the selected galaxy. After doing that, the galaxy properties can be recovered directly from the characteristics of that best-fit SED. To perform this fundamental task, different methods are available in the literature, depending also on the goals of the analysis (e.g., estimating redshift, spectral type, stellar mass, etc.). They can be broadly classified in four classes:

i. The χ^2 template-fitting (e.g. Bolzonella et al. 2000; Arnouts et al. 1999; Ilbert et al. 2006).

ii. Fitting by inversion (e.g. Heavens et al. 2000; Tojeiro et al. 2007).

iii. Bayesian methods (e.g. Noll et al. 2009).

iv. Neural networks (e.g. Collister & Lahav 2004; Cavuoti et al. 2012).

In the present work, I adopt method (i), as detailed in Sect. 2.1.4. The galaxy templates (i.e., the synthetic SEDs) used in the procedure are realised starting from a stellar population synthesis model described in Sect. 2.1.1. The results are summarised in Sect. 2.1.5.

Galaxy templates can also be constructed from the galaxy SEDs observed with state-of-the-art facilities from UV to IR (e.g. Coleman et al. 1980). This kind

of SEDs are useful to determine the distance of a galaxy (i.e. its photometric redshift, e.g. Ilbert et al. 2009) and determine whether it is late- or early-type (see e.g. Pozzetti et al. 2010). However, to estimate for instance galaxy stellar masses, one needs a set of SEDs realised starting from a stellar population synthesis model, because in that case the flux "emitted" by the galaxy template can be expressed per unit of stellar mass. In the present work, the latter approach has been adopted, and is therefore described in the following.

2.1.1 Simple stellar populations

Among the techniques for modelling galactic light, the stellar population synthesis is the most popular one.[1] Its fundamental assumption is that the SED of a galaxy can be described by adding spectra of several simple stellar populations (SSPs Renzini & Pecci 1988).[2] Each SSP represents an ensemble of stars born at the same time with the same chemical abundance. The mass distribution of those stars depends on the initial mass function (IMF, e.g. Salpeter 1955) and the composition of their spectra gives the total flux of the SSP. Sometimes in the literature, SSPs are compared to star clusters (globular or open clusters) even though the latter are now considered more complex than the former: dynamical evolution (e.g., mass segregation) and exotic objects (e.g. blue straggler stars, Ferraro et al. 1992) prevent any meaningful correspondence.

After constructing a set of SSPs, they are combined to obtain a composite stellar population (CSP), which represents a synthetic galaxy SED. SSPs at different ages are chosen according to the star formation history (SFH) assumed in the galaxy model. Another component, i.e. dust, is added to modify the resulting SED as it happens in the observed universe (see Sect. 2.1.3). This scheme is summarised in Fig. 2.1. Each step is detailed in the following.

For a given SSP, a way to compute its SED is through the isochrone synthesis (Chiosi et al. 1988; Charlot & Bruzual 1991). Since all stars have the same age, they lie in a precise *locus* (i.e. an isochrone) of the Hertzsprung-Russel diagram. To identify the position of a star in the diagram – knowing its initial mass, age, and metallicity – the computation of stellar evolutionary tracks is required. Any of these tracks describes the entire life of a star having certain characteristics. By following the evolutionary track of a star, one can predict e.g. how its effective temperature evolves. All information provided by the track is converted in an observable spectrum through (empirical or theoretical) stellar spectral libraries (e.g Lejeune et al. 1997; Le Borgne et al. 2003).

Among the isochrone synthesis codes, the most popular are the Padova models (Bertelli et al. 1994; Girardi et al. 2000; Marigo et al. 2008) and the Geneva models (Schaller et al. 1992; Lejeune & Schaerer 2001). Other widespread used models are described e.g. in Pietrinferni et al. (2004, BaSTI team) and Dotter et al. (2008, Dartmouth collaboration). Even in the state-of-the-art codes, the major sources of

---

[1]Excellent reviews of this technique can be found in Faber (1977); Tinsley (1980); Conroy (2013). For sake of brevity, other approaches (e.g. Faber 1972; Pickles 1985) are not discussed here.

[2] In the following I will not consider SEDs with an AGN component. References to this issue can be found in Polletta et al. (2007); Delvecchio et al. (2014).
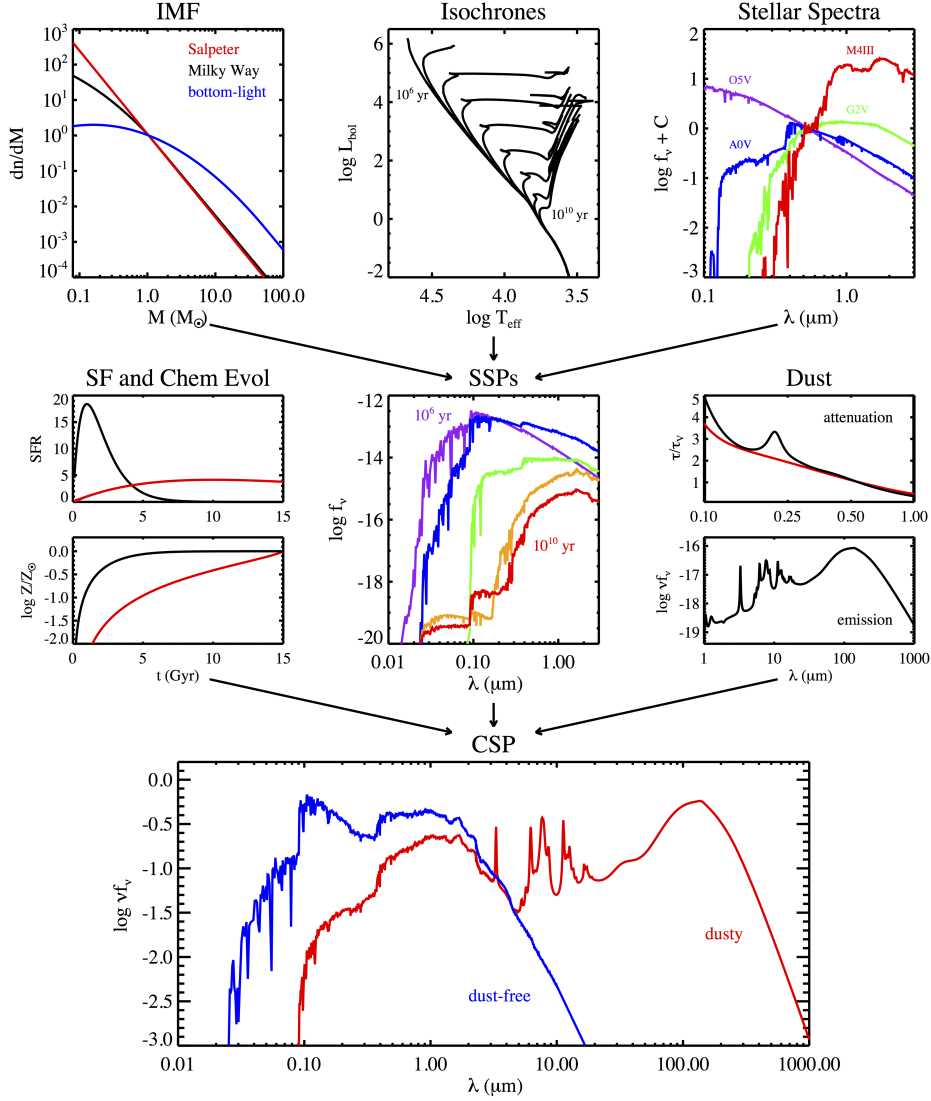
Figure 2.1 Overview of the fundamental steps in the stellar population synthesis of a galaxy. An SSP is built by means of isochrones and related stellar spectra, assuming some IMF. The SSP spectra at various ages are combined according to a given SFH (in some models also the chemical evolution is accounted for). The emission is modified including the presence of dust. The result is a composite stellar population (CSP) that represents the SED of a galaxy. From Conroy (2013).

uncertainty are related to difficulties in modelling stellar evolution: for instance, it is still unclear how to properly account for stellar rotation (see Maeder & Meynet 2012), or the amount of overshooting (especially for evolved giant stars, see Cassisi 2004). Another open issue is the treatment of the thermally pulsing asymptotic giant branch (TP-AGB), which is difficult to model also because observations are still controversial (see discussion below). These uncertainties propagate into derived quantities such as stellar mass, being a major concern in the implementation of any SED fitting technique based on evolutionary stellar synthesis (Conroy & Wechsler 2009).

In this work, I use the GALAXEV population synthesis model (hereafter referred as BC03, Bruzual & Charlot 2003), with the parameters described in Sect. 2.1.4. Some examples of SSPs produced by this model are shown in Fig. 2.2. The isochrone tables adopted by Bruzual & Charlot are those from the Padova 1994 models. By means of the BC03 code, it is possible to build CSPs, i.e. galaxy spectra, from 91 Å to 160 μm, with a resolving power of $\lambda/\Delta\lambda \sim 200$–500. This reproduces well magnitudes and colours of SDSS objects, and is one of the standard libraries used to compute galaxy stellar masses.

An alternative method to compute SSPs is the so-called "fuel consumption" method (Buzzoni 1989). This is the approach followed by Maraston (2005, hereafter M05), in which the evolution (especially in the post main sequence) is characterised by analytical functions related to the consumption of hydrogen and/or helium (i.e., the "fuel" of stars). It is important to note that M05 differs from BC03 also because of the TP-AGB phase, which affects NIR emission of stellar populations that are ~ 1 Gyr old, so a different treatment results in different SEDs (Fig. 2.3). The question about the relevance of TP-AGB in the stellar population synthesis is still open (e.g. Marigo & Girardi 2007), with some evidence that supports BC03 (e.g. Kriek et al. 2010; Zibetti et al. 2013) in contrast to observations favouring M05 (e.g. MacArthur et al. 2010).

2.1.2   Models of galaxy SED

Once chosen a set of SSPs, the next step to build a galaxy SED is to assume a star formation history (SFH), i.e. a recipe that specifies how many stellar populations will be created within the galaxy during its life. The SFH can be parametrised by $\psi(t)$, a simple analytical form such that the galaxy stellar mass assembled since galaxy formation time (t_{form}) is

$$\mathcal{M}(t) = \int_{t_{\mathrm{form}}}^{t} \psi(t') f_r(t_{\mathrm{form}} - t') \, \mathrm{d}t' \,, \tag{2.1}$$

where the stellar mass loss is parametrised by the return fraction f_r (e.g. Conroy & Wechsler 2009). Under the assumption that the galaxy evolves smoothly, $\psi(t)$ is often described by an exponentially declining function:

$$\psi \propto \exp(-t/\tau) \,, \tag{2.2}$$

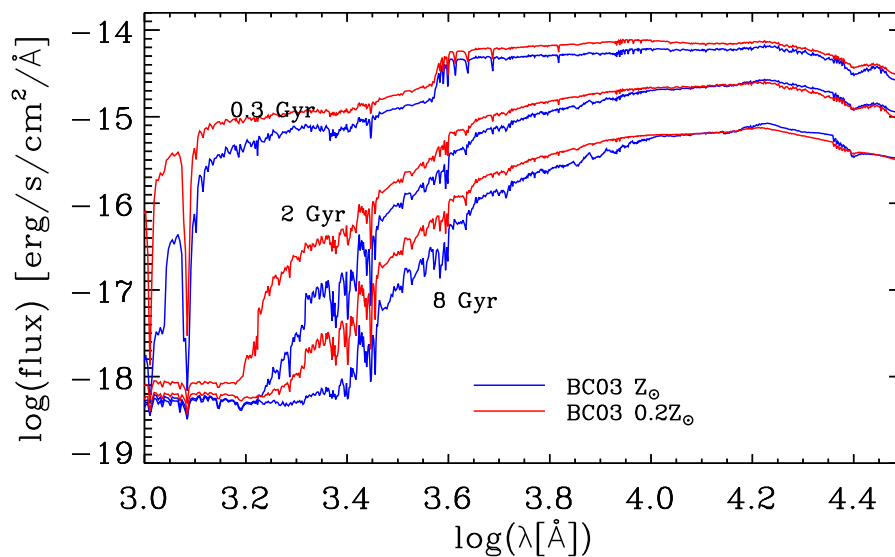where τ is the e-folding timescale.

Figure 2.2 Spectra of a simple stellar population, as modelled by Bruzual & Charlot (2003), assuming solar and subsolar metallicity (blue and red respectively). Three different ages are shown in both cases. The other parameters (e.g. Chabrier's IMF) are kept fixed.

One could argue that such an approximation is too far from the true SFH of a galaxy, which is likely to go through discrete episodes of star formation. Nevertheless, exponentially declining models provide reasonable fits when most of the galaxy stellar mass has been assembled in a single event, because the spectral features of SSPs vary smoothly with time (as suggested by Fig. 2.2). This is indeed the case of early-type galaxies (Thomas et al. 2010). On the other hand, for actively star-forming galaxies in which young stellar populations outshine the older ones, parametrising the SFH with Eq. (2.2) can lead to an underestimate of the galaxy age and stellar mass (Papovich et al. 2001). This effect can be reduced by setting a lower limit on the age parameter, in order to avoid unrealistic solutions that are too young and too dusty (Pforr et al. 2012). Maraston et al. (2010) propose an alternative solution by introducing exponentially increasing SFHs: $\psi(t) \propto e^{t/\tau}$. Another possible issue has been stressed out by Pacifici et al. (2013), who identified a class of massive blue galaxies that assembled their stellar mass over a relatively long period, experiencing a progressive reduction of their star formation at a later evolutionary stage. For such "bell-shaped" SFH, neither increasing nor decreasing τ-models seem to be suitable. A third option consists in delayed τ models ($\propto t e^{-t/\tau}$) having the peak of star formation at $t = \tau > t_{\text{form}}$.

More realistic models of SFH should be provided by superimposing random peaks of star formation on the exponential (or constant) SFR, as proposed by Kauffmann et al. (2003a). In another pioneering work, Finlator et al. (2007) use the SFHs drawn from their hydrodynamic simulations. This kind of stochasticity can also be linked to the accretion history that results from N-body simulation (Pacifici et al. 2013). For some active galaxies, allowing the presence of recent secondary bursts can lead to higher stellar mass estimates with respect to those obtained with smooth functions (Papovich et al. 2001; Pozzetti et al. 2010; Pforr
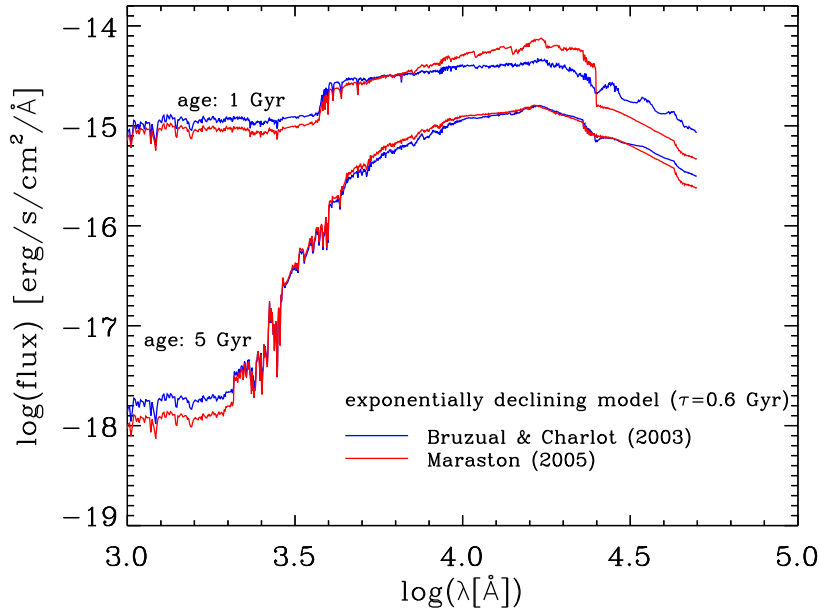
Figure 2.3 Synthetic galaxy SEDs, as modelled by Bruzual & Charlot (2003, blue lines) and Maraston (2005, red lines). For each model, two timesteps are shown, corresponding to galaxy ages of 1 and 5 Gyr. Given the e-folding time of the (exponentially declining) SFH assumed in both cases, the former SED represents a young galaxy still forming stars, while the latter (5 Gyr age) is already passive, as indicated by the deep D4000 break. It should be noticed that the most significant difference between BC03 and M05 is at NIR wavelengths, in the young (age $\simeq 1$ Gyr) star-forming galaxy. The discrepancy at $\log(\lambda) \gtrsim 4.4$, particularly evident comparing the 1 Gyr templates, is due to computational reason (a different extrapolation in the Rayleigh regime).
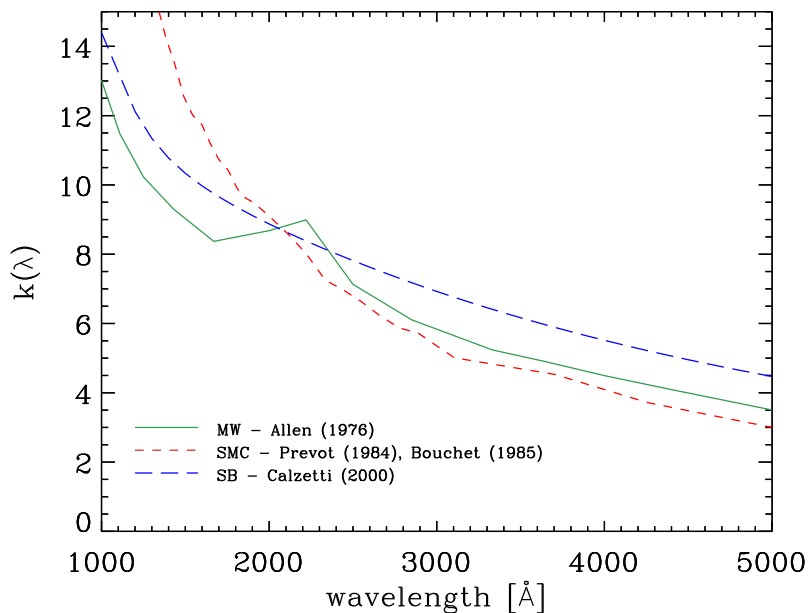
Figure 2.4 Comparison among different extinction models (listed in the legend); curves are taken from the *Hyperz* software package (Bolzonella et al. 2000).

et al. 2012). This happens because the blue colour of this kind of galaxies can now be obtained by a balanced mix of young and old populations. However, the improved description of stellar assembly provided by composite SFHs is limited by unresolved degeneracies (e.g. between dust and metallicity). Moreover, some "multi-bursts" libraries include a large number of templates, thus requiring much longer computational time. Therefore, exponentially declining/increasing SFHs remain a convenient option, indeed used by many authors.

When building a CSP, one should in principle consider that stellar populations born at different epochs do not have the same chemical abundance, since the stars formed earlier had enriched the ISM. In practice, the time evolution of galaxy metallicity is over-simplified in most of the stellar population synthesis models: a single metallicity is assumed for all the SSPs that origin the CSP. This is also the case of the BC03 model adopted in this work.

A noteworthy exception is the versatile spectra analysis (VESPA) developed by Tojeiro et al. (2007). Their code relies on a dynamic parametrization of the SFH and adaptive Z ranges; it works iteratively until it finds the series of star-forming bursts (allowed to have different metallicity) that better recover the observations. Unfortunately, this method works when supplied with high quality data (e.g. SDSS galaxies, Tojeiro et al. 2009) and its application is not feasible with the medium-resolution spectra of VIPERS.

The impact of constant Z has not been extensively investigated yet (but see the notable attempts of Conroy et al. 2009; Mitchell et al. 2013). It should be emphasised that in the optical (i.e., bands redward of V) the broadband evolution of a multi-metallicity population of stars can be fairly described with a single population with Z fixed to the mean of the multi-metallicity one (Conroy et al.

2009).

2.1.3   Including dust effects in the SED

Along with stellar emission, also interstellar medium (ISM) has to be modelled. In particular, dust is one of the ISM ingredients and plays a major role in shaping the observed galaxy SED by reprocessing the light coming from stars (see e.g. Mathis 1990). There are still several questions about dust that need an answer. In particular, its composition and distribution are still unclear. The main components of dust grains are silicates, graphite, and polycyclic aromatic hydrocarbons (PAH, see Leger & Puget 1984). All of them absorb light mainly in the UV-to-optical range, re-emitting it in the IR ($\lambda \gtrsim 10\,\mu$m). More details about the physics of dust can be found e.g. in Draine (2003) and Ciesla et al. (2014).

In SED fitting, the UV-to-optical obscuration by dust is usually described by means of two terms, namely attenuation and reddening. The former, expressed by A_λ, represents the change in magnitude at a given wavelength λ, while reddening can be parametrised by the colour excess $E(B - V) \equiv A_B - A_V$. The attenuation at a given wavelength can be also described by the optical depth τ_λ:

$$I(\lambda) = I_0(\lambda)\exp^{-\tau_\lambda}, \qquad (2.3)$$

where the unobscured radiation would have intensity I_0, and I is the observed intensity. From Eq. (2.3) it follows that $A_\lambda = (2.5 \log e)\tau_\lambda$.

Both A_λ and $E(B - V)$ have been empirically determined, through observations of either the Milky Way (e.g. Cardelli et al. 1989; Fitzpatrick 2004), the Large Magellanic Cloud (LMC, Howarth 1983), the Small Magellanic Cloud (SMC, Prévot et al. 1984; Bouchet et al. 1985), or on small samples of nearby galaxies (e.g. Calzetti et al. 1994, 2000). Several techniques can be used to compute A_λ and $E(B - V)$, based on multi-wavelength analyses, emission line ratios (e.g., Hα/Hβ), or the energy balance between IR and UV (i.e., the infrared luminosity excess IRX $\equiv L_{\mathrm{IR}}/L_{\mathrm{UV}}$). The extinction laws resulting from such studies can be characterised by the parameter

$$k(\lambda) \equiv \frac{A_\lambda}{E(B - V)} \ . \qquad (2.4)$$

As shown in Fig. 2.4, they are very similar at $\lambda > 3\,000\,$Å, while at lower wavelengths the slope is significantly different. Moreover, the absorption peak at $2\,175\,$Å is not always present (cf observations by York et al. 2006, and Stratta et al. 2007). This distinct feature (named "UV bump" by Stecher 1965; Stecher & Donn 1965) is thought to be due to graphite or PAH absorption (e.g. Weingartner & Draine 2001). Buat et al. (2012) find that, when the bump is present, its amplitude is lower in galaxies with very high specific SFR (sSFR $\equiv$ SFR/$\mathcal{M}$).

In order to model the extinction more accurately, Silva et al. (1998) and Charlot & Fall (2000) take into account the distribution of dust grains with respect to stars at different ages, inside different spatial components of the galaxy. Charlot & Fall (2000) consider the optical depth of the HII and HI regions embedding young stars, together with the extinction caused by diffuse interstellar medium. Silva

et al. (1998) account also for the geometrical distribution of stars, dividing the galaxy in three parts, i.e. molecular clouds, disc, and bulge. Both models rely on radiative transfer equations, coupling stellar populations and ISM. In particular, they account for the dense molecular clouds in which stars are born, and their dissipation (i.e., older stars are less attenuated).

The models by Silva et al. (1998) and Charlot & Fall (2000) are angle-averaged. However, one could expect that a general description of dust absorption should take into account also geometrical effects in star-forming galaxies, in particular disc inclination. This is the case of Chevallard et al. (2013), in which the optical depth τ_λ depends also on the galaxy inclination angle. Chevallard et al. adopt four different approaches to deal with radiative transfer (Silva et al. 1998; Tuffs et al. 2004; Pierini et al. 2004; Jonsson et al. 2010), and show that all of them predict a quasi-universal relation after fixing geometry and inclination. In other words, orientation effects affect the overall attenuation curve more than changing the physical properties of dust grains.

The models discussed above are not always well-suited for fitting large galaxy samples, because the large number of parameters broadens significantly the parameter space, and properly exploring it can require a prohibitive amount of computational time. As an alternative, there are simpler models that generate IR templates that include emission features due to dust (e.g. Chary & Elbaz 2001; Dale et al. 2001). By implementing these templates in the SED fitting procedure (together with standard ones that fit from UV to NIR) one can recover e.g. rest-frame luminosity in the desired IR passbands with only a few (or even one) additional parameters.

2.1.4   Fitting SEDs to VIPERS data

In the present work, the SED fitting is performed by means of the code HYPER-ZMASS, a modified version of HYPERZ (Bolzonella et al. 2000, 2010). As anticipated in Sect. 2.1.1, the template library used for input is constructed by adopting the BC03 model. Since the procedure is applied to a spectroscopic galaxy sample, the redshift of the targets is kept fixed: the rest-frame synthetic SEDs will be shifted toward larger wavelengths by a factor $(1 + z_{\mathrm{spec}})$ before comparing them with the photometric data.

To do the comparison, HYPERZMASS determines for each template the flux (or apparent magnitude) in the same passbands that have been observed for the real galaxy. Then, the code uses a maximum-likelihood method to find which template better fits the observations; this is done by searching within the template library the SED that generates the smallest χ^2. For each SED, the χ^2 is defined as

$$\chi^2 \equiv \sum_{i=1}^{N_{\mathrm{filt}}} \left[\frac{F_{\mathrm{gal,i}} - n F_{\mathrm{temp,i}}(t, \tau, Z, k(\lambda), A_V)}{\sigma_i} \right]^2 \; , \qquad (2.5)$$

where $F_{\mathrm{gal,i}}$ and $F_{\mathrm{temp,i}}$ are the fluxes measured in the i-th filter (out of N_{filt}), for the galaxy and the template respectively. Each template is univocally identified by its parameters $t, \tau, Z, k(\lambda), A_V$ as detailed below (see also Table 2.1). It is rescaled

(a)

(b)
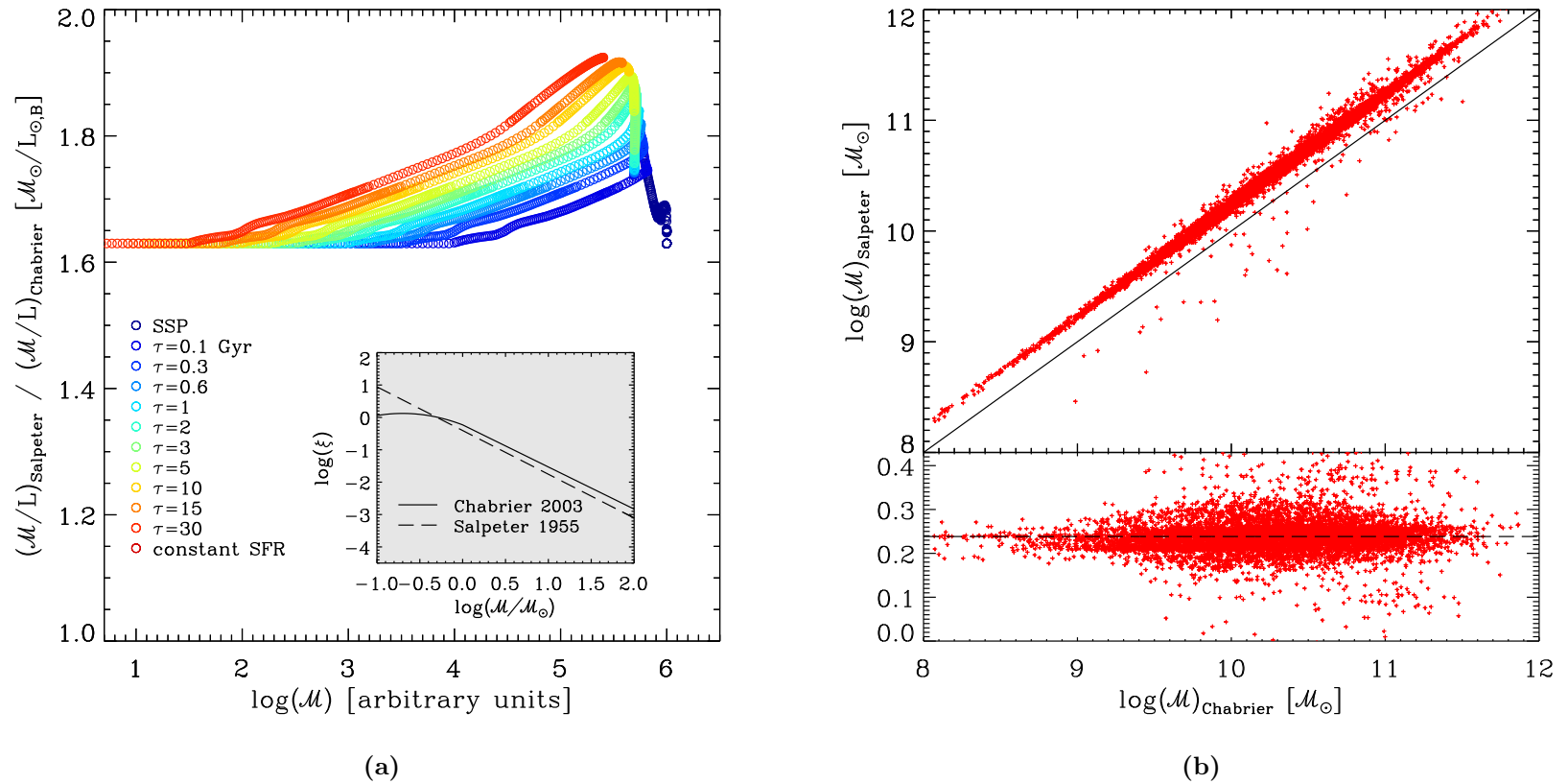
Figure 2.5 The systematic effect caused by changing the IMF. The *left panel* shows a comparison between $\mathcal{M}/L$ of several BC03 SEDs, assuming either Chabrier's or Salpeter's IMF. Each SED is built assuming some SFH (see colour code in the legend), and the ratio $(\mathcal{M}/L)_{\text{Salpeter}}/(\mathcal{M}/L)_{\text{Chabrier}}$ is plotted at different ages (open circles). Note that these templates are arbitrary scaled, and values on the x-axis are provided only as a guide. In the inset, solid and dashed lines represent the logarithmic IMF according to Chabrier (2003) and Salpeter (1955) respectively. The latter is heavier than the former by a factor 1.6–1.9, depending on the mix of old and recent stars (i.e., the SFR and age of the given galaxy template). This factor translates into an offset of 0.2–0.3 dex in logarithmic stellar mass, as shown in the *right panel*. In this plot, for illustrative purposes, it is shown only a subsample of 8 000 VIPERS galaxies at $0.5 < z < 1.2$. The SED fitting on those objects has been performed twice, changing only the IMF. The median offset (horizontal dashed line) is $\log(1.74) = 0.24$.

through the normalisation constant (n) that minimises the χ^2. The uncertainty in the flux measurement is σ_i.

We choose Chabrier (2003) IMF, in agreement with many previous studies on galaxy stellar mass function. Other IMFs widely used in the literature are Salpeter (1955) and Kroupa (2001), which differ from Chabrier by an average scaling factor of ~ 1.7 and ~ 1.1, respectively (Fig. 2.5). Although a large number of observations are consistent with a single bottom-light IMF (see Bastian et al. 2010, for a review), recent work finds a relation between IMF and velocity dispersion (e.g. Treu et al. 2010; Cappellari et al. 2013; Spiniello et al. 2014), pointing out that the IMF of some elliptical galaxies could be more bottom-heavy, like Salpeter (or even steeper, see La Barbera et al. 2013). McGee et al. (2014) account for a non-universal IMF when they estimate the GSMF at $z \simeq 0.1$, which becomes a power-law at the high-mass end. However, evidence is not clear-cut (see Clauwens et al. 2014; Smith 2014). Moreover, those IMF variations need to be precisely quantified, otherwise an incorrect parametrisation could lead e.g. to unphysical stellar-to-halo mass relation (i.e., a stellar fraction higher than the universal baryon fraction, see McGee et al. 2014). As an aside, it should be emphasised that surveys like VIPERS can help in this kind of investigations, because the study of the high-mass end of the GSMF can provide useful constraints to disentangle different models of IMF dependencies (see Fontanot 2014). A similar effort is beyond the scope of this thesis.

The code provided by Bruzual & Charlot (2003) assumes a non-evolving stellar metallicity. I choose SSPs with either $Z = Z_\odot$ or $Z = 0.2Z_\odot$ to encompass the metallicity range observed for galaxies at $z \sim 0.8$ (Zahid et al. 2011; Gallazzi et al. 2014). This choice allows to take into account the different values of metallicity of the VIPERS galaxies, which can be lower than in the nearby universe (Zahid et al. 2011). We do not implement a larger number of metallicities, since such a choice would significantly increase the effect of the age-metallicity degeneracy (see Fig. 2.6). As shown by Mitchell et al. (2013), the SED fitting is improved if one feeds the procedure with an independent estimate of Z, but unfortunately the resolution of the VIPERS spectra is not high enough to put reliable constraints on chemical abundances from spectral line measurements.

After selecting the SSPs, we generate the SEDs for our template library following exponentially declining evolutions (see Eq. 2.2), in which the time scale of star formation (τ) assumes one of the following values: 0.1, 0.3, 0.6, 1, 2, 3, 5, 10, 15, 30 Gyr. A constant SFH (i.e., SFR $\sim 1\,\mathcal{M}_\odot\,\mathrm{yr}^{-1}$) is also considered, for a total of 11 SFHs. The ratio between galaxy age t_{age} and time scale τ indicates the evolutionary phase of the fitted object. Large values of t_{age}/τ represent early-type galaxies, for which the star formation has been quenched since a long time (Thomas et al. 2010). On the other hand, $t_{\mathrm{age}}/\tau \approx 1$ means that the galaxy is still forming stars at a rate similar to its first stage. For each SFH, the evolution follows 221 unequally spaced time steps, from $t = 0.1$ to $t = 20$ Gyr. No fixed redshift of formation is imposed in this model, but during the fitting procedure HYPERZMASS rules out those templates such that, at the redshift of the fitted galaxy, result in a formation age older than the age of the Universe, i.e. $t_{\mathrm{age}}(z_{\mathrm{spec}}) > t_{\mathrm{U}}(z_{\mathrm{spec}})$.

With respect to the dust content, I implement it as a foreground screen that attenuates the galaxy emission. I assume the extinction model of Calzetti et al. (2000) and the one based on the studies of Prévot et al. (1984) and Bouchet et al. (1985).
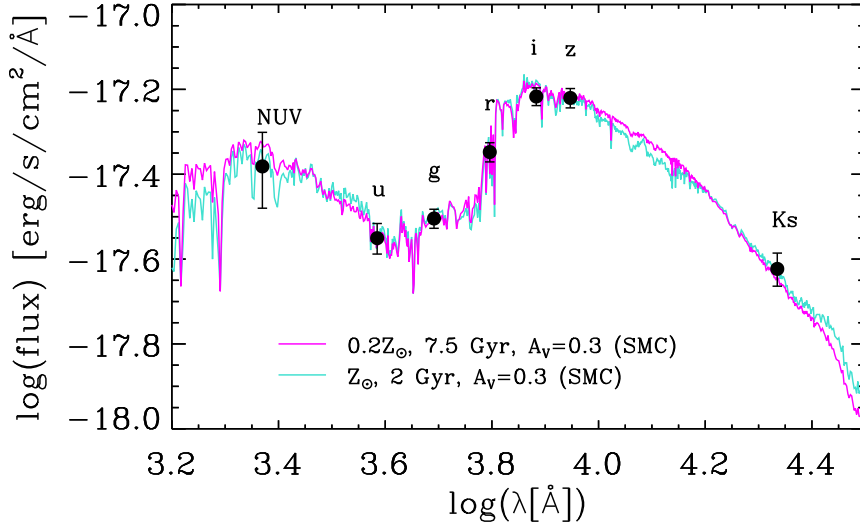
Figure 2.6 An example of SED fitting of one of the VIPERS galaxies. Observed magnitudes in seven photometric bands (filled circles, with labels) are the input data of the SED fitting preformed through *Hyperzmass* (see details in Sect. 2.1.4). To show how the age-metallicity degeneracy can affect this kind of estimates, two SED templates are plotted: one represents a relatively young galaxy with solar metallicity (cyan line), the other is the SED of an older galaxy with $Z = 0.2Z_\odot$ (magenta line). Stellar mass estimates are $10^{10.54}$ and $10^{10.30}\,\mathcal{M}_\odot$ respectively. Except metallicity and age, the other parameters of the two templates (e.g. dust extinction) are the same. This example shows that old stellar populations with low Z can fit data as well as younger ones having higher metal abundance: both the templates have a χ_r^2 probability of about 98%. The solution with subsolar metallicity is selected for the official VIPERS catalogue because of the slightly smaller χ_r^2 value.

Table 2.1 SED fitting to VIPERS data: details about the input parameters assumed in the procedure.

Parameter	range	notes
age	from 9×10^7 yr to $t_{\mathrm{U}}(z_{\mathrm{spec}})$	220 timesteps
SFH	$\tau = [0.1, 0.3, 0.6, 1, 2, 3, 5, 10, 15, 30]$ Gyr and SFR$\sim$const	
Z	$0.02Z_\odot$ or $Z_\odot$	best χ^2 selected
$k(\lambda)$	Calzetti (SB) or Prévot-Bouchet (SMC)	best χ^2 selected
A_V	0–3 mag	steps of 0.1 mag

Values of A_V range from 0 (no dust) to 3 magnitudes (ΔA_V steps equal to 0.1 mag). As pointed out in previous work (e.g. Inoue 2005; Caputi et al. 2008; Ilbert et al. 2009), Calzetti's law is on average more suitable for the bluest SEDs, having been calibrated on nearby starburst (SB) galaxies, whereas the Prévot-Bouchet law is better for mild star-forming galaxies, since it was derived from the dust attenuation of the Small Magellanic Cloud (SMC) (see also Wuyts et al. 2011). Neither the former nor the latter show the UV bump at $2\,175\,\mathrm{\AA}$ (see Fig. 2.4). Hereafter I refer to the Calzetti and Prévot-Bouchet models as SB and SMC extinction laws, respectively. I let the choice between the two extinction laws be free, according to the best-fit model (smallest χ^2), since UV data are not sufficient to differentiate the trends of the two laws (such an attempt has been performed in Ilbert et al. 2009, with the COSMOS photometric baseline).

Given the wide range of physical properties allowed in the SED fitting procedure, some unphysical parameter combination or degeneracy have been excluded *a priori* from the fitting. In particular, I limit the amount of dust in passive galaxies (by imposing $A_V \leqslant 0.6$ for galaxies with age/$\tau > 4$) and avoid very young extremely star-forming galaxies with short τ timescales (i.e. I prevent the selection of models with $\tau \leqslant 0.6$ Gyr when $z_{\mathrm{form}} < 1$ is required).

The VIPERS multi-band photometry used as input in the fitting procedure consists in optical, and IR magnitudes (see Table 1.1). Thus, the SED templates are constrained by data ranging from $\sim 3\,800\,\mathrm{\AA}$ to $\sim 22\,\mu\mathrm{m}$ ($\sim 45\,\mu\mathrm{m}$ when SWIRE photometry is available). Since the formal uncertainty of these magnitudes in some cases can underestimate the real error, I add in quadrature 0.05 mag to the error budget in the CFHTLS and WIRCam bands (0.1 mag in the UKIDSS and SWIRE ones). In a paper in preparation, Moutard et al. find that the uncertainties in the z band, as provided in the CFHTLS-T07 catalogue, are underestimated. This fact causes a systematic effect in the stellar mass computation. The authors solve this issue by increasing the error bars in the same way as done in the present work. As stated above, a larger additional amount (i.e., 0.1 dex instead of 0.05) is added to UKIDSS and SWIRE magnitudes because the photometry of those surveys is less accurate than CFHTLS and WIRCam.

The results obtained through HYPERZMASS are the official SED fitting estimates used in the VIPERS papers (e.g. Marulli et al. 2013; Davidzon et al. 2013; Fritz et al. 2014). In addition, I run again HYPERZMASS on the same galaxies but with different input parameters (for instance, using a single extinction law) to test the

robustness of this analysis and the absence of severe systematics. An extract of these tests is discussed in the following.

Moreover, to quantify the effect of using complex SFHs in VIPERS, I computed stellar masses by using the MAGPHYS package (da Cunha et al. 2008).[3] This code parametrises the star formation activity of each galaxy template starting from the same SSPs as HYPERZMASS (i.e., from the BC03 model), but using two components in the SFH, namely an exponentially declining SFR and a second component of additional bursts randomly superimposed on the former Kauffmann et al. (as done in 2003a). The probability of a secondary burst occurring is such that half of the galaxy templates in the library have experienced a burst in their last $2\,\mathrm{Gyr}$. Each of those episodes can last 3×10^7–$3 \times 10^8\,\mathrm{yr}$, producing stars at a constant rate. The ratio between the stellar mass produced in a single burst and the one formed over the entire galaxy's life by the underlying exponentially declining model is distributed logarithmically between 0.03 and 4.0. The dust absorption model adopted in MAGPHYS is the one proposed by Charlot & Fall (2000), which considers the optical depth of HII and HI regions embedding young stars along with the extinction caused by diffuse interstellar medium. MAGPHYS treats attenuation in a consistent way, including dust re-emission at infrared wavelengths. However, this feature does not represent a significant advantage when dealing with VIPERS data since the cross-correlation of our catalogue with infrared magnitudes (in particular SWIRE-MIPS) results in very few matches. Metallicity values are distributed uniformly between 0.02 and $2\,Z_\odot$. The wide range of tightly sampled metallicities, the different model for the dust extinction, and in particular the complex SFHs in the MAGPHYS library are the major differences with respect to the HYPERZMASS code. I will show in the next Section the impact of these differences on the SED fitting outcomes.

It should be noted that, according to Mitchell et al. (2013), the assumption of exponentially declining SFHs is not one of the major uncertainties. Mitchell et al. (2013) apply the SED fitting technique to mock galaxies, whose observational features have been emulated through a theoretical model of galaxy formation (GALFORM, Cole et al. 2002). Although τ-models in the SED fitting are much simpler than the SFHs in the theoretical model, the stellar mass estimates estimated in the two ways have a negligible offset and scatter (e.g. $\mu = -0.01$ and $\sigma = 0.03$ at $z = 0.5$).

Mitchell et al. (2013) explore other possible sources of bias, in particular the parametrization of metallicity and dust. Their analysis indicates that the use of a few discretely spaced metallicities may be inappropriate for galaxies at $\log(\mathcal{M}/\mathcal{M}_\odot) \sim$ 9–10. Such an issue, mainly caused by parameter degeneracies, should not affect the results of the present work, since it has an effects at masses below the VIPERS completeness limit. However, one should keep in mind the bias due to degeneracies between various parameters, e.g. metallicity and age, that can affect estimates at any mass. Regarding the dust extinction in the SED fitting technique, the assumption of uniform screen has well-known flaws, but the major impact should be limited to very dusty galaxies (Mitchell et al. 2013). It should be also noticed that

---

[3] Since MAGPHYS requires a long computational time, we only estimate the stellar mass for galaxies in the W1 field between $z = 0.5$ and $z = 1.3$.
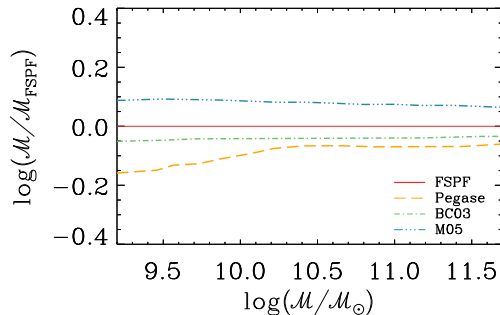
Figure 2.7   The impact of different stellar population synthesis models is measured for SED fitting estimates of $z \simeq 0$ galaxies (photometry from SDSS, 2MASS, and GALEX). In this plot, reference masses (based on the galaxy templates described in Conroy et al. 2009) are compared with those derived from other models of stellar population synthesis, i.e. Bruzual & Charlot (2003, BC03 in the legend), Maraston (2005, M05) and Fioc & Rocca-Volmerange (1997, Pegase). Adapted from Conroy (2013).

the introduction of more refined models would represent an improvement only with IR data. Unfortunately they are not available for the whole survey, therefore it is difficult to recover the dust re-emission. Among the other systematic effects to take into account, the choice of the stellar population synthesis model implies some potential bias (Conroy 2013). Figure 2.7 shows how the stellar mass estimates systematically change assuming different SSPs in the SED fitting. In particular, the Figure shows the difference between BC03 and M05, which is mainly due to the TP-AGB stars (see discussion above).

With respect to statistical uncertainties, typical errors of absolute magnitude (e.g. in the B-band) range from $\sigma_B = 0.04$ to 0.07 at redshift $0.4 < z < 1.1$. They include measurement uncertainties in the zero-point, SED extrapolation, and adopted template libraries (Fritz et al. 2014). For stellar mass estimates, uncertainties in various stages of stellar evolution carry statistical errors of ~ 30–50% (1σ CL), with little dependence on luminosity (Wuyts et al. 2007; Muzzin et al. 2009a,b; Conroy et al. 2009). Clearly, the precision depends on the type of data used.

2.1.5   Results of SED fitting technique in VIPERS

The SED fitting procedure described above yields estimates of several galaxy quantities, in particular absolute magnitudes, stellar mass, and SFR. The absolute magnitude in a given passband is derived starting from the nearest apparent magnitude, i.e. the observed-frame filter that – once shifted to the redshift of the galaxy under consideration – is the closest to the wavelength of the desired rest-frame passband. The k-correction factor applied to the selected apparent magnitude is derived from the shape of the best-fit SED, and it is usually small (see Ilbert et al. 2005, Appendix A). The dust effect is not removed in the computation (i.e., the absolute magnitude of the VIPERS galaxies are not "de-reddened"). In this way, the final results are weakly sensitive to the SED fitting procedure. Absolute magnitudes
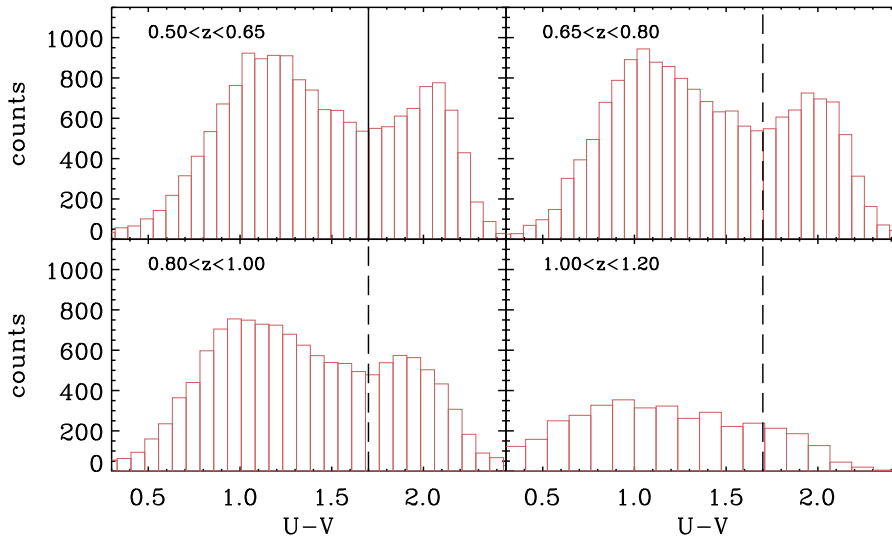
Figure 2.8   Rest-frame $(U-B)$ colour distribution of the VIPERS PDR-1 galaxies, in four redshift bins (as mentioned in each panel). In the lowest z-bin, a black solid line determines the dip that separates the blue peak from the red one; it is reported at higher redshifts as a dashed line, to show the weak evolution in such a bimodal shape up to $z \simeq 1$.

that will be used in the following are derived with respect to the Johnson U, B, V filters; FUV and NUV from GALEX; the Ks filter of WIRCam.

Once evaluated the absolute magnitudes, it is possible to plot e.g. the $(U - V)$ colour distribution (Fig. 2.8) to see the classical bimodality observed in many studies (Strateva et al. 2001; Hogg et al. 2002; Bell et al. 2004, e.g.). In Fritz et al. (2014) we also derive the luminosity functions (Fig. 2.9) of VIPERS. The unique large volume probed by VIPERS leads to a higher completeness for rare, very luminous galaxies ($M_B - 5 \log h < -23$), extending by more than one magnitude the effective sampling of the bright-end of the LF. These very luminous objects correspond to the most massive systems that will be investigated in the following.

Unlike absolute magnitudes, stellar mass and SFR estimates significantly rely on the best-fit template, being derived directly from the modelled stellar content and SFH. Therefore, systematic trends more easily emerge when one compares stellar masses obtained with different SED fitting parameters (Fig. 2.10). In addition to those quantities, for each galaxy template one can obtain the apparent magnitude in the same (observer frame) passbands of VIPERS. Thus, a basic test is comparing the best-fit apparent magnitudes with those of the observed galaxy. This comparison is shown in Fig. 2.11.

In Section 2.1.4 I discussed the reliability of smooth SFHs and the possible improvements that one can get by including secondary bursts. I referred to previous work suggesting that SED fitting estimates for a galaxy sample like VIPERS should not be seriously affected by the absence of complex SFHs in the template library. The same conclusion can be drawn by inspecting Fig. 2.12, in which the estimates of HYPERZMASS are compared to MAGPHYS. The Figure shows the outcomes obtained by allowing for secondary bursts (through the code
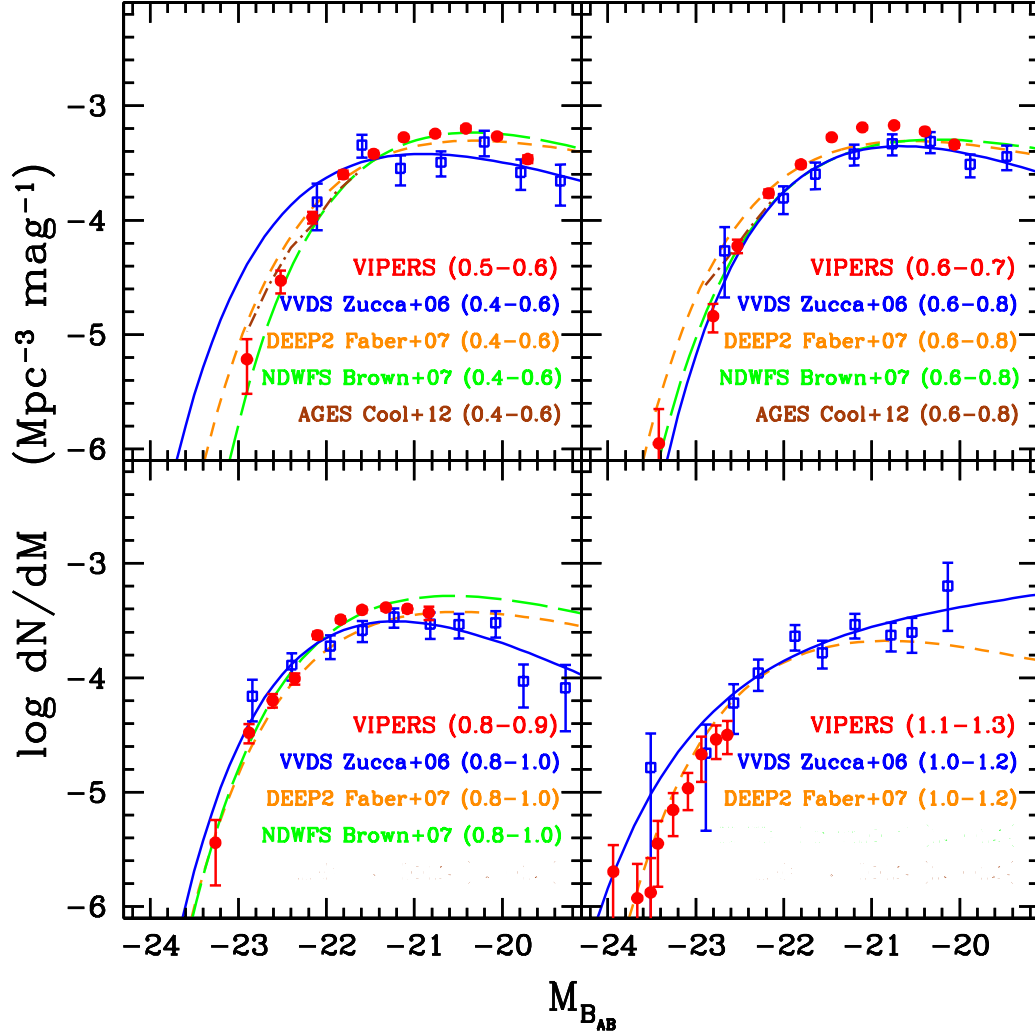
Figure 2.9 Luminosity functions in the *B*-band from five large spectroscopic surveys: VVDS, DEEP2, NDWFS, AGES, VIPERS PDR-1 (Ilbert et al. 2005; Faber et al. 2007; Brown et al. 2007; Cool et al. 2012; Fritz et al. 2014, respectively). Red filled circles are $1/V_{max}$ determinations with Poisson error bars for VIPERS. The same estimator is used for the VVDS sample (blue open squares), with the addition of the Schechter fit (blue solid line). Only the Schechter function is shown for DEEP2 (orange dashed line), NDWFS (green long-dashed line), and AGES (brown dot-dashed line). Luminosity functions taken from the literature are derived in redshift intervals that overlap only partially to VIPERS *z*-bins (see text in each panel). From Fritz et al. (2014)
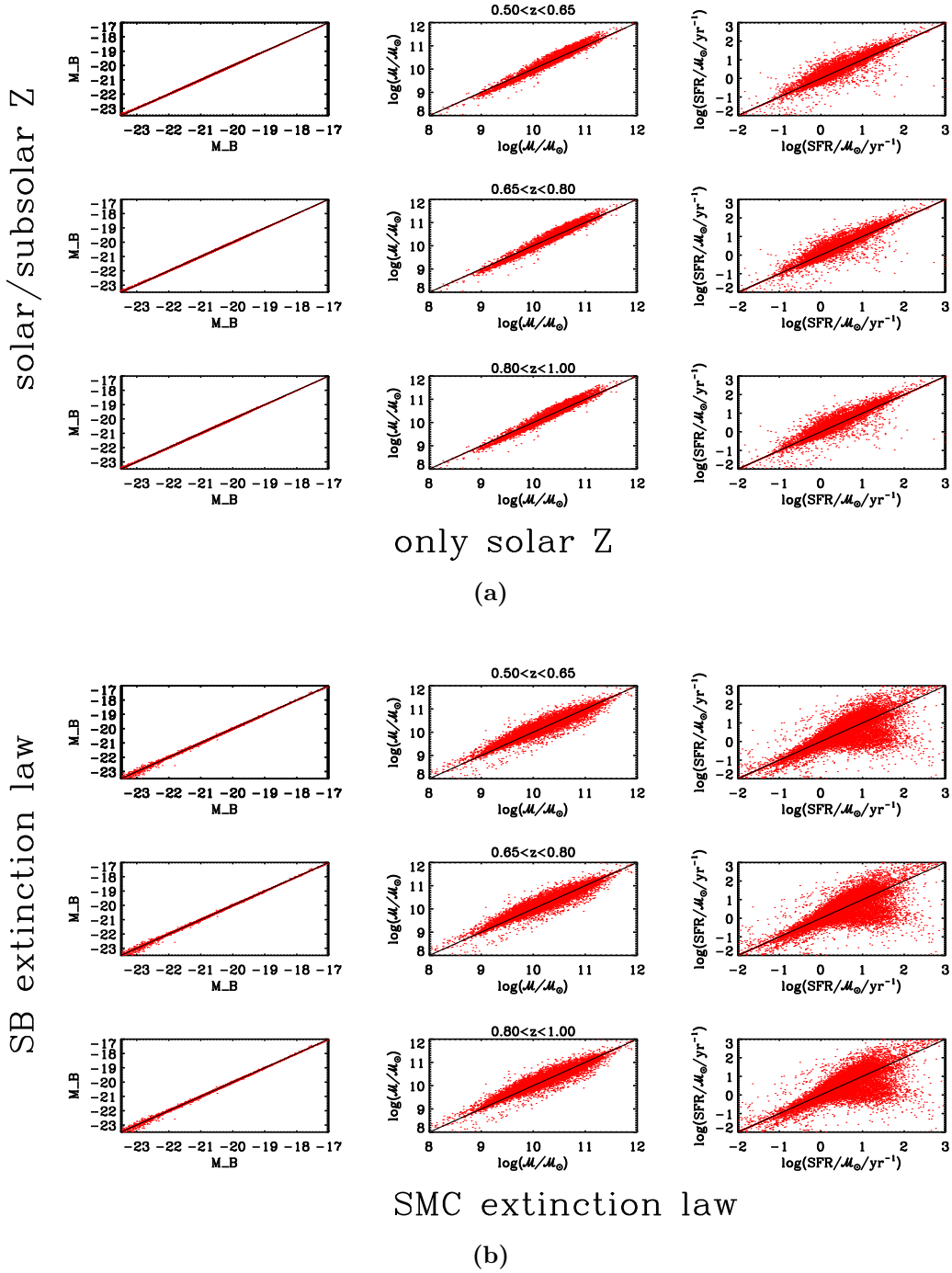
Figure 2.10 Comparison between different SED fitting procedures, The first 3 × 3 panels show estimates obtained with two sets of galaxy templates differing in metallicity: $Z_\odot$ only (estimates on the x-axis) and $0.2Z_\odot, Z_\odot$ (on the y-axis). Rows correspond to different redshift bins (whose range is indicated above the central panel of the row). In each row, the three panels (from left to right) show respectively: absolute magnitude in the B band, stellar mass, and SFR. The other 3 × 3 matrix of plots shows a comparison between two SED fitting procedures that assume a different extinction model: Prévot-Bouchet (SMC, x-axis) and Calzetti's one (SB, quantities on the y-axis). Only a subsample of 10 000 VIPERS galaxies (randomly selected) have been used in this test.
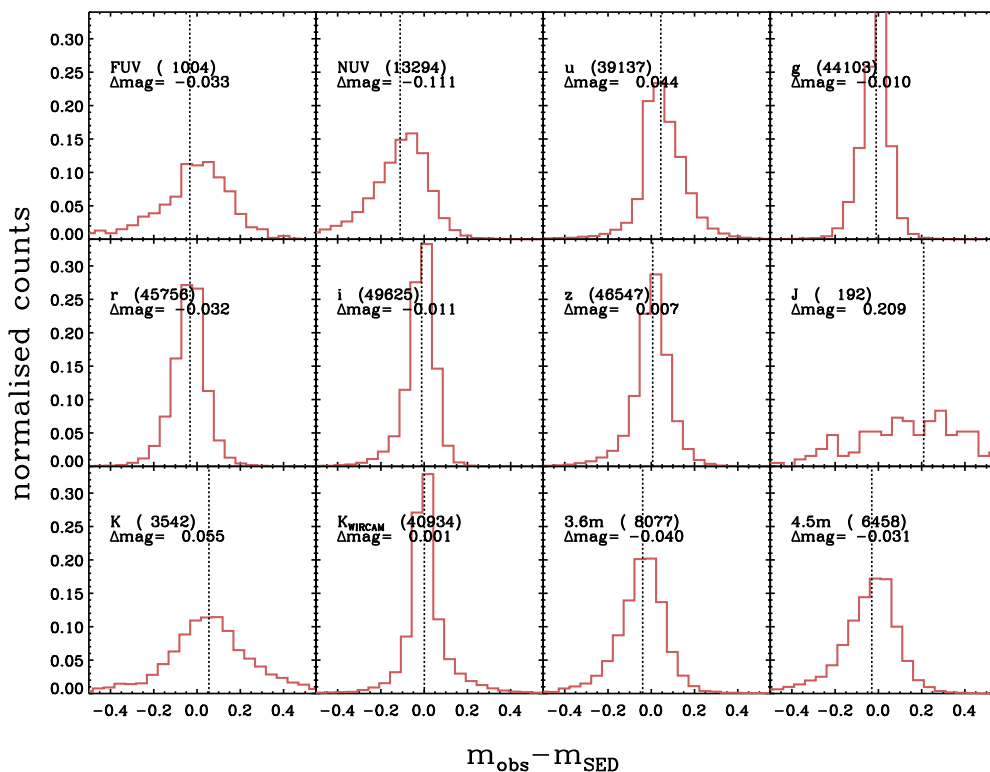
Figure 2.11   Apparent magnitudes derived from the best-fit SED, compared to the observed magnitudes. Histograms show the distribution of the difference between the two quantities, while the median of such values is marked with a vertical dotted line. Observations and SED fitting estimates are taken from the whole PDR-1 catalogue, but in each passband only galaxies with a reliable flux measurement are considered: when the error is larger than $0.2\,\mathrm{mag}$ (0.1 in g, r, i, z) the object is excluded from the histogram. Note also that observations in UV and IR are available only for a fraction of the sample. In particular, the J band is used only when K-band data are not available. Without K, the SED fitting estimates are less reliable, as suggested by the disagreement shown in last panel of the second row.
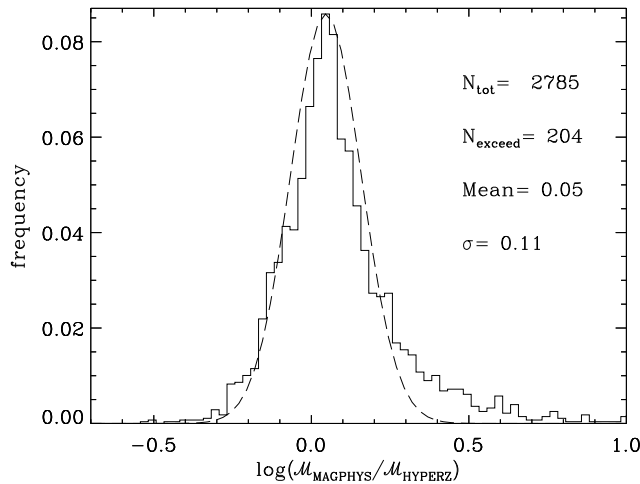
Figure 2.12 Comparison between the stellar mass estimates of Hyperzmass and magphys. The histogram is built with $2\,785$ galaxies that have solar metallicity according to both the SED fitting estimates. In this way it is possible to disentangle the systematics due to the presence/absence of secondary bursts from other effects that are metallicity-dependent.

magphys, see description above). They are in fairly good agreement with the exponentially declining SFHs assumed in Hyperzmass: the distribution of the ratio between the two mass estimates is well reproduced by a Gaussian function plus a small tail towards positive values of $\log(\mathcal{M}_{\mathrm{magphys}}/\mathcal{M}_{\mathrm{Hyperzmass}})$. There is a small offset ($\langle \Delta \log \mathcal{M} \rangle = \langle \log(\mathcal{M}_{\mathrm{magphys}}/\mathcal{M}_{\mathrm{Hyperzmass}}) \rangle \simeq 0.05$) and a small dispersion ($\sigma_{\Delta\mathcal{M}} \simeq 0.11$) for most of the galaxy population, with significant differences between magphys and Hyperzmass (i.e., $\Delta \log \mathcal{M} > 0.22$) for only $\sim 7\%$ of the testing sample. This subset of galaxies should have undergone recent bursts of star formation: for these objects, the best-fit template found by magphys includes a secondary burst of star formation in the last 10^8–10^9 yr. Therefore, by incorrectly fitting young and dusty templates, Hyperzmass systematically underestimates those objects (similarly to what observed in Michałowski et al. 2012, 2014, for submillimeter galaxies). These catastrophic errors, given their small number, do not impair the results of the present work, as I shall show in Sect. 3.2.3.

Another issue mentioned above is the bias caused by the absence of K-band magnitudes. The NIR photometry is useful to break some degeneracies in the SED fitting parameter space, and without these data stellar mass is often underestimated, especially for the most massive galaxies (Fig. 2.13).

2.2 Complementary techniques

Along with the SED fitting, which is the technique most extensively used in this work, other estimators have been applied to the VIPERS data. The main goal of implementing further methods is to obtain independent estimates that can support the results of the previous Section (or highlight possible flaws). However, these
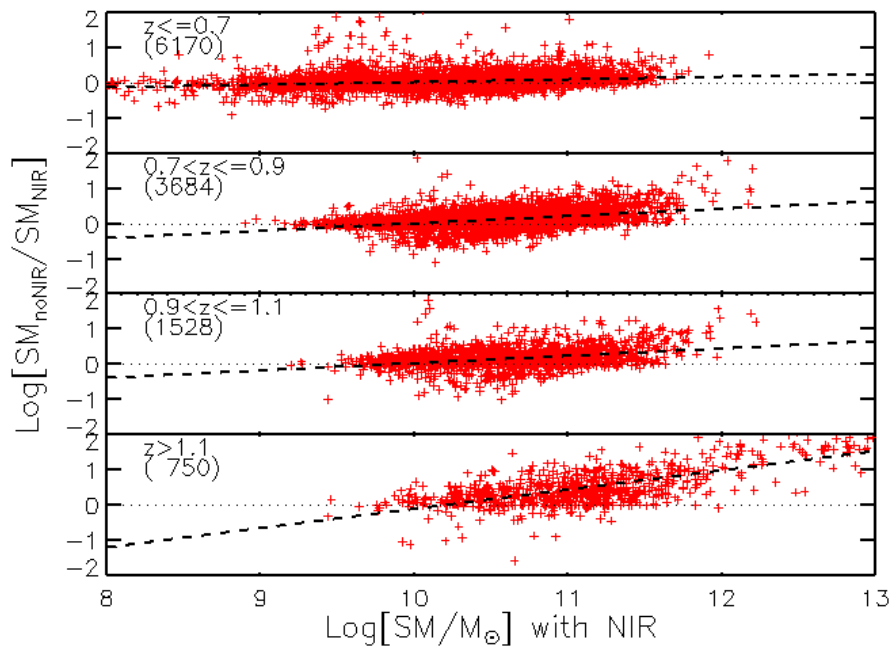
Figure 2.13   Stellar masses of a subsample of VIPERS galaxies, in different z-bins (reported in the top-left corner of each panel, together with the number of objects considered). The absence of K-band photometry in the SED fitting produces a systematic effect: removing that filter, stellar mass estimates are larger than the results obtained using also NIR data. The bias is redshift dependent, as evident especially at $z > 0.9$. It is almost negligible at $z < 0.7$ because part of the rest-frame NIR emission (i.e. old stellar populations) is still observed in the optical z band.

alternative methods are not necessarily more accurate. Therefore the comparison of different techniques mostly gives an idea of the general uncertainties one has to deal with.

2.2.1 Alternative estimates of galaxy stellar mass

An alternative stellar mass estimator is based on the empirical relation between stellar mass-to-light ratio and optical colours of the galaxy as calculated in its rest frame. Such a relation was investigated for the first time by Bell & de Jong (2001). Their work focused on spiral galaxies, because the original goal was to derive $\mathcal{M}/L$ in order to constrain the Tully-Fischer relation Tully & Fisher (1977). By means of a preliminary version of the BC03 model, Bell & de Jong link this correlation to the common origin of galaxy colour and $\mathcal{M}/L$: both are determined by the star formation and the chemical enrichment history of the galaxy.

In the $\mathcal{M}/L_B$ vs $(B-R)$ diagram, galaxies with different SFH and Z occupy the same narrow region (Bell & de Jong 2001, Fig. 2a) and therefore it is possible to describe $\mathcal{M}/L_B$ as a function of $(B-R)$. This property holds also after changing the reference bands in the parameter space (i.e., B and R) with other optical filters. In general, the location of spiral galaxy templates in the $\mathcal{M}/L$ vs colour plane is tight enough that can be fitted with a linear relation, i.e.

$$\log\left(\frac{\mathcal{M}}{L_x}\right) = a_x + b_x(M_x - M_y) \,, \tag{2.6}$$

where luminosity and colour are computed within two optical filters x and y. It should be noticed that this correlation, provided in Bell & de Jong (2001), relies on the assumption of a universal IMF. After estimating the x-band luminosity, it is possible to recover the galaxy stellar mass.

Using redder filters that break the age-metallicity degeneracy (e.g., I and K) the relation becomes less tight because metal-rich and metal-poor spirals occupy now different regions of the $\mathcal{M}/L$-colour diagram. The same happens with optical filters if adopting a larger metallicity range in the models: objects in the diagram spread out and they are no longer well-fitted by a single linear equation (Bell et al. 2005). On the other hand, dust extinction does not alter the relation, at least at the first order. In fact, galaxies become redder but also fainter, and the two effects cancel out (i.e., the reddening vector is parallel to the galaxy trend in the $\mathcal{M}/L$-colour diagram).

Equation (2.6) can be useful when NIR data are not available, since without that information the SED fitting often overestimates stellar masses, especially for massive galaxies (Fig. 2.13). Although this is not the case of VIPERS, I apply this technique to the PDR-1 catalogue: the goal is testing the reliability of this approach through an independent estimator (i.e., the official VIPERS stellar masses estimated via SED fitting). A similar comparison has been performed in Bundy et al. (2006) and Maier et al. (2009). It should be noted that the SED fitting plays a role also in this alternative technique, since it is used to recover the galaxy absolute magnitudes in the required optical bands. However, the results discussed here can be considered an independent estimate with respect to those obtained in Sect. 2.1.5,
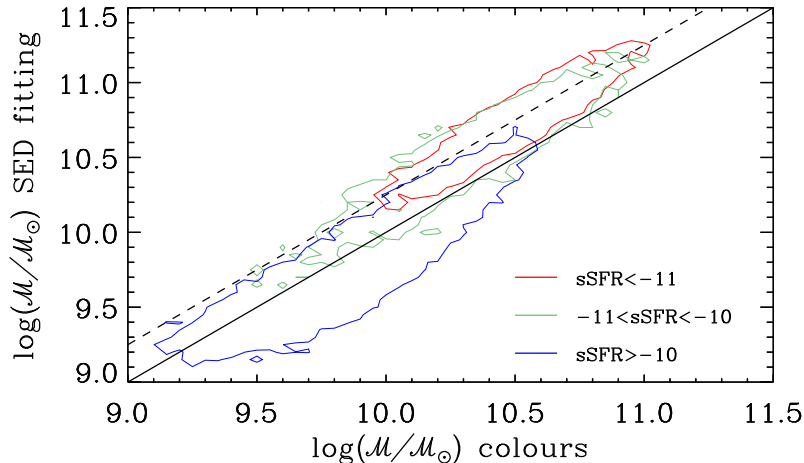
Figure 2.14 Stellar mass estimates obtained through Eq. (2.8) and SED fitting (on the x- and y-axis, respectively). The VIPERS sample is divided into three galaxy classes with respect to the sSFR (see Sect. 3.3.1 for more details about this classification); coloured contours encompass 68% of each subsample. Galaxies with low and intermediate sSFR have red and green contours respectively. For them, the stellar masses estimated by means of the Lin et al. (2007) relation are lower than the ones obtained by SED fitting: the offset is about 0.25 dex (dashed black line) although the dispersion is not large (~ 0.2 dex). High-sSFR galaxies (blue contour) do not show such systematics (see the solid black line that marks the bisector) but have larger scatter.

because they are insensitive to most of the SED fitting drawbacks, which concern stellar mass estimates more than absolute magnitudes (see Fig. 2.10).

With this approach, neglecting secondary bursts can produce a large uncertainty because a recent burst of star formation can heavily affect the single colour used in the relation. However, when such bursts are modest, the relation holds (Bell & Kennicutt, Jr. 2001). Bell et al. (2003) find the random errors of Eq. (2.6) to be $\sim 20\%$, while systematics uncertainties are on the order of 30%. Bell et al. (2005) state an uncertainty of 0.3 dex for the stellar masses they derived through the equation

$$\log(\mathcal{M}/\mathcal{M}_\odot) = -0.4(V - V_\odot) + [1.737(B - V) - 0.628] \ . \qquad (2.7)$$

Lin et al. (2007) provide Eq. (2.6) with additional terms, to account for evolution in colour of their galaxy sample (whose redshift range is $0.1 < z < 1.1$):

$$\log(\mathcal{M}/\mathcal{M}_\odot) = -0.4(B - B_\odot) + 1.305(B - V) + \\ 0.098(U - B) - 0.130(U - B)^2 - 0.268z - 1.003 \ . \qquad (2.8)$$

The comparison with SED fitting estimates indicates that this technique has an rms accuracy of 0.25 dex (Bundy et al. 2006; Lin et al. 2007). Maier et al. (2009), applying Eq. (2.8) to zCOSMOS data, state a statistical rms of ~ 0.13 dex, and an offset of 0.10 dex in the mean.

I apply Eq. (2.8) to the VIPERS galaxies, comparing the resulting stellar mass with the official (SED fitting) estimates described in Sect. 2.1.4. Figure 2.14 shows

such a comparison, for three galaxy types (active, intermediate, passive) classified by means of their sSFR (based on the SED fitting, see Sect. 3.3.1 for more details). Equation (2.8) works better for active galaxies, providing stellar mass estimates in agreement with those derived thorugh SED fitting (although a scatter of $\sim 0.3\,\text{dex}$). Masses of quiescent galaxies (i.e., with intermediate and low values of sSFR) are on average overestimated by about $0.25\,\text{dex}$, but the dispersion of these two samples is about $0.2\,\text{dex}$, smaller than the previous one (see Fig. 2.14). The offset is larger than the one found by Maier et al. (2009) but it goes in the same direction: we argue that the systematics in the zCOSMOS results are also due to the presence of many passive galaxies.

2.2.2   Alternative estimates of star formation rate

Since spectra are available for the VIPERS galaxies, I measured the SFR from emission lines. Given the redshift range of the survey, this task mainly relies on the [OII] emission ($\lambda\lambda 3726, 3729$ doublet, blended because of the VIMOS resolution). The equivalent width (EW) of the [OII] line has to be converted into a normalised flux ($F_{[\text{OII}]}$), and then into luminosity through the formula

$$L_{[\text{OII}]} = 4\pi \, F_{[\text{OII}]} \, D_L(z)^2 \ , \tag{2.9}$$

where D_L is the luminosity distance of the considered galaxy at redshift z. $F_{[\text{OII}]}$ is measured in Garilli et al. (2014) for galaxies in the PDR-1 catalogue through a simple flux integration below the line. Integrations are in counts unit and then are converted into pure fluxes using the counts-to-flux rate derived from the sensitivity function of the spectrograph. The local continuum is computed by averaging counts over two nearby ranges, namely 3600–3700 and 3755–4000 AA. The error on the continuum level is also subtracted, using the noise spectrum associated to the considered source (see Garilli et al. 2014, for more details).

First calibrations of SFR by means of $L_{[\text{OII}]}$ have been provided by Gallagher et al. (1989) and Kennicutt, Jr. (1992), using samples of nearby galaxies consisting respectively of 75 blue irregular galaxies and 90 normal and peculiar galaxies. Either Hα or Hβ fluxes are used in those analyses to calibrate SFR($L_{[\text{OII}]}$). It should be noticed that, once converted to the same calibration, the SFRs provided by Gallagher et al. and Kennicutt, Jr. differ by a scaling factor of ~ 1.6 that reveals how this kind of estimator is sensitive to the excitation differences among various galaxy populations. Indeed, the [OII] emission line has several dependencies (e.g. on reddening, gas fraction, ionization properties, metal abundance) that are not trivial to account for (Hunter 1994; Jansen et al. 2001; Charlot et al. 2002).

Kennicutt, Jr. (1998) combined the results of Gallagher et al. (1989) and Kennicutt, Jr. (1992), finding

$$\text{SFR}(\mathcal{M}_\odot \, \text{yr}^{-1}) = (1.4 \pm 0.4) \times 10^{-41} L_{[\text{OII}]}(\text{erg}\,\text{s}^{-1}) \ , \tag{2.10}$$

where the uncertainty is due to the difference between galaxy types discussed above. According to Kennicutt, Jr. (1992, 1998), the observed luminosity has to be corrected for the extinction measured at Hα.

Kewley et al. (2004), working on a sample of 97 nearby galaxies, find a disagreement between Eq. (2.10) and the SFRs derived from Hα (Kennicutt, Jr. 1998, Eq. 2). The main reasons for that discrepancy are difficulties in reddening and metallicity calibrations. As stated above, the [OII]/Hα and [OII]/Hβ ratios on which this relation relies vary significantly among star-forming galaxies. In particular, the [OII]/Hα ratio assumed in Eq. (2.10) still shows a dependency on $E(B-V)$ (Fig. 2 of Kewley et al. 2004, see also Jansen et al. 2001). Therefore, this average calibration is not expected to match the characteristics of other surveys. Moreover, Eq. (2.10) is based on local galaxies and could not be appropriate at $z > 0.5$. Kewley et al. (2004) devise a new SFR([OII]) indicator, using a sample of 97 nearby galaxies. The difference with respect to Kennicutt, Jr. (1998) is that they correct the observed [OII]/Hα for dust reddening, assuming the attenuation curve of Cardelli et al. (1989). The resulting relation is significantly different from the previous one:

$$\text{SFR}(\mathcal{M}_\odot \, \text{yr}^{-1}) = (6.58 \pm 1.65) \times 10^{-42} L_{[\text{OII}]}(\text{erg}\,\text{s}^{-1}) \,. \qquad (2.11)$$

Also in this case $L_{[\text{OII}]}$ should be corrected for dust extinction. Despite the improvement, Eq. (2.11) is still based on an average calibration and cannot be applied blindly to other samples.

The systematic effects of reddening (and metallicity) can be removed on a galaxy-by-galaxy basis, by using improved estimators as the ones proposed in Moustakas et al. (2006) and Mostek et al. (2012). These estimators make use of either galaxy luminosity or stellar mass as a proxy of dust content. In principle, one can use also the Balmer decrement (Hα/Hβ) to quantify $E(B-V)$, but if the Hα nebular emission is observable then it should be directly used to derive a more reliable estimate of the SFR. In addition, abundance estimates can be obtained from line diagnostics like ([OII] + [OIII])/Hβ or [NII]/[OII] (Zaritsky et al. 1994; Kewley & Dopita 2002).

To address the reddening issue, Moustakas et al. (2006) take advantage of the correlation between attenuation and luminosity, i.e. the fact that galaxies with higher SFR also produce more dust (Jansen et al. 2001). This is especially true in the B-band, where luminosity is mildly sensitive also to metal abundance. The empirical calibration of Moustakas et al., who make use of a local galaxy sample, is provided in bins of either luminosity (L_B) or absolute magnitude (M_B). It is reported in Fig. 2.15. In contrast with previous cases, the [OII] luminosity does not need extinction correction before being used in the formula; for this reason I indicate this estimator as SFR($M_B, L_{[\text{OII}],\text{obs}}$).

Using high-z data from the literature, Moustakas et al. show that the local [OII]/L_B relation qualitatively holds at $z \lesssim 1$. On the other hand, Mostek et al. (2012) warn that SFR($M_B, L_{[\text{OII}],\text{obs}}$) should not be applied to galaxies at intermediate redshifts, because the difference with respect to local samples (i.e., evolution of typical B-band luminosity) introduces a considerable systematic uncertainty in their SFR evaluation ($\gtrsim 0.3\,\text{dex}$ overestimate at $z = 1$). Mostek et al. recommend to correct the M_B values measured at higher z by including a dimming factor (Q) estimated from the evolution of the luminosity function.

I applied the recipe of Moustakas et al. (2006), together with Mostek et al. (2012) prescription, to the VIPERS sample. First, I plot the empirical points in
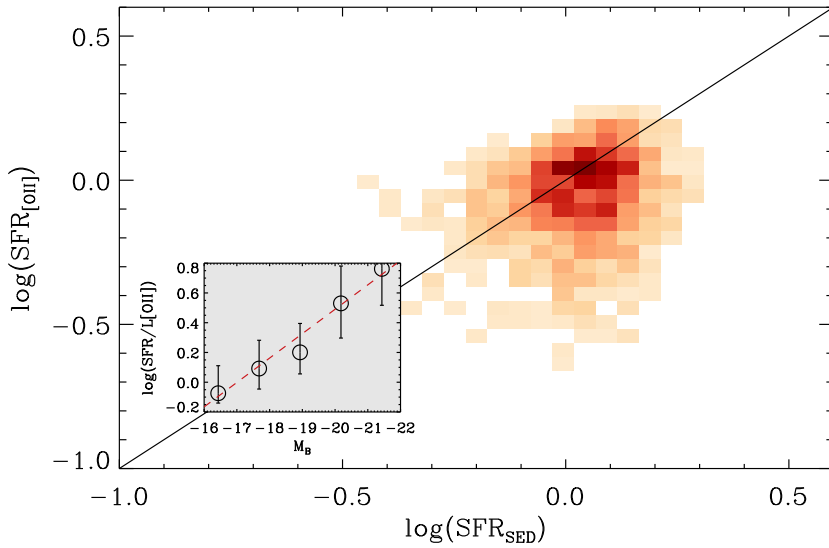
Figure 2.15 Comparison between SFR estimates obtained through SED fitting (on the x-axis, see Sect. 2.1.4 for details) and the measurements by means of Eq. (2.12) relying on the [OII] luminosity (y-axis). Pixels indicate density of objects in the diagram, with a solid line showing the $y = x$ relation. Only a subsample of the VIPERS catalogue is used in this plot, i.e. galaxies with $0.5 < z_{\rm spec} < 0.9$, $2 \leqslant z_{\rm flag} < 9$, and $F_{3.6\mu m} > 0$. The inset reports the observational data used by Moustakas et al. (2006) to calibrate their equation: open circles are the median of the $\log(\mathrm{SFR}/L_{\rm [OII]})$-$M_B$ relation for galaxies in bins of absolute magnitude; error bars are computed from the 25th and 75th percentile in each bin. The red dashed line is the best fit to these points, leading to Eq. (2.12).

the $\log(SFR/L_{\rm [OII],obs})$ vs M_B plane that determine $\mathrm{SFR}(M_B, L_{\rm [OII],obs})$. Each of these points is the median of the $\log(SFR/L_{\rm [OII],obs})$ distribution of galaxies within bins of absolute magnitude (Moustakas et al. 2006, Table 2). Then, I fit the points at $M_B < -16$ with a linear relation, obtaining

$$\log(SFR/L_{\rm [OII],obs}) = -0.164(M_B) - 2.788 \, , \qquad (2.12)$$

where $L_{\rm [OII],obs}$ is in units of $10^{-41}\,\mathrm{erg\,s^{-1}}$ and SFR is expressed in $[\mathcal{M}_\odot\,\mathrm{yr}^{-1}]$.

This result is shown in the inset of Fig. 2.15. In the case of VIPERS, before applying Eq. (2.12) the absolute magnitude has to be corrected as advocated by Mostek et al. (2012), i.e. $M_{B,\rm corr} = M_B - Qz_{\rm spec}$. The dimming factor is $Q = 1$, according to the evolution of the $M_B^\star$ parameter of the Schechter function fitting the zCOSMOS luminosity function (Zucca et al. 2009).[4] The redshift $z_{\rm spec}$, as well as M_B and $L_{\rm [OII],obs}$, are the values measured for the considered galaxy.

---

[4] Note that the original computations of Moustakas et al. (2006) assume Salpeter (1955) IMF. I converted their SFRs into Chabrier (2003) to be in agreement with the VIPERS estimates. Another correction should be the conversion of the filter they use to derive absolute B-band magnitude to the VIPERS (B-Buser) filter. Unfortunately the filter is not clearly stated in the paper, therefore, in the following, another systematic effect could come from a possible difference between VIPERS and Moustakas et al. M_B values, i.e. between the shape of the two filters.
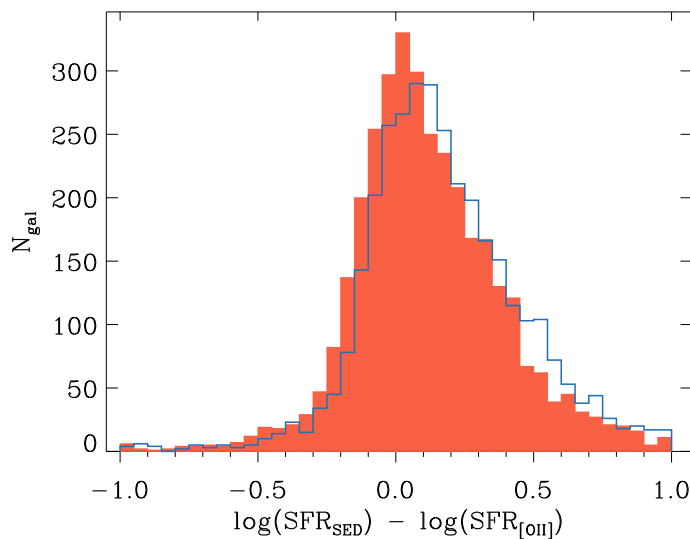
Figure 2.16   The histograms show the agreement between $\mathrm{SFR}(M_B, L_{\mathrm{[OII]},\mathrm{obs}}$ and the SFR obtained through SED fitting (see text). Galaxies considered here are the same of Fig. 2.15. Two kinds of estimate, both relying on [OII] luminosity, are shown: in the solid-red histogram $\mathrm{SFR}_{\mathrm{[OII]}}$ is obtained from Eq. (2.12), while the blue histogram does not assume a correction for L_B evolution (i.e., Q is equal to zero in Eq. 2.12).

In Fig. 2.15 the resulting SFRs are compared with the estimates derived from SED fitting (with the input parameters listed in Table 2.1). Given the large number of uncertainties in the procedure, it is difficult to state that the estimators are in agreement. However, it is important to notice that the M_B correction does improve the estimates, although not dramatically (Fig. 2.16). Moreover, in Fig. 2.15 there is a plume of objects having $\mathrm{SFR}_{\mathrm{SED}} \approx 1\,\mathcal{M}_\odot\,\mathrm{yr}^{-1}$, for which $\mathrm{SFR}_{\mathrm{[OII]}}$ is significantly lower than $\mathrm{SFR}_{\mathrm{SED}}$. I do not investigate the origin of such a discrepancy.

Another SFR indicator is calibrated by Mostek et al. (2012) following the formalism of Gilbank et al. (2010). Instead of B-band luminosity, this empirical calibration (tested on DEEP2 data) relies both on $L_{\mathrm{[OII]}}$ and galaxy stellar mass. In fact, dust attenuation and metal abundance correlate strongly with stellar mass (e.g. Tremonti et al. 2004; Mannucci et al. 2010; Zahid et al. 2013a,b). However, a few tests using VIPERS data show that this estimator is not in agreement with other independent measurements of the SFR. One of the reasons for that could be indeed the stellar mass estimates: the SED fitting procedure selects a dust attenuation curve, and if this assumption is not fully correct it can introduce a significant deviation in the computation of Mostek et al. (2012). Given the lack of results, these tests are not shown in the present work.

Chapter 3

Galaxy stellar mass function of the VIPERS field

As shown before, VIPERS probes a large cosmic volume and collects an impressive amount of data, facilitating therefore a number of important statistical studies. One such fundamental statistic is the luminosity function, already seen in Sect. 2.1.5. Another one is the galaxy stellar mass function (GSMF), defined as the co-moving number density of galaxies within a stellar mass bin $(\mathcal{M}, \mathcal{M} + \mathrm{d}\mathcal{M})$. In the following I describe the methods used to compute the VIPERS GSMF and discuss their outcomes (Sect. 3.2). I also compute the stellar mass functions of different galaxy types (blue/red, active/passive) to get insights on galaxy evolution at intermediate redshifts (Sect. 3.3). The main results of this Chapter have been presented in Davidzon et al. (2013, hereafter D13).

3.1 Methods

3.1.1 Overview of the most used estimators

Many methods can be applied to derive the stellar mass function of a galaxy sample. Some of them are classified as *non-parametric estimators*, since they do not describe the GSMF shape with a specific model. This kind of algorithms simply provide the comoving number density of galaxies in each bin of stellar mass, i.e. $\Phi(\mathcal{M})\mathrm{d}\mathcal{M}$. In addition to them, there are *parametric estimators* that assume a certain shape of Φ. At the first order, the GSMF is well parametrised by the Schechter (1976) function:[1]

$$\Phi(\mathcal{M})\mathrm{d}\mathcal{M} = \Phi_\star \left(\frac{\mathcal{M}}{\mathcal{M}_\star} \right)^\alpha \exp \left(-\frac{\mathcal{M}}{\mathcal{M}_\star} \right) \frac{\mathrm{d}\mathcal{M}}{\mathcal{M}_\star} \,. \tag{3.1}$$

The parameter $\mathcal{M}_\star$ is often referred as the "knee" of the GSMF, where the exponential decline begins, while α is the power-law slope of the low-mass end. The

---

[1] The Schechter function is often described using logarithmic stellar mass ($\log(\mathcal{M})$, expressed in solar units) instead of $\mathcal{M}$; i.e., instead of Eq. (3.1) it is possible to use:

$$\Phi(\mathcal{M}) = \ln(10)\, \Phi_\star \left[10^{[\log(\mathcal{M}) - \log(\mathcal{M}_\star)](1+\alpha)} \right] \exp \left[10^{\log(\mathcal{M}) - \log(\mathcal{M}_\star)} \right]$$

third parameter, $\Phi_\star$, gives the overall normalisation of the mass function. However, an upturn at $\mathcal{M} \simeq 10^{10} \mathcal{M}_\odot$ is visible in many analyses (especially at $z \simeq 0$, e.g. Baldry et al. 2012; Moustakas et al. 2013). Thus, the choice of a double Schechter function, i.e.

$$
\begin{aligned}
\Phi(\mathcal{M})\mathrm{d}\mathcal{M} =& \Phi_1^\star \left(\frac{\mathcal{M}}{\mathcal{M}_\star} \right)^{\alpha_1} \exp \left(-\frac{\mathcal{M}}{\mathcal{M}_\star} \right) \frac{\mathrm{d}\mathcal{M}}{\mathcal{M}_\star} \\
&+ \Phi_2^\star \left(\frac{\mathcal{M}}{\mathcal{M}_\star} \right)^{\alpha_2} \exp \left(-\frac{\mathcal{M}}{\mathcal{M}_\star} \right) \frac{\mathrm{d}\mathcal{M}}{\mathcal{M}_\star} \, ,
\end{aligned} \tag{3.2}
$$

should be more appropriate. Given the difficulty to constrain its exponential decline, the $\mathcal{M}_\star$ value of the secondary Schechter function is assumed to be equal to the one of the massive component (i.e., $\mathcal{M}_{\star 2} = \mathcal{M}_{\star 1} \equiv \mathcal{M}_\star$). It is worth noticing that the shape of the GSMF would deviate significantly from the Schechter function, if the IMF was not universal (McGee et al. 2014).

A non-parametric estimator widespread used in the literature is the $1/V_{\mathrm{max}}$ method (Schmidt 1968). First devised as an estimator of quasar luminosity functions, the $1/V_{\mathrm{max}}$ is frequently used also to compute the GSMF (e.g. York et al. 2000; Cole et al. 2001; Baldry et al. 2008; Pozzetti et al. 2010; Moustakas et al. 2013). Given a galaxy with apparent magnitude i_{gal} in the redshift range $[z_1, z_2]$, V_{max} is the maximum comoving volume within which this galaxy remains observable, i.e.

$$
V_{\mathrm{max}} = \int_{\max(z_1, z_{\mathrm{min}})}^{\min(z_2, z_{\mathrm{max}})} \frac{\mathrm{d}V}{\mathrm{d}z} \, \mathrm{d}z \, . \tag{3.3}
$$

The integration boundaries of Eq. (3.3) depend on the intrinsic brightness of the source and the shape of its SED. Being i_{min} and i_{max} the magnitudes corresponding to the upper and lower limits in flux of the survey, z_{min} and z_{max} are such that

$$
\begin{aligned}
i(z_{\mathrm{min}}) \equiv & \quad M_{\mathrm{gal}} + 5 \log D_L(z_{\mathrm{min}}) + 25 + k(z_{\mathrm{min}}) = i_{\mathrm{min}} \quad \text{and} \tag{3.4} \\
i(z_{\mathrm{max}}) \equiv & \quad M_{\mathrm{gal}} + 5 \log D_L(z_{\mathrm{max}}) + 25 + k(z_{\mathrm{max}}) = i_{\mathrm{max}} \, , \tag{3.5}
\end{aligned}
$$

where M_{gal} is the absolute magnitude of the object, converted to the i-band apparent magnitude through luminosity distance D_L and k-correction (in which the SED dependency resides). Clearly, for other kinds of selection (or surveys with multiple flux limits) the approach will be different than (3.5). In addition to the dimming that makes the galaxy too faint to be observed, one has also to take into account the other limitations of the survey – i.e., the selection effects – as explained below (see Eq. 3.21). From a statistical point of view, the V_{max} of a galaxy with certain characteristics is proportional to the probability of detecting it within the survey volume.

The GSMF in a single stellar mass bin (e.g. $[\mathcal{M}, \mathcal{M} + \Delta\mathcal{M}]$) is therefore

$$
\Phi(\mathcal{M}) = \sum_{\mathcal{M} < \mathcal{M}_j < \mathcal{M} + \Delta\mathcal{M}} \frac{1}{V_{\mathrm{max}}(\mathcal{M}_j)\Delta\mathcal{M}} \, , \tag{3.6}
$$

where $V_{\mathrm{max}}(\mathcal{M}_j)$ has been evaluated by means of Eq. (3.3) for the j-th galaxy having stellar mass equal to $\mathcal{M}_j$. The (Poissonian) uncertainty associated to (3.6)

is

$$\sigma_\Phi = \frac{\Phi(\mathcal{M})}{\sqrt{N}} \simeq \left[\sum_{j=1}^{N} \frac{1}{V_{\mathrm{max}}^2(\mathcal{M}_j)} \right]^{1/2} , \qquad (3.7)$$

where N is the number of galaxies in a certain $\mathcal{M}$-bin (se e.g. Zucca et al. 1997). When in the stellar mass bin there are too few objects (or zero detections) upper limits can be estimated e.g. following Gehrels (1986), who provides for those cases analytical approximations of the confidence limits based on Poisson statistics. Once introduced the window function

$$W(x) \equiv \begin{cases} 1 & -\Delta\mathcal{M}/2 < x \leqslant \Delta\mathcal{M}/2 \\ 0 & \text{elsewhere}, \end{cases} \qquad (3.8)$$

it is possible to describe the GSMF in the whole stellar mass range, after dividing it into N_b bins:

$$\Phi(\mathcal{M}) = \sum_{k=1}^{N_{\mathrm{b}}} \Phi_k W(\mathcal{M}_k - \mathcal{M}) , \qquad (3.9)$$

where Φ_k is the estimate relative to the k-th bin $[\mathcal{M}_k - \Delta\mathcal{M}/2, \mathcal{M}_k + \Delta\mathcal{M}/2]$ (see Eq. 3.6).

One advantage of Eq. (3.6) is that it gives simultaneously both shape and normalisation of the GSMF. It is well known that the $1/V_{\mathrm{max}}$ estimator is unbiased in case of a homogeneous distribution of sources (Felten 1976), but it is affected by the presence of clustering (e.g. Takeuchi et al. 2000) especially in pencil-beam surveys. At variance with the data sets on which the estimator was tested in the past, VIPERS has a specific advantage, thanks to its large volume over two independent fields. The competing effects of over- and under-dense regions on the GSMF estimate should cancel out in such a situation. The impact on the present analysis will also be negligible because an inhomogeneous distribution of sources mainly affects the faint end (i.e. the low-mass end) of the luminosity (stellar mass) function (Takeuchi et al. 2000), while here the main interest is the massive tail of the distribution.

An example of parametric estimator is the one devised by Sandage et al. (1979, hereafter STY). It determines α and $\mathcal{M}_\star$ of Eq. (3.1) through a maximum-likelihood approach. The third parameter ($\Phi_\star$) is computed independently, following a procedure described below. Complementary to the $1/V_{\mathrm{max}}$ estimator in many aspects, the STY method is unbiased to density inhomogeneities (see Efstathiou et al. 1988). Moreover, it does not require binning the sample.

In the STY formalism, $P(\mathcal{M}, z)$ describes the cumulative probability of a galaxy observed at redshift z of being more massive than $\mathcal{M}$. Namely,

$$P(\mathcal{M}, z) = \frac{\int_{\mathcal{M}}^{\infty} \Phi(\mathcal{M}', z)\rho(z)\, \mathrm{d}\mathcal{M}'}{\int_{0}^{\infty} \Phi(\mathcal{M}', z)\rho(z)\, \mathrm{d}\mathcal{M}'} , \qquad (3.10)$$

where $\rho(z)$ is the mean galaxy density at that redshift and Φ is the Schechter function (3.1). The lower boundary of integration (which is zero in Eq. 3.10) can

be set to some value $\mathcal{M}_{\min}$ representing the stellar mass limit of the survey (see Sect. 3.1.3). A differential probability density $p(\mathcal{M}, z)$ is obtained by deriving the cumulative probability defined above:

$$p(\mathcal{M}, z) = \frac{\partial P(\mathcal{M}, z)}{\partial \mathcal{M}} = \frac{\Phi(\mathcal{M}, z)}{\int_0^\infty \Phi(\mathcal{M}', z)\, d\mathcal{M}'} . \tag{3.11}$$

This function – which is proportional to the stellar mass function – represents the probability of a certain galaxy to have stellar mass equal to $\mathcal{M}$ in the redshift range z. Given a sample of N_{gal} galaxies, the product of the probability densities at each data point, i.e.

$$\mathcal{L} = \prod_{j=1}^{N_{\mathrm{gal}}} p(\mathcal{M}_j, z_j) , \tag{3.12}$$

is the joint probability (or likelihood) to observe that sample from some parent distribution. This distribution is the stellar mass function Φ, which is modelled using Eq. (3.1). Therefore, to estimate the maximum likelihood, one has to find the value of the Schechter parameters α and $\mathcal{M}_\star$ that maximise $\mathcal{L}$. This can be done through standard optimization algorithm as the one described in Press et al. (2002, Sect. 10.5).

The formal error of the STY estimates comes from the error ellipsoid defined as

$$\ln(\mathcal{L}) = \ln(\mathcal{L}_{\max}) - \frac{\chi_\beta^2}{2} , \tag{3.13}$$

where χ_β^2 is the point of the χ^2 distribution corresponding to a given CL (e.g., $\chi_\beta^2 = 2.3$ to estimate the error contour with 68% CL, for two degree of freedom). As stated before, the normalisation has to be calculated independently. The reason is that $p(\mathcal{M}, z)$ contains the ratio between the differential and integrated mass functions, and the $\Phi_\star$ term cancels out in Eq. (3.10).[2]

Another maximum likelihood method (in this case, non-parametric) is the stepwise maximum-likelihood method (SWML), conceived by Efstathiou et al. (1988). Like the STY method, SWML completely cancels density information and therefore requires an independent algorithm to normalise the GSMF (see below).

In this formalism, as done for the $1/V_{\max}$, Φ is divided in N_{b} stellar mass bins with $\Delta\mathcal{M}$ width (Eq. 3.9). For instance, in the bin $\mathcal{M}_k - \Delta\mathcal{M}/2 < \mathcal{M} \leqslant \mathcal{M}_k + \Delta\mathcal{M}]$,

$$\Phi_k \Delta\mathcal{M} = \frac{\sum_{j=1}^N W(\mathcal{M}_j - \mathcal{M}_k)}{\sum_{j=1}^N H\left[\mathcal{M}_{\mathrm{lim}}(z_j) - \mathcal{M}_k\right] / \sum_{i=1}^{N_{\mathrm{b}}} \Phi_i H\left[\mathcal{M}_{\mathrm{lim}}(z_k) - \mathcal{M}_k\right] \Delta\mathcal{M}} , \tag{3.14}$$

where $W(\mathcal{M}_j - \mathcal{M})$ is the window function (3.8) and

$$H(\mathcal{M}_{\mathrm{lim}} - \mathcal{M}) \equiv \begin{cases} 1 & \text{if } \mathcal{M} > \mathcal{M}_{\mathrm{lim}} + \frac{\Delta\mathcal{M}}{2} \\ \frac{\mathcal{M}_{\mathrm{lim}} - \mathcal{M}}{\Delta\mathcal{M}} + \frac{1}{2} & \text{if } \mathcal{M}_{\mathrm{lim}} - \frac{\Delta\mathcal{M}}{2} < \mathcal{M} \leqslant \mathcal{M}_{\mathrm{lim}} + \frac{\Delta\mathcal{M}}{2} \\ 0 & \text{if } \mathcal{M} < \mathcal{M}_{\mathrm{lim}} - \frac{\Delta\mathcal{M}}{2} . \end{cases} \tag{3.15}$$

---

[2]This simplification is possible thanks to the fundamental assumption, generally accepted, that the GSMF does not correlate with space position, i.e. $\Phi(\mathcal{M}, x, y, z)\, d\mathcal{M}dV = \Phi(\mathcal{M})\rho(x, y, z)\, d\mathcal{M}dV$. This assumption has been implied in Eq. (3.10).

Equation (3.12) becomes

$$\ln(\mathcal{L}) = \sum_{j=1}^{N} \sum_{k=1}^{N_{\mathrm{b}}} \ln(\Phi_k) W(\mathcal{M}_j - \mathcal{M}_k)$$
$$- \sum_{j=1}^{N} \ln \left\{ \sum_{k=1}^{N_{\mathrm{b}}} \Phi_k H \left[\mathcal{M}_{\mathrm{lim}}(z_j) - \mathcal{M}_k \right] \Delta\mathcal{M} \right\} . \qquad (3.16)$$

Efstathiou et al. (1988) introduce an additional constraint, namely $g \equiv \sum_{k=1}^{N_{\mathrm{b}}} \Phi_k (\mathcal{M}_k/\mathcal{M}_{\mathrm{f}})^{\beta} \Delta\mathcal{M} - 1 = 0$, where $\mathcal{M}_{\mathrm{f}}$ is a fiducial stellar mass and $\beta \simeq -1.5$ (see Efstathiou et al. 1988, Sect. 2.2). Using a Lagrangian multiplier λ, Eq. (3.16) becomes $\mathcal{L}' = \mathcal{L} + \lambda g(\Phi_k)$ and has now to be maximised with respect to both Φ_k and λ. Solving this Equation, it turns out that $\lambda = 0$ and therefore the constraint g does not affect the resulting GSMF shape.

Evaluation of errors relies on the property that the maximum-likelihood estimates (Φ_k) are asymptotically normally distributed with covariance matrix (C) that is the inverse of the information matrix (I, see Eadie et al. 1971). In this case, the constraint g does play a role, since

$$C(\Phi_k) = I(\Phi_k)^{-1} = - \left[\begin{matrix} \frac{\partial^2 \ln(\mathcal{L})}{\partial\Phi_i \partial\Phi_j} \frac{\partial g}{\partial\Phi_i} \frac{\partial g}{\partial\Phi_j} & \frac{\partial g}{\partial\Phi_j} \\ \frac{\partial g}{\partial\Phi_i} & 0 \end{matrix} \right]_{\Phi_k}^{-1} . \qquad (3.17)$$

As stated above, likelihood functions of STY and SWML methods have an arbitrary normalisation. The correct GSMF normalisation (i.e., the parameter $\Phi_\star$ in Eq. 3.1), can be recovered through the mean number density n, since

$$n = \Phi_\star \int_{\mathcal{M}_{\mathrm{min}}}^{\mathcal{M}_{\mathrm{max}}} \Phi(\mathcal{M} \, \mathrm{d}\mathcal{M}) , \qquad (3.18)$$

where $[\mathcal{M}_{\mathrm{min}}, \mathcal{M}_{\mathrm{max}}]$ is the stellar mass range of the galaxy sample. The mean density involves the probability of a galaxy at redshift z to be included in the survey, which is

$$S(z) = \frac{\int_{\mathrm{min}[\mathcal{M}_{\mathrm{lim}}(z),\mathcal{M}_{\mathrm{min}}]}^{\mathcal{M}_{\mathrm{max}}} \Phi(\mathcal{M} \, \mathrm{d}\mathcal{M})}{\int_{\mathcal{M}_{\mathrm{min}}}^{\mathcal{M}_{\mathrm{max}}} \Phi(\mathcal{M} \, \mathrm{d}\mathcal{M})} . \qquad (3.19)$$

According to Efstathiou et al. (1988),

$$\Phi_\star = \frac{\sum_{j=1}^{N} S^{-1}(z_j)}{V \int_{\mathcal{M}_{\mathrm{min}}}^{\mathcal{M}_{\mathrm{max}}} \Phi(\mathcal{M} \, \mathrm{d}\mathcal{M})} . \qquad (3.20)$$

3.1.2   Including statistical weights

At $\mathcal{M} > \mathcal{M}_{\mathrm{lim}}$, not all galaxies – even though bright enough to be included in the VIPERS catalogue – have been spectroscopically observed. There are several factors that contribute to the survey selection function, e.g. the target sampling

rate, the rate of successful spectroscopic measurements, etc. They have been dis-
cussed in Sect. 1.1.2, and included in the statistical weight $w(i, z)$ (see Eq. 1.2).
The latter is the correction to apply to a galaxy at redshift z with magnitude i, in
order to take into account the incompleteness due to the survey selection effects.
Statistical weights have to be included in the procedures described in Sect. 3.1.1
to correctly estimate the GSMF.

For instance, the main Equation of the $1/V_{\max}$ method (Eq. 3.6) becomes

$$\Phi(\mathcal{M}) = \sum_{\mathcal{M} < \mathcal{M}_j < \mathcal{M} + \mathrm{d}\mathcal{M}} \frac{w_j}{V_{\max}(\mathcal{M}_j)\Delta\mathcal{M}} \, , \tag{3.21}$$

where w_j is the statistical weight of the j-th object. In a similar way, weights are
introduced in Eq. (3.14):

$$\Phi_k \Delta\mathcal{M} = \frac{\sum_{j=1}^{N} w_j W(\mathcal{M}_j - \mathcal{M}_k)}{\sum_{j=1}^{N} w_j H\left[\mathcal{M}_{\lim}(z_j) - \mathcal{M}_k\right] / \sum_{i=1}^{N_{\mathrm{b}}} \Phi_i H\left[\mathcal{M}_{\lim}(z_k) - \mathcal{M}_k\right] \Delta\mathcal{M}} \, . \tag{3.22}$$

In the likelihood function (3.12), the weighing factor would artificially shrink the
error contours of Eq. (3.13). For this reason, it has to be balanced by the average
$\langle w \rangle$, i.e.

$$\mathcal{L} = \prod_{j=1}^{N} \left[p(\mathcal{M}_j, z_j)\right]^{\frac{w_j}{\langle w \rangle}} \, . \tag{3.23}$$

3.1.3   Completeness of the sample

The estimators introduced in the previous Section have been described assuming
that all the objects above the lower limit $\mathcal{M}_{\lim}$ were observed. This boundary
is related to the flux limit of the survey and its computation is a crucial task,
as it will be discussed below. Moreover, it considers the incompleteness (in a
given stellar mass range) only due to the objects too faint to be detected. In
a real survey, however, the selection function is more complicated, with several
sources of incompleteness (e.g. missing targets because of some problem during the
observational phase). In the following I will give more details about the estimate
of $\mathcal{M}_{\lim}$.

In the literature, the completeness mass limit of a sample at a given redshift is
often defined as the highest stellar mass a galaxy could have, when its observed
magnitude matches the flux limit (e.g. Pérez-González et al. 2008). Such a max-
imum is usually reached by the rescaled SED of an old passive galaxy. However,
this kind of estimate gives rise to a mass threshold that tends to be very con-
servative. The sample incompleteness is due to galaxies that can be potentially
missed, because their flux is close to the limit of the survey. The estimate of $\mathcal{M}_{\lim}$
is complicated by the wide range of $\mathcal{M}/L$. If one considers the luminosity function
at a given redshift, its completeness limit (in luminosity or absolute magnitude)
will result from the flux limit of the survey after applying the k-correction, which
in general does not introduce a large scatter. For the stellar mass function, the
$\mathcal{M}$ cut is less sharp because galaxies close to $i_{\lim}$ may have very different stellar
masses. This is a consequence of the variety of $\mathcal{M}/L$ (Bell & de Jong 2001).
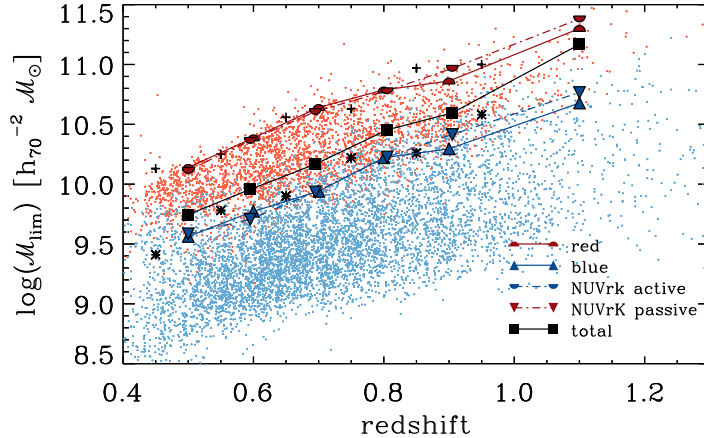
Figure 3.1   The mass completeness threshold $\mathcal{M}_{\text{lim}}$ as a function of redshift, computed for the total sample (the one used in Sect. 3.2, black squares) and for different galaxy types defined as in Sect. 3.3.1: red (upper half-circles), blue (upward triangles), passive (lower half-circles), and active (downward triangles) galaxies. In each redshift bin, the $\mathcal{M}_{\text{lim}}$ estimate relies on the rescaled stellar mass $\mathcal{M}(i = i_{\text{lim}})$ of the 20% faintest galaxies (see text). Small red/blue dots represent $\mathcal{M}(i = i_{\text{lim}})$ of the red and blue galaxies only. In addition, the Figure shows the limiting stellar masses estimated in Pozzetti et al. (2010) for photometric early- and late-type galaxies (plus signs and asterisks respectively, see text for details about their SED-based classification).

Depending on the redshift, such a limit in apparent magnitude can correspond to faint luminosities; in that case, only a small fraction of objects will have a high stellar mass-to-light ratio, since blue galaxies (with lower $\mathcal{M}/L$) will be the dominant population (e.g. Zucca et al. 2006). Thus, if based on the SED of an old passive galaxy, the determination of the stellar mass completeness is somehow biased in a redshift range that depends on the survey depth (see also the discussion in Marchesini et al. 2009, Appendix C).

To avoid this problem I apply the technique devised by Pozzetti et al. (2010), which takes into account typical $\mathcal{M}/L$ of the faintest observed galaxies (see also the discussion in D13). This procedure yields, for a given redshift and flux limit, an estimate of the threshold $\mathcal{M}_{\text{lim}}$ below which some galaxy type cannot be detected any longer. Following this approach, I estimate the stellar mass that each object would have if its magnitude, at the observed redshift, were equal to the i-band limiting magnitude i_{lim}. This limiting mass $\mathcal{M}(i = i_{\text{lim}})$ is obtained by rescaling the original stellar mass of the source at its redshift, i.e.

$$\log \mathcal{M}(i = i_{\text{lim}}) = \log \mathcal{M} + 0.4(i - i_{\text{lim}}) \ . \tag{3.24}$$

The threshold $\mathcal{M}_{\text{lim}}$ is then defined as the value above which 90% of the $\mathcal{M}(i = i_{\text{lim}})$ distribution lies. According to this, the VIPERS GSMF can be considered complete for $\mathcal{M} > \mathcal{M}_{\text{lim}}$. Only objects belonging to the faintest 20% are included in the computation, in order to mitigate the contribution of bright red galaxies with large $\mathcal{M}/L$ when they are not the dominant population around the flux limit, as they may cause the bias discussed above.

When using the $1/V_{\mathrm{max}}$ method, I apply to each redshift bin the $\mathcal{M}_{\mathrm{lim}}$ computed by considering objects inside a narrow redshift interval ($\Delta z = 0.05$) centred on z_{inf} (i.e., the lower limit of the considered redshift bin). This is because the $1/V_{\mathrm{max}}$ intrinsically corrects the sample incompleteness above z_{inf}. For the other estimators (STY, SWML) I include in Eq. (3.24) galaxies within ± 0.025 from the centre of the z-bin; the masses estimated in this way are also listed in Table 3.1, in three redshift bins that will be used in the environmental analysis of Chapter 4.

When working with a particular subsample (e.g., passive galaxies) $\mathcal{M}_{\mathrm{lim}}$ should be specifically evaluated because the typical SED of that galaxy population may differ from the average of the whole sample. Figure 3.1 shows the $\mathcal{M}_{\mathrm{lim}}$ values for the total sample, and for some galaxy populations (blue/red and active/passive) that are defined in Sect. 3.3.1. These latter estimates are used in Sect. 3.3. As shown in the Figure, two different galaxy type classifications give similar results, e.g. the limit of red galaxies at a given z is comparable to the corresponding $\mathcal{M}_{\mathrm{lim}}$ of the passive sample. As expected, the limiting mass increases as a function of z and the values for red galaxies are significantly higher ($\sim 0.5\,\mathrm{dex}$) than those of the blue ones (see Fig. 3.1, solid lines). The trend is similar when comparing the active and passive samples (Fig. 3.1, dot-dashed lines).

In the context of the zCOSMOS project (Lilly et al. 2009), the approach of Pozzetti et al. (2010) produced completeness limits in good agreement with those obtained through mock survey samples (Meneux et al. 2009). In VIPERS, I successfully tested our $\mathcal{M}_{\mathrm{lim}}$ estimates by taking advantage of the VVDS-Deep field, which is located in the W1 field (see Guzzo et al. 2014, Fig. 2). The VVDS sample provides spectroscopically observed galaxies down to a fainter limit, i.e. $I_{\mathrm{AB}} = 24$ (Le Févre et al. 2005). Since the CFHTLS-W1 field contains both VVDS and part of VIPERS, it is possible to compare the stellar masses by relying on a similar photometric baseline ($u, g, r, I, i, z, J^*, K^*$). When applying a VIPERS-like magnitude cut ($I < 22.5$), I can find the fraction of missed objects with respect to the parent $I < 24$ sample as a function of stellar mass. This test is shown in Fig. 3.2, where the $\mathcal{M}_{\mathrm{lim}}$ values of VVDS (limited to $I \leqslant 22.5$) and VIPERS are compared to the distribution of stellar masses belonging to the deeper (i.e., $I \leqslant 24$) VVDS sample. The computed $\mathcal{M}_{\mathrm{lim}}$ values agree with the thresholds at which the stellar mass distribution starts to be incomplete with respect to the deep VVDS sample (i.e. the limit where the $I < 22.5$ sample recovers less than 80% of the parent

Table 3.1   Stellar mass completeness: thresholds for active and passive galaxies in the redshift bins adopted in Chapter 4. In a conservative approach $\mathcal{M}_{\mathrm{lim}}^{\mathrm{pass}}$ is used also for the whole galaxy sample.

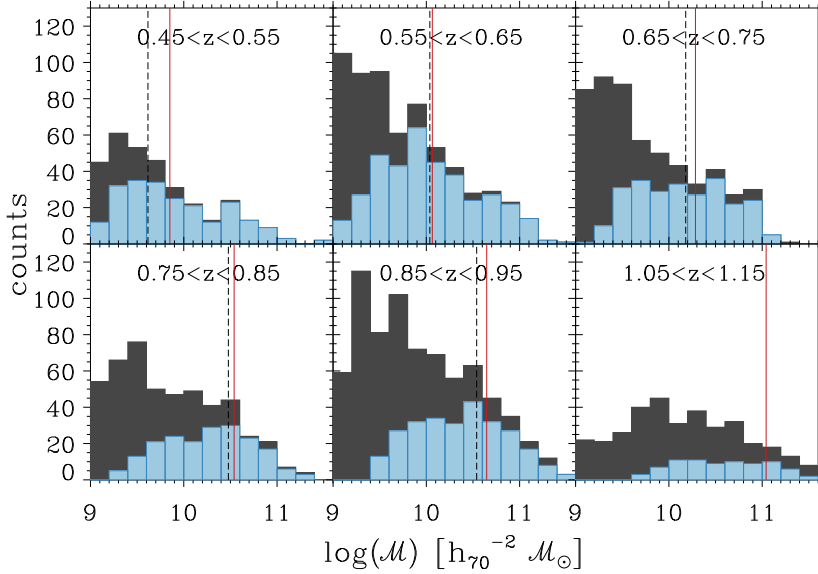| redshift range	median z	$\log(\mathcal{M}_{\mathrm{lim}}^{\mathrm{act}})$ $[\mathcal{M}_{\odot}]$	$\log(\mathcal{M}_{\mathrm{lim}}^{\mathrm{pass}})$ $[\mathcal{M}_{\odot}]$
$0.51 < z \leqslant 0.65$	0.60	10.18	10.39
$0.65 < z \leqslant 0.8$	0.72	10.47	10.65
$0.8 < z \leqslant 0.9$	0.84	10.66	10.86

Figure 3.2 Distributions of stellar masses in six redshift bins for the VVDS-Deep sample in the CFHTLS-W1 field at its limiting magnitude ($I \leqslant 24$, dark histograms), compared to the subset obtained by applying a magnitude cut similar to VIPERS, at $I \leqslant 22.5$ (blue histograms). In each panel, the black dashed line represents the limiting mass for the VVDS sample with $I \leqslant 22.5$. The red solid line instead gives the limiting mass for the VIPERS sample in the W1 field. Both limits, in good agreement with each other, correctly identify the threshold below which the shallower sample starts to miss a significant fraction ($> 20\%$) of objects. In the first z-bin (i.e., $0.45 < z < 0.55$) the agreement is less good, although the difference remains $< 0.2\,\mathrm{dex}$.

sample cut at $I \leqslant 24$).

3.2 Stellar mass function of the VIPERS field

3.2.1 Estimate of the total GSMF

I measure the GSMF through the estimators described in Sect. 3.1.1. The number of galaxies and the volume sampled by VIPERS allows to obtain an estimate of the GSMF with high statistical precision within six redshifts bins in the range $0.5 \leqslant z \leqslant 1.3$. Given the large number of galaxies observed by VIPERS, in terms of Poisson noise it would be possible to choose even narrower bins (e.g. $\Delta z \simeq 0.05$ wide). However, in that case the measurements start being strongly affected by cosmic variance: the presence (or absence) of cosmic structure in one z-bin with respect to another (cf Fig. 1.5b) would cause stochastic fluctuations in the GSMF normalisation that prevent to see any trend as a function of redshift.

I compute the GSMF within each redshift bin by using the estimators described in Sect. 3.1.1. When applying the $1/V_{\mathrm{max}}$ method (Fig. 3.3), in order to optimise the binning in stellar mass, I use an adaptive algorithm that extends the width of

Table 3.2 Total GSMF: $1/V_{\max}$ values in regular bins of stellar mass.

$\log \mathcal{M} \ [h_{70}^{-2} \, \mathcal{M}_\odot]^{\dagger}$	$\log \Phi \ [h_{70}^3 \, \mathrm{Mpc}^{-3}]$					
	$0.5 < z < 0.6$	$0.6 < z < 0.7$	$0.7 < z < 0.8$	$0.8 < z < 0.9$	$0.9 < z < 1.1$	$1.1 < z < 1.3$
9.50	$-2.47^{+0.02}_{-0.02}$	$-2.42^{+0.01}_{-0.02}$	$-2.62^{+0.02}_{-0.02}$	$-2.89^{+0.03}_{-0.03}$	$-3.20^{+0.04}_{-0.04}$	$-4.11^{+0.11}_{-0.15}$
9.70	$-2.51^{+0.02}_{-0.02}$	$-2.49^{+0.01}_{-0.01}$	$-2.56^{+0.02}_{-0.02}$	$-2.78^{+0.02}_{-0.02}$	$-2.95^{+0.03}_{-0.03}$	$-3.95^{+0.07}_{-0.08}$
9.90	$-2.61^{+0.02}_{-0.02}$	$-2.56^{+0.02}_{-0.02}$	$-2.63^{+0.02}_{-0.02}$	$-2.79^{+0.03}_{-0.03}$	$-2.93^{+0.03}_{-0.03}$	$-3.69^{+0.06}_{-0.07}$
10.10	$-2.67^{+0.02}_{-0.02}$	$-2.59^{+0.02}_{-0.02}$	$-2.65^{+0.02}_{-0.02}$	$-2.84^{+0.02}_{-0.02}$	$-2.98^{+0.03}_{-0.03}$	$-3.58^{+0.07}_{-0.08}$
10.30	$-2.68^{+0.02}_{-0.02}$	$-2.59^{+0.01}_{-0.01}$	$-2.69^{+0.02}_{-0.02}$	$-2.85^{+0.02}_{-0.02}$	$-3.07^{+0.03}_{-0.03}$	$-3.53^{+0.06}_{-0.07}$
10.50	$-2.66^{+0.02}_{-0.02}$	$-2.62^{+0.01}_{-0.01}$	$-2.70^{+0.02}_{-0.02}$	$-2.85^{+0.02}_{-0.02}$	$-3.07^{+0.03}_{-0.03}$	$-3.73^{+0.05}_{-0.05}$
10.70	$-2.72^{+0.02}_{-0.02}$	$-2.67^{+0.01}_{-0.01}$	$-2.75^{+0.01}_{-0.02}$	$-2.83^{+0.02}_{-0.02}$	$-3.04^{+0.02}_{-0.02}$	$-3.74^{+0.10}_{-0.13}$
10.90	$-2.91^{+0.02}_{-0.02}$	$-2.81^{+0.02}_{-0.02}$	$-2.83^{+0.02}_{-0.02}$	$-2.97^{+0.02}_{-0.02}$	$-3.16^{+0.02}_{-0.02}$	$-3.71^{+0.06}_{-0.07}$
11.10	$-3.25^{+0.03}_{-0.03}$	$-3.11^{+0.02}_{-0.02}$	$-3.14^{+0.02}_{-0.02}$	$-3.26^{+0.02}_{-0.03}$	$-3.32^{+0.02}_{-0.03}$	$-3.93^{+0.07}_{-0.09}$
11.30	$-3.66^{+0.05}_{-0.05}$	$-3.55^{+0.04}_{-0.04}$	$-3.59^{+0.04}_{-0.04}$	$-3.83^{+0.04}_{-0.05}$	$-3.81^{+0.04}_{-0.04}$	$-4.13^{+0.09}_{-0.12}$
11.50	$-4.34^{+0.09}_{-0.12}$	$-4.22^{+0.07}_{-0.09}$	$-4.29^{+0.07}_{-0.09}$	$-4.54^{+0.09}_{-0.12}$	$-4.39^{+0.07}_{-0.08}$	$-4.65^{+0.11}_{-0.15}$
11.70	$-5.29^{+0.23}_{-0.53}$	$-5.69^{+0.30}_{-\mathrm{inf}}$	$-5.05^{+0.16}_{-0.26}$	$-5.19^{+0.18}_{-0.30}$	$-5.78^{+0.23}_{-0.54}$	$-5.20^{+0.14}_{-0.21}$

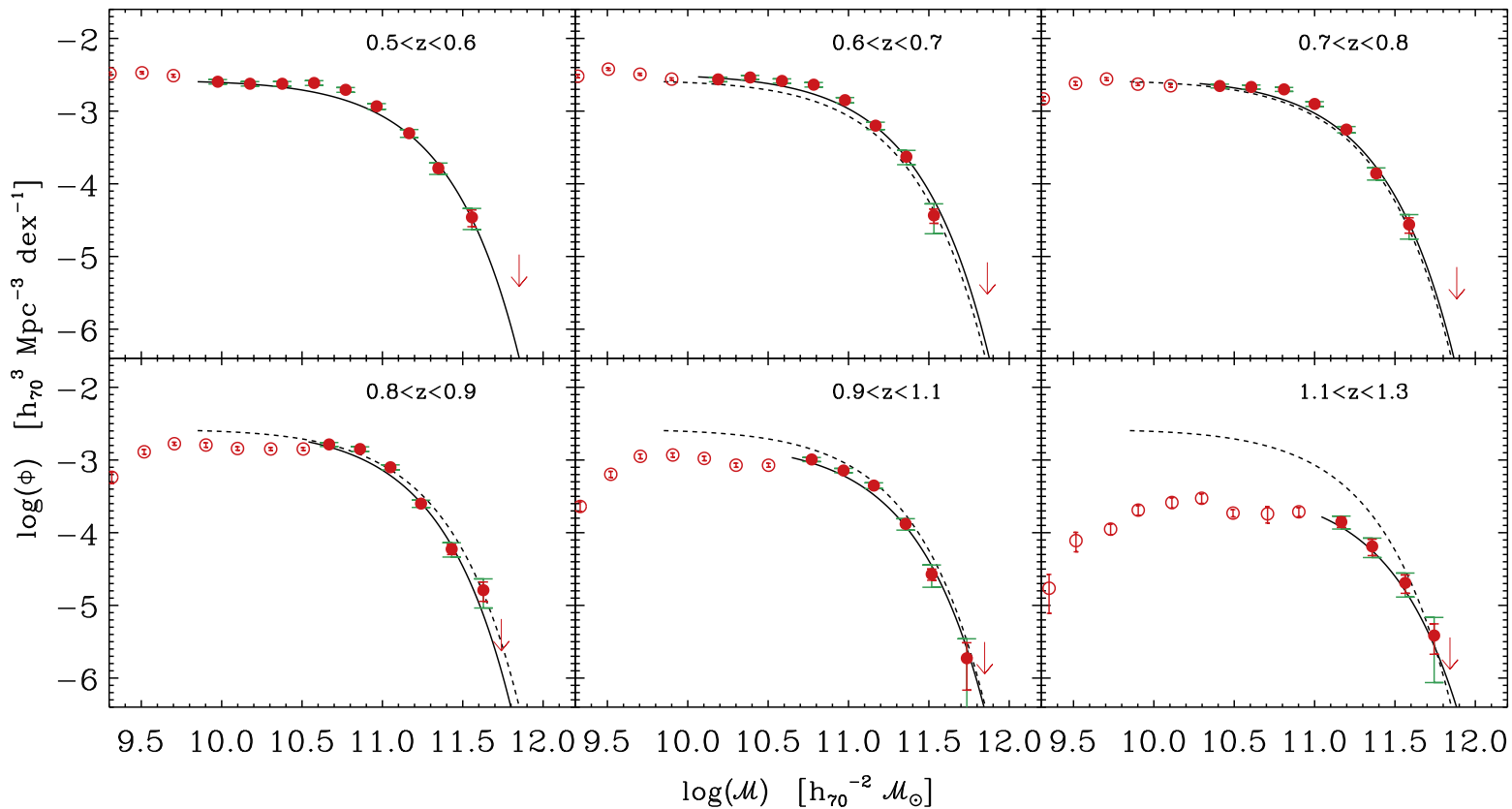†The centre of each stellar mass bin is indicated.

Figure 3.3 The VIPERS galaxy stellar mass function at different redshifts. Circles give the values determined through $1/V_{max}$ in mass bins of $\Delta\mathcal{M} = 0.2\,\mathrm{dex}$; the centre of each bin corresponds to the weighted mean mass of the objects within it. Empty and filled symbols correspond to values below and above the completeness limit, respectively (see Sect. 3.1.3). For the latter points, the red error bars show the uncertainty due to Poisson noise, while green bars account for Poisson noise and cosmic variance. In each panel, a solid line shows the Schechter best-fit to the GSMF filled points, with the dashed line reproducing that of the first redshift bin, as a reference. The downward arrows give an upper limit to Φ where no detection is available.

a bin until it contains a minimum of three objects. The errors associated with the $1/V_{\max}$ estimates are computed as in Eq. (3.7). The upper limits for non-detections (downward arrows in Fig. 3.3) have been estimated following Gehrels (1986). The values of the $1/V_{\max}$ GSMF and associated Poisson errors are given in Table 3.2. I also fit a Schechter function (Eq. 3.1) to these points, as reported in Table 3.3. In fitting the points in the first bin $(0.5 < z < 0.6)$, all parameters of Eq. (3.1) are left free, obtaining a value of the slope $\alpha = -0.95$. Above this redshift, however, the slope of the low-mass end is only weakly constrained, given the relatively high values of the completeness limit $\mathcal{M}_{\lim}$. For this reason, in all the other bins α is fixed to the value -0.95 (see Table 3.3).

The GSMFs estimated by means of the STY method and SWML are both fully in agreement with $1/V_{\max}$ at $z < 0.9$, while there is a small difference at $0.9 < z < 1.1$, just in the lowest stellar mass bin (Fig. 3.4). In the case of the STY estimates (Table 3.4), I let α free in all z-bins, to check the assumption made when fitting the $1/V_{\max}$ points. Up to $z = 0.8$, α is nearly constant $(-1.16 < \alpha < -0.95)$ and becomes steeper (i.e., more negative) at higher redshifts, although with larger uncertainties. It should be emphasised that also $\mathcal{M}_\star$ does not evolve over the entire redshift range of VIPERS.

In Fig. 3.4 the different methods start to differ at $\mathcal{M} < \mathcal{M}_{\lim}$, suggesting that our estimate of the completeness limit should be correct. In fact, such a discrepancy is a necessary but not sufficient condition to state that $\mathcal{M}_{\lim}$ is a good estimate of
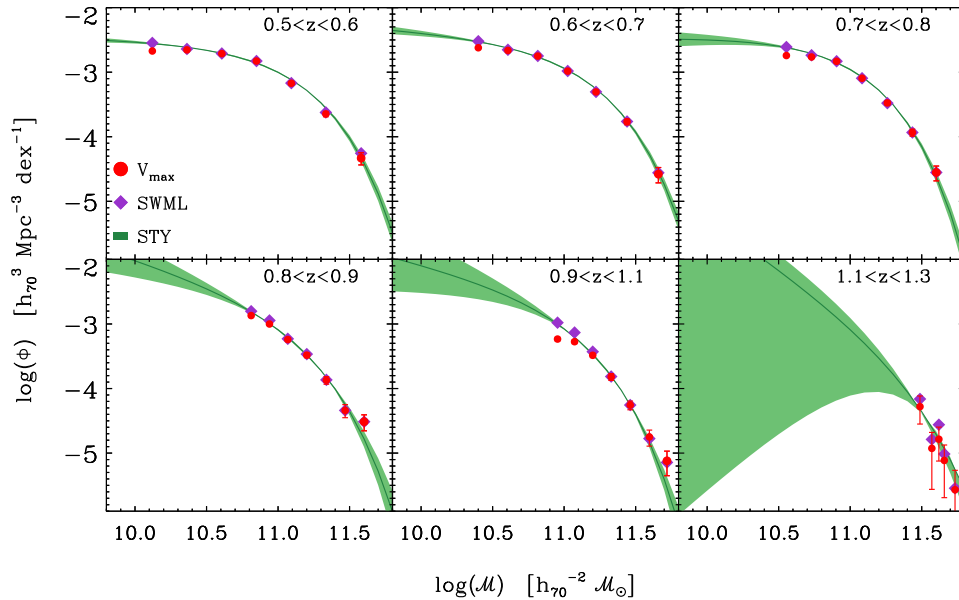

Figure 3.4   The VIPERS galaxy stellar mass function at different redshifts, as provided by the three estimators described in Sect. 3.1. Red circles give the values determined through $1/V_{\max}$ as in Fig. 3.3 (see that Figure for further details). Purple diamonds are given by the SWML method, while the green solid line in each z-bin is the Schechter function derived through the STY method (the shaded area being its 1σ uncertainty).
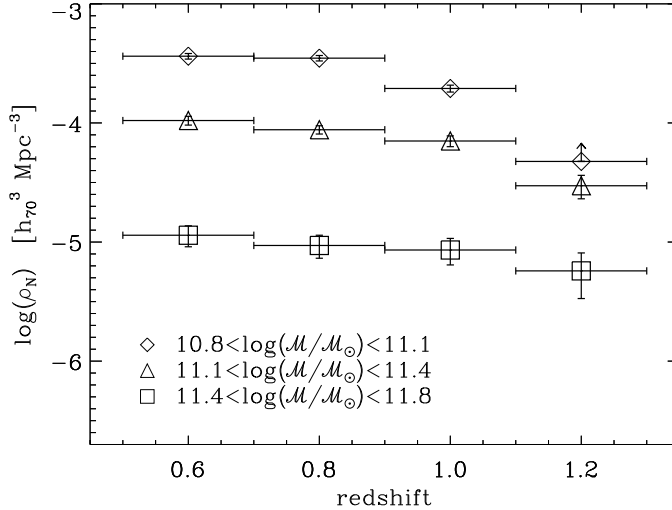
Figure 3.5 Evolution of the galaxy number density in different bins of stellar mass. The error bars of the density estimates include Poisson noise and cosmic variance (see Sect. 3.2.2). At $z \simeq 1.2$, for the lowest mass sample, only a lower limit can be estimated, indicated by the arrow.

the true completeness limit ($\mathcal{M}_{\mathrm{lim,real}}$). If there were some bias affecting the three estimators in the same way (e.g. missing galaxies from an unobserved population) the GSMFs would coincide also at masses where the sample is not complete any longer (e.g., $\mathcal{M}_{\mathrm{lim}} < \mathcal{M} < \mathcal{M}_{\mathrm{lim,real}}$).

At $z < 0.6$ there is some hint of the characteristic dip of the mass function at $\log(\mathcal{M}/\mathcal{M}_{\odot}) \sim 10.2$, with an upturn below that value as observed both locally (e.g. Baldry et al. 2012) and at intermediate redshifts (e.g Drory et al. 2009; Pozzetti et al. 2010). However, this feature is located too close to $\mathcal{M}_{\mathrm{lim}}$ to be assessed effectively. I avoid using a double Schechter function in the fits also to ease comparison with the parameters derived at higher redshifts.

The results of Fig. 3.3 confirm, with impressive statistical precision, the lack of evolution since $z \simeq 1.1$ of the massive end ($\log(\mathcal{M}/\mathcal{M}_{\odot}) > 11$) of the galaxy mass function seen in previous, smaller samples. The exponential tail of the Schechter fit is nearly constant across the five redshift bins, down to $z \simeq 0.5$. However in Fig. 3.5, where the galaxy number density (ρ_N) is plotted versus redshift, I detect a significant decrease in the number density of the most massive galaxies ($\log(\mathcal{M}/\mathcal{M}_{\odot}) > 11.1$) in the redshift bin $1.1 < z < 1.3$. At lower masses ($10.8 < \log(\mathcal{M}/\mathcal{M}_{\odot}) < 11.1$), the first signs of evolution with respect to $z \sim 0.5$ start to be visible at redshift $0.9 - 1.1$. This figure explicitly shows that the most massive galaxies are virtually already in place at $z \simeq 1$. In contrast, galaxies with lower mass keep assembling their stars in such a way that their number density increases by a factor ~ 3.5 from $z = 1.2$ down to 0.6, consistently with the so-called *downsizing* scenario (Cowie et al. 1996; Fontanot et al. 2009). These new measurements confirm previous evidence, but with higher statistical reliability (see Sect. 3.2.4).

Table 3.3   Global GSMF: Schechter parameters fitting the $1/V_{\mathrm{max}}$ points (α fixed at $z > 0.6$).

z range	α	$\log \mathcal{M}_\star$ $[h_{70}^{-2}\,\mathcal{M}_\odot]$	$\Phi_\star$ $[10^{-3}\,h_{70}^3\,\mathrm{Mpc}^{-3}]$
$0.5 < z \leqslant 0.6$	$-0.95^{+0.03}_{-0.02}$	$10.87^{+0.02}_{-0.02}$	$1.42^{+0.06}_{-0.07}$
$0.6 < z \leqslant 0.7$	-0.95	$10.91^{+0.02}_{-0.01}$	$1.58^{+0.05}_{-0.05}$
$0.7 < z \leqslant 0.8$	-0.95	$10.91^{+0.01}_{-0.02}$	$1.38^{+0.06}_{-0.04}$
$0.8 < z \leqslant 0.9$	-0.95	$10.85^{+0.02}_{-0.02}$	$1.29^{+0.09}_{-0.09}$
$9.0 < z \leqslant 1.1$	-0.95	$10.91^{+0.02}_{-0.01}$	$0.82^{+0.05}_{-0.06}$
$1.1 < z \leqslant 1.3$	-0.95	$11.03^{+0.11}_{-0.08}$	$0.20^{+0.05}_{-0.06}$

Table 3.4   Total GSMF: Schechter parameters as resulting from the STY method.

z range	α	$\log \mathcal{M}_\star$ $[h_{70}^{-2}\,\mathcal{M}_\odot]$	$\Phi_\star$ $[10^{-3}\,h_{70}^3\,\mathrm{Mpc}^{-3}]$
$0.5 < z \leqslant 0.6$	$-1.05^{+0.05}_{-0.05}$	$10.98^{+0.03}_{-0.03}$	$1.25^{+0.10}_{-0.10}$
$0.6 < z \leqslant 0.7$	$-1.16^{+0.06}_{-0.06}$	$11.01^{+0.03}_{-0.03}$	$1.31^{+0.13}_{-0.12}$
$0.7 < z \leqslant 0.8$	$-0.95^{+0.10}_{-0.10}$	$10.89^{+0.03}_{-0.03}$	$1.72^{+0.15}_{-0.16}$
$0.8 < z \leqslant 0.9$	$-1.69^{+0.25}_{-0.25}$	$11.01^{+0.09}_{-0.08}$	$0.93^{+0.33}_{-0.31}$
$0.9 < z \leqslant 1.1$	$-1.54^{+0.35}_{-0.34}$	$10.95^{+0.08}_{-0.07}$	$1.19^{+0.29}_{-0.33}$
$0.9 < z \leqslant 1.3$	$-2.5^{+\infty}_{-\infty}$	$11.26^{+0.28}_{-0.40}$	$0.25^{+0.96}_{-0.23}$

3.2.2   Cosmic variance in the VIPERS survey

When dealing with statistical studies using number counts, a severe complication is introduced by the field-to-field fluctuations in the source density, due to the clustered nature of the galaxy distribution and the existence of fluctuations on scales comparable to the survey volume. This sampling or 'cosmic' variance represents a further term of uncertainty to be added to the Poisson shot noise. It can be expressed by removing $\sigma^2_{\mathrm{Poiss}} \equiv 1/\langle N \rangle$ from the total relative error:

$$\sigma^2_{\mathrm{cv}} = \frac{\langle N^2 \rangle - \langle N \rangle^2}{\langle N \rangle^2} - \frac{1}{\langle N \rangle}, \tag{3.25}$$

where $\langle N \rangle$ and $\langle N^2 \rangle$ are the mean and the variance of galaxy number counts in the surveyed volume (Somerville et al. 2004).

Extragalactic pencil-beam surveys, even the deepest ones, are particularly limited by cosmic variance, given the small volume covered per redshift interval. At $z \sim 0.8$, galaxy density fluctuations are found to be still relevant up to a comoving

scale of $\sim 140\,h_{70}^{-1}$ Mpc (Scrimgeour et al. 2012), which roughly corresponds to 5 deg.

This is the result of intrinsic clustering in the matter, as predicted by the power spectrum shape and amplitude at that epoch. Moreover, the effect is amplified by the bias factor, which at high redshift can be very large for some galaxy classes (e.g. Moster et al. 2011; Di Porto et al. 2014). Also the last-generation, largest deep surveys are significantly affected by this issue. For example, the COSMOS field, despite its $2\,\mathrm{deg}^2$ area, turned out to be significantly overly dense between $z = 0.8$ and $z = 1$ (Kovač et al. 2010b).

The gain obtained by enlarging the area of a single field becomes less prominent beyond a certain coverage, owing to the existing large-scale correlations (see Newman & Davis 2002, Fig. 1): σ_{cv} decreases mildly as a function of volume, with an approximate dependence $\sigma_{\mathrm{cv}} \propto V^{-0.3}$ (Somerville et al. 2004, Fig. 2), compared to $\sigma_{\mathrm{Poiss}} \propto V^{-0.5}$. Trenti & Stiavelli (2008) found similar results by characterising Lyman break galaxies surveys: at high values of $\langle N \rangle$, the Poisson noise rapidly drops and cosmic variance remains the dominant source of uncertainty. A more effective way to abate cosmic variance is to observe separated regions of sky. Since counts in these regions, if they are sufficiently distant, are uncorrelated, their variances sum up in quadrature (i.e., σ_{cv} decreases as the square root of the number of fields, Moster et al. 2011). The use of multiple independent fields can then result in a smaller uncertainty than for a single field, even if the latter has a larger effective area (Trenti & Stiavelli 2008). The current VIPERS PDR-1 sample is not only characterised by a significantly large area, compared to previous similar surveys at these redshifts, but it is also split into two independent and well-separated fields of $\sim 7.5\,\mathrm{deg}^2$ each. Therefore, the impact of cosmic variance is expected to be limited.

To quantify this effect directly, I follow two approaches. The first one, based on the observations themselves, provides an upper limit of the VIPERS σ_{cv}. I select five rectangular subregions of about $2\,\mathrm{deg}^2$ within the survey and estimate the mass function Φ_i in each of them, using the $1/V_{\mathrm{max}}$ method described above. I choose non-contiguous regions (separated by ~ 1 deg) to minimise the covariance between subsamples located within the same field (W1 or W4). Within mass bins $\mathcal{M}_j \pm \Delta\mathcal{M}/2$, I derive the total random uncertainty

$$\sigma_{\mathrm{tot,obs}}(\mathcal{M}_j) = \frac{1}{n} \sum_{i=1}^{n} \sqrt{\left[\Phi_i(\mathcal{M}_j) - \Phi_{\mathrm{tot}}(\mathcal{M}_j)\right]^2} \ , \qquad (3.26)$$

where Φ_{tot} is the global GSMF of VIPERS (at that redshift) and $\Phi_i(\mathcal{M}_j)$ the number density of galaxies measured in the j-th mass bin for each of the $n = 5$ subregions. This result should be regarded as an upper limit of the VIPERS cosmic variance, given that the subsamples have a smaller volume than the whole survey, and Eq. (3.26) also includes the variance due to Poisson noise. Conversely, residual correlation among the subfields within each of the VIPERS fields (produced by structures on scales $\gtrsim 1$ deg crossing over two or more subregions) would slightly reduce $\sigma_{\mathrm{tot,obs}}$. More in general, the small number of fields used to perform this test makes the computation of Eq. (3.26) statistically uncertain: for these reasons the estimates of the standard deviation obtained from the field-to-field
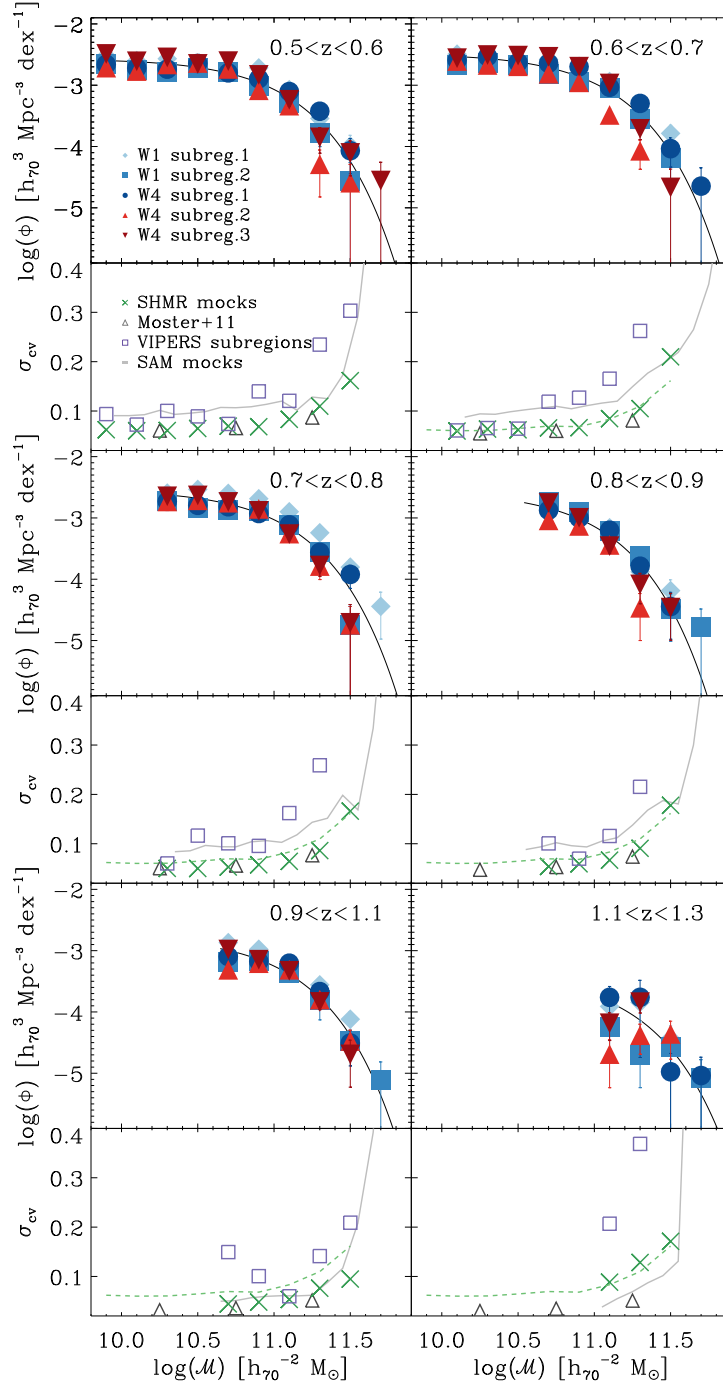
Figure 3.6 Estimates of the contribution of cosmic variance to the total statistical uncertainty of the GSMF measurements. For each redshift bin, the upper panels show the GSMFs obtained through $1/V_{\mathrm{max}}$ for five VIPERS subregions of $2\,\mathrm{deg}^2$, located respectively in the W1 field (blue diamonds, circles, and squares) and in the W4 field (red triangles, and downward triangles). The Schechter fit to the total GSMF of Fig. 3.3 is shown as reference (black solid line). The lower panels show the standard deviations estimated in each redshift bin from these five measurements (purple squares, Eq. 3.26), together with the estimates of σ_{cv} obtained from 57 SHMR mocks by means of Eq. (3.25) (green crosses). To highlight how the effect of cosmic variance decreases at higher z, $\sigma_{\mathrm{cv,SHMR}}$ of the first redshift bin is plotted also in the other panels (green dashed lines). In addition, the sample variance measured in 50 SAM mocks (grey solid line) and the estimates provided by Moster et al. (2011) method (black triangles) are shown as reference.

fluctuations among the five subsamples ($\sigma_{\mathrm{tot,obs}}$, squares in Fig. 3.6) show rather irregular behaviour.

The second approach is based on the use of simulated mock surveys. First, I use a set of 57 mock samples (26 and 31 in W1 and W4, respectively), built using specific recipes for the stellar-to-halo mass relation. They are based on the MultiDark dark matter simulation (Prada et al. 2012) and have been constructed to reproduce the detailed geometry and selection function of the VIPERS survey up to $z = 1.2$. (see de la Torre et al. 2013, for details). The dark matter haloes identified in the simulation, as well as artificial sub-haloes drawn from the Giocoli et al. (2010) subhalo mass function, have been associated with galaxies using the stellar-to-halo mass relations of Moster et al. (2013). The latter are calibrated on previous stellar mass function measurements in the redshift range $0 < z < 4$. These catalogues are named "SHMR mock catalogues". I apply Eq. (3.25) to estimate the amount of cosmic variance independently among the 26 W1 and 31 W4 mock catalogues. The global estimate of cosmic variance ($\sigma_{\mathrm{cv,SHMR}}$) on the scales of the VIPERS survey is obtained by combining the results from the two fields (see Moster et al. 2011, Eq. 7). As expected, $\sigma_{\mathrm{cv,SHMR}}$ decreases with redshift, as larger and larger volumes are probed, and increases with stellar mass owing to the higher bias factor (and thus higher clustering) of massive galaxies (Somerville et al. 2004). Both trends are clearly visible in Fig. 3.6, where measurements of $\sigma_{\mathrm{cv,SHMR}}$ are presented for different bins of redshift and stellar mass. These values are included in the error bars of Fig. 3.3 to account for the cosmic variance uncertainty. It should be noticed that in the highest redshift bin $\sigma_{\mathrm{cv,SHMR}}$ represents a conservative estimate, given the different redshift range in SHMR mock catalogues ($1.1 < z < 1.2$) and observations ($1.1 < z < 1.3$).

In Fig. 3.6 it is also shown, as a reference, the estimates provided by the public code `getcv` (Moster et al. 2011) for the same area of the SHMR mock catalogues. These results, limited at $\log(\mathcal{M}/\mathcal{M}_{\odot}) \leqslant 11.5$, are in good agreement with $\sigma_{\mathrm{cv,SHMR}}$, with the exception of the highest redshift bin, mainly because of the $z = 1.2$ cut of SHMR mocks. However, I prefer to use $\sigma_{\mathrm{cv,SHMR}}$ to quantify the cosmic variance uncertainty in that z-bin, although it should be regarded as an upper limit, since the outcomes of Moster et al. (2011) code do not reach the high-mass tail of the GSMF, and are also more uncertain because the galaxy bias function used in this method is less constrained at such redshifts.

Besides these SHMR mocks, I also used a different set of 50 VIPERS-like light cones built from the Millennium simulation (Springel et al. 2005b), in which dark-matter haloes are populated with galaxies through the semi-analytical model (SAM) of De Lucia & Blaizot (2007). Galaxy properties were determined by connecting the astrophysical processes with the mass accretion history of the simulated dark matter haloes. Each mock sample covers $7 \times 1\,\mathrm{deg}^2$, with a magnitude cut in the i band equal to that of the observed sample. Although the geometry of these mocks (and therefore their volume) differs slightly from the design of the real survey, they provide an independent test, with a completely different prescription for galaxy formation. SAM mocks in Fig. 3.6 show a trend similar to that of $\sigma_{\mathrm{cv,SHMR}}$, although with some fluctuations e.g. between $z = 0.7$ and 0.8. The values of $\sigma_{\mathrm{cv,SAM}}$ are systematically higher mainly because the SAM mocks do not reproduce two independent fields. Further differences with respect to the other
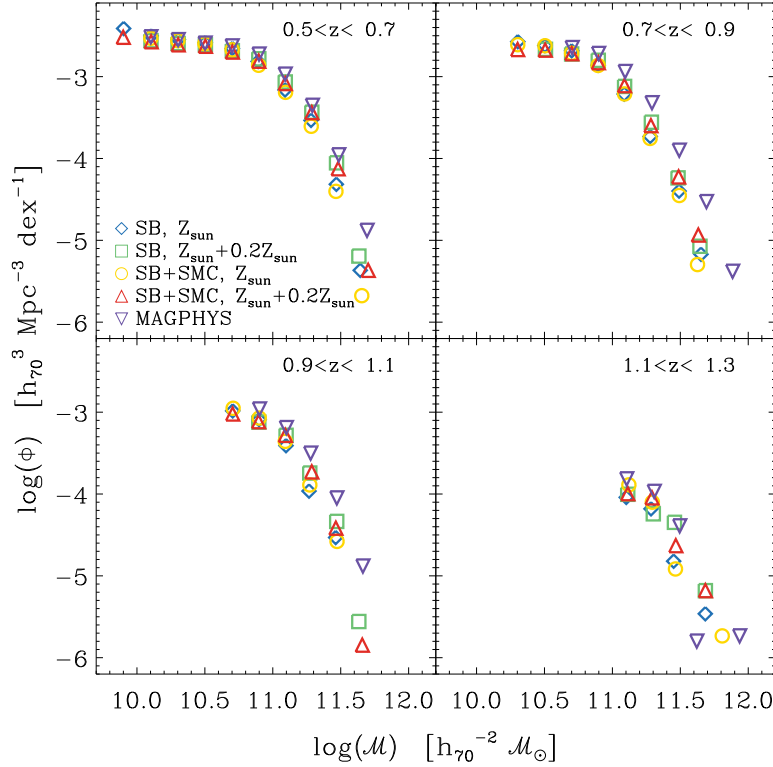
Figure 3.7 Dependence of the mass function on the input parameters of the SED fitting (five different cases are considered). Specifically, the points correspond to different choices of the stellar population synthesis code, metallicity (Z), extinction law (SB+SMC or SB alone), or the addition of secondary bursts to the smooth star-formation histories. Four cases correspond to SED fitting using HYPERZMASS, for which the values of the adopted parameters are given in the bottom-left of the first panel; the fifth is based on MAGPHYS.

estimates may be due to the different recipes in the simulations.

3.2.3   Other sources of uncertainty

In describing the procedure to derive stellar masses by means of the SED fitting technique (Sect. 2.1), I emphasised the number of involved parameters and their possible influence on the estimates. As already discussed, the assumptions that have the strongest impact on the results are the choices of the stellar population synthesis model, IMF, SFH, metallicity, and dust extinction law (Conroy 2013; Mitchell et al. 2013; Marchesini et al. 2009).

In this Section I briefly test the impact on the GSMF of choosing different values of Z (whether including subsolar metallicities or not), the extinction laws (SB and SMC, or SB alone), and the addition of secondary bursts to the smooth SFHs (i.e. complex SFHs instead of exponentially declining τ-models). I do not modify the other two main ingredients in our procedure, i.e. the universal IMF that we assumed (Chabrier 2003) and the stellar population synthesis model (BC03).

To perform this test I use stellar mass estimates obtained by assuming five different sets of SED fitting templates, four of them differing in metallicity and extinction

law: $Z_{\odot}$ only and SB; two metallicities ($Z_{\odot}$ and $0.2Z_{\odot}$) and SB; solar metallicity and two extinction laws (SB and SMC); two metallicities ($Z_{\odot}$ and $0.2Z_{\odot}$) and two extinction laws (SB and SMC). The fifth SED fitting estimate has been derived with the MAGPHYS code assuming the following parameters: complex SFHs, extinction model derived from Charlot & Fall (2000), and a wider range of metallicity (including super-solar ones). More details can be found in Sect. 2.1.5, where these stellar mass estimates were used to show the robustness (but also a few systematics) of the SED fitting technique. The following tests are limited to the data in the VIPERS W1 field, i.e. about half of the total sample, given the better overall photometric coverage in this area and the large computational time involved.

The mass functions resulting from these five different SED-modelling assumptions are shown in Fig. 3.7. As expected (see discussion in Sect. 2.1.5 and Fig. 2.12), the MAGPHYS mass function corresponds to the highest estimated values of galaxy density especially at high stellar masses (at least up to $z \simeq 1.1$). This trend is expected, because the four other estimates, obtained by assuming smooth SFHs templates, are insensitive to an underlying old stellar population that is outshone by a recent burst of star formation (Fontana et al. 2004; Pozzetti et al. 2010; but see Moustakas et al. 2013 for an opposite result). As seen in Fig. 2.12, when using complex SFHs templates one can produce stellar mass estimates that are higher than those obtained with smooth SFHs for a low percentage of objects. This effect has major consequences in the high-mass tail of the GSMF.

The other estimates, produced by HYPERZMASS, are in quite good agreement with each other. The mass functions are slightly higher (on average by about $0.1\,\mathrm{dex}$) when obtained through SED fitting procedures that can choose between two values of metallicity. In fact, in this case, red galaxies can be fit with $0.2\,Z_{\odot}$ and older ages (cf Fig. 2.6), consequently resulting in higher stellar mass values. The effect of the extinction law is instead marginal, probably because most of the objects in the stellar mass range of VIPERS are passive galaxies with small amount of dust. Therefore, a change in the dust extinction model should have a more visible impact in the low-mass end of the GSMF.

3.2.4   Comparison with other observational estimates

I compare the GSMF of VIPERS with results from other galaxy surveys. I correct the GSMFs (if necessary) to be in the same cosmological model with $\Omega_m = 0.3$, $\Omega_{\Lambda} = 0.7$, $h_{70} = 1$, and Chabrier (2003) IMF. With respect to Fig. 3.3, I also modify the binning in redshift to be similar to other work.

I chose eight surveys that adopt comparable z-bins, half of them based on photometric redshifts (Fontana et al. 2006; Pérez-González et al. 2008; Ilbert et al. 2010; Bielby et al. 2012) and half on spectroscopic redshifts (Fontana et al. 2004; Pozzetti et al. 2007, 2010; Moustakas et al. 2013). The spectroscopic redshift sample used by Moustakas et al. (2013) is obtained through a pioneering technique based on a low dispersion prism and slitmasks (Coil et al. 2011), which results in a precision of $\sigma_z \simeq 0.007(1 + z)$ (for their high quality sample $Q \geqslant 3$, see Cool et al. 2013), i.e. comparable to the precision of the best photometric redshifts available today in the literature (see Ilbert et al. 2013, who obtain $\sigma_z \simeq 0.008(1 + z)$ and a very low percentage of outliers).
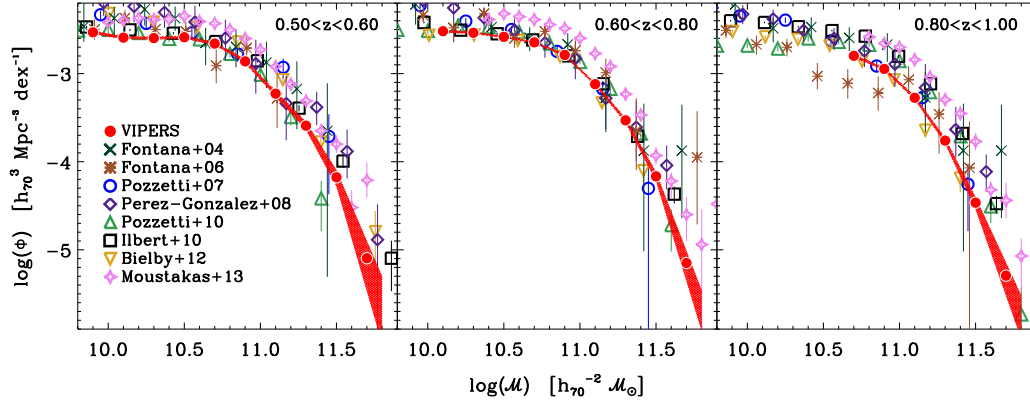
Figure 3.8 The VIPERS galaxy stellar mass functions from $z = 0.5$ to 1 (filled red circles, with a red shaded area accounting for the Poisson uncertainty). The $1/V_{\mathrm{max}}$ determinations of previous surveys are also shown by different symbols, along with their respective Poisson error bars. In the left-hand panel, whereas the VIPERS range is $0.5 < z < 0.6$, the other GSMFs are computed between $z = 0.4$ and 0.6, with the exception of Moustakas et al. (2013) who use $0.5 < z < 0.65$, $0.65 < z < 0.8$, $0.8 < z < 1.0$; notice the very small error bars of the VIPERS data, despite the narrower redshift range. In the other two panels, the bins of VIPERS are the same as the other surveys; also at these higher redshifts the error bars of the VIPERS GSMF are small compared to them.

The redshift ranges of the GSMFs shown in Fig. 3.8 are $0.4 < z < 0.6$, $0.6 < z < 0.8$, $0.8 < z < 1.0$, with the exception of PRIMUS (Moustakas et al. 2013), which is at $0.5 < z < 0.65$, $0.65 < z < 0.8$, $0.8 < z < 1.0$, and the first bin of VIPERS (i.e., $0.5 < z < 0.6$). In the case of Bielby et al. (2012), who provide the GSMFs in four CFHTLS-Deep quadrants, I consider the results in the D3 field ($1\,440\,\mathrm{arcmin}^2$), which is located in a region of sky uncorrelated with the other selected surveys. For the VIPERS GSMFs, the error bars account only for σ_{Poiss}, i.e. without adding the uncertainty due to sample variance, in order to be consistent with most of the literature data, for which only Poisson errors are available.

Nonetheless, through the recipe of Moster et al. (2011) one can obtain, for each survey, an approximate estimate of the uncertainty due to cosmic variance to a first approximation, and have a rough idea of how much the error bars would increase in Fig. 3.8 when accounting for it. For Pozzetti et al. (2007), Pérez-González et al. (2008), and Bielby et al. (2012), within the redshift ranges considered in Fig. 3.3, with only a small evolution with redshift, the GSMF uncertainty related to cosmic variance is approximatively the same: $\sim 15\%$ between $\log \mathcal{M}/\mathcal{M}_\odot = 10.0$ and 10.5, $\sim 23\%$ between $\log \mathcal{M}/\mathcal{M}_\odot = 11.0$ and 11.5. (It should be noticed that data used by Pérez-González et al. cover an area of $273\,\mathrm{arcmin}^2$, but split in three fields.) For Ilbert et al. (2010) and Pozzetti et al. (2010), $\sigma_{\mathrm{cv}} \simeq 10\%$ when $10.0 < \log \mathcal{M}/\mathcal{M}_\odot < 10.5$ and $\sigma_{\mathrm{cv}} \simeq 17\%$ when $11.0 < \log \mathcal{M}/\mathcal{M}_\odot < 11.5$. In the same bins of stellar mass, for Fontana et al. (2004) σ_{cv} is 20% and 30%, respectively, while $\sigma_{\mathrm{cv}} \simeq 30\%$ and 45% in Fontana et al. (2006). The estimates provided by Moustakas et al. (2013) in their paper are generally below 10%, except at $\log \mathcal{M}/\mathcal{M}_\odot > 11.6$ where the uncertainty rises by a factor of $2 - 4$.

VIPERS results lie on the lower boundary of the range covered by other GS-

MFs, and are in reasonably good agreement with most of them. At $0.8 < z < 1.0$, the difference with Ilbert et al. (2010, COSMOS survey over $2\,\mathrm{deg}^2$) and Pozzetti et al. (2010, zCOSMOS, $1.4\,\mathrm{deg}^2$) is noteworthy: the likely reason is the presence of a large structure detected in the COSMOS/zCOSMOS field (Kovač et al. 2010b), demonstrating the impact of cosmic variance in this kind of comparison. A discrepancy (nearly by a factor of two) is also evident with the estimates by Moustakas et al. (2013). The explanation could be partly related to the statistical weighing, in particular for the faintest objects, because the lower the sampling rate estimates, the greater the uncertainty in such a correction. At magnitudes $i \simeq 22.5$, the SSR of PRIMUS is approximately 45%, dropping below 20% at the limit of the survey ($i < 23$, see Cool et al. 2013). Instead, in VIPERS the SSR is $\sim 75\%$ down to our magnitude limit $i = 22.5$ and to $z \simeq 1$, making the statistical weight corrections smaller and more robust. In addition to this, it should be noticed that although several overdensities have been observed in PRIMUS, cosmic variance seems unable to fully justify the difference between the GSMFs of the two surveys: the number of independent fields (PRIMUS consists of five fields with a total of $5.5\,\mathrm{deg}^2$) should reduce this problem, at least to some degree. The disagreement could also be partially ascribed to the different ways stellar masses are estimated: Moustakas et al. derived their reference SEDs according to the SSP model of Conroy & Gunn (2010), which results in stellar mass estimates systematically higher than those obtained by assuming BC03 (see Moustakas et al. 2013, Fig. 19). Regarding the choices of SEDs, it is worth noticing that Pérez-González et al. (2008) also used a template library different from BC03, which they derived from the PEGASE stellar population synthesis model (Fioc & Rocca-Volmerange 1997), bounding the parameter space by means of a training set of ~ 2000 galaxies with spectroscopic z and wide photometric baseline. The other surveys quoted in Fig. 3.8 (Fontana et al. 2004, 2006; Pozzetti et al. 2007, 2010; Ilbert et al. 2010; Bielby et al. 2012) adopt BC03.

VIPERS data provide tight constraints on the high-mass end of the GSMF. Previous surveys, such as K20, MUSIC, and VVDS-Deep (i.e. Fontana et al. 2004, 2006; Pozzetti et al. 2007), were unable to probe this portion of the GSMF ($\log(\mathcal{M}/\mathcal{M}_\odot) \gtrsim 11.5$) because of their relatively small area (about 52, 150, and $1\,750\,\mathrm{arcmin}^2$ respectively). Instead, GSMFs derived from photometric redshift surveys are characterised by a Poisson noise that is in general comparable to the one in VIPERS (Pérez-González et al. 2008; Ilbert et al. 2010), but they can be affected by failures on photometric redshift estimates: even a small fraction of catastrophic redshift measurements can be relevant at high masses (Marchesini et al. 2009, 2010). Moreover, the sky area generally covered by high-z photometric surveys is not large enough for cosmic variance to be negligible.

3.2.5   Comparison with models

Besides the comparison with other surveys, it is important to check the agreement of our results with simulations. The tight constraints posed by VIPERS can be very useful when studying whether these models adequately reproduce the real universe. Although only a preliminary analysis is discussed in this work, it provides intriguing results. The four semi-analytical models (SAMs) I consider here rely on

the halo-merger trees of the Millennium Simulation (MS, Springel et al. 2005b) and the Millennium-II Simulation (MSII, Boylan-Kolchin et al. 2009); namely, three of them (Bower et al. 2006; De Lucia & Blaizot 2007; Mutch et al. 2013) use the MS (comoving box size $L = 714\,h_{70}^{-1}$ Mpc, particle mass $= 1.23 \times 10^9\,h_{70}^{-1}\,\mathcal{M}_\odot$), while the last one (Guo et al. 2011) is based on both MS and MSII ($L = 143\,h_{70}^{-1}$ Mpc, particle mass $= 9.83 \times 10^6\,h_{70}^{-1}\,\mathcal{M}_\odot$).

Figure 3.9 shows the mass functions derived from the models of Bower et al. (2006), De Lucia & Blaizot (2007), and Guo et al. (2011), together with the VIPERS results. All the model GSMFs are computed from snapshots at the same redshifts. The narrow redshift binning that can be set in VIPERS ($\Delta z = 0.1$) allows to compare simulated galaxies to observed ones at cosmic times that are very close to the snapshot considered. In the case of De Lucia & Blaizot model, I also derived the stellar mass functions from the VIPERS-like light cones introduced in Sect. 3.2.2, but they are not shown in Fig. 3.9 since they lead to results that are indistinguishable from those obtained from snapshots. For all three SAMs, I find that the low-mass end of the GSMF is over-estimated. Such a discrepancy, already observed in other work (Somerville et al. 2008; Cirasuolo et al. 2010), is mainly due to an over-predicted fraction of passive galaxies on those mass scales. This can be caused by an under-efficient supernova feedback and/or some issue as to how the star formation efficiency is parametrised at high redshifts (Fontanot et al. 2009; Guo et al. 2011). Rescaling the simulations to an up-to-date value of σ_8 (in MS it is equal to 0.9), with the consequence of reducing the small-scale clustering of dark-matter haloes, alleviates the tension only in part (e.g. Guo et al. 2013).

At a first glance, De Lucia & Blaizot (2007) and Bower et al. (2006) seem to agree with the observed GSMFs at $\log(\mathcal{M}/\mathcal{M}_\odot) \gtrsim 11.0$, while the Guo et al. (2011) mass function lies systematically below by $\simeq 0.4\,$dex. However, it should be emphasised that in Fig. 3.9 the GSMFs from SAMs are plotted without taking the observational uncertainties on stellar mass into account. I verified that adding this kind of error would increase the density of massive objects in the exponential tail of the mass function, and therefore the De Lucia & Blaizot (2007) and Bower et al. (2006) results should be considered at variance with observations also at $\log(\mathcal{M}/\mathcal{M}_\odot) \geqslant 11$.

The effect of introducing observational uncertainties is shown in Fig. 3.9 only for the Guo et al. (2011) model, which foresees a lower density of objects in the massive end with respect to the other two models. I recomputed the Guo et al. GSMFs after convolving stellar masses with a Gaussian of dispersion $0.15\,$dex. The predictions of Guo et al. (2011) are then in fair agreement with VIPERS. With respect to De Lucia & Blaizot (2007), the main distinguishing features of Guo et al. (2011) model are the high efficiency of supernova feedback and a lower rate of gas recycling at low mass. The transition from central to satellite status in the Guo et al. prescription also differs, resulting in a larger number of satellite galaxies than in De Lucia & Blaizot model.

It should be emphasised that only Guo et al. (2011) choose most of the parameters in order to fit the observed local mass function, whereas Bower et al. (2006) and De Lucia & Blaizot (2007) use the local luminosity function to adjust their recipes. In recent studies, the parameters of these models have been tuned again by means of a different approach, based on Bayesian inference (Henriques et al.
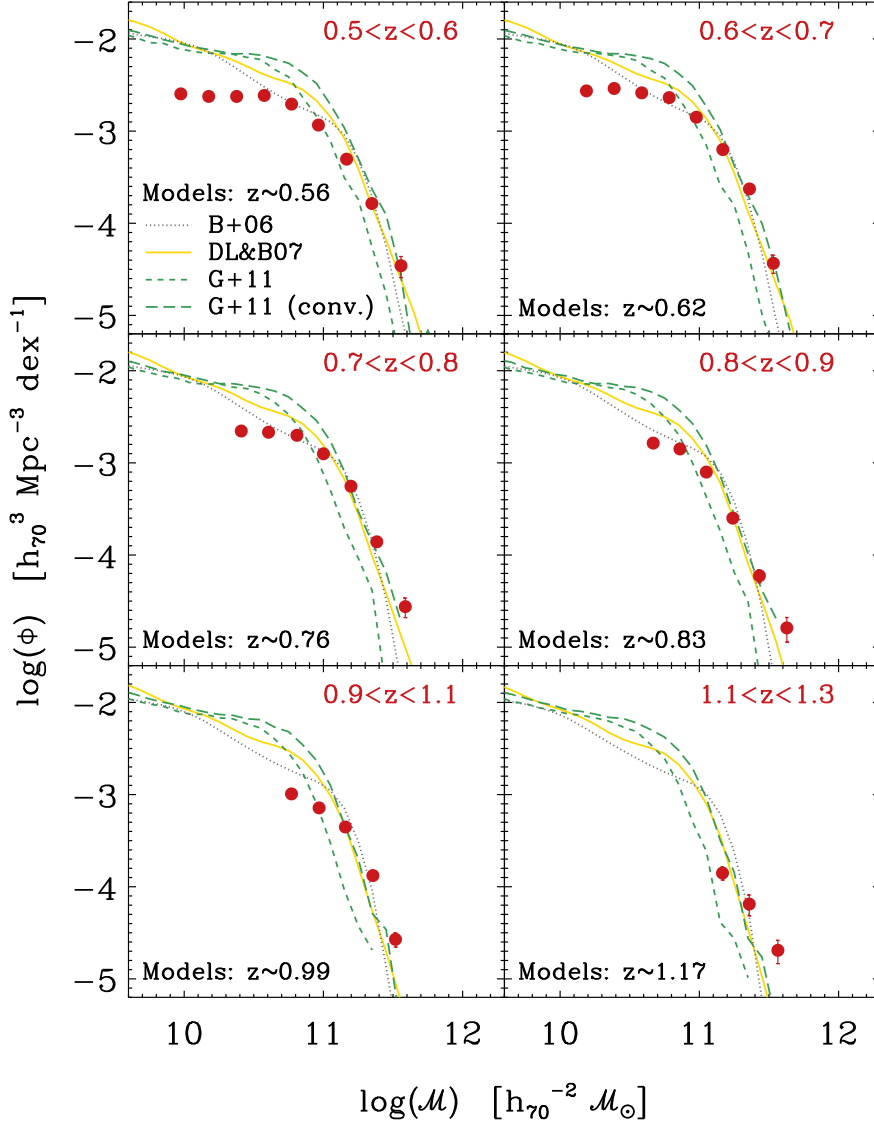
Figure 3.9   Comparison of the VIPERS mass function (red points, as in Fig. 3.8) with the semi-analytical models of Bower et al. (2006), De Lucia & Blaizot (2007), and Guo et al. (2011) (grey dotted, yellow solid, green short-dashed lines), whose GS-MFs have been derived directly from the tables available in the Millennium database (Lemson & Virgo Consortium 2006). The Guo et al. (2011) stellar masses have also been convolved with a Gaussian of dispersion 0.15 dex, to reproduce observational uncertainty on stellar mass determinations; the resulting GSMFs are represented with green long-dashed lines.
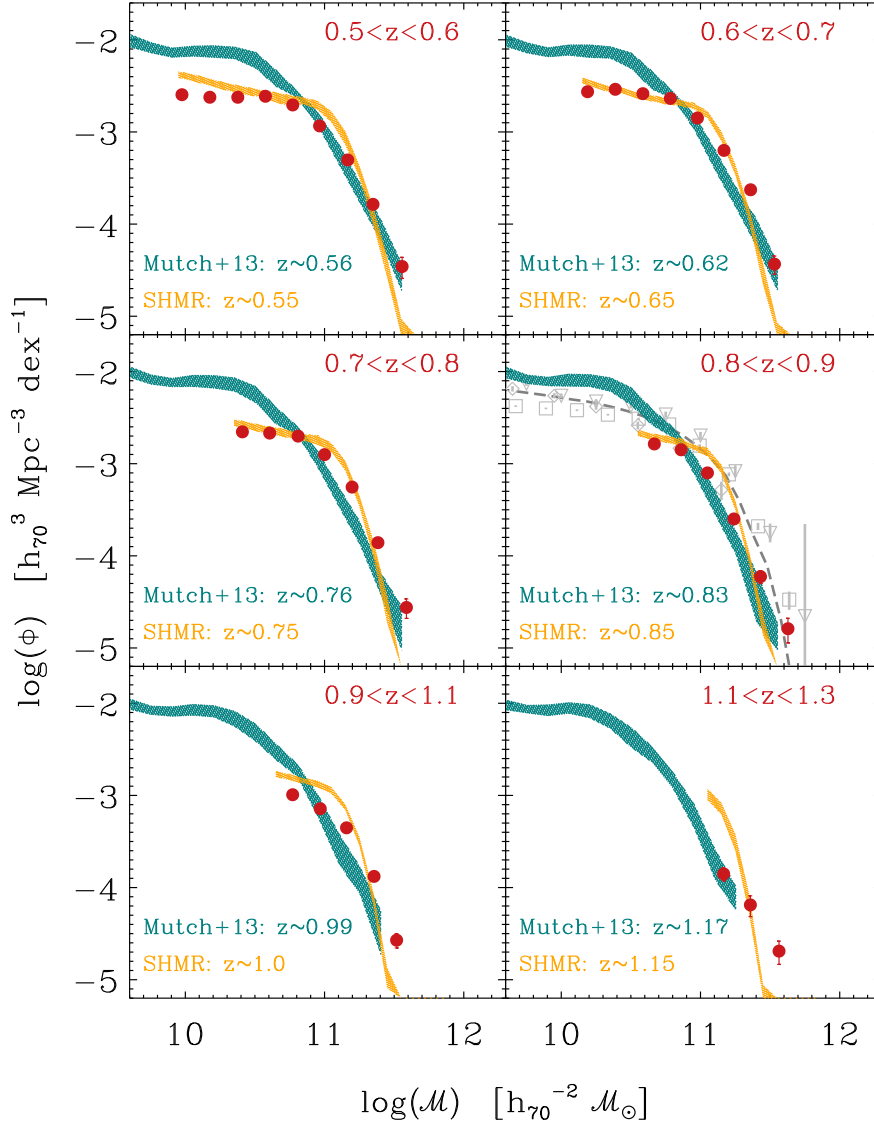
Figure 3.10   Comparison of the VIPERS mass function (red points) with the semi-analytical model of Mutch et al. (2013) (green shaded area at 95% confidence limits). In several redshift bins Mutch et al. GSMF does not reach masses as high as VIPERS because of the smaller the volume of the simulation (with a comoving box size $L = 89.3\, h_{70}^{-1}$ Mpc). In the right-hand middle panel ($0.8 < z < 0.9$), a grey dashed line represents the mass function that Mutch et al. obtain by combining observational data from three different surveys (Pozzetti et al. 2007; Drory et al. 2009; Ilbert et al. 2010, grey triangles, diamonds, and squares, respectively). In addition, the yellow shaded regions represent the dispersion of the mass functions derived from the 57 SHMR mocks (see Sect. 3.2.2), in the same redshift bins as the VIPERS ones.

2009; Bower et al. 2010, e.g.). From this perspective, a particular kind of calibration has been proposed by Mutch et al. (2013), who modify the input parameters in the SAM of Croton et al. (2006) to match observations at $z = 0$ and $z \simeq 0.8$ simultaneously. The results obtained by Mutch et al. (2013) are compared to the VIPERS mass functions in Fig. 3.10. The plot shows reasonable agreement beyond $\mathcal{M} \simeq 10^{11} \, \mathcal{M}_\odot$, not only at the redshift of calibration ($z \simeq 0.83$) but also in the other bins. The authors do not convolve their mass functions with a Gaussian uncertainty on stellar masses, because at least part of the uncertainties this procedure accounts for should already be included in the observational constraints they use. The Mutch et al. (2013) model is calibrated at $z = 0.83$ by using the results of Pozzetti et al. (2007), Drory et al. (2009), and Ilbert et al. (2010). Among these three GSMFs, only Pozzetti et al. (2007) is based on spectroscopic data (VVDS-Deep), which are unfortunately quite limited at high masses. The other two estimates (Drory et al. 2009; Ilbert et al. 2010) are derived from the COSMOS survey, which contains a significant over-density at $z \simeq 0.8$.

The strategy adopted by Mutch et al. to combine such information may lead to overconfidence in the adopted constraints, especially in the highest mass range, where observations are most difficult. To reconcile SAM and observations at $\log(\mathcal{M}/\mathcal{M}_\odot) > 10.8$, Mutch et al. (2013) have assumed a star formation efficiency much higher than the one imposed by Croton et al. (2006), and consequently they were forced to parametrise supernova feedback efficiency with a range of values that is not completely supported by observations (Rupke et al. 2002; Martin 2006). The authors would significantly relieve these tensions if they were to add VIPERS data to their analysis.

From a different perspective, the SHMR mocks introduced in Sect. 3.2.2 are also calibrated at multiple redshifts. I decided to test their reliability by deriving their GSMFs (Fig. 3.10). The agreement is remarkable: VIPERS data confirm the validity of the stellar-to-halo mass relation of Moster et al. (2013) that was used to construct these mocks. This relation connects galaxies with their hosting dark matter halo by means of a redshift-dependent parametrisation that has been calibrated through the GSMFs of Pérez-González et al. (2008) and Santini et al. (2012) up to $z = 4$. The SHMR mass functions diverge at high mass from our estimates probably because of the constraints used by Moster et al. (e.g., the data from Pérez-González et al. 2008) do not reach stellar masses as higher as VIPERS (see Fig. 3.8).

Improvements in the numerical techniques (e.g. Springel 2010) made hydro-dynamical simulations on cosmological scales also feasible (e.g. Dave et al. 2013). With respect to SAMs, the advantage of these models is the possibility of implementing physical processes (e.g. radiative cooling, star formation, metal enrichment, etc.) in the code by tracing baryons as well as dark matter. However, the finite resolution (the so-called "sub-grid physics", see Schaye et al. 2010) still limits this kind of simulations. I compare the VIPERS GSMF with the one predicted by the EAGLE project (Furlong et al. 2014) to show the improvement achieved by the state-of-the-art hydrodynamical simulations, which now reach a level of agreement with observations close to (or even better than) that attained by SAMs (see also Illustris project Vogelsberger et al. 2014; Genel et al. 2014). The comparison between VIPERS and EAGLE has been made at $z \simeq 0.7$ and is shown in Fig. 3.11.
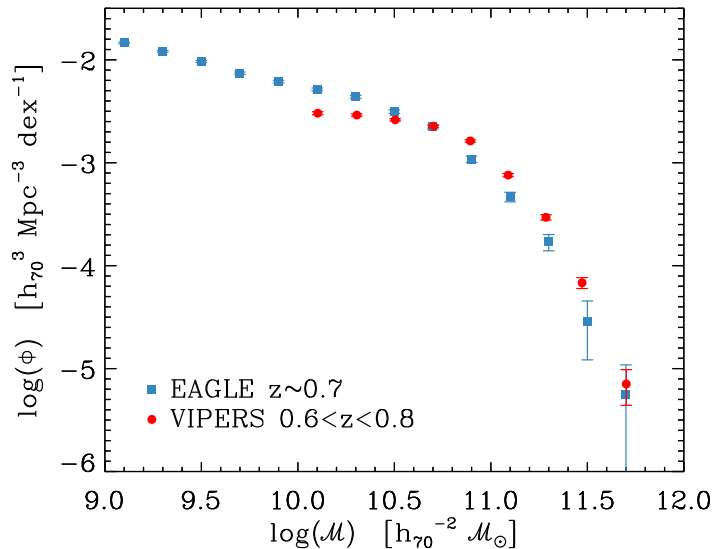
Figure 3.11 Comparison between the VIPERS data (red circles) and the GSMF at $z \simeq 0.7$ (blue squares) predicted by the hydrodynamical simulations developed within the Virgo Consortium's EAGLE project (Schaye et al. 2014; Furlong et al. 2014). The VIPERS GSMF estimated between $z = 0.6$ and 0.8 is the same shown in Fig. 3.8. Error bars take into account Poisson noise in both cases.

The stellar mass function of EAGLE is computed in a box having a size of 100 comoving Mpc ($H_0 = 100 \, \mathrm{km \, s^{-1} Mpc^{-1}}$), containing $1\,504^3$ dark matter particles with mass $9.70 \times 10^6 \, \mathcal{M}_{\odot}$. The initial number and mass of the baryonic particles are respectively $1\,504^3$ and $1.81 \times 10^6 \, \mathcal{M}_{\odot}$. The number of galaxies in the simulated box is about $40\,000$. Feedback processes from massive stars and AGN are calibrated using $z \simeq 0$ data (i.e., the local galaxy stellar mass function and the galaxy-black hole mass relation, for more details see Schaye et al. 2014). There is an excess of low-mass galaxies in the power-law tail of the GSMF, while the difference at high masses is smaller ($\sim 0.2 \, \mathrm{dex}$). Although the simulation seems to be biased like the GSMFs of SAMs (i.e., the low-mass end is too steep), quantitatively speaking the differences between EAGLE and observations are comparable to the plausible uncertainties in the interpretation of the data (in particular, stellar mass estimates, see the thorough discussion in Furlong et al. 2014).

3.3   Mass functions of different galaxy types

Studies on the GSMF by dividing blue/active from red/quiescent objects provided insights in galaxy evolution. For instance, large galaxy samples (as in COSMOS and zCOSMOS, Drory et al. 2009; Ilbert et al. 2010; Pozzetti et al. 2010) showed that the double Schechter profile (Eq. 3.2) of the total GSMF is due to the combined contribution of passive and start-forming objects. The GSMF is an effective tool to investigate the various processes resulting in such a galaxy mix, since the transformation of star-forming galaxies into "red and dead" objects may happen

in various ways (see e.g. Faber et al. 2007).

3.3.1   Galaxy type classifications

The most evident aspect of the distribution of galaxy colours is the colour bimodality (Fig. 2.8). This can be observed also in the colour-magnitude diagram (e.g. Fritz et al. 2014), where the two peaks found in the colour distribution become the so-called red-sequence and blue-cloud. In the VIPERS data, as in local surveys, this is a very general feature that reflects the presence of different galaxy populations (e.g. Strateva et al. 2001; Hogg et al. 2002; Bell et al. 2004). I adopt the method described in Fritz et al. (2014) and D13, which classifies the VIPERS galaxies by means of their $(U - V)$ colour, as it is highly sensitive to the slope of the blue/ultraviolet continuum, representing therefore a natural tracer for SF galaxies. In particular, the U-band filter represents a good measure of the overall star formation activity in our galaxies. Unfortunately, the colour bimodality does not take into account the contamination of the red population by AGN or dust-obscured red galaxies. Nonetheless, this method is quite reliable: as discussed by Mignoli et al. (2009) using zCOSMOS data, 86% (93%) of the galaxies selected as being photometrically red (blue) are also quiescent (star-forming) according to their spectra.

In VIPERS, a bimodal colour distribution is evident across the whole redshift interval, but a fixed cut (as in Fig. 2.8) would be too simplistic to divide blue and red galaxies, because it would not account for redshift evolution. In Fritz et al. (2014) we thus separate red galaxies from blue ones by measuring the local minimum in the colour distribution within each redshift bin individually. A simple linear evolution with redshift is assumed, and by fitting these observed local minima we derive a separation in the rest-frame $(U-V)$ between the two main populations. This threshold evolves as $(U - V) = 1.1 - 0.25z$.

To verify and validate such a selection, D13 derived galaxy photometric types by fitting VIPERS photometry with the empirical set of 62 templates used in Ilbert et al. (2006), which was optimised to refine the match between photometric and spectroscopic redshifts in the VVDS. The same set was also used to classify galaxies in several other papers (e.g. Zucca et al. 2006, 2009; Pozzetti et al. 2010; Moresco et al. 2010). The classification of VIPERS galaxies resulting from this second method matches reasonably well with the $(U - V)$ colour selection (Fig. 3.12). More than 70% of the red galaxies are defined as early-type objects by the SED analysis (E/S0 templates), while more than 95% of blue galaxies are classified as late types. For red galaxies this worsens beyond $z = 1.1$, where only 55% of the red galaxies are classified as early types in terms of their SED. In the same redshift range, instead, 98% of blue galaxies are classified as late-type objects. In Fig. 3.12 Sa/Sb galaxies (according to their photometric type) are grouped in a distinct sample, to highlight the location of the green valley.

In order to separate different galaxy types, I also apply the method described in Arnouts et al. (2013), based on the (NUV $- r$) vs $(r - K)$ diagram (NUVrK in the following). With this method, recent star formation on a scale of 10^6–10^8 yr
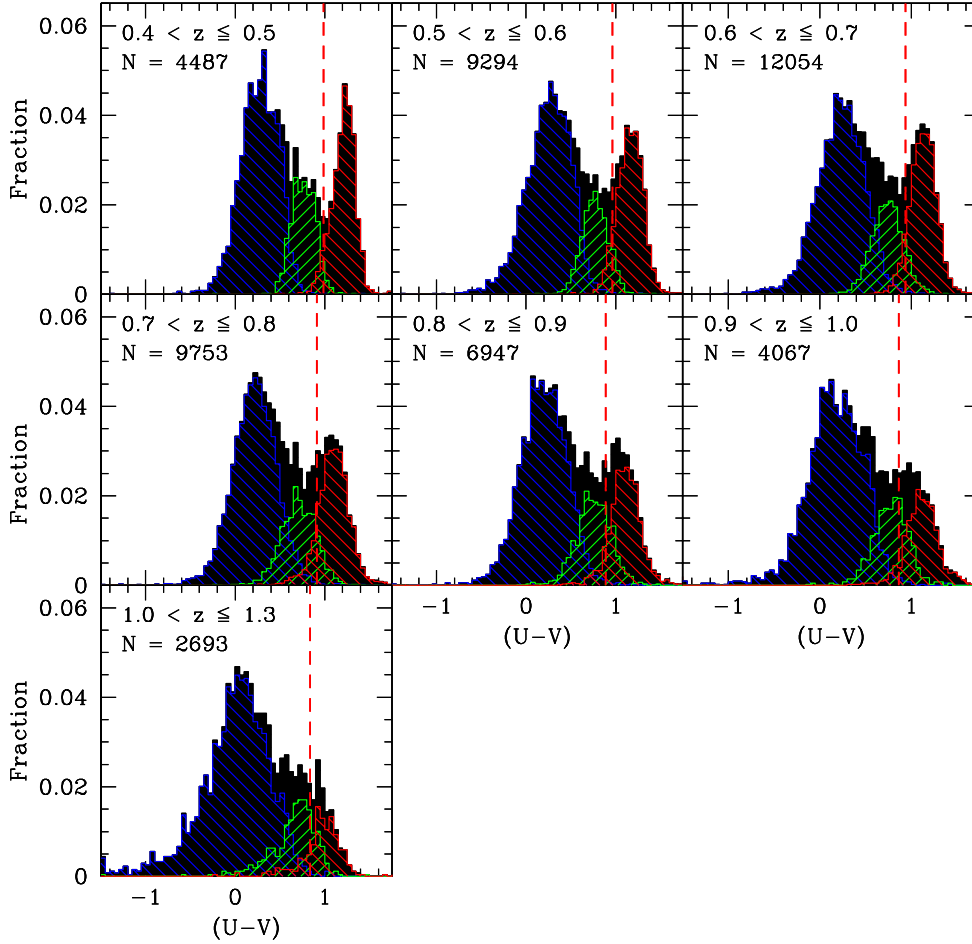
Figure 3.12   The rest-frame $(U - V)$ colour distribution (black histogram) in different redshift bins (the number of objects in each bin is reported in the relative panel). In this plot, magnitudes are in the Vega system. The separation between blue and red galaxies is marked by a red dashed line. Galaxies are also split into three broad groups, according to their SED type: the blue histogram includes Sc, Sd, SB and irregular galaxies; the green histogram Sa and Sb; the red one E and S0 (see text for more details). From Fritz et al. (2014).

is traced by the $(NUV - r)$ colour (Salim et al. 2005), while $(r - K)$ is sensitive to the inter-stellar medium (ISM) absorption. The absolute magnitudes used here have been estimated as detailed in Sect. 2.1, through the filters NUV, r, and Ks of GALEX, MegaCam, and WIRCam respectively. It should be noticed that VIPERS redshift range is fully within the interval $0.2 < z < 1.3$ used by Arnouts et al. in their analysis. Their diagram is similar to the $(U - V)$ vs $(V - J)$ plane proposed by Williams et al. (2009), but by sampling more extreme wavelengths it results in a sharper separation between quiescent and star-forming galaxies (cf also Ilbert et al. 2013). Indeed, I shall refer to the samples built through this method as *passive* and *active* galaxies. Moreover, the position of an object in the NUVrK diagram correlates well with its infrared excess (i.e. the $L_{\rm IR}/L_{\rm NUV}$ ratio) and sSFR, at least when $\log(\mathcal{M}/\mathcal{M}_\odot) \geqslant 9.3$ (for further details, see Arnouts et al. 2013).

With classification methods based on a single-colour bimodality the passive sample is partially contaminated by star-forming galaxies reddened by dust, as shown e.g. by Moresco et al. (2013). In the NUVrK, the simultaneous use of two colours disentangles those different populations. This effect is shown in Fig. 3.13, in which the NUVrK classification is compared to the results of $(U - V)$ bimodality. Another degeneracy, between dust content and galaxy inclination, cannot be removed. In fact, the larger the ISM optical depth is, the redder $(r - K)$ will result, but this may indicate either that the dust content is intrinsically larger, or the path of photons toward the observer is longer. Nevertheless, the identification of the passive population should not be affected by that, given their low amount of dust (Smith et al. 2012).

As illustrated in Fig. 3.14, a galaxy is regarded as passive when

$$\begin{cases} (\text{NUV} - r) > 3.75 \,, \\ (\text{NUV} - r) > 1.37(r - K) + 3.2 \,, \\ (r - K) < 1.3 \,. \end{cases} \tag{3.27}$$

With respect to the definition of Arnouts et al. (2013) I add a further cut, namely $(r - K) < 1.3$. In this way I take into account the geometrical effect they observe after including the dust prescription of Chevallard et al. (2013) in their analysis. According to that study, the reddest $(r - K)$ colours can be reached only by edge-on disc galaxies with a flat attenuation curve. I also verified through a set of BC03 templates that passive galaxies ($\tau = 0.1$–$3\,\text{Gyr}$) have always $(r - K) < 1.15$. This result, considering the typical uncertainties in magnitude estimates, justifies the third condition in Eq. (3.27). It should be noted that, with an analogue argument, Whitaker et al. (2011) modify the passive *locus* of Williams et al. (2009) diagram.

In the NUVrK, sSFR increases as galaxies move along a preferential direction, identified in Fig.3.14 by a vector. Therefore, lines orthogonal to that direction work as a cut in sSFR; for instance, the boundary we defined for the passive *locus* roughly corresponds to sSFR $< 10^{-11}\,\text{yr}^{-1}$. The use of NUV$rK$ is preferred to a direct selection in sSFR, since the SED fitting estimates of SFR are generally less reliable than colours (as discussed in Sect. 2.1), especially when far-IR data are not available. Nevertheless, it is worth noticing that the sSFR values obtained from HYPERZMASS are on average in good agreement with the NUVrK classification, providing an additional test for its robustness (see Fig. 3.14). Among the galaxies
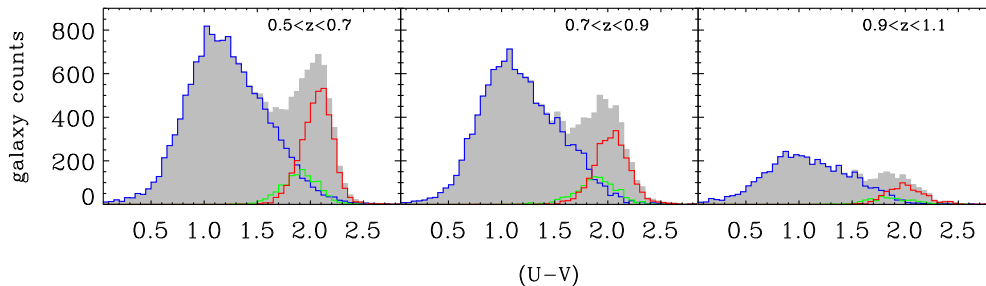
Figure 3.13 Contribution of galaxies in the various NUVrK classes to the $(U - V)$ bimodality (grey histograms, VIPERS galaxies with $2 \leqslant z_{\mathrm{flag}} \leqslant 9$ divided in three redshift bins). The red and blue histograms represent the colour distribution of passive and active objects respectively, while the green histogram includes the intermediate galaxies (according to NUVrK, see Fig. 3.14).

that have been classified as passive, about 95% have a (SED fitting derived) sSFR lower than $10^{-11}\,\mathrm{yr}^{-1}$ (i.e., the typical cut used e.g. in Pozzetti et al. 2010).

I introduce another boundary in the colour-colour space, that is

$$\begin{cases} (\mathrm{NUV} - r) > 3.15\,, \\ (\mathrm{NUV} - r) > 1.37(r - K) + 2.6\,, \\ (r - K) < 1.3\,, \end{cases} \tag{3.28}$$

in order to delimit the area likely corresponding to the "green valley" with respect to galaxies with a significant level of star formation. Equations (3.27) and (3.28) thus encompass galaxies that are probably shutting off their star formation, as we will discuss below. I consider those galaxies as part of the active sample, but in a few passages of the following analysis I will distinguish them from the other star-forming objects, referring to those objects as *intermediate* galaxies. They match the low-sSFR population that Arnouts et al. (2013) identify by tracing similar boundaries. For that population, which has sSFR $\simeq 10^{-10}\,\mathrm{yr}^{-1}$, Arnouts et al. observe that the NUVrK method becomes uncertain: for instance, the L_{IR} estimates they obtain in this particular region of the diagram seems to be overestimated with respect to the one derived from the observed $24\,\mu\mathrm{m}$ flux[3]. Despite the absence of a robust estimator, the sSFR should be low in this intermediate region: given the global trend in the diagram (see the NUVrK vector in Fig. 3.14) those galaxies are expected to be in transition towards the passive *locus* (cf Schawinski et al. 2014). We can inspect the intermediate sample taking advantage of the VIPERS spectra. The spectral features measured in Garilli et al. (2014) confirm the peculiar evolutionary phase of those objects: they already have a low [OII] flux, while their D4000 break has not reached yet the typical values of passive galaxies (Fig. 3.15).

---

[3] However, for this peculiar class of galaxies not only the NUVrK method could be biased, but also the IR luminosity derived from data at $24\,\mu\mathrm{m}$, because such an estimator adopts a ratio $L_{\mathrm{IR}}/L_{24\mu\mathrm{m}}$ that could be too high in this case (as suggested by recent work, e.g. Smith et al. 2012)

This can be interpreted as a characteristic of galaxies that have started to quench their star formation recently and cannot be considered passive yet.

With the aim of selecting post-starburst galaxies in their sample, Muzzin et al. (2012) apply a classification based on D_n4000 and [OII]; the stacked spectrum of their post-starburst candidates is classified as a $k+a$ galaxy (cf Vergani et al. 2010). Only part of our intermediate galaxies satisfy (*a posteriori*) the selection criteria of Muzzin et al. (2012). For instance, about 35% of these galaxies are within $1.0 < D_n4000 < 1.45$, i.e. the range that those authors use as a constraint. We also find a median EW([OII]) of -4.1 $\mathring{A}$, while the stacked spectrum of Muzzin et al. has EW([OII]) $= 0.9 \pm 0.7$ $\mathring{A}$. This difference is not surprising, also because in the VIPERS catalogue the EW is measured only if line emission is detected (see right-hand histogram in Fig. 3.15). Thus, the NUVrK-intermediate selection cannot be fully considered as a post-starburst classification. The VIPERS galaxies in this "corridor" (i.e. between solid and dashed lines in Fig. 3.14) probably represent a more miscellaneous sample than a population selected in the D_n4000-EW([OII]) space.

Summarising, passive galaxies lie above the broken-line border identified by Eq. (3.27), whereas active objects are below that. In addition, inside the region of active galaxies, a transition area is identified between the boundaries of Equations (3.27) and (3.28); active galaxies within this area are also referred as "in transition".

In a paper in preparation, Krywult et al. carry out a morphological analysis by measuring structural parameters of the VIPERS catalogue. They estimate the Sérsic (1963) profile of galaxies between $z = 0.5$ and 1.2, that is expressed as

$$I(R) = I_e \exp \left\{ -b_n \left[\left(\frac{R}{R_e} \right)^{1/n_{\mathrm{Sersic}}} - 1 \right] \right\} , \qquad (3.29)$$

where I_e is the intensity at the half-right radius R_e and n_{Sersic} is the so-called Sersic index, which describes the shape of the light profile (b_n is a constant whose value depends on the adopted n_{Sersic}). The parameters in Eq. (3.29) are determined by using the GALFIT software (Peng et al. 2010a) with the CFHTLS images in the i and r bands. Krywult et al. use a novel approach to model the VIPERS point-spread function (PSF), so that GALFIT can provide reliable estimates even for objects at such high redshift. Among the various products of the software, the Sersic index is remarkably useful, in particular to classify galaxies on the basis of their morphology: if $n_{\mathrm{Sersic}} > 2.5$, the object is considered elliptical, and disc-like otherwise. I will use also this kind of classification in the following, even though it will be limited to a few tests and preliminary results, since the morphological analysis is still ongoing (Krywult et al., in prep.).

3.3.2 Stellar mass functions of different galaxy types

Using the classifications described in Sect. 3.3.1, it is possible to quantify the contribution of different galaxy populations (e.g., blue/red galaxies) to the GSMF and, in particular, to its high-mass end.

The results for the $(U - V)$ classification are shown in Fig. 3.16. The mass functions for each class (Φ_{blue}, Φ_{red}) are estimated in bins of $\log \mathcal{M}$, by means of
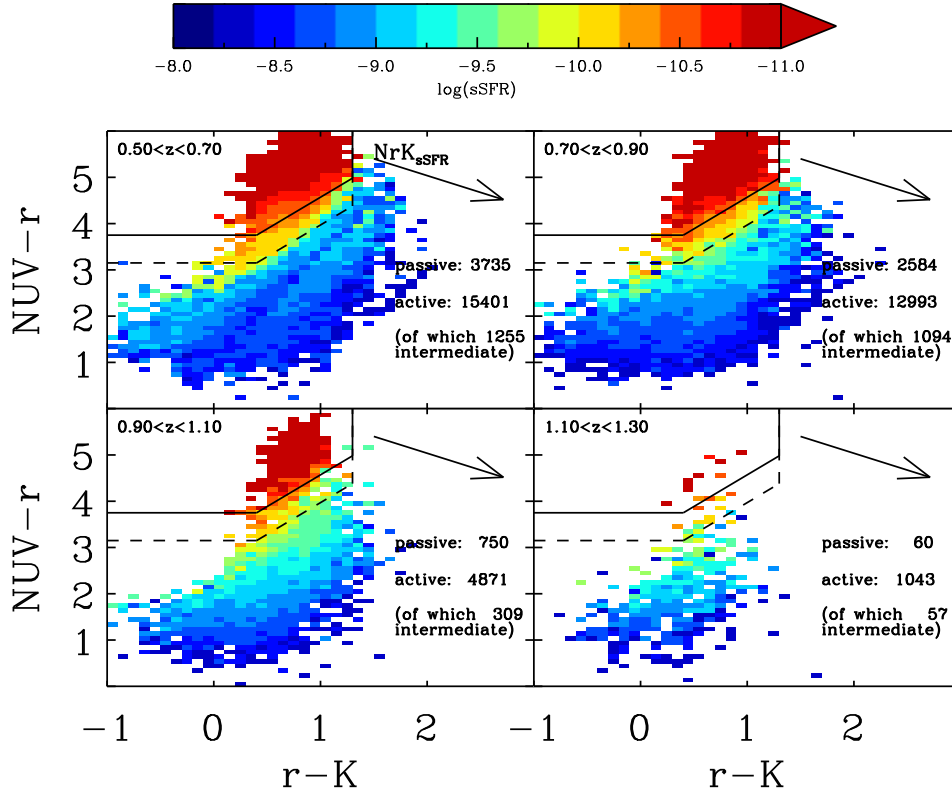
Figure 3.14   The colour-colour diagram $(NUV-r)$ vs $(r-K)$ in four redshift bins. A solid line marks the end of the *passive locus* that is located in the upper part of each panel. Between this boundary and the dashed line, there is a "green valley" of galaxies with intermediate characteristics (see Fig. 3.15). In the diagrams, the colour of each pixel corresponds to the median sSFR of the galaxies inside it (the sSFR of those galaxies is estimated through SED fitting). According to that, the NUVrK classification seems to hold at least up to $z=1.1$. Arnouts et al. (2013) find that in this diagram the sSFR increases as moving along the direction $\cos(54°)\hat{x}, -\sin(54°)\hat{y}$, identified by the top-right vector NrK$_{\text{sSFR}}$ (note that the different scale in x and y-axis warps the angles).
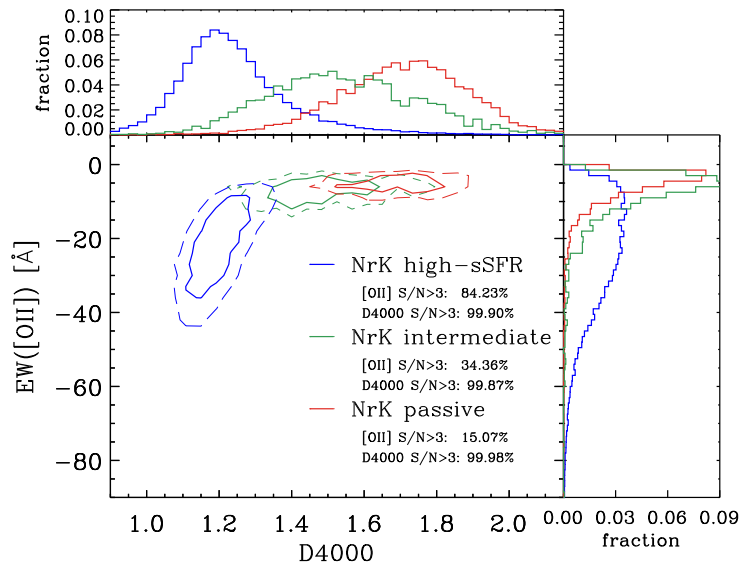
Figure 3.15   Measurements of the D4000 break and the [OII] equivalent width, for the same galaxies of Fig. 3.14, without dividing in z-bins. The quiescent sample is shown in red, while the active galaxies are split in two sub-samples: intermediate (green lines) and high-sSFR (blue lines, see Sect. 3.3.1 for details about this classification). Note that the EW is negative for emission lines. In the central panel, contour levels enclose 25 and 50% of each sample (solid and dashed lines respectively). The percentage of galaxies with a signal-to-noise ratio greater than three is reported in the legend. Projected histograms show the [OII] and D4000 distributions of the three samples (each one normalised to the number of its elements).

the $1/V_{\mathrm{max}}$ method described above. Fits with the usual Schechter function are provided, as described in the caption, to highlight evolution (or absence thereof) in redshift. The stellar mass functions of active/passive galaxies (Φ_{act}, Φ_{pass}), along with those of elliptical/disc galaxies, are shown in Fig. 3.17. This latter classification leads to similar results to those obtained by using the NUVrK diagram, the main difference being due to bulge-dominated galaxies with low mass that are still forming stars. These objects are included in the elliptical ($n_{\mathrm{Sersic}} > 2.5$) sample, but are identified as active in the NUVrK (see Fig. 3.18). Their $\mathcal{M}/L$ is usually small and for this reason the limiting mass of the elliptical sample is systematically smaller than the passive one, although by only $\sim 0.1\,\mathrm{dex}$. Apart from that, the GSMFs relying on the NUVrK and on GALFIT agree within the uncertainties (Fig. 3.17). Nevertheless, the following discussion will focus – in addition to the $(U - V)$ – on the NUVrK classification only, which is at present more reliable than the morphological analysis (see Sect. 3.3.1).

   The predominance of red (passive) objects among the massive galaxies is clearly visible in all redshift bins, with blue (active) galaxies mainly contributing at lower masses ($\mathcal{M} < \mathcal{M}_{\star}$). Since the completeness limit for the blue population ($\mathcal{M}_{\mathrm{lim}}^{\mathrm{blue}}$) extends to sufficiently low masses, I can perform the Schechter fit by leaving $\mathcal{M}_{\star}$, $\Phi_{\star}$, and α free. The slope of the low-mass end remains almost constant in redshift for this population, with $-1.3 < \alpha_{\mathrm{blue}} < -1.2$, up to $z \simeq 0.9$, as seen in previous
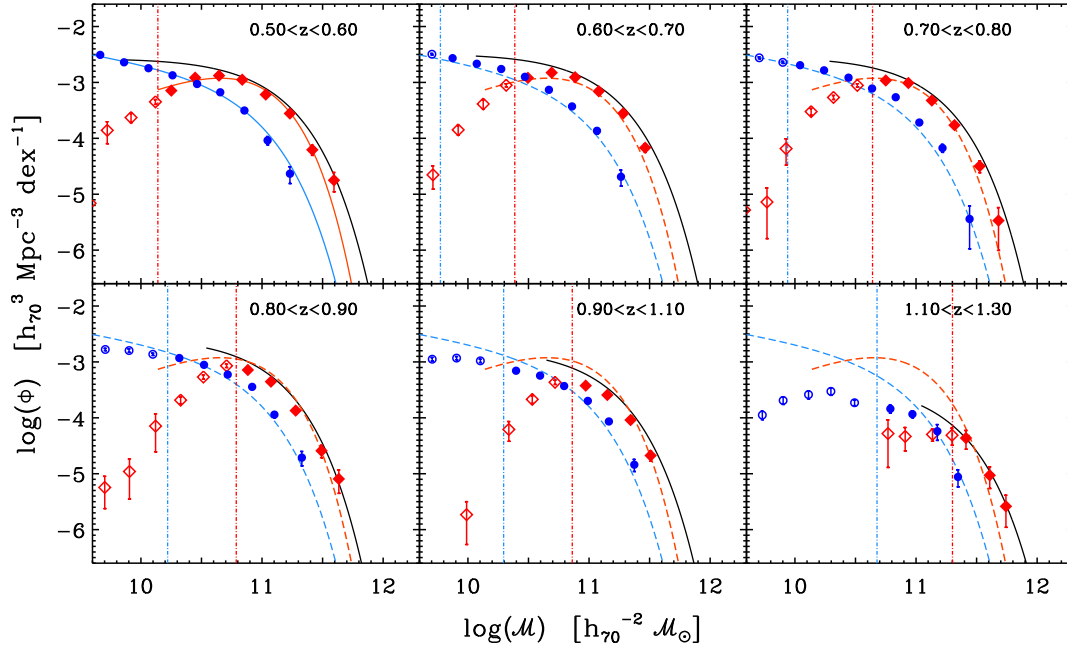
Figure 3.16   The galaxy stellar mass functions of the blue and red populations in VIPERS, derived using the $1/V_{\max}$. Symbols (circles and diamonds, respectively) are filled for data above the corresponding completeness limit $\mathcal{M}_{\lim}$ (vertical lines) and empty below. Error bars account for Poisson noise alone. The Schechter fit of the two populations in the bin $0.5 < z < 0.6$ (solid blue and red lines) is reported for reference as a dashed line in the other panels. The solid black line in each panel gives the Schechter best fit to the whole VIPERS sample in that redshift bin.
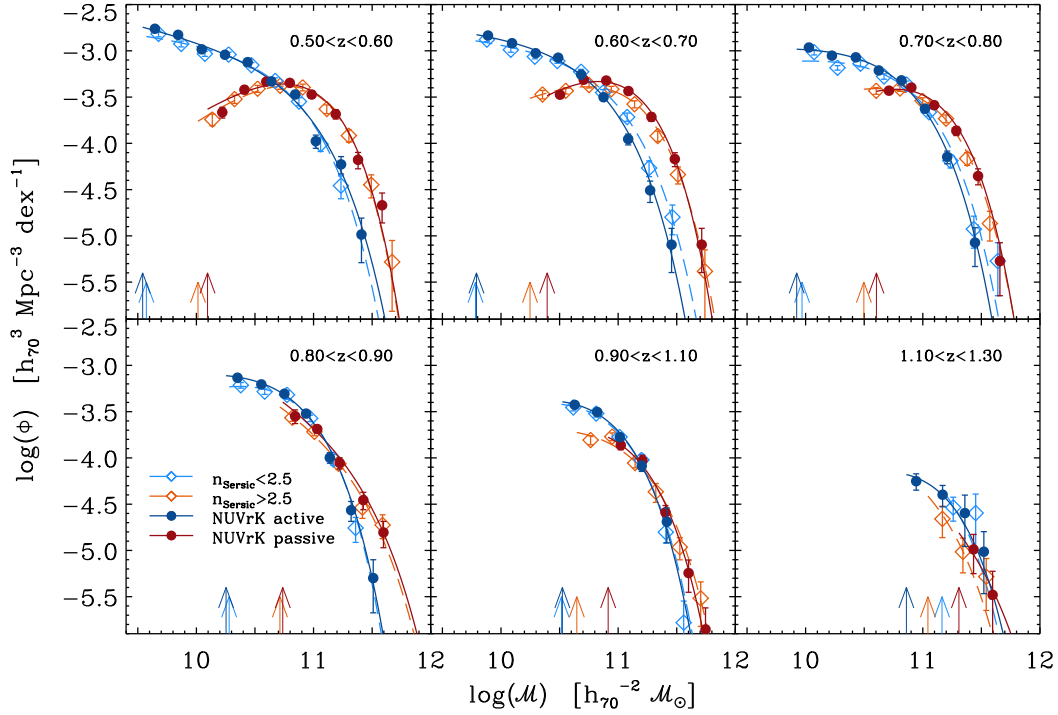
Figure 3.17 Stellar mass functions of galaxy types determined by the NUVrK diagram in six redshift bins: $1/V_{\mathrm{max}}$ estimates are represented by the filled circles, to which a Schechter function is fit (solid line). Blue symbols are related to active galaxies while the passive population is in red. Stellar mass functions from the morphological classification are shown with lighter colour (red for galaxies with $n_{\mathrm{Sersic}} \geqslant 2.5$, blue for $n_{\mathrm{Sersic}} < 2.5$). Empty diamonds indicate the $1/V_{\mathrm{max}}$ determinations, their Schechter fit to these points is a dashed line. For sake of clarity, the completeness limits are shown at the bottom of each panel with upward arrows (same colour code as the GSMFs).
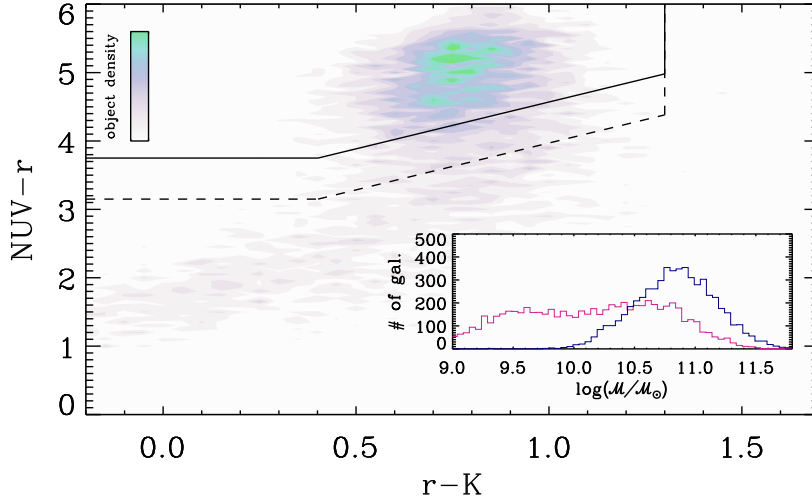
Figure 3.18 Elliptical galaxies in $(NUV - r)$ vs $r - K$ space. In this Figure only objects having $n_{\mathrm{Sersic}} > 2.5$ are included, with the contour levels (from white to green) showing their concentration in the upper part of the diagram (see Fig. 3.14 for a description of the various subregions of the plot). In addition, a "plume" of elliptical galaxies spreads toward the bottom-left corner. The inset shows the stellar mass distribution of both subsamples (blue histogram for the ellipticals in the *passive locus* and magenta histogram for those belonging to the plume).

works (e.g. Pozzetti et al. 2010; Ilbert et al. 2013). When assuming the NUVrK classification, the slope of the active GSMF is similar ($\alpha_{\mathrm{act}} \simeq -1.2$) but there is a larger number of objects at $\log(\mathcal{M}/\mathcal{M}_\odot) \simeq \mathcal{M}_\star$. This difference is due to star-forming galaxies strongly affected by reddening (see Sect. 3.3.1). For the same reason, when comparing the passive GSMF with the red one at the same redshift, Φ_{pass} is lower than Φ_{red}. At redshift higher than 0.9 the low-mass tail can no longer be constrained. With respect to the red (or the passive) population, the high values of the mass completeness limit (see Sect. 3.1.3) prevent us from studying those galaxies at masses $\lesssim \mathcal{M}_\star$; for instance, it is not possible to determine the evolution of α (Ilbert et al. 2010) or an upturn of the GSMF (cf. Drory et al. 2009) in a reliable way.

From these measurements I can determine the value of $\mathcal{M}_{\mathrm{cross}}$, where the blue and red GSMFs intersect, i.e. the dividing line between the ranges in which blue and red galaxies respectively dominate the mass function (Kauffmann et al. 2003b). The physical meaning of $\mathcal{M}_{\mathrm{cross}}$ has been questioned (Bell et al. 2007), but it is in general considered as a proxy to the transition mass of physical processes such the quenching of star formation (responsible for the migration from the blue cloud to the red sequence), or the AGN activity (e.g. Kauffmann et al. 2003a). Moreover, its clear dependence on environment (Bolzonella et al. 2010) points to an interpretation of the galaxy transformation that is not only linked to secular processes.

I quantify the value of the transition mass in each redshift bin using the $1/V_{\mathrm{max}}$ measurements (Fig. 3.19). Beyond $z \simeq 0.9$, the $\mathcal{M}_{\mathrm{cross}}$ estimates should be formally considered as upper limits, since they fall below the mass completeness limit

of red/passive galaxies, but at least up to $z = 1.0$, they can be considered as a good approximation of the real values, given their proximity to the limit. In Fig. 3.19 results from previous studies are also shown. In this respect, it is important to underline that the value of $\mathcal{M}_{\mathrm{cross}}$ provided by the various authors can differ significantly from each other, depending on the adopted classification. For instance, the results of the morphological classification used by Bundy et al. (2006) on the DEEP2 survey fall between 10^{11} and $10^{12}\,\mathcal{M}_\odot$, well above all the estimates shown in Fig. 3.19. This could be related to part of the "red and dead" galaxies at such redshifts becoming ellipticals (in a morphological sense) at a later stage (Bundy et al. 2010). In fact, when they split the DEEP2 sample on the basis of the $(U - B)$ bimodality, the results are in agreement with our findings based on colour bimodality.

For the red/blue classification, the VIPERS transition mass increases from $\log(\mathcal{M}_{\mathrm{cross}}/\mathcal{M}_\odot) = 10.4$ at $z \simeq 0.55$ to $\log(\mathcal{M}_{\mathrm{cross}}/\mathcal{M}_\odot) = 10.6$ at $z \simeq 0.75$. This trend is very well fitted by a power law $\propto (1 + z)^3$. Estimates of $\mathcal{M}_{\mathrm{cross}}$ for the passive/active samples are 0.2–0.3 dex higher, and evolve proportionally to $(1 + z)^{4.5}$.

The NUVrK estimates are fairly consistent with those of Pozzetti et al. (2010) and Moustakas et al. (2013), which rely on the sSFR, i.e. an approach very similar to the NUVrK method. Namely, Pozzetti et al. (2010) use a simple cut to separate star-forming and passive (sSFR $\gtrsim 10^{-11}\,\mathrm{yr}^{-1}$) while Moustakas et al. (2013) define active galaxies as lying in the main sequence of the SFR (estimated from the SED fitting) vs $\mathcal{M}$ diagram. They find a flatter evolution, with $\mathcal{M}_{\mathrm{cross}} \propto (1 + z)^{1.5}$. The results of Vergani et al. (2008) are also in agreement with VIPERS, PRIMUS, and zCOSMOS. In this case, the authors rely on the identification of the D4000 break in the VVDS spectra and have a similar redshift evolution to ours, namely $\mathcal{M}_{\mathrm{cross}} \propto (1 + z)^4$. Besides the sSFR classification, Pozzetti et al. (2010) derived $\mathcal{M}_{\mathrm{cross}}$ using other two criteria: morphology (spheroidal vs disc/irregular galaxies), as well as best-fit SEDs (same photometric types discussed in Sect. 3.3.1).

3.3.3   Evolution of the different galaxy populations

To collect further evidence of star-formation quenching processes that cause the transition of galaxies from the so-called blue cloud to the red sequence (Faber et al. 2007), I measured the evolution of the galaxy number density of blue and red populations, namely $\rho_N^{\mathrm{blue}}(z)$ and $\rho_N^{\mathrm{red}}(z)$, in addition to the active and passive samples, i.e. $\rho_N^{\mathrm{act}}(z)$ and $\rho_N^{\mathrm{pass}}(z)$. These estimates are derived using the $1/V_{\mathrm{max}}$ method, taking both Poisson noise and cosmic variance into account. I also verified that the results would essentially be the same if I had measured number densities by integrating the Schechter best-fitting functions. I explore four narrow bins of stellar mass to highlight the dependence of the quenching processes on this parameter. To improve statistics at high stellar masses, the adopted redshift bins are wider than before: 0.5–0.7, 0.7–0.9, 0.9–1.1, 1.1–1.3. The results are all shown in Fig. 3.20.

At intermediate masses ($10.6 < \log(\mathcal{M}/\mathcal{M}_\odot) < 11.0$), the number density of red galaxies ρ_N^{red} increases by a factor of ~ 3 from $z = 1$ to $z = 0.6$, whereas at higher masses ($\log(\mathcal{M}/\mathcal{M}_\odot) > 11.0$) the variation is ~ 0.3 dex (about a factor 2) in the same redshift interval. The picture slightly changes when studying the evolution of
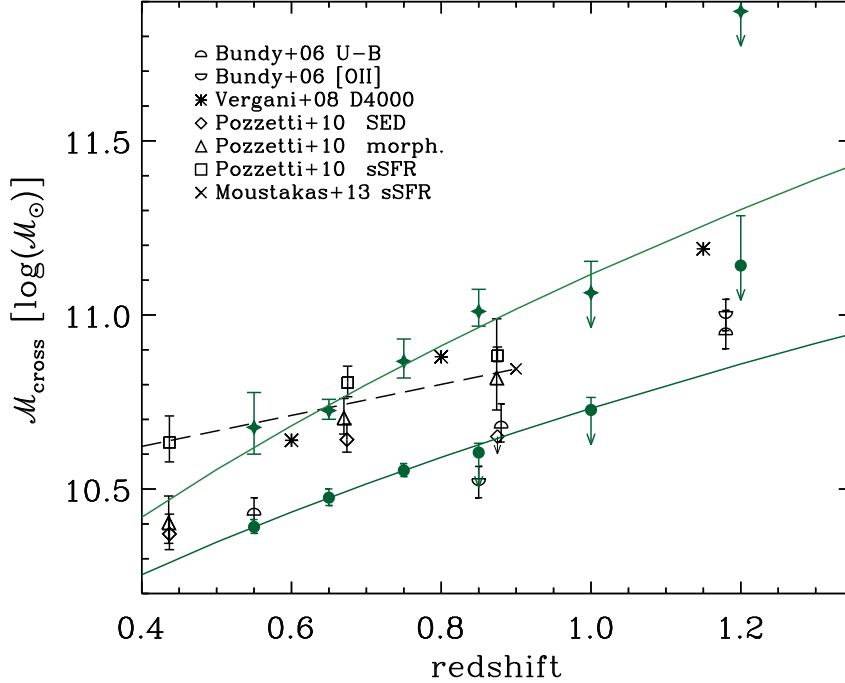
Figure 3.19 The values of the transition mass $\mathcal{M}_{cross}$ as computed from the blue/red GSMFs (Fig. 3.16) and from the active/passive (Fig. 3.17), plotted as a function of redshift. The VIPERS measurements are given in green (filled circles for the former classification, stars for the latter), with a downward arrow when the transition mass is below the completeness mass of at least one of the two complementary classes. The solid line is a fit with a $(1+z)^3$ power law to the VIPERS points between $z = 0.5$ and $z = 0.8$ in the case of the $(U-V)$ classification, while it results $(1+z)^{4.5}$ when using the NUVrK. These are compared to literature estimates (in black). Points from Pozzetti et al. (2010) are obtained using three different classifications: a separation according to the galaxy sSFR (squares), a best-fit SED classification (diamonds), and a morphological classification (triangles). The points of Bundy et al. (2006) are based on either the $(U-B)$ bimodality or [OII] emission (upper and lower half-circles respectively). The points by Vergani et al. (2008) (asterisks) are based on a spectral classification (D4000 break). The value from PRIMUS (Moustakas et al. 2013) at $z = 0.9$ is reported as a cross, while the dashed line traces an evolution $\propto (1+z)^{1.5}$, as suggested in that paper; these authors classified active and quiescent galaxies with respect to their position in the SFR vs $\mathcal{M}$ diagram.
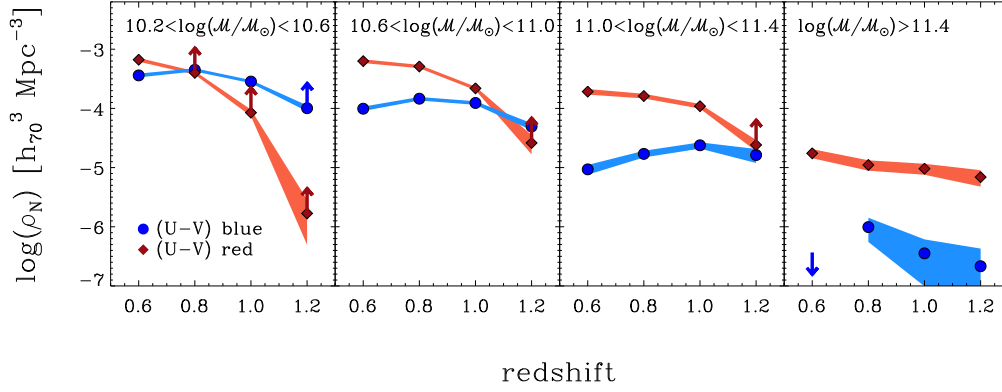
(a)
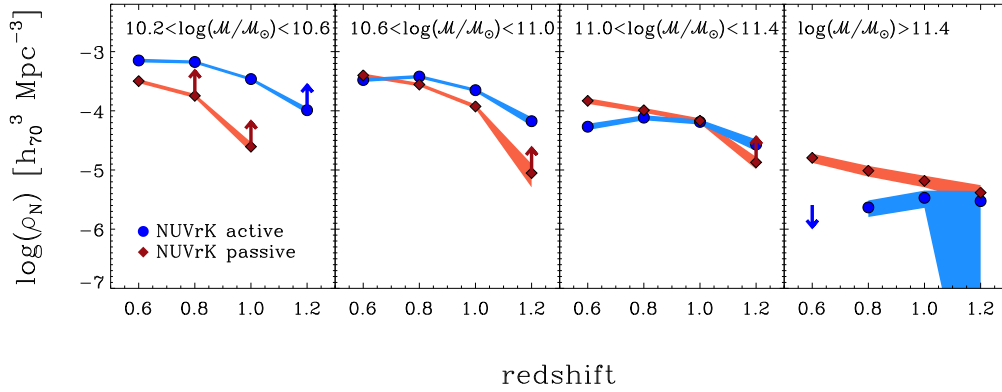
(b)

Figure 3.20 *Panel (a):* evolution of the number density of the blue and red galaxy populations in VIPERS (blue circles and red diamonds, respectively) with different stellar masses. *Panel (b):* same analysis of the number density, but dividing the VIPERS sample in active (blue circles) and passive (red diamonds), by means of the NUVrK. In both panels, upward arrows represent lower limits when ρ_N is estimated in a bin of mass affected by incompleteness, while a downward arrow represents the upper limit in case of zero detection (rightmost panel). The error corridors reflect the overall uncertainties, which include both Poisson noise and cosmic variance added in quadrature.

the passive fraction. At $z \gtrsim 1$ passive galaxies in the VIPERS volume represent a smaller sample than the red ones, as discussed above. On the other hand, at lower redshift, their number density is comparable: for instance, for stellar masses above $10^{11.4} \mathcal{M}_\odot$, $\rho_N^{\mathrm{pass}}(z \simeq 0.6) = (1.6 \pm 0.2) \times 10^{-5}$ and $\rho_N^{\mathrm{red}}(z \simeq 0.6) = (1.7 \pm 0.2) \times 10^{-5}$. A similar trend is observed at $11.0 < \log(\mathcal{M}/\mathcal{M}_\odot) < 11.4$. For this reason, with respect to galaxies that seem to have quenched their star formation, one finds that their number density increases more steeply when the estimate is based on the definition of "red and dead galaxy" provided by the NUVrK method, instead of a simple colour bimodality. For instance, above $10^{11.4} \mathcal{M}_\odot$, ρ_N^{pass} starts from $(0.7 \pm 0.2) \times 10^{-5} \, h_{70}^3 \, \mathrm{Mpc}^{-3}$ at $z \simeq 1$ and reaches $(1.6 \pm 0.1) \times 10^{-5} \, h_{70}^3 \, \mathrm{Mpc}^{-3}$ at $z \simeq 0.6$ (increasing by nearly a factor 2.5). However, with both classifications we observe a mild evolution of the red/passive population (0.2–0.4 dex) from redshift ~ 1 down to 0.5.

With the VIPERS data we are able for the first time to provide significant evidence of this trend for such massive galaxies at these redshifts. This result is in line with the mass-assembly downsizing scenario highlighted in previous works (Cimatti et al. 2006; Pozzetti et al. 2010; Ilbert et al. 2010): barring systematic effects due to the uncertainty on $\mathcal{M}$, red galaxies with $\log(\mathcal{M}/\mathcal{M}_\odot) > 11$ build their stellar mass well before the less massive ones and do not experience any strong evolution between $z \simeq 1.2$ and $z \simeq 0.6$. At these redshifts, quenching mechanisms seem to be more efficient at low and intermediate masses, as also recently suggested by Moustakas et al. (2013). With respect to PRIMUS, the VIPERS survey extends this finding to higher masses ($\log(\mathcal{M}/\mathcal{M}_\odot) > 11.4$) and redshifts (up to $\simeq 1.2$). The evidence of mass dependence of quenching agrees, for instance, with Peng et al. (2010b), although other mechanisms could play a non-negligible role (e.g. galaxy mergers, Xu et al. 2012).

The co-moving number density of star-forming galaxies varies significantly in absolute terms, depending whether they are classified as $(U - V)$-blue or NUVrK-active (Fig. 3.20a and 3.20b respectively). This fact is a reflection of what observed for the GSMFs and in particular the values of $\mathcal{M}_{\mathrm{cross}}$. However, the evolution as a function of redshift is similar: ρ_N^{act} and ρ_N^{blue} are found to be relatively stable between $z \simeq 1$ to $z \simeq 0.6$ for objects with mass below $10^{11} \mathcal{M}_\odot$. A steeper increase is observed between $z = 1.3$ and 1 in the same mass range. At $10.8 \leqslant \log(\mathcal{M}/\mathcal{M}_\odot) < 11.1$, where both the samples are complete at all redshifts, the number density also shows an increase between $z \simeq 1.2$ and $z = 0.8$, which is milder for blue galaxies. Interestingly enough, the most massive blue/active objects ($\log(\mathcal{M}/\mathcal{M}_\odot) \geqslant 11.4$) are not detected at $z \lesssim 0.6$ (see Fig. 3.20), suggesting that, at such high masses, star formation already turns off at earlier epochs. When the whole VIPERS sample is available, the analysis of the massive-end build-up will continue with more robust statistics.

Chapter 4

Mass functions in the VIPERS environments

In this Chapter, I present the stellar mass function of VIPERS galaxies living in different "environments". With this term, one generally refers to external conditions that may have an impact on the evolution of galaxies, but clearly there are different ways to define it, as I shall discuss in Sect 4.1. In the same Section it is described the definition of environment, based on the galaxy local density, used by the VIPERS collaboration. The GSMFs are shown in Sect. 4.2 and discussed in Sect. 4.3. The main goal is to provide new pieces of evidence in this context, in particular by studying the GSMF evolution as a function of redshift. The results of this Chapter constitute the core of an incoming paper of the VIPERS series (Davidzon et al., in prep.).

4.1 Defining the environment in VIPERS

A fundamental step in this work is to identify the galaxies residing in two opposite environments, i.e. regions of low density (LD) and high density (HD). Broadly speaking, the former ones are regions without a pervasive presence of cosmic structure, whereas the latter are associated with the highest peaks of the matter distribution. However, since the dark matter component is not directly observed, any classification has to rely on some proxy of the overall density field. Such a classification relies on the galaxy density contrast evaluated in Sect. 4.1.2.

4.1.1 Different environment definitions

In general, one possibility is to identify high-density regions as galaxy groups and clusters, in opposition to a low-density "field", sometimes ambiguously defined. When halo mass estimates are feasible, the classification is more tightly related to the underlying distribution of dark matter, with galaxies often divided in satellite and central objects (e.g. van den Bosch et al. 2008; Skibba et al. 2009). Other methods, involving galaxy counts, can identify a broad range of densities with a resolution from a few Megaparsecs down to $\sim 100\,\mathrm{kpc}$; for instance, they are based on two-point clustering (e.g. Abbas & Sheth 2005), Voronoi tessellation (e.g.

Marinoni et al. 2002), or the galaxy number density inside a window function (regarding this last kind of estimators, see Muldrew et al. 2012).

Each method has its peculiarities, and generates an environment parametrisation linked to different aspects of the galaxy surroundings. With respect to the scales probed, several studies questioned the importance of the large-scale environment, favouring the picture in which galaxies are affected by external factors mostly on sub-halo scales (Kauffmann et al. 2004; Wilman et al. 2010; Vulcani et al. 2012). However, different scales are expected to correlate, thus a possible small-scale signal should persist with a lower resolution (e.g. Cucciati et al. 2006; Cappellari et al. 2011; Bassett et al. 2013).

4.1.2   Galaxy density contrast

In this work, I rely on the galaxy density contrast (δ) to characterise the different environments in which galaxies live (Sect. 4.1). This quantity is related to the local concentration of galaxies (i.e. the galaxy density field ρ) and the mean galaxy density ($\bar{\rho}$) such that $\delta = (\rho - \bar{\rho})/\bar{\rho}$. Although ρ is a point field indirectly connected to matter density, it is a good proxy of the underlying matter distribution: through various smoothing schemes (included the one described here) it is possible to recover the latter from the former with a scale-independent bias factor (Amara et al. 2012). The procedure adopted here is thoroughly described in Cucciati et al. (2014).

To derive the local density around a given galaxy, we count objects inside a filter centred on it. Those objects that trace ρ are part of a "volume-limited" sample that includes both spectroscopic and photometric galaxies within a certain luminosity range. The photometric galaxies come from the photometric parent catalogue of VIPERS. To build such a sample, only galaxies with $M_B < -20.4 - Qz$ are selected, in both W1 and W4 fields. The factor Q takes into account the evolution in redshift of $M_B^\star$, with $Q = 1$ according to the zCOSMOS luminosity function (Zucca et al. 2009). The choice of a volume-limited sample (instead of e.g. one limited in flux) is motivated by the goal of the analysis: in order to study galaxy evolution across cosmic time, the environment has to be defined in a consistent way at different redshift. Relying on a rest-frame property like the B-band luminosity ensures that we are using the same type of galaxy tracers in all z-bins.

The tracer sample described above is complete up to $z = 0.9$, and thanks to the cut in luminosity it traces the underlying cosmic structure avoiding strongly evolving bias (cf Amara et al. 2012). I will refer to this volume-limited sample as the sample of "tracers" (to be distinguished from the VIPERS sample for which we will compute δ).

I use z_{spec} for 19 035 tracers having $z_{\mathrm{flag}} \in [2, 9]$. Such a large number of spectroscopic redshifts and their accuracy are crucial to robustly determine the density field in the 3-dimensional (redshift) space: generally, when using photometric redshifts only, the reconstruction along the line of sight is prevented by their larger photo-z errors (e.g. Cooper et al. 2005; Scoville et al. 2013). In VIPERS, δ is computed for galaxies beyond $z = 0.51$, to avoid that the steep decrease of $N(z)$ at $z \lesssim 0.5$ (see Fig. 1.5) could affect our density estimates.

In the tracer sample there are also galaxies with only z_{phot}. Thanks to them,

there is a sufficient number of (photometric) tracers also in the gaps produced by the footprint of VIMOS and in the missing quadrants. Nevertheless, Cucciati et al. (2014) demonstrate that the major source of uncertainties in the procedure is not the presence of gaps but the incompleteness of the spectroscopic sample (i.e. the $\sim 35\%$ sampling rate). In absence of a secure spectroscopic measurement, Cucciati et al. treat the photometric redshifts using a modified version of the method described in Kovač et al. (2010b). The fundamental idea in Kovač et al. technique is that the galaxy distribution along the line of sight, recovered by using spectroscopic galaxies, provides information about the "most likely" radial positions of a photometric object (within the 1σ range of z_{phot}, it has a higher probability to lie where galaxies are more clustered). Thus, to each photometric tracer we assign a distribution of z_{peak} values, together with an ensemble of statistical weights. For each value of z_{peak}, the associated weight w_{peak} represents the relative probability for the object to be at that given redshift (the sum of weights is normalised to unity). In other words, the z_{peak} values are the most likely radial positions of a photometric tracer. In detail, the procedure to determine z_{peak} and w_{peak}, is the following. The starting point is the probability distribution function (PDF) of the measured z_{phot}, assumed to be a Gaussian with rms equal to σ_{zphot}. The other required input is the galaxy distribution along the line of sight, i.e. $N(z)$, around the target galaxy. This is computed by using all the objects of the spectroscopic sample lying inside a cylinder with $7.1\,h_{70}^{-1}$ Mpc radius[1] and half-depth of $\pm 3\sigma_{\mathrm{zphot}}$; the cylinder is centred in the coordinates (RA, Dec, z_{phot}) of the considered galaxy. The desired $N(z)$ distribution is obtained from those objects, using their z_{spec} values (without errors) in bins of $\Delta z = 0.003$. Then, we multiply the PDF of z_{phot} by $N(z)$ and renormalise the resulting function. In this way we obtain a new PDF whose peaks represent the desired set of z_{peak} values. Their respective w_{peak} are provided according to the relative height of each peak (the sum of them being equal to one).

Given the galaxy coordinates $r_g = (\mathrm{RA}_g, \mathrm{Dec}_g)$ and redshift z_g, the local density $\rho(r_g, R_{5\mathrm{NN}})$ is equal to the number of tracers inside a cylindrical filter centred in r_g; the cylinder has half-depth $\Delta v = \pm 1000\,\mathrm{km\,s^{-1}}$ and radius equal to $R_{5\mathrm{NN}}$, i.e. the projected distance of the fifth closest tracer (fifth nearest neighbour, hereafter 5NN). By means of the 5NN we defined δ on a scale that is not unique for the entire sample, because $R_{5\mathrm{NN}}$ differs from one galaxy to another. In fact, it ranges from ~ 2.8 to $8.6\,h_{70}^{-1}$ Mpc as moving from the densest regions toward galaxies with the lowest ρ. Probing a non-uniform scale does not impair the analysis because the main interest here is the *relative* classification of different environments (see Sect. 4.1.3), and the 5NN estimator leads to the desired ranking. The 5NN has been adopted because it is an adaptive estimator that efficiently samples a broad range of densities. One could have used, instead, a fixed radius of $\sim 3\,h_{70}^{-1}$ Mpc (i.e., comparable to the 5NN distance in the highest densities), but in that case the density reconstruction would be highly affected by shot noise in the VIPERS regions with medium/low density. In those regions, the number of tracers inside a filter with small fixed aperture is very low: considering for instance that at $z \simeq 0.7$

---

[1] This value corresponds to a radius equal to 5 Mpc if one assumes $H_0 = 100\,\mathrm{km\,s^{-1}\,Mpc^{-1}}$ (as in Cucciati et al. 2014)

the mean surface density of tracers is about 85 objects per deg^2, only three tracers are expected on average within a cylinder having $R \simeq 3\,h_{70}^{-1}$ Mpc. Filters with fixed aperture larger than $\sim 3\,h_{70}^{-1}$ Mpc would dilute too much the signal at small scales, i.e. at high densities.

The use of cylinders, instead of e.g. spherical filters, minimises the impact of redshift-space distortions (Cooper et al. 2005). The depth along the line of sight ($2\,000\,\mathrm{km\,s^{-1}}$) is optimal not only for spectroscopic redshifts, but also for photometric ones after multiplying their PDF by $N(z)$ as described above. The reconstruction of the density field trough the procedure described here is extensively tested in Cucciati et al. (2014) using spherical filters with $R_{\mathrm{fixed}} = 7.1$ and $11.4\,h_{70}^{-1}$ Mpc (5 and 8 Mpc setting $H_0 = 100\,\mathrm{km\,s^{-1}\,Mpc^{-1}}$). Cucciati et al. (in prep.) also verified the quality of the density reconstruction when replacing spheres with cylinders. For a detailed comparison among different filters (spheres or cylinders, fixed or adaptive apertures, etc.) I refer to Kovač et al. (2010b) and Muldrew et al. (2012). Eventually, the local density contrast of a given galaxy is

$$\delta(r_g, z_g, R_{\mathrm{5NN}}) = \frac{\rho(r_g, z_g, R_{\mathrm{5NN}}) - \bar{\rho}(z_g)}{\bar{\rho}(z_g)}, \qquad (4.1)$$

where $\bar{\rho}(z_g)$ is a function of redshift obtained by smoothing the spectroscopic distribution $N(z)$ with the V_{max} statistical approach, in a similar way to Kovač et al. (2010b).

For galaxies near the survey edges, δ is corrected as done in Cucciati et al. (2006), i.e. by rescaling the measured density by the fraction of the cylinder volume within the survey borders. It should be noticed however that the scatter in the density field reconstruction is mainly due to the survey strategy (e.g., the sampling rate). The impact of border effects is much smaller, and becomes significant only when most of the cylinder volume ($> 50\%$) is outside the survey area. When it happens, I prefer to discard the object from the sample. I also remove galaxies for which the cylinder is inside the survey borders, but less than 60% is included in the spectroscopically observed volume (e.g., when more than 40% of it falls in gaps or in a missing VIMOS quadrant). In that case the density contrast should rely mostly on photometric neighbours, and its estimate would be less accurate. With these two constraints, about 9% of the objects is removed (almost all located near the edges of the survey).

4.1.3 The VIPERS environment

In this analysis, I discriminate LD from HD environments by means of the local density contrast. I include in the LD (HD) sample galaxies that have a density contrast smaller (larger) than a certain value of δ. These thresholds can be fixed according to some physical prescription (e.g. to match detections of galaxy groups or clusters, as in Kovač et al. 2010b), or determined in a relative way, e.g. by considering the extreme tails of the $1 + \delta$ distribution. Following the latter approach, Bolzonella et al. (2010, based on zCOSMOS 10k sample) assume as reference for low and high densities the 25th and 75th percentile (i.e., first and third quartile) of the δ distribution, respectively. The authors compute the distribution in each of their redshift bins, independently; however, it should be noticed that the quartiles
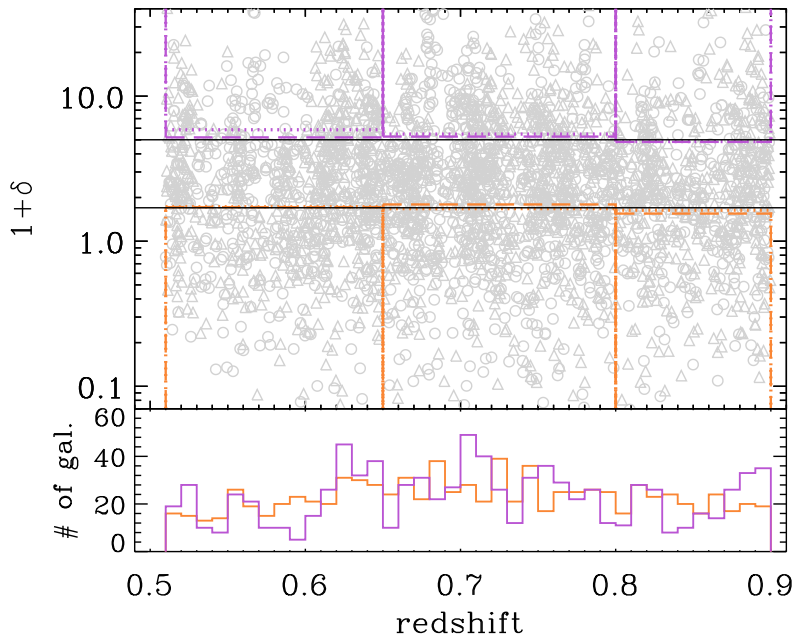
Figure 4.1 *Upper panel:* galaxy density contrast of a mass-limited sample having $\log(\mathcal{M}/\mathcal{M}_\odot) > 10.86$. Galaxies from the W1 field are marked with open triangles, from W4 with open circles. For each redshift bin, galaxies below the first (above the third) quartile of the δ distribution are enclosed by orange (violet) rectangles (dotted lines for W1, short-dashed lines for W4). Thresholds that define LD and HD, as discussed in Sect. 4.1, are shown by black solid lines. *Lower panel:* combining the two fields together, histograms represent the redshift distribution of the LD and HD subsamples, in orange and violet respectively.

they estimate in bins between $z = 1$ and 0.5 are almost constant (see also Peng et al. 2010b, Fig. 9).

Similarly to Bolzonella et al. (2010), I compute the distribution of δ (distinctly in W1 and W4) within three redshift bins: $0.51 < z \leqslant 0.65$, $0.65 < z \leqslant 0.8$, $0.8 < z \leqslant 0.9$. These bins will be also adopted for the mass functions in Sect. 4.2. Here I take into account only galaxies with $\log(\mathcal{M}/\mathcal{M}_\odot) > 10.86$, to work with a complete sample in all z-bins. Indeed, such a value corresponds to the stellar mass limit of the passive population at $z \simeq 0.9$ (see Table 3.1). This is a more conservative choice than the one of Bolzonella et al. (2010), who use the stellar mass limit of the whole galaxy sample.

The resulting first and third quartiles vary among the three z-bins and the two fields by less than $\sim 20\%$, namely $1.55 < 1 + \delta_{\mathrm{LD}} < 1.79$ and $4.84 < 1 + \delta_{\mathrm{HD}} < 5.87$. These changes do not represent a monotonous increase as a function of redshift, but rather random variations between one z-bin and another, and between one field and the other (see Fig. 4.1).

In Sect. 4.1.4 it is shown, by means of cosmological simulations, that these small quartile fluctuations are mainly due to sample variance, and do not reflect the growth of structure over cosmic time. Therefore, one can safely use constant

thresholds to classify LD and HD environments in VIPERS: I define galaxies with $\delta < 0.7$ as belonging to LD, and galaxies with $\delta > 4$ to HD. These limits, applied from $z = 0.9$ to 0.51, are the mean of first and third quartiles computed above (see Fig. 4.1). Despite the name, chosen for sake of clarity, it should be noted that the HD regions in VIPERS have actually intermediate densities in absolute terms. Very concentrated structures, such as massive galaxy clusters, typically have $\delta \simeq 15$–20 (Kovač et al. 2010b) and should approximately match the upper 5% of environmental density. However, the HD environment defined here, although on average less extreme than clusters, is certainly interesting to study, since it has evolved more recently (Smith et al. 2005; Fritz et al. 2005).

As stated above, the 5NN in VIPERS tends to probe scales of 3–$8\,h_{70}^{-1}\,\mathrm{Mpc}$, i.e. inter-halo separations. Hence, a possible signal at smaller scale could lessen (or even vanish) in the present analysis. However, this is not the case, as it is shown in the following. Environmental dependencies at large scales have already been measured e.g. in Cucciati et al. (2006) and Bassett et al. (2013). These findings can be due to physical mechanisms operating at distances larger than the halo virial radius (e.g. Lu et al. 2012a). Another possibility is that a connection between large-scale environment and halo properties preserves the small-scale signal even when working with lower resolution. Also from a theoretical point of view, different scales are expected to correlate in a dark matter hierarchical model (see e.g. Mo & White 1996).

Besides the tests mentioned above, Sect. 4.1.4 contains details about the purity and completeness of the LD and HD samples. By working on mock galaxy catalogues, I show that the adopted parametrisation of environment is not harmed by the effects of the VIPERS design: more than 70% of LD/HD galaxies are expected to be assigned to the correct environment, while a small tail of objects ($< 8\%$) end up being interlopers in the opposite class.

4.1.4   Tests with mock galaxy catalogues

In the previous Section, two opposite environments (LD and HD) have been defined at all redshifts by using the same thresholds in δ. The choice of a constant threshold is based on the assumption that galaxy overdensities do not evolve significantly from $z = 0.9$ to 0.5. Indeed this is the case, as I will show in the following, and the observed scatter in the quartile values (see Fig. 4.1) is not due to redshift evolution, but rather to statistical fluctuations and cosmic variance.

In Sect. 4.1.3 the VIPERS galaxies have been associated to LD and HD environments by means of their density contrast δ. I used constant values for this classification, in spite of the small variations among the quartiles estimated in different z-bins (and different fields, see Fig. 4.1). In part, such variations are due to statistical fluctuations, since a limited number of galaxies are sampling the tails of a nearly-Gaussian distribution (Di Porto et al. 2014). In fact, each z-bin contains only galaxies that were spectroscopically observed, and the δ ranking is sensitive to this incompleteness. From this perspective the scatter is originated by the survey selection: datasets drawn from the same galaxy population can yield different quartile values just because they populate in different ways the tails of the distribution.

To verify the previous assumption, I perform a Monte Carlo simulation by extracting 100 000 times the same number of galaxies used in VIPERS in the various z-bins (keeping W1 and W4 separate). Every time, I assign to those objects a density contrast according to the PDF derived from the observed $1 + \delta$ distribution. In other words, this task consists in reproducing many times the plot shown in Fig. 4.1 as it would appear if one targeted different galaxies from the parent photometric sample. The quartiles resulting from each realisation have a scatter of the order of 10–15% the mean value (see Fig. 4.2).

Another reason for the fluctuations seen in Fig. 4.1 could be cosmic variance. In this case, it is not the subsample of observed objects to vary but the density field itself, e.g. because of field-to-field variations in large-scale clustering (Moster et al. 2011, and references therein).

In VIPERS, thanks to its large volume, that effect is generally small, as shown in D13 and Fritz et al. (2014). In order to estimate the impact of cosmic variance on the definition of environment (Sect. 4.1) I use 10 independent mock galaxy catalogues, which originate from the halo occupation distribution (HOD) modelled by de la Torre et al. (2013, see also the description in Cucciati et al. 2014). Each catalogue reproduces the two VIPERS fields, but it has 100% sampling rate, no masked area, and galaxy redshifts without observational errors (i.e., they are cosmological redshifts perturbed by peculiar velocities). I refer to them as "reference" mock catalogues. The galaxy density contrast of their simulated galaxies has been computed in Cucciati et al. (2014) and in Cucciati et al. (in prep.) through the projected 5NN, as described above for the real sample. Also the quartiles have been estimated in the same z-bins used in VIPERS. Among the 10 realisations, the quartile values that determine LD and HD have 6–10% scatter. This outcome implies that the LD and HD thresholds in real data vary also because of cosmic variance.

In conclusion, the quartiles estimated for VIPERS in the two fields and in three z-bins (Sect. 4.1) spread over a range comparable to the range resulting in the simulations from the undersampling of the $1 + \delta$ distribution and cosmic variance. No redshift evolution of the galaxy density field is necessary to explain those fluctuations. Moreover, by means of cosmological simulations based on the Millennium Simulation (the same used in Di Porto et al. 2014) I checked also that the PDF of the underlying matter density field is almost constant between $z = 1$ and 0.5. These tests confirm that we can safely classify galaxies by using a constant threshold in $1 + \delta$.

In addition, I can estimate purity and completeness of the LD and HD samples by means of the 10 mock galaxy catalogues already used to test cosmic variance effects. We manipulate these reference mocks to make them similar to VIPERS: we reproduce the VIMOS footprint and add redshift measuring errors to have z_{phot} and z_{spec}. We call the resulting catalogues "VIPERS-like" mocks. Then, we parametrise galaxy environments as done with data, in both the VIPERS-like and the reference mocks, and classify the (LD and HD) environments. The comparison indicates that the environment parametrisation in the VIPERS-like mock catalogue is not harmed by the effects of the VIPERS design: in each VIPERS-like mock the classification is in good agreement with the one obtained in the reference (i.e. working without the limitations of the observational strategy). About 70% of
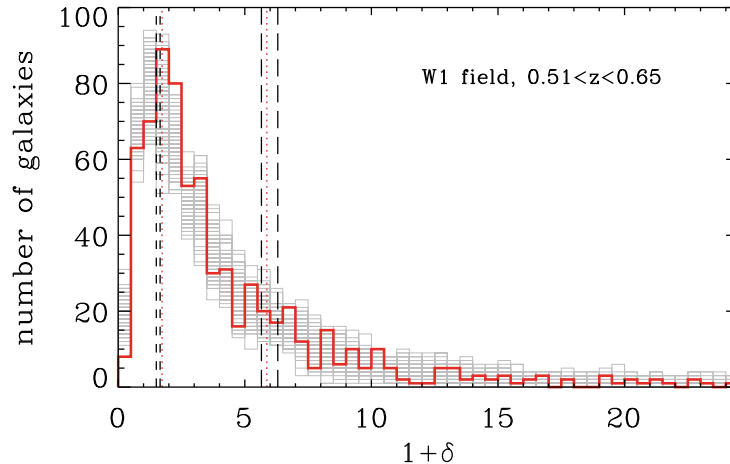
Figure 4.2 Results of the Monte Carlo simulation to test the variation of the $1+\delta$ quartiles caused by galaxy sampling. Each grey histogram is derived from the density contrast of a galaxy sample obtained from the same density distribution of VIPERS data at $0.51 < z < 0.65$ (W1 field only, red histogram). Only 100 realisations (out of 100 000) are shown for sake of clarity. To give an idea of the scatter of the quartiles, dashed lines encompass the rms of their values (short- and long-dashed lines for first and third quartiles respectively). Red dotted lines are the quartiles of the real distribution.

galaxies for which $1+\delta$ is below the first (above the third) quartile in the reference mocks, remain in the LD (HD) environment also in the VIPERS-like ones. For the purity, in D14 we considered the interlopers that should have been associated to LD or HD (according to the reference estimate) but erroneously fall in the opposite environments. With respect to that, less than 8% of low-density galaxies in the reference are misclassified as high-density in the VIPERS-like mocks, and a similar percentage of HD galaxies become LD interlopers.

4.2 Mass function in the VIPERS environments

I compute the stellar mass functions with respect to the two environments presented in Sect. 4.1.3, within the three redshift bins adopted there: $0.51 < z \leqslant 0.65$, $0.65 < z \leqslant 0.8$, $0.8 < z \leqslant 0.9$. As in Chapter 3, different estimators are used, in particular the $1/V_{\max}$ and STY methods. The SWML method is used here only to verify the reliability of the other estimators, and it is not shown in the plots. The details about the $1/V_{\max}$, STY, and SWML methods have already been included in Sect. 3.1, together with the discussion about the completeness limits in stellar mass (see Table 3.1). Both in LD and HD, I consider not only the whole galaxy sample, but also the passive and active classes (see Sect. 3.3.1) individually. Moreover, I compare our results with the literature highlighting how VIPERS adds new evidence to more uncertain results found by previous surveys.

4.2.1   GSMF normalisation

When estimating the GSMFs, I consider the effective area of the whole survey ($\sim 10.31\,\mathrm{deg}^2$) to compute comoving volumes. In this case such a normalisation has to be corrected, because the LD and HD regions do not occupy the total volume of VIPERS, but only part of it. The correction is done by performing the Voronoi decomposition (e.g. Marinoni et al. 2002, and references therein) on our spectroscopic sample. This procedure (performed in Cucciati et al., in prep.) allows us to rescale the stellar mass functions of each environment after estimating the fraction of survey volume that the LD and HD represent respectively.

Around a chosen galaxy, a Voronoi polyhedron is unambiguously defined as the set of points closer to that object than to any other. The decomposition is potentially affected by missing objects, which would have modified the polyhedra faces. We account for that by assigning to each Voronoi cell a weighting factor, based on the sampling rate of the spectroscopic quadrant in which the related galaxy lies (quadrant sampling rates are evaluated in de la Torre et al. 2013). Moreover, we fill gaps and missing quadrants cloning spectroscopic objects from the nearby quadrants (this method is detailed in Cucciati et al. 2014). Once realised such a partition of the VIPERS space, we add together the polyhedra of LD or HD galaxies to estimate the volume of the two environments.

According to the Voronoi 3-dimensional decomposition, HD regions occupy $\sim 8\%$ of the total survey volume, while LD regions are the $\sim 50\%$. Figure 4.3 is an example of the resulting Voronoi decomposition in a portion of the W1 field. In this Figure it is possible to see the elongated shapes of the HD regions, which recover nodes and filaments of the cosmic structure. On the other hand, the LD environment is composed by roundish regions that can be compared with the voids found by Micheletti et al. (2014).
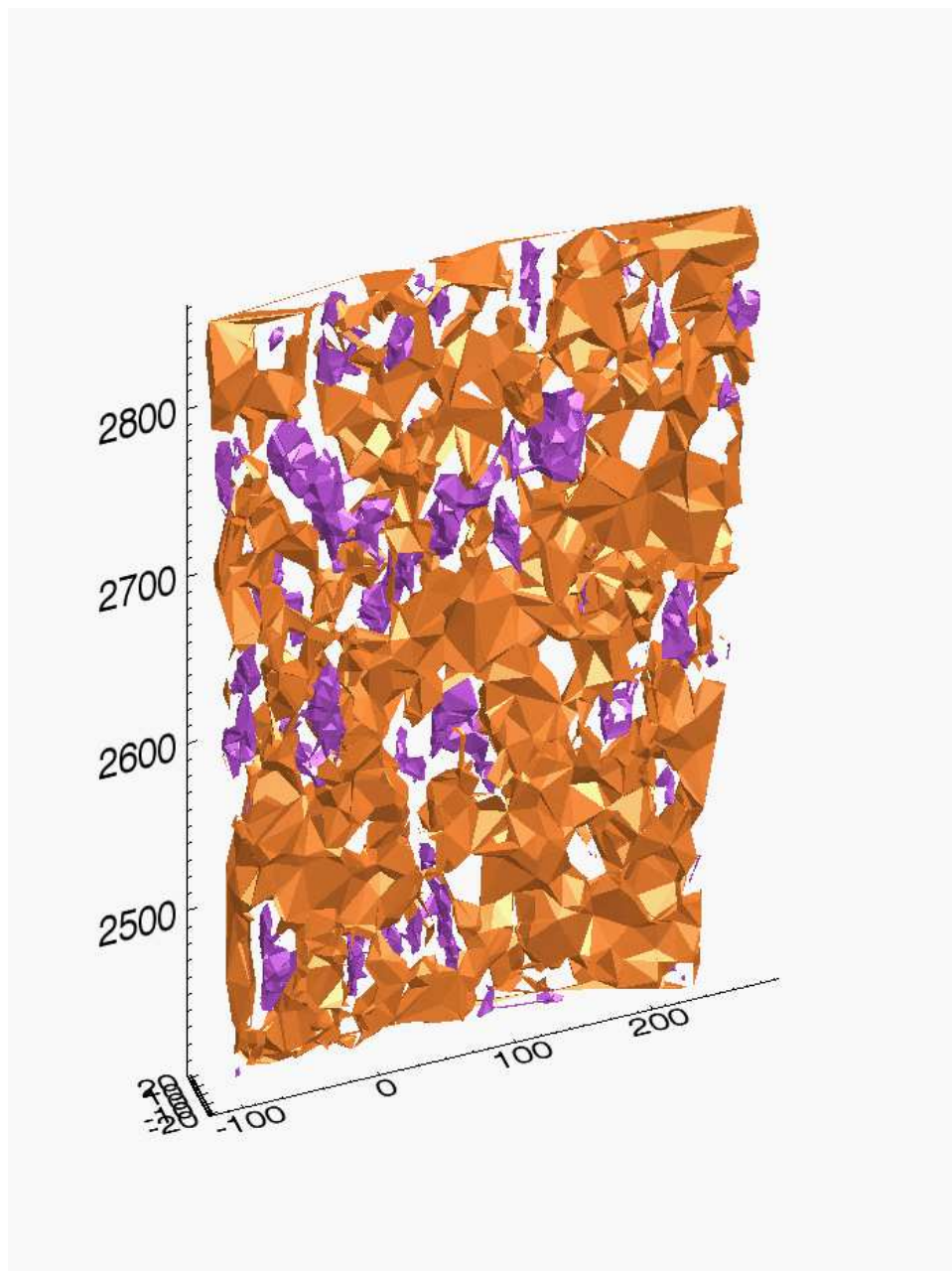
Figure 4.3 Voronoi decomposition in a portion of the VIPERS volume (W1 field, redshift $0.65 < z < 0.8$). The Voronoi cells around LD (HD) galaxies are orange (violet) polyhedra. Added together, they provide us with an estimate of the effective volume occupied by each environment. Units on x and y axes are in comoving Mpc, arbitrary centred. On the z axis the redshift range is converted in comoving Mpc. Courtesy of Olga Cucciati.
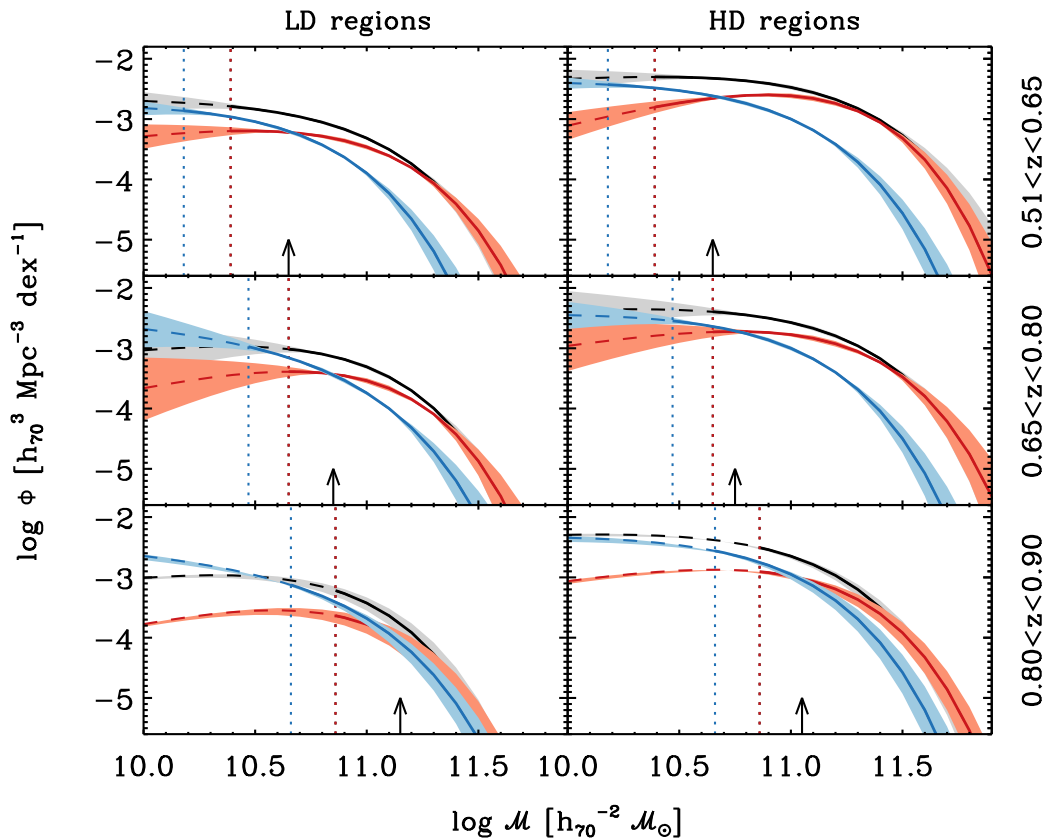
Figure 4.4   Stellar mass functions of the total, active, and passive samples (black, blue, and red lines respectively) in the lowest/highest densities (left/right column) of VIPERS. The GSMFs (solid lines) are estimated through the STY method, with a shaded area representing the 68% CL of this maximum likelihood technique. The line is dashed below the limiting mass, which is indicated by a vertical dotted line (total and passive samples have the same limit). The normalisation of each GSMF has been done accounting for the fraction of the survey volume occupied by each environment (see details in the text). In each panel, a black arrow indicates $\mathcal{M}_{cross}$, i.e. the stellar mass value at which active and passive mass function overlap each other.
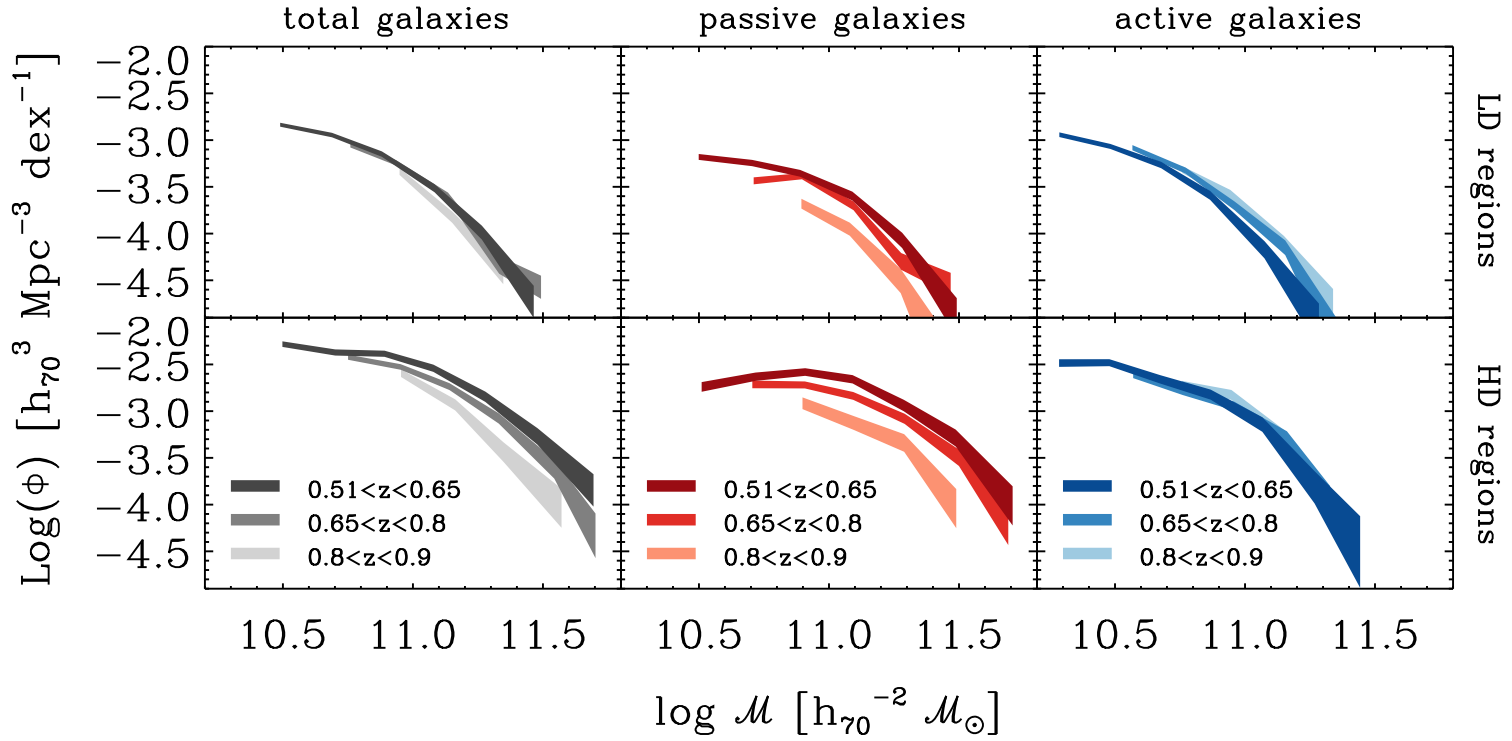
Figure 4.5 Evolution of the GSMF in the different VIPERS environments (total, passive, and active samples in black, red, and blue colours respectively). Each shaded area is obtained from the $1/V_{max}$ estimates with their Poissonian uncertainty (only points above the stellar mass completeness limit are considered).

As expected, after the normalisation, the mass function is higher in the densest regions (larger $\Phi_\star$) since galaxies are more clustered. This is also evident in Fig. 4.4, comparing left- and right-side panels. Quantitatively, this difference in normalisation between LD and HD regions is summarised in Table 4.1, where $\Phi_\star$ values are reported along with α and $\mathcal{M}_\star$ for each GSMF computed by means of the STY method. Thanks to the Voronoi decomposition I can also compare a given GSMF (e.g., the one of active LD galaxies) computed in different z-bins, to see whether its amplitude evolves. Such a comparison is shown in Fig. 4.5. One striking feature of this Figure is the absence of significant evolution (both in shape and normalisation) of the active mass functions, in both the environments. On the other hand, the passive population increases with cosmic time, and so its stellar mass function.

4.2.2 Environmental differences in the VIPERS mass functions

The GSMFs shown in Fig. 4.6 are the same of Fig. 4.4, but in this case, to compare their shapes, I renormalise the GSMFs in such a way that their number density is equal to unity when the GSMF is integrated at $\mathcal{M} > \mathcal{M}_{\mathrm{lim}}$. Each GSMF (total, passive, and active) estimated in the LD environment is plotted together with its equivalent in HD, in the redshift bins $0.51 < z \leqslant 0.65$, $0.65 < z \leqslant 0.8$, and $0.8 < z \leqslant 0.9$.

The results are remarkable especially in the high-mass regime, where VIPERS benefits from the large number statistics. Regarding the total mass functions, there is a significant difference between the LD and HD galaxies at $z \leqslant 0.8$: a large fraction of massive galaxies inhabit the densest regions, resulting in a higher exponential tail of the HD mass function with respect to the LD environment. At higher redshifts this difference becomes less evident. Quantitatively, the difference is well described by the Schechter parameter $\mathcal{M}_\star$, which is larger in the HD regions (see the likelihood contours for α and $\mathcal{M}_\star$ shown in Fig. 4.7, and the evolution of $\mathcal{M}_\star$ for passive galaxies in Fig. 4.8). In the first and second redshift bin, $\Delta \mathcal{M}_\star \equiv \mathcal{M}_{\star,\mathrm{HD}} - \mathcal{M}_{\star,\mathrm{LD}} = 0.24 \pm 0.12$ and 0.27 ± 0.15 dex respectively. A similar deviation appears at $0.8 < z \leqslant 0.9$ ($\Delta \mathcal{M}_\star = 0.21 \pm 0.11$ dex) although in that case the formal $\mathcal{M}_\star$ uncertainty has been reduced by keeping α fixed in the fit.

Looking at the GSMFs divided by galaxy types (Fig. 4.6, central and right-hand panels), it turns out that the behaviour seen for the whole sample is mainly due to the passive population, which also shows an excess of massive objects in the HD environment (see Fig. 4.6). A similar trend is observed also in the active GSMFs at $z \leqslant 0.8$, but we note that if the intermediate galaxies are not included in these GSMFs the difference between HD and LD is reduced (see Sect. 4.3.1).

At intermediate masses, our analysis becomes less stringent. Given the completeness limit of VIPERS, it is difficult to constrain the power-law slope of the GSMF. We find that α_{HD} and α_{LD} are compatible within the errors, with the exception of the passive sample at $0.51 < z \leqslant 0.65$, for which the stellar mass function is steeper in the LD regions.
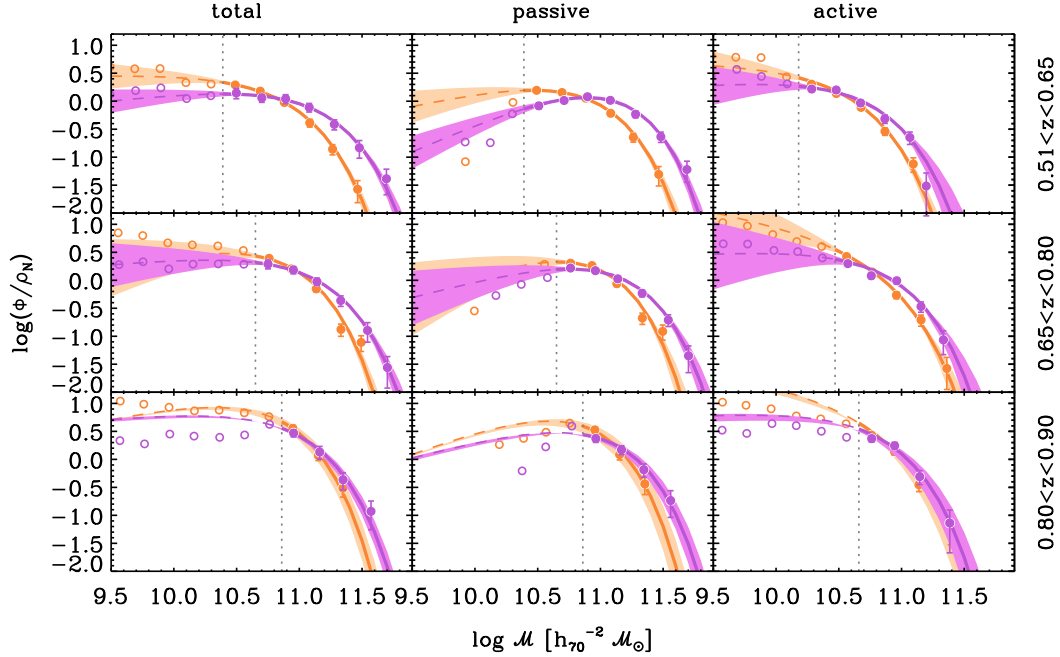
Figure 4.6 Stellar mass functions of galaxies at low density (orange symbols) and high density (violet symbols) in three different redshift bins, namely $0.51 < z \leqslant 0.65$, $0.65 < z \leqslant 0.8$, and $0.8 < z \leqslant 0.9$ (from top to bottom). Left-side panels show the total GSMFs, while central panels refer to passive galaxies. The GSMFs of the active sample in the same z-bins are shown on the right side. In each plot, filled (open) circles represent the $1/V_{max}$ points above (below) the completeness mass $\mathcal{M}_{lim}$ (vertical dot line), with error bars accounting for Poisson uncertainty. In the total GSMFs, also the uncertainty due to cosmic variance is added in the error bars. Solid lines represent the Schechter functions estimated through the STY method, with the 1σ uncertainty highlighted by a shaded area. With this estimator all the Schechter parameters are free, except at $0.8 < z \leqslant 0.9$, where α is fixed to the value found in the previous z-bin (see Table 4.1). To compare the shape of mass functions in LD and HD, we renormalise them in such a way that their number density (ρ_N) is equal to unity when we integrate the GSMF at $\mathcal{M} > \mathcal{M}_{lim}$.
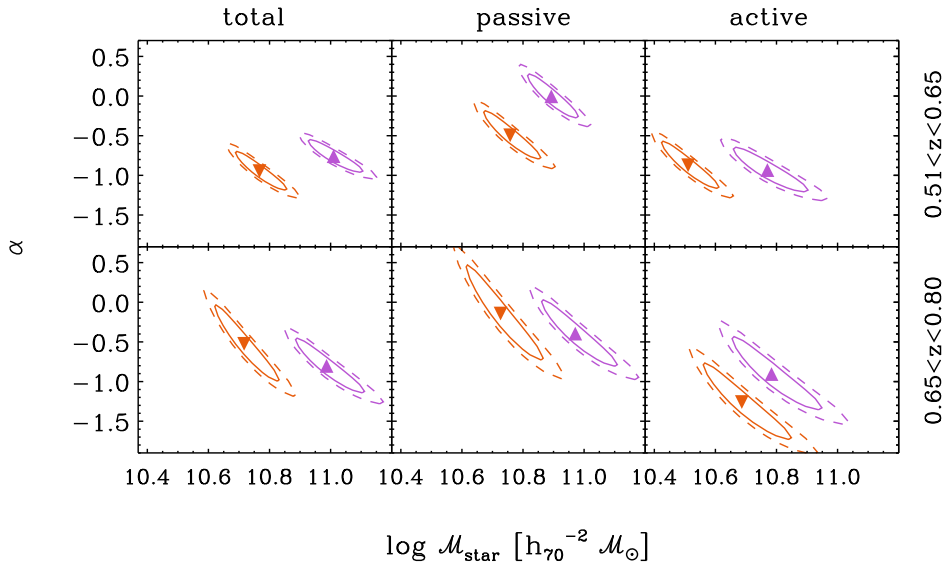
Figure 4.7 Schechter (1976) parameters (filled symbols) of the GSMFs at redhisft $0.51 < z < 0.65$ and $0.65 < z < 0.8$ (upper and lower rows, respectively). These are the bins where, during the STY fitting, α was let free (cf Fig. 4.6). The solid- and dashed-line contours represent the 68.3 and 90% CL respectively. Orange lines and downward triangles are the estimates for galaxies in the LD regions, violet lines and upward triangles are used for the HD ones. Each panel concerns a different sample (total, passive, and active galaxies from left to right). All the values are obtained by using the Algorithm for Luminosity Function (ALF), the code devised by Ilbert et al. (2005).
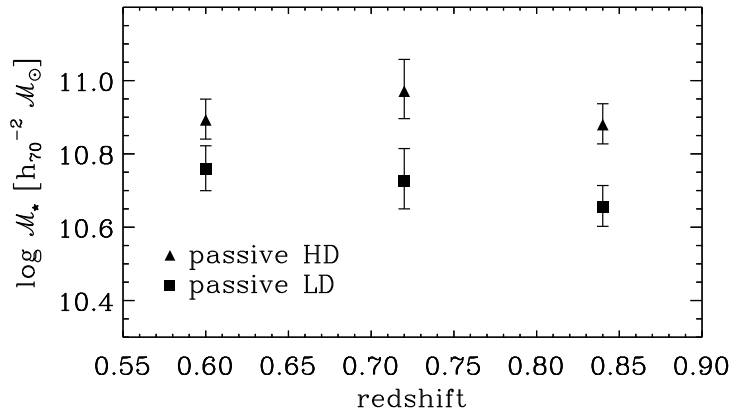

Figure 4.8 Values of the Schechter $\mathcal{M}_\star$ parameter for the passive mass functions of VIPERS in three redshift bins. For the GSMF in the HD regions, $\mathcal{M}_\star$ is represented by triangles, while squares correspond to the GSMFs in the LD regions. Error bars are the 1σ likelihood, as estimated with the STY method.

Table 4.1 GSMF in low- and high-density regions: Schechter parameters resulting from the STY method, when applied to different galaxy populations at different redshifts. Before fitting data at $0.8 < z < 0.9$, α has been fixed to the value of the previous z-bin.

galaxy sample	α	$\log \mathcal{M}_\star$	$\Phi_\star$	α	$\log \mathcal{M}_\star$	$\Phi_\star$
		$[h_{70}^{-2}\,\mathcal{M}_\odot]$	$[10^{-3}\,h_{70}^3\,\mathrm{Mpc}^{-3}]$		$[h_{70}^{-2}\,\mathcal{M}_\odot]$	$[10^{-3}\,h_{70}^3\,\mathrm{Mpc}^{-3}]$
$0.51 < z < 0.65$		low density			high density	
total	$-0.95^{+0.16}_{-0.16}$	$10.77^{+0.06}_{-0.05}$	$1.15^{+0.16}_{-0.17}$	$-0.76^{+0.14}_{-0.13}$	$11.01^{+0.06}_{-0.06}$	$3.98^{+0.51}_{-0.54}$
passive	$-0.49^{+0.20}_{-0.20}$	$10.76^{+0.06}_{-0.06}$	$0.66^{+0.05}_{-0.07}$	$-0.00^{+0.18}_{-0.18}$	$10.89^{+0.06}_{-0.05}$	$3.04^{+0.14}_{-0.14}$
active	$-0.87^{+0.20}_{-0.19}$	$10.51^{+0.06}_{-0.06}$	$1.07^{+0.15}_{-0.17}$	$-0.93^{+0.19}_{-0.18}$	$10.77^{+0.08}_{-0.08}$	$2.34^{+0.48}_{-0.49}$
$0.65 < z < 0.80$		low density			high density	
total	$-0.52^{+0.32}_{-0.31}$	$10.72^{+0.07}_{-0.06}$	$1.08^{+0.07}_{-0.11}$	$-0.80^{+0.23}_{-0.22}$	$10.99^{+0.08}_{-0.07}$	$3.28^{+0.47}_{-0.59}$
passive	$-0.14^{+0.40}_{-0.39}$	$10.73^{+0.09}_{-0.08}$	$0.49^{+0.03}_{-0.04}$	$-0.40^{+0.28}_{-0.27}$	$10.97^{+0.09}_{-0.07}$	$2.07^{+0.16}_{-0.27}$
active	$-1.26^{+0.32}_{-0.31}$	$10.69^{+0.10}_{-0.09}$	$0.75^{+0.20}_{-0.23}$	$-0.91^{+0.31}_{-0.30}$	$10.78^{+0.10}_{-0.09}$	$2.18^{+0.44}_{-0.55}$
$0.80 < z < 0.90$		low density			high density	
total	-0.52	$10.64^{+0.05}_{-0.04}$	$1.12^{+0.07}_{-0.07}$	-0.80	$10.85^{+0.05}_{-0.04}$	$3.89^{+0.28}_{-0.28}$
passive	-0.14	$10.66^{+0.06}_{-0.05}$	$0.34^{+0.03}_{-0.03}$	-0.40	$10.88^{+0.06}_{-0.05}$	$1.49^{+0.15}_{-0.15}$
active	-1.26	$10.70^{+0.07}_{-0.07}$	$0.81^{+0.05}_{-0.05}$	-0.91	$10.75^{+0.07}_{-0.06}$	$2.84^{+0.21}_{-0.21}$

4.2.3   Comparison with previous work

The comparison with other authors is not always straightforward, given the different definitions of environment and galaxy types. A piece of work with a very similar approach is Bolzonella et al. (2010). In that paper, low- and high-density galaxies in the zCOSMOS survey ($0.1 < z < 1.0$) are classified by means of the galaxy density contrast (derived from the 5NN, as in our case). Bolzonella et al. observe a higher fraction of massive galaxies in overdense regions, although within the uncertainties of the GSMF estimates. Down to the redshift range not reached by VIPERS ($0.1 < z < 0.5$) they also find an upturn of the high-density GSMF below $\log \mathcal{M}/\mathcal{M}_\odot \lesssim 10$.

I can directly compare our GSMFs to those of Bolzonella et al. (2010) at least in one redshift bin, which is similar in the two analyses ($0.5 < z < 0.7$ in their paper, $0.51 < z < 0.65$ in this work). I find a good agreement for both passive and active galaxies (see Fig. 4.9). With respect to the latter sample, higher consistency is reached considering only high-sSFR galaxies, i.e. when I remove the NUVrK-intermediate objects. This improvement is probably due to the fact that the high-sSFR subsample is more similar to the late-type galaxies of Bolzonella et al. (2010), which they identify using an empirical set of galaxy templates. Figure 4.9 illustrates the improvement VIPERS represents with respect to zCOSMOS: it is now possible to robustly discriminate the LD and HD mass functions, finding differences that were not statistically significant before.

Bolzonella et al. (2010) detect environmental effects in zCOSMOS when they analyse the evolution with redshift: since $z \simeq 1$, the passive population grows more rapidly inside regions of high density. The authors find this trend by studying the redshift evolution of $\mathcal{M}_{\mathrm{cross}}$, i.e. the value of stellar mass at which the active and passive GSMFs intersect each other. With respect to that, VIPERS is limited by the narrower redshift range, which spans only $\sim 2.3\,\mathrm{Gyr}$ of the history of the universe. Nevertheless, it is worth noticing that in VIPERS, like zCOSMOS, $\mathcal{M}_{\mathrm{cross}}$ depends on environment, i.e. it is slightly lower in the HD regions (Fig. 4.4; see also Peng et al. 2010b; Annunziatella et al. 2014).

Using a slightly different classification, based on the third nearest neighbour, Bundy et al. (2006) seek for environmental effects in the stellar mass function of DEEP2 galaxies, from $z = 0.4$ to 1.4. As in zCOSMOS, also in their analysis a difference between LD and HD mass functions is visible but not significant (Bundy et al. 2006, Fig. 11). Being VIPERS less affected by cosmic variance, it can be exploited to draw more robust conclusions.

Also the evolution of the DEEP2 galaxies shows a (milder) dependence on local environment, although Bundy et al. (2006) quantify it as a secondary driver with respect to stellar mass. In the local Universe, Baldry et al. (2006, SDSS data) observe an increase of $\mathcal{M}_\star$ as a function of the environment (which they estimate as an average between the fourth and fifth nearest neighbour). Their result is in agreement with our findings.

Other studies compare the stellar mass functions of clusters, groups, and isolated (or "field") galaxies. Kovač et al. (2010a), using the 10k zCOSMOS catalogue, confirm the trend noted by Bolzonella et al. (2010): massive galaxies preferentially reside inside groups. On the other hand, Calvi et al. (2013) and Vulcani et al. (2012,
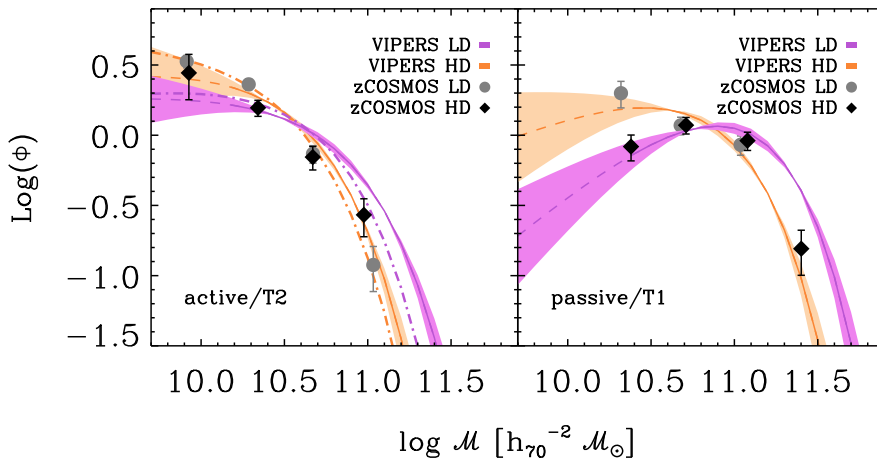
Figure 4.9 VIPERS (this work) and zCOSMOS (Bolzonella et al. 2010) stellar mass functions of galaxies in LD/HD regions (orange/violet and grey/black colours, see the legend in the top-right corner of each panel). The comparison is restricted to a single redshift bin that is similar in the two surveys ($0.5 < z < 0.7$ in zCOSMOS, $0.51 < z < 0.65$ in VIPERS). All the GSMFs are rescaled in order to have $\rho_N(\mathcal{M} > \mathcal{M}_{\rm lim}) = 1$, as in Fig. 4.6. In both panels, solid lines represent the STY estimates for the various galaxy samples, with a shaded area encompassing the 1σ uncertainty (the line is dashed below the stellar mass limit). Filled circles and diamonds are the $1/V_{\rm max}$ determinations of the GSMFs of zCOSMOS (LD and HD respectively). The *left panel* includes the stellar mass functions of star-forming galaxies, classified by Bolzonella et al. (2010) according to their photometric types (T2, i.e. late-type galaxies), and by means of the NUVrK diagram for VIPERS. I also show with dot-dashed lines the stellar mass function of the VIPERS galaxies having high sSFR (i.e., those remaining after removing the NUVrK-intermediate objects from the active sample). In the *right panel*, the VIPERS passive sample and the zCOSMOS early-type galaxies (i.e., T1 spectrophotometric types) are considered.

2013) compare galaxy clusters and general field, without detecting any significant difference in the respective GSMFs. Calvi et al. (2013) study the GSMF in the local universe, contrasting general field and $0.04 < z < 0.07$ galaxy clusters (WINGS survey, Fasano et al. 2006). Vulcani et al. (2012, 2013) extend this field vs clusters comparison up to $z = 0.8$ using respectively ICBS and EDisCS catalogues (Dressler et al. 2013; White et al. 2005).

van der Burg et al. (2013) also find similar shapes for active/passive mass functions in both environments, although the total GSMFs differ each other because of the different percentage of passive galaxies in their GCLASS clusters at $0.86 < z < 1.34$ (see Muzzin et al. 2012) with respect to the (UltraVISTA/COSMOS) field (Muzzin et al. 2013).

The lack of environmental dependency in the field/cluster GSMFs can be due to the various (local) environments embraced in the broad definition of "field" (i.e., a sky region without clusters) that can include single galaxy, pairs, and even galaxy groups. Indeed, when Calvi et al. (2013) consider only isolated galaxies, they obtain a stellar mass function that differs from the others. The presence of

structures in the field can thus be crucial in this kind of analysis.

Also the (relatively large-scale) environment represented by a galaxy cluster is composed by regions with different local conditions. For instance we note that in Vulcani et al. (2012) the local galaxy density assumes a wide range of values also in clusters. The issue is discussed also by Annunziatella et al. (2014), who analyse a cluster from the CLASH-VLT survey; they find that the stellar mass function of passive galaxies decreases – as moving towards low masses – more steeply in the core than in the outskirts.

In addition, I emphasise that VIPERS has more statistical power than current cluster surveys at $\mathcal{M} > \mathcal{M}_\star$. For instance, van der Burg et al. (2013) have 12 spectroscopic members in their 10 GCLASS clusters with $11.2 < \log(\mathcal{M}/\mathcal{M}_\odot) < 11.6$, and no detection at higher masses; instead, our HD regions contain a few hundreds (spectroscopic) galaxies above $\log(\mathcal{M}/\mathcal{M}_\odot) = 11.2$.

4.3 Discussion on the environmental effects in VIPERS

The difference between LD and HD in the high-mass tail of the GSMF can be interpreted as a reflection of the dark matter mass segregation. In hierarchical models, massive haloes preferentially populate the densest regions (e.g. Mo & White 1996), and the correlation between halo mass and galaxy stellar mass produces in turn a concentration of massive galaxies in the HD environment (cf Abbas & Sheth 2005, 2006; Scodeggio et al. 2009b; De La Torre et al. 2010). This picture is consistent with the mass segregation observed by van der Burg et al. (2013) in the GCLASS clusters at $z \simeq 1$. They normalise their stellar mass function by estimating the total mass (baryons and dark matter) contained within the virial radius of each cluster. After normalising the GSMF in the UltraVISTA field multiplying its volume by the average matter density of the Universe, they find that the GSMF is higher in clusters than in the field (see van der Burg et al. 2013, Fig. 8).

Galaxy quenching could also play a role in shaping the mass functions, as suggested by the difference between passive GSMFs in the LD and HD environments, which increases going to lower z (see Fig. 4.6). However, the environmental effects of quenching are also connected to dark matter. In fact, the different GSMF shapes can be linked to their "environmental histories": haloes in different environments have not the same formation time and accretion history, even when their final mass is comparable (see De Lucia et al. 2012, and discussion therein). In the present work we apply an alternative approach, to describe the GSMF evolution in different environments as a function of redshift.

4.3.1 An empirical description

I use VIPERS data to test the empirical description of quenching proposed by Peng et al. (2010b, hereafter P10), which tracks the evolution of galaxies as a function of $\mathcal{M}$, SFR, and environment. I emphasise that in P10 the environment is defined in a way similar to the one described in Sect. 4.1, i.e. using the extreme quartiles of the $1 + \delta$ distribution, with δ derived using the 5NN.

Three observational facts are fundamental in P10:

- the stellar mass function of star-forming galaxies has the same shape at different redshifts (i.e., α and $\mathcal{M}_\star$ are nearly constant, see e.g. Ilbert et al. 2010), with little increase in normalisation moving towards lower redshifts;

- there is a tight relation between SFR and stellar mass for star-forming galaxies (the so-called "main sequence") with SFR $\propto \mathcal{M}^{1+\beta}$ (e.g. Noeske et al. 2007; Elbaz et al. 2007; Daddi et al. 2007);

- average sSFR can be parametrised with respect to stellar mass and redshift/cosmic time (Speagle et al. 2014, and references therein), while it is independent of environment (P10; Muzzin et al. 2012; Wetzel et al. 2012).

In spite of the large consensus in the literature, one should keep in mind that these three findings have been established only recently: new data may be in tension with them, casting doubts on the work of Peng et al..

The keystone of P10 is that the halt of star formation can be due to two fundamental mechanisms, either *mass quenching* or *environment quenching*, which depend respectively on $\mathcal{M}$ and δ. Using data from local Universe (SDSS-DR7 Abazajian et al. 2009) and at $z \sim 1$ (zCOSMOS, Lilly et al. 2007) Peng et al. show that the two effects are fully separable. The authors express both mechanisms analytically; in particular the mass quenching rate is

$$\lambda_m = \frac{\text{SFR}}{\mathcal{M}_\star} = \mu\text{SFR}\,, \tag{4.2}$$

where $\mathcal{M}_\star$, namely the Schechter parameter of the star-forming mass function, is constant. According to observations, they assume $\mathcal{M}_\star \equiv \mu^{-1} \simeq 10^{10.6}\,\mathcal{M}_\odot$. Equation (4.2) can be regarded as the probability of a galaxy to become passive via mass quenching. This analytical form is required by the constraints listed above. The empirical laws of P10 do not shed light on the physical processes responsible for quenching, however they describe its evolutionary characteristics. We will make an extensive use of this formalism in Sect. 4.3.2. In Peng et al. (2012), mass and environment quenching are linked to halo occupation: satellite galaxies are subject to the latter, whereas the former is the quenching channel of central galaxies (see also van den Bosch et al. 2008)

With these simple prescriptions, it is possible to reproduce several statistical properties of galaxies across cosmic time. Regarding the GSMF, one should observe

i same values of α and $\mathcal{M}_\star$ for active GSMFs in the LD and HD regions;[2]

ii in LD, the stellar mass function of passive galaxies should have same $\mathcal{M}_\star$ of the active one, but less negative α (namely, $\alpha_{\text{pass,LD}} - \alpha_{\text{act,LD}} \simeq 1$);

iii comparing passive galaxies in LD and HD regions, the latter should differ from the former because of "post-quenching" effects (i.e. dry merging), with a larger value of $\mathcal{M}_\star$. [3]

---

[2] For sake of simplicity, we use our notation (LD and HD) also when referring to the low-/high-density galaxies of P10, which are named D1 and D4 in the original paper.

[3] P10 fit the passive mass functions with a double Schechter function. Here I refer only to what concerns the primary (most massive) component.

These features are actually observed in the SDSS red/blue mass functions (see P10). The unprecedented precision of the VIPERS estimates can be useful to verify whether they are present also at $z \simeq 0.7$. It is worth noticing that at $z > 0$ the environmental signatures (i)–(iii) have not been confirmed yet: several studies provided contrasting clues (cf Bolzonella et al. 2010; Vulcani et al. 2012; Giodini et al. 2012; van der Burg et al. 2013; Annunziatella et al. 2014), which remark the higher uncertainties affecting non-local surveys.

With respect to the passive GSMFs, the STY method applied to VIPERS data yields a larger $\mathcal{M}_\star$ parameter in the region of higher density, as stated in (iii). I find such a trend in all three redshift bins (see Table 4.1). This result advocates the P10 phenomenological representation. This evidence is discussed in Sect. 4.3.2: it can be related to the fact that dry mergers are more likely to happen in the overdense regions.

Turning to the active GSMFs, I verified (i) and (ii) at $z > 0.65$: the shape of the active GSMF is similar in the two VIPERS environments, being both α and $\mathcal{M}_\star$ compatible within the errors. Moreover, $\mathcal{M}_\star^{\mathrm{act,LD}}$ is consistent with $\mathcal{M}_\star^{\mathrm{pass,LD}}$, and the difference $\alpha_{\mathrm{pass,LD}} - \alpha_{\mathrm{act,LD}} = 1.12 \pm 0.72$ is in agreement with the expectations of P10.

On the other hand, the VIPERS estimates at $0.51 < z < 0.65$ pose a few questions about (i) and (ii), because these conditions are not satisfied any longer. I argue that such a discrepancy is due to the GSMF parametrisation of the active sample, which we (and Peng et al.) model with Eq. (3.1). In many studies, introducing a double Schechter function (Eq. 3.2) improves the fit of the active GSMF (e.g. Pozzetti et al. 2010; Baldry et al. 2012; Ilbert et al. 2013). Also in VIPERS, in the lowest z-bin, there is some hint of this characteristic shape. The active mass function shows a dip at $\log(\mathcal{M}/\mathcal{M}_\odot) \simeq 10.2$ and an upturn below that value (see also the mass function of the whole VIPERS field in Sect. 3.2). This fact may be considered as a limitation of P10, since their phenomenological description does not account for these two distinct components. This aspect however is not the only source of bias in the comparison. Another difficulty in testing P10 with VIPERS data is the different galaxy classification adopted in the two studies. In fact, P10 apply a cut in the $(U - V)$ vs $\mathcal{M}$ plane to separate blue and red galaxies. In this way, star-forming galaxies reddened by dust can be misclassified as passive; those objects are active in the NUVrK diagram (see Fig. 4.10).

I did not fit Eq. (3.2) to the active sample at $0.51 < z < 0.8$, because for this task we should have included galaxies much below the stellar mass limit. However, we apply the STY estimator again (with Eq. 3.1) starting from $\mathcal{M} > 10^{10} \mathcal{M}$, i.e. only ~ 0.2 lower than $\mathcal{M}_{\mathrm{lim}}^{\mathrm{act}}$.[4] I find that the new GSMF estimates are not at variance with relations (i) and (ii). Both α and $\mathcal{M}_\star$ do not change significantly in different environments, and the difference between $\alpha_{\mathrm{pass,LD}}$ and $\alpha_{\mathrm{act,LD}}$ is now closer to unity (0.75 ± 0.32).

To summarise, I find supporting evidence to P10, especially for the passive population, but also some divergence when we test their "empirical predictions" with the GSMF of the VIPERS active sample at $z \simeq 0.6$. In agreement with

---

[4] Despite this small shift, the GSMF low-mass end should be considered as a lower boundary, since we extend the computation to a mass range that is potentially incomplete.
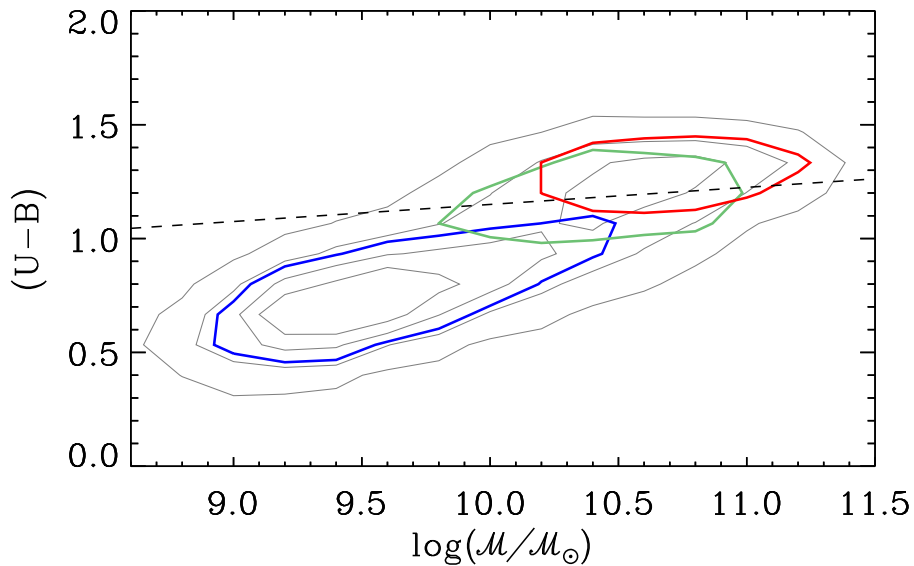
Figure 4.10 The $(U - B)$ vs $\log(\mathcal{M}/\mathcal{M}_\odot)$ diagram used by Peng et al. (2010b) to classify blue and red galaxies (which lie below and above the dashed line respectively). In this Figure, the diagram is populated with the VIPERS galaxies between $z = 0.5$ and 0.7 (grey density contours). Since the Peng et al. cut (i.e., the dashed line) is calibrated with COSMOS data, it may not be fully appropriate for the VIPERS sample because of possible systematics in the colour estimates (e.g., different shapes of U and B filters used in the two surveys). Nevertheless, our high-sSFR galaxies (classified with the NUVrK diagram) are correctly identified as blue, and most of the passive ones are above the threshold, as expected (see blue and red contour, enclosing 68% of each galaxy population). On the other hand, the NUVrK-intermediate galaxies (i.e., those with low-sSFR) are in between, with a significant fraction lying in the red sequence *locus* (see green contour).

P10, the stellar mass function of the VIPERS passive galaxies shows a mild (but significant) dependence on the environment, with values of $\mathcal{M}_\star$ slightly larger in the HD regions. When considering the active sample at $z > 0.65$ the shape of the active mass function does not depend significantly on the environment, as stated in P10. Moreover, the results are consistent with the relation $\alpha_{\mathrm{pass}} = \alpha_{\mathrm{act}} + 1$, which is a consequence of the build-up of the passive mass function by means of mass quenching (see P10 for more details). At $z < 0.65$, however, the shape of the active mass function does not agree with the expectations of P10. I observe that the P10 framework requires the active GSMF, which should be the sum of two Schechter functions, to be fitted with only one. Thus, the disagreement could be partly due to a not optimal choice of the GSMF parametrisation.

4.3.2   Evolution in different environments

I investigate more in detail the GSMF evolution of the VIPERS passive population with an approach similar to P10. In that study, the authors generate a galaxy sample at $z = 10$, and evolve it down to $z = 0$ by applying their quenching recipe: at any epoch, a fraction of blue galaxies become passive, according to the environment and mass quenching rates (see Sect. 4.3.1). The GSMFs that result at $z = 0$ are in very good agreement with the SDSS mass functions, both in LD and HD regions. I perform a similar task in the VIPERS redshift range. I start in a given z-bin with the observed passive mass function and evolve it to a lower redshift, then comparing such "predicted" GSMF with data.

The simple simulation of P10 shows also that environmental quenching is more effective at $\log(\mathcal{M}/\mathcal{M}_\odot) < 10.5$, whereas mass quenching is dominant in the VIPERS stellar mass range (see Fig. 4.11). This is a consequence of the different quenching rates that characterise the two mechanisms (see also Peng et al. 2012). Therefore, in a first approximation, the fraction of VIPERS active galaxies that migrate into the passive GSMF will be proportional only to λ_{m}. In addition to this, P10 regard galaxy mergers as a secondary (but not negligible) driver of the GSMF evolution at $z > 0.5$. In the following, I will first consider the effect of mass quenching only. Then I will introduce dry merging and eventually (wet) mergers between active galaxies. Proceeding in this way, I aim at highlighting the role of each ingredient of the model.

To apply Eq. (4.2), one has to assume a functional form for the specific SFR, i.e.

$$\mathrm{sSFR}(t, \mathcal{M}) = 2.5 \left(\frac{\mathcal{M}}{10^{10}\,\mathcal{M}_\odot} \right)^{\beta} \left(\frac{t}{3.5\,\mathrm{Gyr}} \right)^{-2.2} . \qquad (4.3)$$

In a given bin centred at $\mathcal{M}_{\mathrm{b}}$, the evolution of the passive GSMF from z_1 to $z_2 < z_1$ is

$$\begin{aligned}
\Phi_{\mathrm{pass}}(z_2) &= \Phi_{\mathrm{pass}}(z_1) + \int_{t(z_1)}^{t(z_2)} \Phi_{\mathrm{act}}(z)\lambda_{\mathrm{m}}\,\mathrm{d}t \\
&= \Phi_{\mathrm{pass}}(z_1) + \tilde{\Phi}_{\mathrm{act}}\,\mu \int_{z_1}^{z_2} \mathcal{M}_{\mathrm{b}}\,\mathrm{sSFR}(z, \mathcal{M}_{\mathrm{b}})\,\mathrm{d}z ,
\end{aligned} \qquad (4.4)$$

where the GSMF of the active sample is assumed to be constant between z_1 and z_2, regardless of the environment in which it is computed. This assumption is
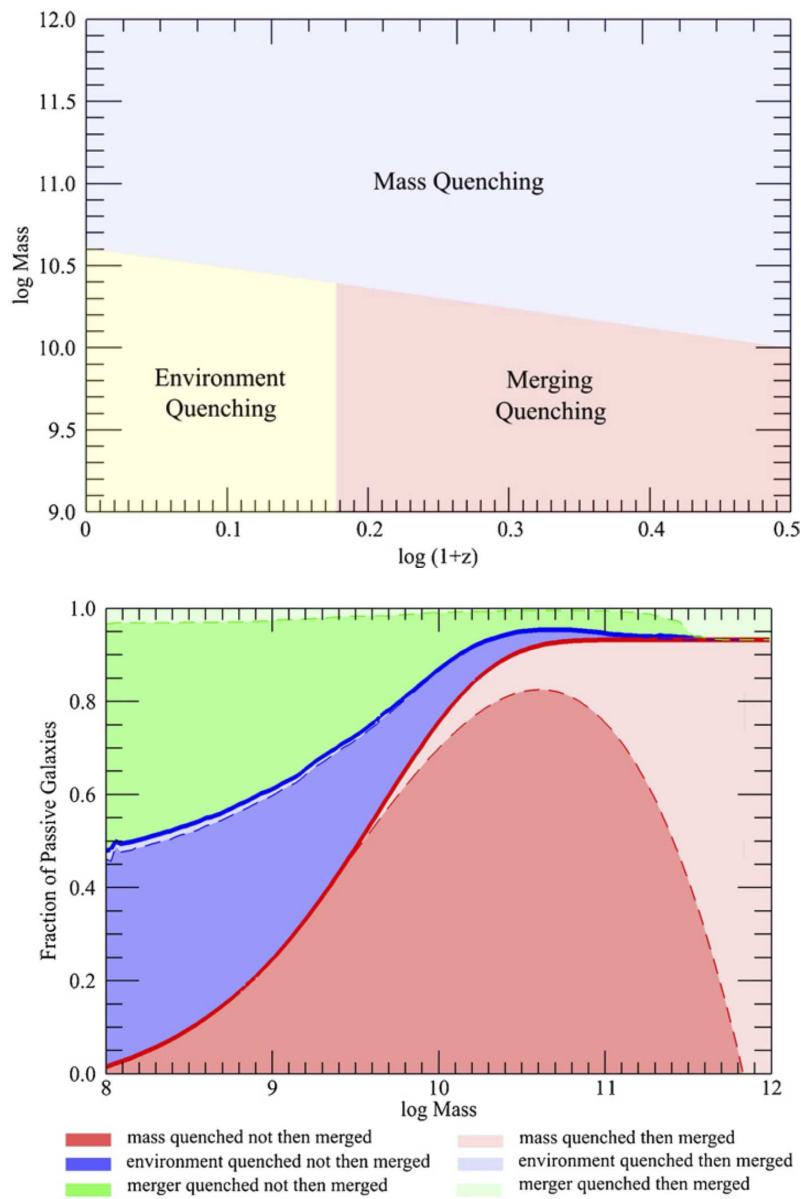
Figure 4.11 Plots from Peng et al. (2010b) with the findings resulting from the evolution of a mock galaxy catalogue according to their empirical prescriptions. *Upper panel:* schematic representation of the dominant quenching mechanism at different redshifts and stellar masses. *Lower panel:* fraction of galaxies in the simulated sample that become passive because of environment quenching (blue shaded area), mass quenching (red), or merging (green). The colour of these three classes are lighter for the fraction of objects that, after halting their star formation, undergo a (post-quenching) merger.
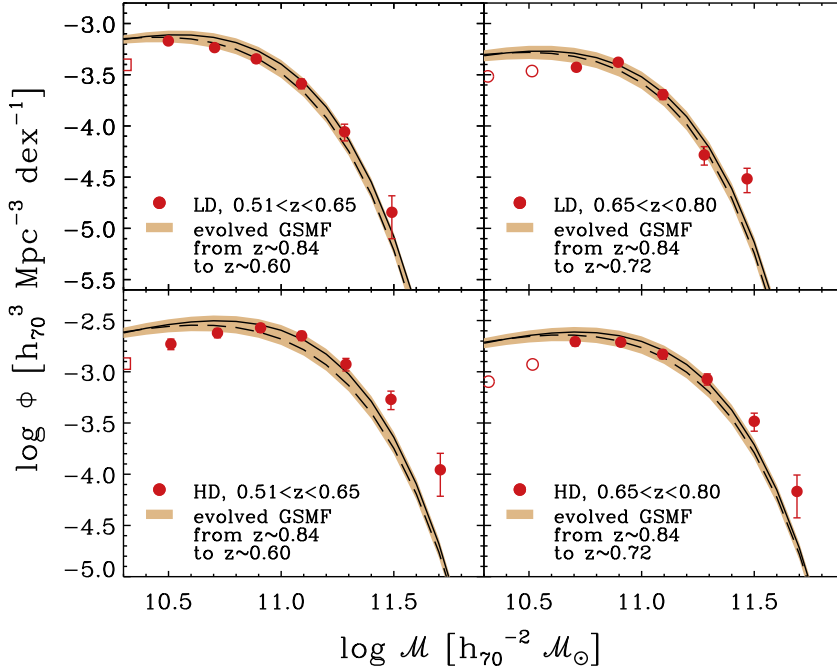
Figure 4.12 Comparison between the GSMFs constructed with the P10 recipe and the VIPERS data. In each panel, red filled circles are the $1/V_{\mathrm{max}}$ points (with Poissonian errors) of the VIPERS passive mass function, in the redshift bin and environment indicated in the legend; lines and shaded area represent the evolution of the GSMF observed at $0.8 < z < 0.9$, down to the same redshift of the plotted data points. Applying the quenching description of P10, I obtain two different estimates when using either Eq. (4.3) or Eq. (4.5), the latter being the original sSFR parametrisation of P10 (solid line) and the former the equation provided in Speagle et al. (2014, dashed line); a further error is introduced to account for the uncertainties in the integration (see Eq. 4.2), giving the final width of the shaded area.

supported by our data (see Fig. 4.5). The constant $\tilde{\Phi}_{\mathrm{act}}$ is determined by averaging the Φ_{act} estimates at z_1 and z_2.

First, I apply Eq. (4.4) using the estimates derived in the LD environment. I use data at $0.8 < z < 0.9$ (median redshift $\tilde{z} = 0.84$) and I evolve them down to $\tilde{z} = 0.72$ and $\tilde{z} = 0.6$. The resulting passive GSMFs, built under the action of mass quenching only, are in good agreement with those observed in the corresponding redshift bins (see Fig. 4.12, upper panels). I repeat the procedure starting from $0.65 < z < 0.8$ and obtain a good agreement with the passive GSMF at $0.51 < z < 0.65$ (this comparison is not shown in the Figure). The major uncertainty in this technique is related to sSFR$(z, \mathcal{M})$. To quantify the impact of different parametrisations, I also use, instead of the equation provided in P10, the "concordance function" obtained by Speagle et al. (2014) fitting data of 25 studies from the literature:

$$\mathrm{sSFR}(t, \mathcal{M}) = \mathcal{M}^{-(0.16+0.026t)}\, 10^{-(6.51-0.11t)} \ . \tag{4.5}$$

I also estimate the uncertainty of $\tilde{\Phi}_{\mathrm{act}}$ by replacing it with upper and lower values of $\Phi_{\mathrm{act}}(z_1)$ and $\Phi_{\mathrm{act}}(z_2)$ respectively. It should be noted that the Φ_{act} approx-

imation introduces a much smaller uncertainty with respect to the $\mathrm{sSFR}(z, \mathcal{M})$ parametrisation.

Evolving the galaxies that live in the HD regions, I find that when the model accounts for mass quenching only, it does not well reproduce the GSMF of the VIPERS passive sample (Fig. 4.12, lower panels). In P10, this difference is interpreted as the effect of dry merging: after quenching, galaxies in the higher densities can merge and then modify the shape of the passive GSMF. In particular, they cause an increase of $\mathcal{M}_\star$ (see point iii in Sect. 4.3.1). P10 assume a simple model in which a fraction of the passive population merges with 1:1 mass ratio. Similar prescriptions are used also in the "backward evolutionary models" of Boissier et al. (2010), an analytical approach not very different from P10. Both P10 and Boissier et al. (2010) highlight that dry (major) mergers are expected to enhance the exponential tail of the passive GSMF, causing the increase of $\mathcal{M}_\star$ with respect to its value in the LD environment. They also consider minor mergers fully negligible in the GSMF evolution, at least at $\mathcal{M} \geqslant 10^{10}\,\mathcal{M}_\odot$, because the stellar mass accreted through these processes is small compared to the mass of the host galaxy (cf López-Sanjuan et al. 2011; Ferreras et al. 2014).

I introduce dry mergers in the evolution of $\Phi_{\mathrm{pass,HD}}$, assuming that two objects with nearly equal mass can merge together without triggering new episodes of star formation. Despite its simplicity, such a model (the same of P10 and Boissier et al. 2010) is sufficient for our qualitative analysis. I set the fraction of galaxies undergoing a 1:1 merger to be equal to $f_{\mathrm{dry}}(z)$, with no dependence on the stellar mass of the initial pair. This is a reasonable approximation, considering that in general the merger fraction (f_{m}) is weakly dependent on $\mathcal{M}$:

$$f_{\mathrm{m}} \propto \left(\frac{\mathcal{M}}{10^{10.7}\mathcal{M}_\odot} \right)^{0.3} , \qquad (4.6)$$

according to the cosmological N-body simulations of Kitzbichler & White (2008). That implies that there is less than 50% variation across the stellar mass range of the VIPERS passive sample. Moreover, for sake of simplicity, I do not discriminate among different orbits and inclination of the companion with respect to the host galaxy.

The value of $f_{\mathrm{dry}}(z)$ can be derived from the major-merger rate (R_{m}) as estimated in observational studies. For example, Man et al. (2014) determine R_{m} for (star-forming and passive) galaxies with $\log(\mathcal{M}/\mathcal{M}_\odot) > 10.8$, in the UltraVISTA/COSMOS field. In that study, the projected separation of galaxy pairs is $14.3\,h_{70}^{-1}\,\mathrm{kpc} < r_{\mathrm{proj}} < 42.9\,h_{70}^{-1}\,\mathrm{kpc}$ (i.e., 10–30 kpc with $H_0 = 100\,\mathrm{km\,s^{-2}Mpc^{-1}}$) but the authors checked for consistency with estimates obtained using other selection boundaries (e.g., $5\,\mathrm{kpc} < r_{\mathrm{proj}} < 20\,\mathrm{kpc}$ with $H_0 = 100\,\mathrm{km\,s^{-2}Mpc^{-1}}$). They find

$$R_{\mathrm{m}}(z) = (0.06 \pm 0.02)(1 + z)^{0.41 \pm 0.33}\,\mathrm{Gyr^{-1}} , \qquad (4.7)$$

for mergers having 1:1 to 1:4 stellar mass ratio.[5] Man et al. (2014) emphasise that at $z > 2$ their selection in mass is biased against wet (i.e., star forming)

---

[5] It should be emphasised that Man et al. analysis, being performed on the COSMOS field, can be compared to many other studies (e.g. de Ravel et al. 2011; Xu et al. 2012; López-Sanjuan et al. 2012), with which it shows fairly good agreement. In particular P10, to account for

mergers, because in that case the satellite galaxy has smaller $\mathcal{M}/L$ and thus lower probability to lie above the stellar mass cut with respect to passive ones (see also discussion in Sect. 3.1.3). In other words, Eq. (4.7) should be regarded (at least at $z > 2$) as an underestimate, but it is more suitable to study dry mergers. Interestingly enough, the merger rates inferred by Man et al. using the stellar mass ratio selection are consistent with those of gas-poor galaxies in the SAM simulation of Hopkins et al. (2010a). When the authors replace that selection with the one based on the H-band flux ratio, their estimates agree with the gas-rich merger rate of the same simulation. This systematics is visible, although within the uncertainties, also at $z < 2$. For instance, by considering flux-ratio selected pairs, the major-merger fraction increases from 10 to about 14%.

By integrating Eq. (4.7), one can estimate the number of mergers that a galaxy undergoes between $t = t(z_1)$ and $t(z_2)$, i.e.

$$N_{\mathrm{dry}} = \int_{t_1}^{t_2} R_{\mathrm{dry}}(z(t)) \, \mathrm{d}t = \int_{t(z_1)}^{t(z_2)} \frac{R_{\mathrm{dry}}(z)t_H}{(1+z)E(z)} \, \mathrm{d}z \, , \qquad (4.8)$$

where t_H is the Hubble time ($t_H \equiv H_0^{-1}$), and $E(z) \equiv H(z)/H_0 = [\Omega_m(1+z)^3 + \Omega_\Lambda]^{1/2}$ (e.g. Dodelson 2003). I remind that $R_{\mathrm{dry}}(z)$ has been defined for galaxies above $\log(\mathcal{M}/\mathcal{M}_\odot) > 10.8$ that collide with a companion having at least one fourth of its stellar mass. Applying Eq. (4.8), I estimate the probability of the VIPERS galaxies to merge: from $z \simeq 0.84$ to 0.72 a galaxy experiences on average $0.05^{+0.03}_{-0.02}$ mergers, while from $z \simeq 0.84$ to 0.6 $N_{\mathrm{dry}} = 0.10^{+0.06}_{-0.04}$ (these translate in merger fractions of about 5 and 10%, respectively). Moreover, one should expect R_{dry} being a function of the environment, with the majority of mergers occurring where galaxies are more clustered. In fact, the merger fraction can be $\sim$2–3 time higher in HD than in LD environments (Kampczyk et al. 2013; see also Lin et al. 2010; Lotz et al. 2013). For this reason I test a range of value of f_{dry}: from 0.05 to 0.15 in the evolution from $z \simeq 0.84$ to 0.72 ($\sim$0.7 Gyr) and 0.1–0.3 across $\sim$1.4 Gyr (i.e., from $z \simeq 0.84$ to 0.6). Dry mergers modifies the "predicted" passive mass function towards a better agreement with observations (Fig. 4.13). Higher f_{dry} values reconcile even more the low-mass tail, but such an amount of mergers is unlikely.

It could be argued that this scenario is plausible under the assumption that the merging timescale (τ_{dry}) is shorter than the time elapsing from one z-bin and the other. Otherwise, the galaxies interacting at $z \simeq 0.84$ will not coalesce in a more massive galaxy before $z = 0.5$, as assumed above. Given the complexity of the process (see Hopkins et al. 2010a, for a review) τ_{dry} can be determined at best to a factor $\sim$2 accuracy (Hopkins et al. 2010b). I take as a reference Xu et al. (2012), who combine results from different suites of simulations (Kitzbichler & White 2008; Lotz et al. 2013) focusing on close encounters of massive galaxies. They find

$$\tau_{\mathrm{dry}} = 0.3 \, \mathrm{Gyr} \times \left(\frac{\mathcal{M}}{10^{10.7}\mathcal{M}} \right)^{-0.3} \left(1 + \frac{z}{8} \right) \, , \qquad (4.9)$$

mergers, use the rate derived by de Ravel et al. (2011) for the zCOSMOS galaxies, which is equal to $0.027(1+z)^{1.2} \, \mathrm{Gyr}^{-1}$. Their function is consistent with Eq. (4.7). Another advantage of the COSMOS field is that an accurate estimate of the cosmic variance is available in López-Sanjuan et al. (2014); in that study, $\sigma_{\mathrm{cv}} = 0.17$ for massive galaxies, and $\sigma_{\mathrm{cv}} = 0.07$ for $\log(\mathcal{M}/\mathcal{M}_\odot) > 10$ (the uncertainty σ_{cv} has been defined in Eq. 3.25).
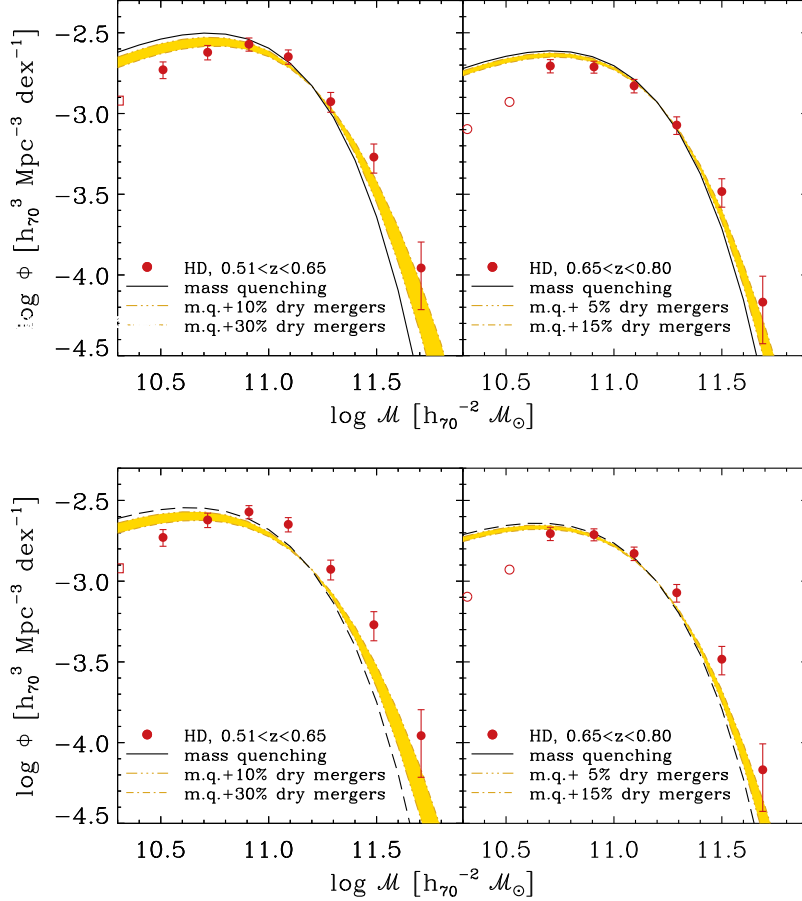
Figure 4.13 Evolution of the passive mass function in the HD environment, including dry mergers. *Upper panels:* solid line is the predicted GSMF in the HD environment, as in Fig. 4.12, assuming mass quenching only and the sSFR parametrization of P10; yellow shaded area is the GSMF modified by dry mergers, whose percentage ranges from 5–10% (triple-dot-dashed line) to 15–30% (dot-dashed line) depending on the redshift bin. In each z-bin, red circles are the $1/V_{\mathrm{max}}$ estimate (with Poissonian error) of the stellar mass function of the VIPERS passive galaxies (symbols are filled above the completeness limit $\mathcal{M}_{\mathrm{lim}}^{\mathrm{pass}}$). *Lower panels:* dashed line is the predicted GSMF in the HD environment, as in Fig. 4.12, assuming mass quenching only and the sSFR parametrization of Speagle et al. (2014). This mass function is then modified by dry mergers and compared with the observed mass function (codified with the same symbols of the upper panel).
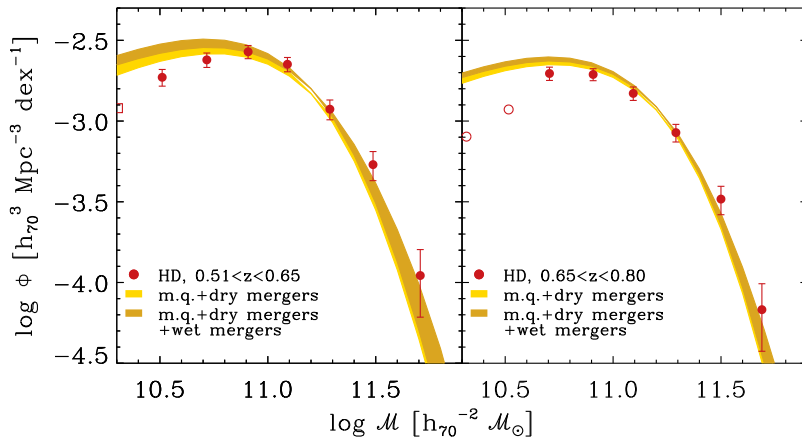
Figure 4.14 Comparison between the GSMFs constructed with the full P10 recipe (mass quenching, dry and wet mergers) and the passive mass function of VIPERS in the HD regions. In each panel, the yellow shaded area represents, as in Fig. 4.13, the predicted GSMF obtained by assuming a certain percentage of dry mergers. The brown shaded area encompasses the same variety of mass function, but including also wet mergers (see text). Red circles represent the observed GSMF estimated by means of the $1/V_{max}$ technique (symbols are filled above $\mathcal{M}_{lim}^{pass}$).

for galaxy pairs with stellar mass ratio $\leqslant 3$ and separation $7.1\,h^{-1}\,\mathrm{kpc} < r_{proj} < 28.6,\,h^{-1}\,\mathrm{kpc}$ (i.e., between 5 and 20 kpc assuming $H_0 = 100\,\mathrm{km\,s^{-2}Mpc^{-1}}$). In the VIPERS redshift range, Eq. (4.9) leads to a major-merger timescale of $\tau_{dry} \simeq 0.3\,\mathrm{Gyr}$ for galaxies with $\mathcal{M} \simeq \mathcal{M}_\star$ (see also timescales used in Keenan et al. 2014, and references therein). Moreover, galaxies may have started their interaction at $z \gtrsim 0.9$ and terminate the merging phase at $0.51 < z < 0.8$ without changing dramatically the picture, because the merger rate does not vary much between z=1.5 and 0.5 (e.g. Xu et al. 2012; Keenan et al. 2014; Man et al. 2014).

Then, I introduce the third element of the model, i.e. major mergers between active galaxies. Even though the result of these (wet) mergers is the cessation of the star formation, P10 keep them distinct from the environment quenching, which is a mechanism related to the transition of a galaxy in a denser region (thus, possibly related to gas stripping, strangulation, and other physical processes happening during accretion into a more massive halo). For sake of simplicity, I assume $R_{wet} = R_{dry}$. Given the different mass range of the active sample, (i.e., much less objects above $10^{11}\,\mathcal{M}_\odot$ than the passive sample) wet mergers do not change the exponential tail of the passive mass function. At lower masses they produce an increase of Φ_{pass} of $\lesssim 0.1\,\mathrm{dex}$ (Fig. 4.14). Thus, wet mergers do not affect significantly the results described above.

I caution that this analysis is based on simplified assumptions (e.g., mergers with 1:1 mass ratio only) to describe qualitatively the GSMF evolution in the overdense regions of VIPERS. A more detailed study, e.g. with an estimate of R_{dry} based on the VIPERS galaxy pairs, is beyond the goal of the present work. Moreover, alternative models can explain the observed trends. Among them, the interpretation proposed by Knobel et al. (2014) is especially intriguing, because the authors go beyond the widespread used central/satellite classification (which

is tightly connected to the dichotomy of mass and environment quenching, see Peng et al. 2012). They suggest a "group quenching" mechanism, environmentally driven, that strongly affects also galaxies at $\log(\mathcal{M}/\mathcal{M}_\odot) > 10.5$, both satellite and central ones. In this context, mass and environment quenching should be considered as two manifestations linked to the same underlying process (see discussion in Knobel et al. 2014; Carollo et al. 2014). Nevertheless, even though its physical origin is still unclear, the observational evidence detailed in this Section is outstanding: the rate at which galaxies in the LD regions become passive is consistent with an internal quenching mechanisms $\propto \mathrm{SFR}/\mathcal{M}_\star$, while in the HD regions this "mass quenching" is not enough. Environmental effects (galaxy mergers and/or other environment-dependent mechanism) are required to explain the shape and the normalisation of the GSMF where the galaxy density contrast is high.

Chapter 5

Conclusions

In this work, I measured the stellar mass function of galaxies between $z = 0.5$ and $z = 1.3$ using the first data release of VIPERS, i.e. a catalogue of more than 50 000 spectroscopic galaxy redshifts. The galaxy stellar masses were estimated through the SED fitting technique, relying on a large photometric baseline and, in particular, on a nearly full coverage of the two VIPERS fields with near-infrared data. I performed several tests to verify that the systematics intrinsic to the method of SED fitting (e.g. the parametrisation of the SFH) do not introduce any significant bias into the analysis. The large volume probed by VIPERS results in extremely high statistics, dramatically reducing the uncertainties due to Poisson noise and sample variance. I estimated the latter by using 57 galaxy mock catalogues based on the MultiDark simulation (Prada et al. 2012) and the stellar-to-halo mass relation of Moster et al. (2013). Each mock catalogue closely reproduce the characteristics of the VIPERS survey. I empirically determined a completeness threshold $\mathcal{M}_{\mathrm{lim}}$ above which the mass function can be considered complete. This limiting mass evolves as a function of z, ranging from $\log(\mathcal{M}/\mathcal{M}_\odot) = 9.8$ to 11 in the redshift interval 0.5–1.1. I focused on the high-mass end of the GSMF, where VIPERS detects a particularly high number of rare massive galaxies. The main results I obtain follow.

- VIPERS data tightly constrain the exponential tail of the Schechter function, which does not show significant evolution at high masses below $z = 1.1$. The same result is provided by analysis of the co-moving number density ρ_N, calculated in different bins of stellar mass. At $z \simeq 1.2$ most of the massive galaxies with $\log(\mathcal{M}/\mathcal{M}_\odot) \geqslant 11.4$ are already in place, whereas below $\log(\mathcal{M}/\mathcal{M}_\odot) = 11.4$, the galaxy number density increases by a factor of ~ 3.5 from $z \simeq 1.2$ to $z \simeq 0.6$.

- The observed GSMFs are compared with those derived from semi-analytical models (De Lucia & Blaizot 2007; Bower et al. 2006; Guo et al. 2011). While the discrepancy at low masses between models and observations is well established and has been exhaustively discussed in literature, predictions at the high-mass end of the GSMF have not yet been verified with sufficient precision. I show that the high accuracy of the VIPERS mass functions makes them suitable for this kind of test, although further improvement to reduce stellar mass uncertainties would be beneficial. From a first analysis,

the VIPERS data appear to be consistent with the Guo et al. (2011) model at $\log(\mathcal{M}/\mathcal{M}_\odot) \geqslant 11$, once the uncertainties in the stellar mass estimates are taken into account. I show that VIPERS GSMFs can be effectively used to constrain models at multiple redshifts simultaneously, in small steps of Δz. This could shed light on the time scale of the physical mechanisms that determine the evolution at higher masses (for instance, the AGN-feedback efficiency). The stellar mass function of VIPERS is used to calibrate simulations e.g. in Torrey et al. (2014) and Okamoto et al. (2014). It is also used to test model predictions in Benson et al. (in prep.).

- I divided the VIPERS sample by means of a colour criterion based on the $(U-V)$ bimodality (Fritz et al. 2014) and by means of the NUVrK diagram devised by Arnouts et al. (2013). I discuss the differences between the two definition, e.g. the reddened active galaxies that are misclassified when relying on $(U-V)$ instead of NUVrK. In the latter, I can also distinguish a "green valley" in which star-forming galaxies are in transition towards the passive *locus*. Spectral features of the VIPERS galaxies, namely D_n4000 and EW([OII]) measurements, represent useful information information to test this new classification. I find that the transition mass above which the GSMF is dominated by red galaxies is about $\log(\mathcal{M}_{\mathrm{cross}}/\mathcal{M}_\odot) \simeq 10.4$ at $z \simeq 0.55$ and evolves proportional to $(1+z)^3$. Things slightly change if one uses the NUVrK diagram: passive objects overcome active ones above $\log(\mathcal{M}_{\mathrm{cross}}/\mathcal{M}_\odot) \simeq 10.7$ at $z \simeq 0.55$ with a redshift evolution $\propto (1+z)^{4.5}$.

- The number density of the red sample shows an evolution that depends on stellar mass, being steeper at lower masses. At high stellar masses, the quenching of active galaxies has not been thoroughly studied because of their rareness. I obtained a first impressive result with VIPERS, by detecting at $z \simeq 1$ a significant number of very massive active galaxies with $\log(\mathcal{M}/\mathcal{M}_\odot) \geqslant 11.4$, which have all migrated onto the red sequence by $z = 0.6$, i.e. in about 2 Gyrs.

The first data release of VIPERS allowed also to study the dependency of the GSMF on galaxy density contrast (δ), which has been calculated exploiting both spectroscopic and photometric redshifts. The unprecedented volume at $z = 0.5$–0.9, and the high sampling rate, make VIPERS the ideal survey to reconstruct cosmic environment in the 3-dimensional space. I identified regions of low (high) density on the basis of the $1+\delta$ distribution, selecting objects in the first (fourth) quartile. By means of the mock catalogues mentioned above I verified the reliability of this classification, which is not impaired by the observational strategy (e.g., the gaps between VIMOS quadrants). After estimating the stellar mass function of galaxies in the low- and high-density regions (LD and HD, respectively) I achieve the following results.

- Rescaling the mass functions in order to compare their shape, I find that the exponential tail is higher in HD than in LD. This difference remains significant also when I restrict the comparison to the passive sample alone,

and it is marginally significant considering only active galaxies. I emphasise that the difference between the opposite environments is clearly visible in VIPERS thanks to its larger statistics: previous surveys like zCOSMOS (Bolzonella et al. 2010) hardly detected the massive objects that determine such an enhancement in overdense regions.

- Examining this finding in the context given by the literature, the contribution of this work is clear: it adds important clues in favour of a major role of the environment in galaxy evolution. The piece of evidence shown here is in agreement with previous studies (e.g. Bundy et al. 2006; Bolzonella et al. 2010; Annunziatella et al. 2014); the present analysis not only strengthens but also extends their results.

- In particular, the Schechter parameters of the passive mass function provide a robust test of the phenomenological model of Peng et al. (2010b, also referred as P10). The model assumes the shape of the passive GSMF resulting the combined effect of two quenching mechanisms, *mass* and *environment quenching*, along with (post-quenching) dry mergers. As expected in P10 the value of $\mathcal{M}_\star$ is larger in HD than LD. It is more difficult to confirm the predictions related to the active galaxies, because the parametrization of their stellar mass function is affected by larger uncertainties. Nevertheless, at two (out of three) z-bins the GSMFs of VIPERS show the same trends found in P10, e.g. the α parameter in LD is expected to be less negative for the passive than the active sample.

- Turning to the GSMF evolution across cosmic time, I use the P10 formalism to interpret the observations. I evolve the VIPERS galaxies at $0.8 < z < 0.9$ to lower redshifts, comparing the resulting GSMFs (in LD and HD) to the observed ones. I restrict this task to the passive mass functions, while for the active sample a larger dataset is needed, to reduce the uncertainties at high masses. In LD, the GSMF evolution can be explained accounting for mass quenching only. In HD, this is not sufficient, and the introduction of galaxy major mergers (according to the P10 recipe) improves the agreement between the predicted GSMF and the observed one.

These results represent a first step to investigate the environmental effects at intermediate redshifts. In forthcoming studies I shall make use of more refined models to describe, also in a quantitative way, the evolution of the stellar mass function. Galaxy pairs in the VIPERS field may provide better constraints to merger rates, and by means of cosmological simulations should it should be possible to extend the analysis to the underlying dark matter distribution. The completion of the survey will result in further improvements, thanks to the larger volume probed, and the increased number of spectroscopic measurements.

Bibliography

Abazajian, K. N., Adelman-McCarthy, J. K., Agüeros, M. A., et al. 2009, ApJS, 182, 543

Abbas, U., & Sheth, R. K. 2005, MNRAS, 364, 1327

—. 2006, MNRAS, 372, 1749

Amara, A., Lilly, S., Kovac, K., et al. 2012, MNRAS, 12

Annunziatella, M., Biviano, A., Mercurio, A., et al. 2014, A&A, accepted, arXiv:1408.6356

Arnouts, S., Cristiani, S., Moscardini, L., et al. 1999, MNRAS, 310, 540

Arnouts, S., Le Floch, E., Chevallard, J., et al. 2013, 67, 1

Baldry, I., Balogh, M., Bower, R., et al. 2006, MNRAS, 373, 469

Baldry, I., Glazebrook, K., & Driver, S. 2008, MNRAS, 388, 945

Baldry, I., Driver, S., Loveday, J., et al. 2012, MNRAS, 421, 621

Balogh, M., Baldry, I., Nichol, R., et al. 2004, ApJ, 615, L101

Barnes, J. E., & Hernquist, L. E. 1991, ApJ, 370, L65

Bassett, R., Papovich, C., Lotz, J. M., et al. 2013, ApJ, 770, 58B

Bastian, N., Covey, K. R., & Meyer, M. R. 2010, ARA&A, 48, 339

Behroozi, P., Wechsler, R., & Conroy, C. 2013, ApJ, 762, L31

Behroozi, P. S., Conroy, C., & Wechsler, R. H. 2010, ApJ, 717, 379

Bel, J., Marinoni, C., Granett, B. R., et al. 2014, A&A, 563, A37

Bell, E., McIntosh, D., Katz, N., & Weinberg, M. 2003, ApJS, 149, 289

Bell, E., Zheng, X., Papovich, C., et al. 2007, ApJ, 663, 834

Bell, E., Wolf, C., Meisenheimer, K., et al. 2004, ApJ, 608, 752

Bell, E. F., & de Jong, R. S. 2001, ApJ, 550, 212

Bell, E. F., & Kennicutt, Jr., R. C. 2001, ApJ, 548, 681

Bell, E. F., Papovich, C., Wolf, C., et al. 2005, ApJ, 625, 23

Benson, A., Bower, R., Frenk, C., et al. 2003, ApJ, 599, 38

Bertelli, G., Bressan, A., Chiosi, C., Fagotto, F., & Nasi, E. 1994, A&AS

Bertin, E., & Arnouts, S. 1996, A&AS, 117, 393

Bielby, R., Hudelot, P., McCracken, H., et al. 2012, A&A, 545, A23

Birnboim, Y., & Dekel, A. 2003, MNRAS, 345, 349

Blanton, M., Eisenstein, D., Hogg, D., Schlegel, D., & Brinkmann, J. 2005, ApJ, 629, 143

Blanton, M. R. 2006, ApJ, 648, 268

Blanton, M. R., & Moustakas, J. 2009, ARA&A, 47, 159

Boissier, S., Buat, V., & Ilbert, O. 2010, A&A, 522, A18

Bolzonella, M., Miralles, J.-M., & Pelló, R. 2000, A&A, 363, 476

Bolzonella, M., Kovač, K., Pozzetti, L., et al. 2010, A&A, 524, A76

Borch, A., Meisenheimer, K., Bell, E., et al. 2006, A&A, 453, 869

Boselli, A., & Gavazzi, G. 2006, PASP, 118, 517

Bottini, D., Garilli, B., Maccagni, D., et al. 2005, PASP, 117, 996

Bouchet, P., Lequeux, J., Maurice, E., Prevot, L., & Prevot-Burnichon, M. 1985, A&A, 149, 330

Bower, R., Benson, A., Malbon, R., et al. 2006, MNRAS, 370, 645

Bower, R., Vernon, I., Goldstein, M., et al. 2010, MNRAS, 407, 2017

Boylan-Kolchin, M., Springel, V., White, S., Jenkins, A., & Lemson, G. 2009, MNRAS, 398, 1150

Brown, M. J. I., Dey, A., Jannuzi, B. T., et al. 2007, ApJ, 654, 858

Bruzual, G., & Charlot, S. 2003, MNRAS, 344, 1000

Buat, V., Noll, S., Burgarella, D., et al. 2012, A&A, 545, A141

Bundy, K., Ellis, R., Conselice, C., et al. 2006, ApJ, 651, 120

Bundy, K., Scarlata, C., Carollo, C., et al. 2010, ApJ, 719, 1969

Buzzoni, A. 1989, ApJS, 71, 817

Calvi, R., Poggianti, B. M., Vulcani, B., & Fasano, G. 2013, MNRAS, 432, 3141

Calzetti, D., Armus, L., Bohlin, R., et al. 2000, ApJ, 533, 682

Calzetti, D., Kinney, A. L., & Storchi-Bergmann, T. 1994, ApJ, 429, 582

Cappellari, M., Emsellem, E., Krajnovi, D., et al. 2011, MNRAS, 416, 1680

Cappellari, M., McDermid, R. M., Alatalo, K., et al. 2013, MNRAS, 432, 1862

Caputi, K. I., Lilly, S. J., Aussel, H., et al. 2008, ApJ, 680, 939

Cardelli, J. A., Clayton, G. C., & Mathis, J. S. 1989, ApJ, 345, 245

Carollo, C. M., Cibinel, A., Lilly, S. J., et al. 2014, ArXiv e-prints, 23

Cassisi, S. 2004, Mem. Soc. Astron. Italiana

Cavuoti, S., Brescia, M., Longo, G., & Mercurio, A. 2012, A&A, 546, A13

Chabrier, G. 2003, PASP, 115, 763

Chandrasekhar, S. 1943, ApJ, 97, 255

Charlot, S., & Bruzual, A. G. 1991, ApJ, 367, 126

Charlot, S., & Fall, S. 2000, ApJ, 539, 718

Charlot, S., Kauffmann, G., Longhetti, M., et al. 2002, MNRAS, 330, 876

Charlton, J. C., Ding, J., Zonak, S. G., et al. 2003, ApJ, 589, 111

Chary, R., & Elbaz, D. 2001, ApJ, 556, 562

Chen, H.-W., Wild, V., Tinker, J. L., et al. 2010, ApJ, 724, L176

Chevallard, J., Charlot, S., Wandelt, B., & Wild, V. 2013, MNRAS, 432, 2061

Chiappetti, L., Clerc, N., Pacaud, F., et al. 2012, ArXiv e-prints

Chiosi, ., Bertelli, ., & Bressan, . 1988, A&A, 196, 84

Ciesla, L., Boquien, M., Boselli, A., et al. 2014, A&A, 565, A128

Cimatti, A., Daddi, E., & Renzini, A. 2006, A&A, 453, L29

Ciotti, L., Ostriker, J. P., & Proga, D. 2009, ApJ, 699, 89

Cirasuolo, M., McLure, R., Dunlop, J., et al. 2010, MNRAS, 401, 1166

Clauwens, B., Schaye, J., & Franx, M. 2014, 12

Coil, A., Blanton, M., Burles, S., et al. 2011, ApJ, 741, 8

Cole, S., Lacey, C. G., Baugh, C. M., & Frenk, C. S. 2002, MNRAS, 319, 168

Cole, S., Norberg, P., Baugh, C., et al. 2001, MNRAS, 326, 255

Coleman, G. D., Wu, C.-C., & Weedman, D. W. 1980, ApJS, 43, 393

Collister, A. A., & Lahav, O. 2004, PASP, 116, 345

Conroy, C. 2013, ArXiv e-prints, arXiv:1301.7095

Conroy, C., & Gunn, J. 2010, ApJ, 712, 833

Conroy, C., Gunn, J., & White, M. 2009, ApJ, 699, 486

Conroy, C., & Wechsler, R. H. 2009, ApJ, 696, 620

Conseil, S., Vibert, D., Amouts, S., et al. 2011, in Astronomical Society of the Pacific Conference Series, Vol. 442, Astronomical Data Analysis Software and Systems XX, ed. I. Evans, A. Accomazzi, D. Mink, & A. Rots, 107

Cool, R., Moustakas, J., Blanton, M., et al. 2013, ArXiv e-prints, arXiv:1303.2672

Cool, R. J., Eisenstein, D. J., Kochanek, C. S., et al. 2012, ApJ, 748, 10

Cooper, M., Newman, J., Madgwick, D., et al. 2005, ApJ, 634, 833

Cooper, M., Newman, J., Weiner, B., et al. 2008, MNRAS, 383, 1058

Cooper, M., Coil, A., Gerke, B., et al. 2010, MNRAS, 409, 337

Cooper, M. C., Newman, J. A., Coil, A. L., et al. 2007, MNRAS, 376, 1445

Cooper, M. C., Griffith, R. L., Newman, J. A., et al. 2012, MNRAS, 419, 3018

Coupon, J., Ilbert, O., Kilbinger, M., et al. 2009, A&A, 500, 981

Cowie, L., Songaila, A., Hu, E., & Cohen, J. 1996, AJ, 112, 839

Cowie, L. L., & Songaila, A. 1977, Nature, 266, 501

Croton, D., Springel, V., White, S., et al. 2006, MNRAS, 365, 11

Cucciati, O., Iovino, A., Marinoni, C., et al. 2006, A&A, 458, 39

Cucciati, O., Iovino, A., Kovac, K., et al. 2010, A&A, 524, A2

Cucciati, O., Granett, B. R., Branchini, E., et al. 2014, A&A, 565, A67

da Cunha, E., Charlot, S., & Elbaz, D. 2008, MNRAS, 388, 1595

Daddi, E., Dickinson, M., Morrison, G., et al. 2007, ApJ, 670, 156

Dale, D. A., Helou, G., Contursi, A., Silbermann, N. A., & Kolhatkar, S. 2001, ApJ, 549, 215

Dave, R., Katz, N., Oppenheimer, B. D., Kollmeier, J. A., & Weinberg, D. H. 2013, MNRAS, 434, 2645

Davidzon, I., Bolzonella, M., Coupon, J., et al. 2013, A&A, 558, A23

Davis, M., & Geller, M. J. 1976, ApJ, 208, 13

de la Torre, S., Guzzo, L., Peacock, J., et al. 2013, A&A, 557, A54

De La Torre, S., Guzzo, L., Kovač, K., et al. 2010, MNRAS, 409, 867

De Lucia, G., & Blaizot, J. 2007, MNRAS, 375, 2

De Lucia, G., Weinmann, S., Poggianti, B. M., Aragón-Salamanca, A., & Zaritsky, D. 2012, MNRAS, 423, 1277

de Ravel, L., Kampczyk, P., Le Fèvre, O., et al. 2011, ArXiv e-prints

Dekel, A., Sari, R., & Ceverino, D. 2009a, ApJ, 703, 785

Dekel, A., & Silk, J. 1986, ApJ, 303, 39

Dekel, A., Birnboim, Y., Engel, G., et al. 2009b, Nature, 457, 451

Delvecchio, I., Gruppioni, C., Pozzi, F., et al. 2014, MNRAS, 439, 2736

Di Matteo, T., Springel, V., & Hernquist, L. 2005, Nature, 433, 604

Di Porto, C., Branchini, E., Bel, J., et al. 2014, A&A, submitted

Dickinson, M., Papovich, C., Ferguson, H., & Budavári, T. 2003, ApJ, 587, 25

Dodelson, S. 2003, Modern cosmology (Amsterdam (Netherlands): Academic Press), XIII + 440 p.

Dotter, A., Chaboyer, B., Jevremović, D., et al. 2008, ApJS, 178, 89

Doyle, M. T., Drinkwater, M. J., Rohde, D. J., et al. 2005, MNRAS, 361, 34

Draine, B. 2003, ARA&A, 41, 241

Dressler, A. 1980, ApJ, 236, 351

Dressler, A., Oemler, A., Poggianti, B. M., et al. 2013, ApJ, 770, 62

Drory, N., Bundy, K., Leauthaud, A., et al. 2009, ApJ, 707, 1595

Eadie, W. T., Drijard, D., & James, F. E. 1971, Statistical methods in experimental physics

Efstathiou, G. 2000, MNRAS, 317, 697

Efstathiou, G., Ellis, R. S., & Peterson, B. A. 1988, MNRAS, 232, 431

Elbaz, D., Daddi, E., Le Borgne, D., et al. 2007, A&A, 468, 33

Faber, S. M., Willmer, C. N. A., Wolf, C., et al. 2007, ApJ, 665, 265

Faber, . 1972, A&A, 20

—. 1977, Evolution of Galaxies and Stellar Populations

Farouki, R., & Shapiro, S. L. 1981, ApJ, 243, 32

Fasano, G., Marmo, C., Varela, J., et al. 2006, A&A, 445, 805

Felten, J. 1976, ApJ, 207, 700

Ferraro, ., FusiPecci, ., & Buonanno, . 1992, MNRAS, 256, 376

Ferreras, I., Trujillo, I., Marmol-Queralto, E., et al. 2014, MNRAS, 444, 906

Finlator, K., Dave, R., & Oppenheimer, B. D. 2007, MNRAS, 376, 1861

Fioc, M., & Rocca-Volmerange, B. 1997, A&A, 326, 950

Fitzpatrick, . 2004, Astrophysics of Dust, 309

Fontana, A., Donnarumma, I., Vanzella, E., et al. 2003, ApJ, 594, L9

Fontana, A., Pozzetti, L., Donnarumma, I., et al. 2004, A&A, 424, 23

Fontana, A., Salimbeni, S., Grazian, A., et al. 2006, A&A, 459, 745

Fontanot, F. 2014, MNRAS, 442, 3138

Fontanot, F., De Lucia, G., Monaco, P., Somerville, R., & Santini, P. 2009, MNRAS, 397, 1776

Fritz, A., Ziegler, B. L., Bower, R. G., Smail, I., & Davies, R. L. 2005, MNRAS, 358, 233

Fritz, A., Scodeggio, M., Ilbert, O., et al. 2014, 563, A92

Furlong, M., Bower, R. G., Theuns, T., et al. 2014, ArXiv e-prints

Gallagher, J. S., Hunter, D. A., & Bushouse, H. 1989, AJ, 97, 700

Gallazzi, A., Bell, E. F., Zibetti, S., Brinchmann, J., & Kelson, D. D. 2014, ApJ, 788, 72

Gallazzi, A., Bell, E., Wolf, C., et al. 2009, ApJ, 690, 1883

Garilli, B., Fumana, M., Franzetti, P., et al. 2010, PASP, 122, 827

Garilli, B., Paioro, L., Scodeggio, M., et al. 2012, PASP, 124, 1232

Garilli, B., Guzzo, L., Scodeggio, M., et al. 2014, A&A, 562, A23

Gehrels, N. 1986, ApJ, 303, 336

Genel, S., Vogelsberger, M., Springel, V., et al. 2014, MNRAS, 445, 175

Gilbank, D. G., Baldry, I. K., Balogh, M. L., Glazebrook, K., & Bower, R. G. 2010, MNRAS, 405, no

Giocoli, C., Tormen, G., Sheth, R., & van den Bosch, F. 2010, MNRAS, 404, 502

Giodini, S., Finoguenov, A., Pierini, D., et al. 2012, A&A, 538, A104

Girardi, L., Bressan, A., Bertelli, G., & Chiosi, C. 2000, A&AS, 141, 371

Gómez, P. L., Nichol, R. C., Miller, C. J., et al. 2003, ApJ, 584, 210

Grützbauch, R., Conselice, C. J., Varela, J., et al. 2011, MNRAS, 411, 929

Guillaume, M., Llebaria, A., Aymeric, D., Arnouts, S., & Milliard, B. 2006, in Society of Photo-Optical Instrumentation Engineers (SPIE) Conference Series, Vol. 6064, Society of Photo-Optical Instrumentation Engineers (SPIE) Conference Series, ed. E. Dougherty, J. Astola, K. Egiazarian, N. Nasrabadi, & S. Rizvi, 332–341

Gunn, J. E., & Gott, J. R. I. 1972, ApJ, 176, 1

Guo, Q., White, S., Angulo, R., et al. 2013, MNRAS, 428, 1351

Guo, Q., White, S., Boylan-Kolchin, M., et al. 2011, MNRAS, 413, 101

Guzzo, L., Scodeggio, M., Garilli, B., et al. 2014, A&A, 566, A108

Hammersley, ., Christensen, ., Dekker, ., et al. 2010, The Messenger, 142, 8

Heavens, A. F., Jimenez, R., & Lahav, O. 2000, MNRAS, 317, 965

Henriques, B., Thomas, P., Oliver, S., & Roseboom, I. 2009, MNRAS, 396, 535

High, F. W., Stubbs, C. W., Rest, A., Stalder, B., & Challis, P. 2009, AJ, 138, 110

Hogg, D., Blanton, M., Strateva, I., et al. 2002, AJ, 124, 646

Hopkins, P. F., Bundy, K., Croton, D., et al. 2010a, ApJ, 715, 202

Hopkins, P. F., Croton, D., Bundy, K., et al. 2010b, ApJ, 724, 915

Howarth, . 1983, MNRAS, 203, 301

Hunter, D. A. 1994, AJ, 107, 565

Ilbert, O., Tresse, L., Zucca, E., et al. 2005, A&A, 439, 863

Ilbert, O., Arnouts, S., McCracken, H., et al. 2006, A&A, 457, 841

Ilbert, O., Capak, P., Salvato, M., et al. 2009, ApJ, 690, 1236

Ilbert, O., Salvato, M., Le Floc'h, E., et al. 2010, ApJ, 709, 644

Ilbert, O., McCracken, H. J., Le Fèvre, O., et al. 2013, A&A, 556, A55

Inoue, A. K. 2005, MNRAS, 359, 171

Iovino, A., Cucciati, O., Scodeggio, M., et al. 2010, A&A, 509, A40+

Jansen, R. A., Franx, M., & Fabricant, D. 2001, ApJ, 551, 825

Jonsson, P., Groves, B. A., & Cox, T. J. 2010, MNRAS, 403, 17

Kajisawa, M., Ichikawa, T., Tanaka, I., et al. 2009, ApJ, 702, 1393

Kampczyk, P., Lilly, S. J., de Ravel, L., et al. 2013, ApJ, 762, 43

Kauffmann, G., White, S. D. M., Heckman, T. M., et al. 2004, MNRAS, 353, 713

Kauffmann, G., Heckman, T., White, S., et al. 2003a, MNRAS, 341, 33

—. 2003b, MNRAS, 341, 54

Keenan, R. C., Foucaud, S., De Propris, R., et al. 2014, arXiv:1408.3468

Kennicutt, Jr., R. C. 1992, ApJ, 388, 310

—. 1998, ARA&A, 189

Kereš, D., Katz, N., Weinberg, D. H., & Dave, R. 2005, MNRAS, 363, 2

Kewley, L. J., & Dopita, M. A. 2002, ApJS, 142, 35

Kewley, L. J., Geller, M. J., & Jansen, R. A. 2004, AJ, 127, 2002

Kitzbichler, M. G., & White, S. D. M. 2008, MNRAS, 391, 1489

Knobel, C., Lilly, S. J., Woo, J., & Kovac, K. 2014, 22

Koo, D. C. 1985, AJ, 90, 418

Kovač, K., Lilly, S., Knobel, C., et al. 2010a, ApJ, 718, 86

Kovač, K., Lilly, S., Cucciati, O., et al. 2010b, ApJ, 708, 505

Kriek, M., Labbé, I., Conroy, C., et al. 2010, ApJ, 722, L64

Kroupa, P. 2001, MNRAS, 322, 231

La Barbera, F., Ferreras, I., Vazdekis, A., et al. 2013, 433, 3017

Lamareille, F. 2010, A&A, 509, A53

Lanzetta, K. M., Yahil, A., & Fernández-Soto, A. 1996, Nature, 381, 759

Larson, R. B., Tinsley, B. M., & Caldwell, C. N. 1980, ApJ, 237, 692

Le Borgne, J.-F., Bruzual, G., Pell, R., et al. 2003, A&A, 402, 433

Le Fèvre, O., Saisse, M., Mancini, D., et al. 2003, in Instrument Design and Performance for Optical/Infrared Ground-based Telescopes, ed. M. Iye & A. F. M. Moorwood, Vol. 4841, 1670–1681

Le Févre, O., Vettolani, G., Garilli, B., et al. 2005, A&A, 439, 845

Leger, ., & Puget, . 1984, A&A, 137

Lejeune, T., Cuisinier, F., & Buser, R. 1997, A&AS, 125, 229

Lejeune, T., & Schaerer, D. 2001, A&A, 366, 538

Lemson, G., & Virgo Consortium, T. 2006, ArXiv e-prints

Lewis, I., Balogh, M., De Propris, R., et al. 2002, MNRAS, 334, 673

Li, C., & White, S. D. M. 2009, MNRAS, 398, 2177

Lilly, S., Le Févre, O., Renzini, A., et al. 2007, ApJS, 172, 70

Lilly, S., Le Brun, V., Maier, C., et al. 2009, ApJS, 184, 218

Lin, L., Koo, D., Weiner, B., et al. 2007, ApJ, 660, L51

Lin, L., Cooper, M. C., Jian, H.-Y., et al. 2010, ApJ, 718, 1158

López-Sanjuan, C., Le Fèvre, O., de Ravel, L., et al. 2011, A&A, 530, A20

López-Sanjuan, C., Le Fèvre, O., Ilbert, O., et al. 2012, A&A, 548, A7

López-Sanjuan, C., Cenarro, A. J., Hernández-Monteagudo, C., et al. 2014, 18

Lotz, J. M., Papovich, C., Faber, S. M., et al. 2013, ApJ, 773, 154

Lu, T., Gilbank, D. G., McGee, S. L., Balogh, M. L., & Gallagher, S. 2012a, MNRAS, 420, 126

Lu, Y., Mo, H., Katz, N., & Weinberg, M. 2012b, MNRAS, 421, 1779

MacArthur, L., McDonald, M., Courteau, S., & Jesús González, J. 2010, ApJ, 718, 768

Maeder, A., & Meynet, G. 2012, Reviews of Modern Physics, 84, 25

Maier, C., Lilly, S., Zamorani, G., et al. 2009, ApJ, 694, 1099

Małek, K., Solarz, A., Pollo, A., et al. 2013, A&A, 557, A16

Man, A. W. S., Zirm, A. W., & Toft, S. 2014, ArXiv e-prints, arXiv:1410.3479

Mannucci, F., Cresci, G., Maiolino, R., Marconi, A., & Gnerucci, A. 2010, MNRAS, 408, 2115

Maraston, C. 2005, MNRAS, 362, 799

Maraston, C., Pforr, J., Renzini, A., et al. 2010, MNRAS, 407, 830

Maraston, C., Pforr, J., Henriques, B. B. M., et al. 2013, MNRAS, 25, 1

Marchesini, D., van Dokkum, P., Förster Schreiber, N., et al. 2009, ApJ, 701, 1765

Marchesini, D., Whitaker, K., Brammer, G., et al. 2010, ApJ, 725, 1277

Marchetti, A., Granett, B., Guzzo, L., et al. 2013, MNRAS, 428, 1424

Marigo, P., & Girardi, L. 2007, A&A, 469, 239

Marigo, P., Girardi, L., Bressan, A., et al. 2008, A&A, 482, 883

Marinoni, C., Davis, M., Newman, J. A., & Coil, A. L. 2002, ApJ, 580, 122

Martin, C. L. 2006, ApJ, 647, 222

Marulli, F., Bolzonella, M., Branchini, E., et al. 2013, A&A, 557, A17

Mathis, J. S. 1990, ARA&A, 28, 37

McGee, S. L., Goto, R., & Balogh, M. L. 2014, MNRAS, 438, 3188

Meneux, B., Guzzo, L., de La Torre, S., et al. 2009, A&A, 505, 463

Michałowski, M. J., Dunlop, J. S., Cirasuolo, M., et al. 2012, A&A, 541, A85

Michałowski, M. J., Hayward, C. C., Dunlop, J. S., et al. 2014, ArXiv e-prints

Micheletti, D., Iovino, A., Hawken, A. J., et al. 2014, ArXiv e-prints

Mignoli, M., Zamorani, G., Scodeggio, M., et al. 2009, A&A, 493, 39

Mignoli, M., Vignali, C., Gilli, R., et al. 2013, A&A, 556, A29

Mihos, J. C., & Hernquist, L. 1994, ApJ, 425, L13

—. 1996, ApJ, 464, 641

Mitchell, P. D., Lacey, C. G., Baugh, C. M., & Cole, S. 2013, MNRAS, 435, 87

Mo, H. J., & White, S. D. M. 1996, MNRAS, 282, 347

Moore, B., Katz, N., Lake, G., Dressler, A., & Oemler, A. 1996, Nature, 379, 613

Moore, B., Lake, G., & Katz, N. 1998, ApJ, 495, 139

Moore, B., Lake, G., Quinn, T., & Stadel, J. 1999, MNRAS, 304, 465

Moresco, M., Pozzetti, L., Cimatti, A., et al. 2010, ArXiv e-prints, arXiv:1009.3376

—. 2013, A&A, 558, A61

Mortlock, A., Conselice, C., Bluck, A., et al. 2011, MNRAS, 413, 2845

Mostek, N., Coil, A. L., Moustakas, J., Salim, S., & Weiner, B. J. 2012, ApJ, 746, 124

Moster, B., Naab, T., & White, S. 2013, MNRAS, 428, 3121

Moster, B., Somerville, R., Newman, J., & Rix, H.-W. 2011, ApJ, 731, 113

Moster, B. P., Somerville, R. S., Maulbetsch, C., et al. 2010, ApJ, 710, 903

Moustakas, J., Kennicutt, Jr., R. C., & Tremonti, C. A. 2006, ApJ, 642, 775

Moustakas, J., Coil, A., Aird, J., et al. 2013, ApJ, 767, 50

Muldrew, S. I., Croton, D. J., Skibba, R. A., et al. 2012, MNRAS, 419, 2670

Mutch, S. J., Poole, G. B., & Croton, D. J. 2013, MNRAS, 428, 2001

Muzzin, A., Marchesini, D., van Dokkum, P. G., et al. 2009a, ApJ, 701, 1839

Muzzin, A., van Dokkum, P., Franx, M., et al. 2009b, ApJ, 706, L188

Muzzin, A., Wilson, G., Yee, H. K. C., et al. 2012, ApJ, 746, 188

Muzzin, A., Marchesini, D., Stefanon, M., et al. 2013, ApJS, 206, 8

Newman, J., & Davis, M. 2002, ApJ, 564, 567

Noeske, K., Weiner, B., Faber, S., et al. 2007, ApJ, 660, L43

Noll, S., Burgarella, D., Giovannoli, E., et al. 2009, A&A, 507, 1793

Nulsen, P. E. J. 1982, MNRAS, 198, 1007

Oemler, A. 1974, ApJ, 194, 1

Okamoto, T., Shimizu, I., & Yoshida, N. 2014, PASJ, 66, 70

Oke, J. 1974, ApJS, 27, 21

Oppenheimer, B. D., & Dave, R. 2006, MNRAS, 373, 1265

Ostriker, J. P., & Tremaine, S. D. 1975, ApJ, 202, L113

Pacifici, C., Kassin, S., Weiner, B., Charlot, S., & Gardner, J. 2013, ApJ, 762, L15

Papovich, C., Dickinson, M., & Ferguson, H. C. 2001, ApJ, 559, 620

Pasquali, A., van den Bosch, F. C., Mo, H. J., Yang, X., & Somerville, R. 2009, MNRAS, 394, 38

Pello, R., Miralles, J. M., Le Borgne, J.-F., et al. 1996, A&A

Peng, C. Y., Ho, L. C., Impey, C. D., & Rix, H.-W. 2010a, AJ, 139, 2097

Peng, Y.-j., Lilly, S. J., Renzini, A., & Carollo, M. 2012, ApJ, 757, 4

Peng, Y.-j., Lilly, S., Kovač, K., et al. 2010b, ApJ, 721, 193

Pérez-González, P., Rieke, G., Villar, V., et al. 2008, ApJ, 675, 234

Pforr, J., Maraston, C., & Tonini, C. 2012, MNRAS, 422, 3285

Pickles, A. J. 1985, ApJS, 59, 33

Pierini, D., Gordon, K. D., Witt, A. N., & Madsen, G. J. 2004, ApJ, 617, 1022

Pietrinferni, A., Cassisi, S., Salaris, M., & Castelli, F. 2004, ApJ, 612, 168

Polletta, M., Tajer, M., Maraschi, L., et al. 2007, ApJ, 663, 81

Postman, M., & Geller, M. J. 1984, ApJ, 281, 95

Pozzetti, L., Bolzonella, M., Lamareille, F., et al. 2007, A&A, 474, 443

Pozzetti, L., Bolzonella, M., Zucca, E., et al. 2010, A&A, 523, A13

Pozzi, F., Vignali, C., Comastri, A., et al. 2007, A&A, 468, 603

Prada, F., Klypin, A., Cuesta, A., Betancort-Rijo, J., & Primack, J. 2012, MNRAS, 423, 3018

Press, W. H., Teukolsky, S. A., & Vetterling, W. T. 2002, Numerical Recipes in C++: the art of scientific computing

Prévot, M., Lequeux, J., Prevot, L., Maurice, E., & Rocca-Volmerange, B. 1984, A&A, 132, 389

Quider, A. M., Nestor, D. B., Turnshek, D. A., et al. 2011, AJ, 141, 137

Rao, S. M., Belfort-Mihalyi, M., Turnshek, D. A., et al. 2011, MNRAS, 416, 1215

Rao, S. M., Turnshek, D. A., & Nestor, D. B. 2006, ApJ, 636, 610

Renzini, A., & Pecci, F. F. 1988, ARA&A, 26, 199

Rudnick, G., Rix, H.-W., Franx, M., et al. 2003, ApJ, 599, 847

Rupke, D. S., Veilleux, S., & Sanders, D. B. 2002, ApJ, 570, 588

Salim, S., Charlot, S., Rich, R. M., et al. 2005, ApJ, 619, L39

Salpeter, E. 1955, ApJ, 121, 161

Sandage, A., Tammann, G. A., & Yahil, A. 1979, ApJ, 232, 352

Sandage, A., & Visvanathan, N. 1978, ApJ, 225, 742

Santini, P., Fontana, A., Grazian, A., et al. 2012, A&A, 538, A33

Schaller, G., Schaerer, D., Meynet, G., & Maeder, A. 1992, A&AS, 96, 269

Schawinski, K., Urry, C. M., Simmons, B. D., et al. 2014, MNRAS, 440, 889

Schaye, J., Vecchia, C. D., Booth, C. M., et al. 2010, MNRAS, 402, 1536

Schaye, J., Crain, R. A., Bower, R. G., et al. 2014, ArXiv e-prints, 38

Schechter, P. 1976, ApJ, 203, 297

Schlegel, D. J., Finkbeiner, D. P., & Davis, M. 1998, ApJ, 500, 525

Schmidt, M. 1968, ApJ, 151, 393

Scodeggio, M., Franzetti, P., Garilli, B., Le Fèvre, O., & Guzzo, L. 2009a, The Messenger, 135, 13

Scodeggio, M., Franzetti, P., Garilli, B., et al. 2005, PASP, 117, 1284

Scodeggio, M., Vergani, D., Cucciati, O., et al. 2009b, A&A, 501, 21

Scoville, N., Arnouts, S., Aussel, H., et al. 2013, ApJ, 206, 3

Scrimgeour, M., Davis, T., Blake, C., et al. 2012, MNRAS, 425, 116

Sérsic, J. 1963, Boletin de la Asociacion Argentina de Astronomia, 6, 41

Sheth, R. K. 2005, MNRAS, 364, 796

Silva, L., Granato, G. L., Bressan, A., & Danese, L. 1998, ApJ, 509, 103

Skibba, R. A., Bamford, S. P., Nichol, R. C., et al. 2009, MNRAS, 399, 966

Smith, G., Treu, T., Ellis, R., Moran, S., & Dressler, A. 2005, ApJ, 620, 78

Smith, M. W. L., Gomez, H. L., Eales, S. A., et al. 2012, ApJ, 748, 123

Smith, R. J. 2014, MNRAS, 443, L69

Somerville, R., Hopkins, P., Cox, T., Robertson, B., & Hernquist, L. 2008, MNRAS, 391, 481

Somerville, R., Lee, K., Ferguson, H., et al. 2004, ApJ, 600, L171

Speagle, J. S., Steinhardt, C. L., Capak, P. L., & Silverman, J. D. 2014, ApJS, 214, 15

Spiniello, C., Trager, S., Koopmans, L. V. E., & Conroy, C. 2014, 438, 1483

Springel, V. 2010, ARA&A, 48, 391

Springel, V., Di Matteo, T., & Hernquist, L. 2005a, MNRAS, 361, 776

Springel, V., & Hernquist, L. 2003, MNRAS, 339, 289

Springel, V., White, S., Jenkins, A., et al. 2005b, Nature, 435, 629

Stecher, T. P. 1965, ApJ, 142, 1683

Stecher, T. P., & Donn, B. 1965, ApJ, 142, 1681

Stern, D., Eisenhardt, P., Gorjian, V., et al. 2005, ApJ, 631, 163

Strateva, I., Ivezić, v., Knapp, G., et al. 2001, AJ, 122, 1861

Stratta, G., Maiolino, R., Fiore, F., & D'Elia, V. 2007, ApJ, 661, L9

Takeuchi, T., Yoshikawa, K., & Ishii, T. 2000, ApJS, 129, 1

Thacker, R. J., Tittley, E. R., Pearce, F. R., Couchman, H. M. P., & Thomas, P. A. 2000, MNRAS, 319, 619

Thomas, D., Maraston, C., Schawinski, K., Sarzi, M., & Silk, J. 2010, MNRAS, 404, 1775

Tinsley, B. M. 1980, Fund. Cosmic Phys., 5, 287

Tojeiro, R., Heavens, A. F., Jimenez, R., & Panter, B. 2007, MNRAS, 381, 1252

Tojeiro, R., Wilkins, S., Heavens, A. F., Panter, B., & Jimenez, R. 2009, ApJS, 185, 1

Torrey, P., Vogelsberger, M., Genel, S., et al. 2014, MNRAS, 438, 1985

Totani, T. 2005, New Astronomy Reviews, 49, 205

Tremonti, C. A., Heckman, T. M., Kauffmann, G., et al. 2004, ApJ, 613, 898

Trenti, M., & Stiavelli, M. 2008, ApJ, 676, 767

Treu, T., Auger, M. W., Koopmans, L. V. E., et al. 2010, ApJ, 709, 1195

Treu, T., Ellis, R., Kneib, J.-P., et al. 2003, ApJ, 591, 53

Tuffs, R. J., Popescu, C. C., Völk, H. J., Kylafis, N. D., & Dopita, M. A. 2004, A&A, 419, 821

Tully, ., & Fisher, . 1977, A&A, 54, 661

van den Bosch, F., Aquino, D., Yang, X., et al. 2008, MNRAS, 387, 79

van der Burg, R. F. J., Muzzin, A., Hoekstra, H., et al. 2013, A&A, 557, A15

van der Wel, A., Bell, E., Holden, B., Skibba, R., & Rix, H.-W. 2010, ApJ, 714, 1779

Vergani, D., Scodeggio, M., Pozzetti, L., et al. 2008, A&A, 487, 89

Vergani, D., Zamorani, G., Lilly, S., et al. 2010, A&A, 509, A42

Vogelsberger, M., Genel, S., Springel, V., et al. 2014, Nature, 509, 177

Vulcani, B., Poggianti, B. M., Fasano, G., et al. 2012, MNRAS, 420, 1481

Vulcani, B., Poggianti, B., Oemler, A., et al. 2013, A&A, 550, A58

Wang, L., De Lucia, G., & Weinmann, S. 2013, MNRAS, 793

Weingartner, J., & Draine, B. 2001, ApJ, 548, 296

Weinmann, S., van den Bosch, F., Yang, X., et al. 2006, MNRAS, 372, 1161

Wetzel, A. R., Tinker, J. L., & Conroy, C. 2012, MNRAS, 424, 232

Whitaker, K. E., Labbé, I., van Dokkum, P. G., et al. 2011, ApJ, 735, 86

White, S. D. M., Clowe, D. I., Simard, L., et al. 2005, A&A, 444, 365

Williams, R. J., Quadri, R. F., Franx, M., van Dokkum, P., & Labbé, I. 2009, ApJ, 691, 1879

Wilman, D., Zibetti, S., & Budavári, T. 2010, MNRAS, 406, 1701

Wuyts, S., Labbe, I., Franx, M., et al. 2007, ApJ, 655, 51

Wuyts, S., Förster Schreiber, N., Lutz, D., et al. 2011, ApJ, 738, 106

Xu, C. K., Zhao, Y., Scoville, N., et al. 2012, ApJ, 747, 85

York, D., Adelman, J., Anderson Jr., J., et al. 2000, AJ, 120, 1579

York, D. G., Khare, P., Vanden Berk, D., et al. 2006, MNRAS, 367, 945

Zahid, H., Kewley, L., & Bresolin, F. 2011, ApJ, 730, 137

Zahid, H. J., Yates, R. M., Kewley, L. J., & Kudritzki, R. P. 2013a, ApJ, 763, 92

Zahid, H. J., Kashino, D., Silverman, J. D., et al. 2013b, 19

Zaritsky, D., Kennicutt, Robert C., J., & Huchra, J. P. 1994, ApJ, 420, 87

Zibetti, S., Gallazzi, A., Charlot, S., Pierini, D., & Pasquali, A. 2013, MNRAS, 428, 1479

Zibetti, S., Menard, B., Nestor, D. B., et al. 2007, ApJ, 658, 161

Ziparo, F., Popesso, P., Biviano, A., et al. 2014, MNRAS, 437, 458

Zucca, E., Zamorani, G., Vettolani, G., et al. 1997, A&A, 326, 477

Zucca, E., Ilbert, O., Bardelli, S., et al. 2006, A&A, 455, 879

Zucca, E., Bardelli, S., Bolzonella, M., et al. 2009, A&A, 508, 1217